THE UNIVERSITY OF QUEENSLAND

AUSTRALIA

Flow Physics of a Hypervelocity Mixing Wake with Oxygen Enrichment

David Petty

B.E. (Mechanical and Space), B.Sc. (Mathematics)

A thesis submitted for the degree of Doctor of Philosophy at

The University of Queensland in 2014

The School of Mechanical and Mining Engineering

Abstract

Hypervelocity scramjet engines promise to be an efficient air-breathing propulsion technology capable of performing as part of an access-to-space system. However, difficulties arise when operating a scramjet engine at high altitudes and flight Mach numbers, notably above Mach 10.0. These difficulties arise due to a reduction in captured air flow by the engine, residence time of flow within the engine, and turbulence intensity which facilitates effective fuel-air mixing. Oxygen enrichment is a technique proposed to augment scramjet thrust under these adverse conditions, whereby a small amount of oxygen is mixed with fuel before injection into the engine combustor. Previous experimental studies conducted by Razzaqi and Smart (2011) have shown that Oxygen Enrichment (OxEn) enhances the combustion efficiency of a scramjet by an amount equal to the enrichment percentage. These findings suggest that oxygen enrichment should be considered in the design of scramjet engines. However, the previous studies do not offer sufficient information about the effects of OxEn on the turbulence characteristics of the hypervelocity flow and consequently the physical mechanisms that drive the mixing of fuel and oxygen. Effective design of a scramjet engine which utilises oxygen enrichment requires a thorough understanding of these physical processes. A simplified scramjet engine configuration ground tested at Mach 12.3 and a dynamic pressure of 40.5 kPa, based upon the aforementioned experiments, has been selected to perform as the basis for several numerical simulations to assess the benefits of oxygen enrichment upon fuel-air mixing driven by compressible shear. The Reynolds number of the free shear flow, based upon the core flow conditions ingested by the isolator and the height of the centre-body is 56,650. This engine configuration comprises a planar duct with an intrusive centre-body wherein combustible propellant is injected through a rear-facing slot. The fluid flow which forms down-stream of injection is referred to as a mixing wake.

Reynolds Averaged Navier-Stokes (RANS) is the current standard for the computational analysis of the characteristic turbulent, supersonic fluid flows within a scramjet engine during flight. RANS provides information about the mean flow field as well as key modelled turbulence parameters. Large Eddy Simulation (LES) is a high fidelity numerical methodology which resolves the large scale unsteady behaviour of turbulence flow, enabling a statistical description of the turbulence to be established, but at increased computational expense. Both Reynolds-Averaged Navier-Stokes and Large Eddy simulations of this mixing wake flow are performed in this work. Results from

RANS simulations of the simplified scramjet engine have shown that combustion between fuel and ingested oxygen is promoted by oxygen enrichment. This enhancement has been attributed to greater shearing velocity difference across the mixing layers that form between the ingested and injected fluid streams, as oxygen enrichment results in a slower moving injectant. Consequently, a greater production of turbulence kinetic energy enhances mixing of fuel and ingested air within the mixing layers. Analysis of the turbulence model parameters indicates compressibility effects influence the turbulent flow behaviour, and that turbulence within the mixing layers may not be fully developed.

To test the validity of the previous findings and gain more insight into the effects of oxygen enrichment on the turbulent flow structure, LES of the hypervelocity mixing wake were performed. The LES results showed that the initial mixing layers which develop between the injected fuel and ingested air streams is strongly influenced by compressibility. This is evident from the near-stream-wise oriented vortices which form and slow transverse growth rate of the layers and visible shocklets in the near field. However, reducing compressible effects coincide with a transition in the behaviour of the wake, characterised by dominant large scale span-wise vortices similar to those expected within an incompressible wake. This turbulent regime significantly boosts the spreading rate of the wake and entrainment of oxygen. LES of oxygen enriched fuel injection found that the mixing of ingested oxygen and injection hydrogen was slightly reduced in comparison to the pure fuel injection case. Despite increasing the turbulence production within the initially developing mixing layers, oxygen enrichment caused a delay in the wake roll-up. The dynamic effect of injecting a greater flow rate is to further displace the mixing layers away from the fuel rich core flow. Additionally, greater compressible effects suppress the generation of cross-stream turbulent disturbances that activate the wake roll-up. Mixing of ingested oxygen and fuel remains limited whilst wake roll-up is delayed. Direct comparison of RANS and LES results has shown that the former method reproduces the mean turbulent behaviour of the initial, highly compressible mixing layers. However, the RANS method fails to predict the effects of wake roll-up and subsequently under predicts the mixing of ingested oxygen with injected fuel. This under prediction is exacerbated in the pure fuel injection case as the wake roll-up occurs more rapidly than in the oxygen enriched fuel case. Consequently, RANS predicts that oxygen enrichment augments fuel-air mixing which conflicts with the findings of LES.

Declaration by author

This thesis is composed of my original work, and contains no material previously published or written by another person except where due reference has been made in the text. I have clearly stated the contribution by others to jointly-authored works that I have included in my thesis.

I have clearly stated the contribution of others to my thesis as a whole, including statistical assistance, survey design, data analysis, significant technical procedures, professional editorial advice, and any other original research work used or reported in my thesis. The content of my thesis is the result of work I have carried out since the commencement of my research higher degree candidature and does not include a substantial part of work that has been submitted to qualify for the award of any other degree or diploma in any university or other tertiary institution. I have clearly stated which parts of my thesis, if any, have been submitted to qualify for another award.

I acknowledge that an electronic copy of my thesis must be lodged with the University Library and, subject to the policy and procedures of The University of Queensland, the thesis be made available for research and study in accordance with the *Copyright Act 1968* unless a period of embargo has been approved by the Dean of the Graduate School.

I acknowledge that copyright of all material contained in my thesis resides with the copyright holder(s) of that material. Where appropriate I have obtained copyright permission from the copyright holder to reproduce material in this thesis.

David J. Petty

Publications during candidature

Barth, J. E.; Wheatley, V.; Smart, M. K.; Petty, D. J.; Basore, K. D. (2011).

"Flow Physics Inside a Shape-Transitioning Scramjet Engine." *18th AIAA/3AF International Space Planes and Hypersonic Systems and Technology Conference, Tours, France*. - Barth was responsible for 75% of the analysis, 65% of the interpretation of results, and 85% of drafting and writing. Wheatley was responsible for 10% of the analysis, 20% of the interpretation of results, and 10% of drafting and writing. Smart was responsible for 5% of the analysis, 10% of the interpretation of results, and 5% of drafting and writing. Petty (Candidate) was responsible for 5% of the analysis, 0% of the interpretation of results, and 0% of drafting and writing. Basore was responsible for 5% of the analysis, 0% of the interpretation of results, and 0% of drafting and writing.

Petty, D. J.; Wheatley, V.; Smart, M. K. (2011).

"A Parametric Study of Oxygen Enriched Scramjet Combustion." *11th Australian Space Science Conference, Canberra, ACT, Australia*. - Petty (Candidate) was responsible for 85% of the analysis, 60% of the interpretation of results, and 80% of drafting and writing. Wheatley was responsible for 10% of the analysis, 30% of the interpretation of results, and 15% of drafting and writing. Smart was responsible for 5% of the analysis, 10% of the interpretation of results, and 5% of drafting and writing.

Petty, D. J.; Wheatley, V.; Smart, M. K.; Razzaqi, S. A. (2010).

"Effects of Oxygen Enrichment on Scramjet Performance." *10th Australian Space Science Conference, Brisbane, QLD, Australia*. - Petty (Candidate) was responsible for 75% of the analysis, 60% of the interpretation of results, and 75% of drafting and writing. Wheatley was responsible for 10% of the analysis, 25% of the interpretation of results, and 15% of drafting and writing. Smart was responsible for 10% of the analysis, 10% of the interpretation of results, and 5% of drafting and writing. Razzaqi was responsible for 5% of the analysis, 5% of the interpretation of results, and 5% of drafting and writing.

Publications included in this thesis

Petty, D. J.; Wheatley, V.; Smart, M. K.; Razzaqi, S. A. (2013).

"Effects of Oxygen Enrichment on Scramjet Performance." *AIAA Journal*. Accepted for publication 27 June 2012. - Petty (Candidate) was responsible for 70% of the analysis, 55% of the interpretation of results, and 60% of drafting and writing. Wheatley was responsible for 20% of the analysis, 30% of the interpretation of results, and 25% of drafting and writing. Smart was responsible for 5% of the analysis, 10% of the interpretation of results, and 10% of drafting and writing. Razzaqi was responsible for 5% of the analysis, 5% of the interpretation of results, and 5% of drafting and writing.

Contributions by others to the thesis

I would like to thank Vincent Wheatley for contributing towards to interpretation of Large Eddy Simulation data, specifically regarding the mixing wake flow physics discussed in Chapter 4.

Statement of parts of the thesis submitted to qualify for the award of another degree

No parts of the thesis have been submitted to qualify for the award of another degree.

Acknowledgements

There have been numerous people who have supported this work over the past few years. I would like to take this opportunity to express my appreciation.

Firstly, I would like to thank my wife, Claire for her love, patience, and support during my candidature; I celebrate our friendship and marriage. To my parents, John and Denise, you have always encouraged me to pursue my dreams and supported my endeavours. For this, I thank you.

I thank my supervisor Dr. Vincent Wheatley for his continued guidance throughout my graduate studies. This work has involved a great deal of learning on my part and Vince never turned me away during the challenging times. I would also like to recognise the encouragement from Prof. Michael Smart to undertake this research topic after supervising my space engineering project and undergraduate thesis. In addition, Carlos Pantano-Rubino is due thanks for allowing me the opportunity to study at University of Illinois, Urbana-Champaign for six weeks whilst providing invaluable assistance in establishing my simulations in the VTF framework. Mention must also be made of the contributions Rob Baurle has made in supporting NASA's VULCAN code whilst NASA and UQ maintained a usage agreement. I would also like to thank Sarah Razzaqi for spending time with me to describe her experiment and her research findings. Thanks to all my colleagues in the Center for Hypersonics at UQ including Daniel Oberg, Wilson Chan, Rolf Gehre, James Barth, Dawid Preller, Kevin Basore, and Luke Doherty just to name a few. I wish you all the best with your future pursuits and I'm sure we'll keep in touch.

Finally, I want to acknowledge the financial support provided by the UQ Research Scholarship in addition to the people involved in UQ's High Performance Computing team and the National Computational Infrastructure organisation for maintaining the computer clusters which enable the large simulations performed as part of my studies.

Keywords

Large Eddy Simulation (LES), Scramjet propulsion, Oxygen enrichment, Turbulent mixing, Hypervelocity Flow

Australian and New Zealand Standard Research Classification (ANZSRC)

ANZSRC code: 090107, Hypersonic Propulsion and Hypersonic Aerodynamics, 70%

ANZSRC code: 020303, Fluid Physics, 20%

ANZSRC code 080205, Numerical Computations, 10%

Fields of Research (FoR) Classification

FoR code: 0901, Aerospace Engineering, 70%

FoR code: 0203, Classical Physics, 20%

FoR code 0802, Computational Theory and Mathematics, 10%

Contents

List of Figures **xiii**

List of Tables **xxi**

1 Introduction **1**

1.1 Overview ... 3

1.2 Research Aims ... 6

1.3 Thesis Outline ... 8

2 Literature Review **9**

2.1 Supersonic Combustion Ramjets ... 11

2.1.1 Aero-Vehicle Configurations ... 14

2.1.2 Access-to-Space Trajectories ... 14

2.1.3 Oxygen Enrichment ... 15

2.2 Turbulent Fluid Motion ... 18

2.2.1 Scales of Turbulence ... 18

2.2.2 Turbulence Energy Spectra ... 21

2.2.3 Compressibility effects on turbulence ... 23

2.3 Free-shear Turbulence ... 24

2.3.1 Mixing Layer ... 25

2.3.2 Wake Flow ... 32

2.4 Computational Fluid Dynamics ... 35

2.4.1 Reynolds Averaged Navier-Stokes Simulations ... 36

2.4.2 Large Eddy Simulation ... 42

2.5 Conclusions ... 53

3 Preliminary Simulations **55**

3.1 Trajectory Analysis ... 57

3.2 RANS Numerical Methodology ... 61

3.2.1 Vulcan Solver ... 61

3.2.2 Computational Grid ... 64

3.3 Planar Intake RANS Simulations ... 67

3.3.1 Compressible Flow Features 67
3.4 Rectangular Duct RANS Simulations 68
3.4.1 Compressible flow features 69
3.4.2 Ignition 70
3.4.3 Combustion Efficiency 72
3.4.4 Turbulence Scaling 80
4 Large Eddy Simulation with Pure Fuel Injection 87
4.1 LES Numerical Methodology 89
4.1.1 Virtual Test Facility Solver 90
4.1.2 Computational Grid 92
4.1.3 Boundary Conditions 98
4.2 LES Execution 101
4.2.1 Statistical Convergence 103
4.3 Overall Flow Structure 107
4.3.1 Shear Layer Properties 109
4.3.2 Turbulence Statistics 112
4.3.3 Mixing and Entrainment 123
4.4 Local Flow Structure 132
4.4.1 Near Field Flow Structure 132
4.4.2 Wake Transition 141
4.4.3 Shock-Turbulence Interactions 146
4.4.4 Dominant Wake Field 148
4.5 Conclusions 149
5 Large Eddy Simulations with Oxygen Enriched Fuel Injection 151
5.1 LES Execution 153
5.2 Overall Flow Structure 154
5.2.1 Shear Layer Properties 157
5.2.2 Turbulence Statistics 160
5.2.3 Mixing and Entrainment 165
5.3 Local Flow Structures 170
5.3.1 Near Field Flow Structure 170
5.3.2 Shock-Turbulence Interactions 177

5.4 LES - RANS Comparison 180
5.5 Conclusions 187
6 Conclusions 189
6.1 Principal Findings 191
6.2 Recommendations for Future Work 195
Reference List 199
A1 Governing Equations 213
A1.1 Constitutive Equations of Fluid Mechanics 213
A1.1.1 Conservation of Mass 213
A1.1.2 Conservation of Linear Momentum 213
A1.1.3 Conservation of Total Internal Energy 214
A1.1.4 Conservation of a Passive Scalar 215
A1.2 Equations of State 216
A1.2.1 Ideal Gas Law 216
A1.2.2 Specific Gas Constant 219
A1.2.3 Specific Heat Capacity 219
A1.2.4 Specific Enthalpy and Internal Energy 223
A1.3 Transport Properties 224
A1.4 Compressible Laminar Boundary-Layer 228

List of Figures

Figure 2.1.: Diagram of combustion process within a typical scramjet engine 12

Figure 2.2: Altitude (km) of several accelerating access-to-space trajectories based upon the Standard Atmosphere (NASA, 1976) 15

Figure 2.3: Diagram of combustion process within a scramjet engine utilising oxygen enrichment 16

Figure 2.4: Schematic of the experimental model (units in millimeters) (Razzaqi & Smart, 2011) 17

Figure 2.5: Notional turbulence energy spectra as a function of wave-number 23

Figure 2.6: Schematic of the canonical turbulent mixing layer (Brown & Roshko, 1974) 25

Figure 2.7: Shadowgraphs of the turbulent mixing layer between helium (upper) and nitrogen (lower) with a proprtional Reynolds number of: (i) 20, (ii) 40, and (iii) 80 (Brown & Roshko, 1974) 27

Figure 2.8: Growth rate of the compressible shear layer trend with convective Mach number (Slessor, et al., 2000) 31

Figure 2.9: Aluminium flake visualisations of laminar and turbulent incompressible wake vortex sheets (Williamson, 1996) 33

Figure 2.10: Schematic of the DLR scramjet combustor (Génin & Menon, 2010) 47

Figure 2.11: Instantaneous density-gradient contours taken for (top to bottom): i) the hybrid RANS/LES simulation, and ii) experimental schliren photograph (Potturi & Edwards, 2014). 48

Figure 2.12: Comparison of pressure: a) perspective view of the pressure distribution on the upper and lower strut walls and an iso-surface of temperature (1400 K), and time averaged wall pressure distributions along the lower combustor wall for b) inter H2 injection, and c) combustion (Berglund, et al., 2010) 49

Figure 2.13: Instantaneous iso-surface of the Q criterion superimposed upon contours of the static density gradient magnitude (Simon, et al., 2007)..... 51

Figure 2.14: Cross-sectional contour plots of hydrogen mole fraction within an inlet fuelled scramjet engine (Peterson, et al., 2013)..... 52

Figure 3.1: Schematic of the idealised flow upstream of the scramjet engine..... 58

Figure 3.2: Normalised mass flow rate and Reynolds number of the captured flow. 60

Figure 3.3: Planar intake numerical model (mesh coarsened by a factor of 8 in each direction)64

Figure 3.4: Rectangular duct numerical model (mesh coarsened by a factor of 16 in each direction)..... 66

Figure 3.5: Static density gradient magnitude contour of the flow through the planar intake . 68

Figure 3.6: Contours of static density gradient magnitude (top to bottom): (i) $\phi = 0.0$ $EP = 0.0\%$, (ii) $\phi = 1.0$, $EP = 0.0\%$, and (iii) $\phi = 1.0$, $EP = 10.0\%$ 69

Figure 3.7: Net production rate of atomic hydrogen (top to bottom): (i) $\phi = 1.0$, $EP = 0.0\%$, (ii) $\phi = 1.4$, $EP = 0.0\%$, and (iii) $\phi = 1.0$, $EP = 15.0\%$. 71

Figure 3.8: Combustion efficiency against x/h (left to right): (i) $EP = 0.0\%$, and (ii) $\phi = 1.0$ . . 73

Figure 3.9: Static temperature contours (top to bottom): (i) $\phi = 0.0$, $EP = 0.0\%$, (ii) $\phi = 1.0$, $EP = 0.0\%$, and (iii) $\phi = 1.4$, $EP = 20.0\%$. 74

Figure 3.10: Combustion efficiency against EP (left to right): (i) $x = 9.19h$, and (ii) $x = 18.37h$ where * refers to experimental data (Razzaqi & Smart, 2011). 75

Figure 3.11: Combustion Enhancement Factor against *EP*. 77

Figure 3.12: Oxygen enrichment modified combustion efficiency against *EP* (left to right): (i) $x = 9.19h$, and (ii) $x = 18.37h$ 78

Figure 3.13: Turbulence kinetic energy contours (top to bottom): (i) $\phi = 1.0$, $EP = 5.0\%$, (ii) $\phi = 1.0$, $EP = 10.0\%$, and (iii) $\phi = 1.0$, $EP = 15.0\%$. 79

Figure 3.14: Turbulence Reynolds number cross-stream maximum and contour: (i) $\phi = 1.0$, $EP = 0.0\%$, (ii) $\phi = 1.0$, $EP = 5.0\%$, and (iii) $\phi = 1.2$, $EP = 10.0\%$ 81

Figure 3.15: Taylor length (mm) cross-stream minimum and contour: (i) $\phi = 1.0$, $EP = 0.0\%$, (ii) $\phi = 1.0$, $EP = 5.0\%$, and (iii) $\phi = 1.2$, $EP = 10.0\%$. 83

Figure 3.16: Taylor Reynolds number cross-stream maximum and contour: (i) $\phi = 1.0$, $EP = 0.0\%$, (ii) $\phi = 1.0$, $EP = 5.0\%$, and (iii) $\phi = 1.2$, $EP = 10.0\%$ 84

Figure 3.17: Kolmogorov length (μm) cross-stream minimum and contour: (i) $\phi = 1.0$, $EP = 0.0\%$, (ii) $\phi = 1.0$, $EP = 5.0\%$, and (iii) $\phi = 1.2$, $EP = 10.0\%$ 85

Figure 4.1: Computational Domain and Boundary Condition Schematic 93

Figure 4.2: Contour of the LES grid spacing using: i) Taylor length, ii) Taylor length and flow discontinuities, and iii) restricted Taylor length and flow discontinuities 97

Figure 4.3 Visualisation of the adaptive grid just downstream of injection, taken at the instant $t = 4.0t_c$, superimposed onto (left to right): i) contours of static density gradient magnitude within the near field , and ii) regions of active WENO shaded in brown 102

Figure 4.4 Visualisation of the entire adaptive grid superimposed on contours of static density and active WENO taken at the instant (top to bottom): i), $t = 3.0t_c$, ii) $t = 4.0t_c$, and iii) $t = 5.0t_c$ 102

Figure 4.5 (left to right): i) Trends in instantaneous and cumulative time-averaged (from time t to $5.0t_c$) static density (kg/m^3) with time at $x = 9.0h$, $y = 0.0$, and $z = 0.0$, and ii) the l^2-norm of the cumulative time-average residual of the static density field 104

Figure 4.6 (left to right): i) Trends in instantaneous and cumulative time-averaged (from time t to $5.0t_c$) stream-wise velocity (km/s) with time at $x = 9.0h$, $y = 0.0$, and $z = 0.0$, and ii) the l^2-norm of the cumulative time-average residual of the stream-wise velocity field 105

Figure 4.7 (left to right): i) Trends in instantaneous and cumulative time-averaged (from time t to $5.0t_c$) static pressure (kPa) with time at $x = 9.0h$, $y = 0.0$, and $z = 0.0$, and ii) the l^2-norm of the cumulative time-average residual of the static pressure field 105

Figure 4.8 (left to right): i) Trends in instantaneous and cumulative time-averaged (from time t to $5.0t_c$) stream-wise momentum advection (MPa) in the stream-wise direction with time

at $x = 9.0h$, $y = 0.0$, and $z = 0.0$, and ii) the l^2-norm of the cumulative time-average residual of the static pressure field 106

Figure 4.9: Span-wise normal $(z = 0.0)$ contours of static density gradient magnitude taken at the instant: (i) $t = 3.0t_c$, (ii) $t = 4.0t_c$, and (iii) $t = 5.0t_c$. 107

Figure 4.10: Visualisations taken at the instant $t = 4.0t_c$ of: (i) Stream-wise normal contours of static density gradient magnitude, and (ii) constant second invariant of the velocity gradient tensor. 108

Figure 4.11: Shear layer properties of the mixing wake (clockwise from top left): transverse extent normalised by the duct height, velocity ratio, convective Mach number, and density ratio. 111

Figure 4.12: Favre averaged turbulence kinetic energy (kJ/kg) trends with stream-wise location and contour. 113

Figure 4.13: Reynolds averaged stream-wise Reynolds normal stress (kPa) trends with stream-wise location and contour. 114

Figure 4.14: Reynolds averaged cross-stream Reynolds normal stress (kPa) trends with stream-wise location and contour. 114

Figure 4.15: Reynolds averaged span-wise Reynolds normal stress (kPa) trends with stream-wise location and contour. 116

Figure 4.16: Reynolds averaged Reynolds shear stress (kPa) trends with stream-wise location and contour. 117

Figure 4.17: Reynolds averaged turbulence cross-stream flux of hydrogen (kg/(m^2.s)) trends with stream-wise location and contour. 117

Figure 4.18: Reynolds averaged turbulence resolution metric trend with stream-wise location and contour. 118

Figure 4.19: Ratio of sub-grid scale cut-off length to Kolmogorov length trend with stream-wise location and contour. 120

Figure 4.20: Logarithmic turbulence energy spectra trend with frequency (Hz) taken at (left to right): (i) $y = 0.00$, and (ii) $y = 0.10h$ 122

Figure 4.21: Stream-wise normal contours taken at the instant $t = 4.0t_c$ of: (i) static density gradient magnitude, and (ii) stoichiometric mixture iso-surface. 124

Figure 4.22: Stream-wise normal contours of well mixed hydrogen mass flux (kg/(m^2.s)) taken at the instant: (i) $t = 3.0t_c$, (ii), $t = 4.0t_c$, and (iii) $t = 5.0t_c$ 128

Figure 4.23: Span-wise normal contours of well mixed hydrogen mass flux (kg/(m^2.s)) taken at the instant: (i) $t = 3.0t_c$, (ii), $t = 4.0t_c$, and (iii) $t = 5.0t_c$. 129

Figure 4.24: Trends of Reynolds averaged entrainment fraction and mixing efficiency with stream-wise location (pure fuel injection only). 130

Figure 4.25: Span-wise normal contours of static density gradient magnitude within the near field taken at the instant (clockwise from top left): i) $t = 2.0t_c$, ii), $t = 3.0t_c$, iii) $t = 5.0t_c$, and iv) $t = 4.0t_c$. 133

Figure 4.26: Span-wise normal contours of stream-wise velocity (km/s) behind the centre-body, with superimposed streamlines, taken at the instant (clockwise from top left): i) $t = 2.0t_c$, ii), $t = 3.0t_c$, iii) $t = 5.0t_c$, and iv) $t = 4.0t_c$. 134

Figure 4.27: Stream-wise normal contours of hydrogen mass fraction within the near field taken at the instant $t = 4.0t_c$ 135

Figure 4.28: Stream-wise normal contours of static density gradient magnitude within the near field taken at the instant $t = 4.0t_c$. 136

Figure 4.29: Span-wise normal contours of stream-wise baroclinic torque (GHz/s) behind the centre-body taken at the instant (clockwise from top left): i) $t = 2.0t_c$, ii), $t = 3.0t_c$, iii) $t = 5.0t_c$, and iv) $t = 4.0t_c$ 138

Figure 4.30: Trend in temporal inviscid linear growth rate ω_i with wave angle θ for several convective Mach numbers M_c (Sandham & Reynolds, 1991). 139

Figure 4.31: Span-wise normal contours of velocity divergence within the near field taken at the instant (clockwise from top left): i) $t = 2.0t_c$, ii), $t = 3.0t_c$, iii) $t = 5.0t_c$, and iii) $t = 4.0t_c$ 140

Figure 4.32: Faver-Reynolds averaged turbulence Mach number trend with stream-wise location and contour..... 140

Figure 4.33: Span-wise normal contours of static density gradient magnitude taken at the instant: i) $t = 3.0t_c$, ii), $t = 4.0t_c$, and iii) $t = 5.0t_c$ 141

Figure 4.34: Stream-wise normal contours of static density gradient magnitude of the mixing layers at the instant $t = 4.0t_c$ 143

Figure 4.35: Stream-wise normal contours of hydrogen mass fraction of the mixing layers taken at the instant $t = 4.0t_c$ 144

Figure 4.36:Normalised mean stream-wise velocity and Atwood number cross-stream profiles during the wake transition..... 145

Figure 4.37: Normalised mean Reynolds stresses cross-stream profiles during the wake transition. 146

Figure 4.38: Normalised span-wise vorticity cross-stream profiles during the wake transition.146

Figure 4.39: Normalised mean span-wise vorticity cross-stream profiles during the primary shock-turbulence interaction. 147

Figure 4.40: Mean stream-wise velocity and Atwood number cross-stream profiles proceeding the primary shock-turbulence interaction 148

Figure 4.41: Mean Reynolds stress cross-stream profiles proceeding the primary shock-turbulence interaction 149

Figure 5.1: Span-wise normal $(z = 0.0)$ contours of static density gradient magnitude taken at the instant $t = 4.0t_c$ with: (i) $\phi = 1.0$ and $EP = 0.0\%$, and (ii) $\phi = 1.11$ and $EP = 10.0\%$. 154

Figure 5.2: Stream-wise normal contours of static density gradient magnitude taken at the instant $t = 4.0t_c$ with: (i) $\phi = 1.0$ and $EP = 0.0\%$, and (ii) $\phi = 1.11$ and $EP = 10.0\%$. 155

Figure 5.3: Surfaces of constant second invariant of the velocity gradient tensor taken at the instant $t = 4.0t_c$ with: (i) $\phi = 1.0$ and $EP = 0.0\%$, and (ii) $\phi = 1.11$ and $EP = 10.0\%$. 156

Figure 5.4: Comparison of mixing wake shear layer properties (clockwise from top left): transverse extent normalised by the duct height, velocity ratio, convective Mach number, and density ratio. 157

Figure 5.5: Comparison of Favre averaged turbulence kinetic energy (kJ/kg) trends with stream-wise location and contours with: (i) $\phi = 1.0$ and $EP = 0.0\%$, and (ii) $\phi = 1.11$ and $EP = 10.0\%$. 160

Figure 5.6: Comparison of Reynolds averaged cross-stream Reynolds normal stress (kPa) trends with stream-wise location and contours with: (i) $\phi = 1.0$ and $EP = 0.0\%$, and (ii) $\phi = 1.11$ and $EP = 10.0\%$. 162

Figure 5.7: Comparison of logarithmic span-wise averaged turbulence energy spectra trend with frequency (Hz) taken at $y = 0.00$ with: (left) $\phi = 1.0$ and $EP = 0.0\%$, and (right) $\phi = 1.11$ and $EP = 10.0\%$.. 164

Figure 5.8: Comparison of the stoichiometric mixture iso-surface taken at $t = 4.0t_c$ with: (i) $\phi = 1.0$ and $EP = 0.0\%$, and (ii) $\phi = 1.11$ and $EP = 10.0\%$. 166

Figure 5.9: Stream-wise normal contours of well mixed hydrogen mass flux (kg/(m^2.s)) taken at the instant $t = 4.0t_c$ with: (i) $\phi = 1.0$ and $EP = 0.0\%$, and (ii) $\phi = 1.11$ and $EP = 10.0\%$. 168

Figure 5.10: Trends of Reynolds averaged entrainment fraction and mixing efficiency with stream-wise location (pure and oxygen enriched fuel injection). 169

Figure 5.11: Span-wise normal $(z = 0.0)$ contours of stream-wise velocity (km/sec) behind the centre-body, with superimposed streamlines, for $EP = 0.0\%$ (left) and $EP = 10.0\%$ (right) taken at the instants (top to bottom): $t = 3.0t_c$, $t = 3.5t_c$, $t = 4.0t_c$, $t = 4.5t_c$, and $t = 5.0t_c$ ... 172

Figure 5.12: Span-wise normal $(z = 0.0)$ contours of static density gradient magnitude within the near field with $EP = 0.0\%$ (left) and $EP = 10.0\%$ (right) taken at the instant $t = 3.0t_c$ (top), $t = 4.0t_c$ (middle) and $t = 5.0t_c$ (bottom). 173

Figure 5.13: Comparison of Reynolds-averaged static density cross-stream profiles of the mixing wake between $x = 1.0h$ and $x = 2.5h$ with $EP = 0.0\%$ (left) and $EP = 10.0\%$ (right). 174

Figure 5.14: Contours of hydrogen mass fraction within the near field with $EP = 10.0\%$ taken at the instant $t = 4.0t_c$ 175

Figure 5.15: Contours of static density gradient magnitude within the near field with $EP = 10.0\%$ taken at the instant $t = 4.0t_c$ 176

Figure 5.16: Span-wise normal $(z = 0.0)$ contours of velocity divergence within the near field with $EP = 0.0\%$ (left) and $EP = 10.0\%$ (right) taken at the instant $t = 3.0t_c$ (top), $t = 4.0t_c$ (middle) and $t = 5.0t_c$ (bottom). 177

Figure 5.17: Normalised mean Reynolds stresses cross-stream profiles during the first shock turbulence interaction with $EP = 0.0\%$ (left) and $EP = 10.0\%$ (right)..... 179

Figure 5.18: Span-wise normal $(z = 0.0)$ contours of static density gradient magnitude with $EP = 0.0\%$ using: (i) LES data taken at the instant $t = 4.0t_c$: (ii) Reynolds averaged LES data, and (ii) RANS data. 181

Figure 5.19: Span-wise normal $(z = 0.0)$ contours of static density gradient magnitude with $EP = 10.0\%$ using: (i) LES data taken at the instant $t = 4.0t_c$: (ii) Reynolds averaged LES data, and (ii) RANS data. 181

Figure 5.20: Comparison of Favre averaged turbulence kinetic energy (kJ/kg) trends with stream-wise location and contours with $EP = 0.0\%$ using: (i) LES data, and (ii) RANS data. 182

Figure 5.21: Comparison of Favre averaged turbulence kinetic energy (kJ/kg) trends with stream-wise location and contours with $EP = 10.0\%$ using: (i) LES data, and (ii) RANS data. 183

Figure 5.22: Normalised mean Reynolds stresses cross-stream profiles during the wake transition with $EP = 0.0\%$ using: (left) LES data, and (right) RANS data..... 184

Figure 5.23: Comparison of Reynolds averaged mixing efficiency trends of with stream-wise location: RANS and LES; pure and oxygen enriched fuel injection. 186

Figure A1.62: Trends in Schmidt number with static temperature for binary mixing between hydrogen, oxygen and nitrogen. 228

List of Tables

Table 3.1: Grid convergence study of the planar intake model 65

Table 3.2: Grid convergence study of the planar duct model 67

Table 3.3: Combustion efficiency surface fit coefficients 77

Table A1.1: Empirical thermodynamic coefficients of molecular hydrogen 221

Table A1.2: Empirical thermodynamic coefficients of molecular oxygen 222

Table A1.3: Empirical thermodynamic coefficients of molecular nitrogen 223

Table A1.4: Sutherland coefficients of kinematic molecular viscosity 225

Table A1.5: Sutherland coefficients of thermal conductivity 225

1 Introduction

This chapter introduces fundamental concepts relevant to this study in section 1.1, which includes: orbital space access, the supersonic combustion ramjet, oxygen enrichment, and computational fluid dynamics. A gap in current literature concerning high altitude scramjet operation, which utilises oxygen enrichment, has been identified. This has provided motivation to undertake this current study, of which the research aims are detailed in section 1.2 and outlined in section 1.3.

1.1 Overview

Many modern technologies such as credit cards, GPS navigation, and weather forecasting rely on artificial satellites orbiting in space, which send and receive information to Earth. These satellites are currently launched into orbit exclusively by rocket propulsion. In 2013, 78 space launches were successfully performed worldwide (OECD, 2014). Although rocket technology is well established, only eight countries in 2014 maintain a fleet of operational space launchers. Australia is one of many nations that currently utilises satellite technology by relying on the international space launching community (Commonwealth of Australia, 2013). The current cost for space bound cargo is approximately USD 20,000 per kilogram (Coopersmith, 2011), due principally to factors such as the complexity of multi-stage rockets and the need for on-board oxidant. Reducing the cost of launching satellites into space may enable countries such as Australia to enjoy the benefits of greater participation in space exploration and utilisation.

An air-breathing engine is a more efficient alternative to the rocket motor as it captures atmospheric oxygen rather than storing oxidiser on-board. However, mature air-breathing engines such as the turbojet and ramjet cannot operate at the hypersonic speeds required to escape the atmosphere. The supersonic combustion ramjet, or scramjet, engine avoids excessive drag forces and heating loads associated with hypersonic ramjet operation by maintaining a supersonic internal flow through the engine. In addition, scramjet powered vehicles can be recovered and launched multiple times.

One of the critical design challenges is high altitude operation of the scramjet engine, where the air becomes rarefied. At its operation ceiling, a scramjet engine will generate just enough thrust force to overcome the drag force acting to slow the vehicle. Travelling into a low Earth orbit would require switching to a rocket before reaching the operational ceiling of the scramjet engine. The University of Queensland is currently engaged in researching the feasibility of a three stage rocket-scramjet-rocket space launcher concept. The intended scramjet component utilises a Rectangular-to-Elliptical-Shape-Transition (REST) scramjet inlet designed by Smart (Smart, 1999), which has been the subject of several experimental studies in the T4 impulse facility at The University of Queensland (Turner & Smart, 2009a; Suraweera & Smart, 2009).

Oxygen enrichment, or OxEn, is a technique proposed to augment scramjet thrust by mixing the fuel with small amounts of oxygen stored on-board. Although this notion is counter to the concept of a purely air-breathing engine, it will nonetheless reduce the reliance on rockets to propel the vehicle to the desired orbital altitude by increasing the scramjet engine's operational ceiling. Therefore, scramjets Scramjets using OxEn have the potential to make satellite enabled technologies more affordable as well as improving the economic viability of space-based industry and space exploration.

The study aims to further investigate the potential benefits oxygen enrichment has upon scramjet engine performance at high altitudes, focusing on numerical simulations of hypervelocity fuel-air mixing. With fluids travelling at supersonic speeds within a scramjet engine, effective mixing of fuel and air is difficult to accomplish without incurring prohibitive drag force penalties. Compressibility effects associated with supersonic fluid flow add further complexities to the analysis of fuel-air mixing within a scramjet engine. These compressible effects can be significant, for example the spreading rate of fuel and oxygen can be reduced to less than a quarter of the rate at incompressible conditions. In such extreme cases, compressibility alters the turbulent fluid motion which acts to mix the fuel and air by retarding the production of turbulence energy induced by shearing velocity differences. In contrast, the interaction between a shock wave and fuel-air mixing interface has the capacity to enhance turbulent mixing due to the action of baroclinic torque.

Parallel injection of fuel via an intrusive centre-body (Figure 2.4) is one of the more idealised scramjet engine configurations. Turbulent mixing is achieved by injecting fuel into the wake flow generated by the centre-body. The subsequent velocity difference between the fuel wake and the high speed ingested air stream produces the shear necessary for turbulence to develop. The fluid flow which forms behind the centre body will henceforth be referred to as a mixing wake. The principal drawback of such an injection scheme is the large pressure drag force imposed on the engine due to the immersion of centre-body in the ingested air stream. Nonetheless, this configuration generates a flow field representative of the conditions inside a more practical scramjet combustor during operation.

Over the past few decades, Computational Fluid Dynamics (CFD) has become a standard analysis technique for fluid flow problems. The ambition of CFD is to accurately solve the governing fluid

dynamics equations using a numerical methodology. The increased reliance upon CFD to solve fluid problems has been driven by an exponential increase in computer performance in addition to several key benefits over the more traditional experimental approach. These benefits include: more cost effective to implement in comparison to experiment, where design and manufacture of facility and apparatus can be expensive, the ability to measure multiple flow quantities at a particular location and instant within the flow, and that experimentally difficult to obtain physical quantities can be measured. The final two points are a direct result of solving the complete set of govern fluid dynamics equations. Despite the improved capability of computers, current simulations of practical fluid flow problems still rely on the modelling of physical phenomena such as turbulence and chemical kinetics. Simulations of the hypervelocity mixing wake must capture multiple physical phenomena such as shock-waves, high temperature effects, scalar mixing, viscous transport, turbulence and combustion which act concurrently to form a complex flow field.

1.2 Research Aims

The body of work contained in this thesis was motivated by the following research question:

> *How does the introduction of oxygen into an injected hydrogen fuel stream change the mixing process between fuel and air within a hypervelocity mixing wake?*

An experimental investigation into oxygen enriched parallel hydrogen fuel injection conducted by Razzaqi & Smart (2011) showed that premixing oxygen with fuel was beneficial to scramjet performance. However, the T4 impulse facility capabilities at the time only provided limited pressure measurements, which were used to infer the performance characteristics of the experimental engine. In addition, no visualisations of hypervelocity mixing wake flow were obtained.

The effect of oxygen enrichment on scramjet performance can be explored in greater detail using numerical simulations. The advantage of numerical simulations over currently available experimental techniques is that a more complete description of a fluid flow is recorded. The level of detail provided from such simulations is dependent on the numerical methodology employed. Conventional Reynolds-Averaged Navier-Stokes simulations determine a mean solution of the flow field by modelling all turbulent motion. The intent of oxygen enrichment is to only pre-mix a small stoichiometric amount of oxidiser relative to the total amount of fuel. In order to correctly identify the benefits oxygen enrichment may have upon scramjet performance, it is critical to accurately simulate the mixing between fuel and ingested air. Recent improvements in computer power has made state-of-the-art Large Eddy Simulations (LES) of compressible flows such as the hypervelocity mixing wake practicable, albeit non-trivial. LES is more computationally expensive in comparison to RANS as it resolves the large unsteady structures of the flow field and only models turbulent interactions on scales smaller than the computational grid spacing. Consequently, performing an LES provides additional information about the simulated turbulent fluid motion relative to an equivalent RANS calculation. This study employs both numerical methods to expand the current body of knowledge regarding oxygen enrichment's effect on hypervelocity mixing.

The following three research objectives were identified as necessary milestones in answering the research question:

(i) be the first to visualise, describe and understand the detailed physical phenomena present within a hypervelocity mixing wake flow using high fidelity LES.

To date, pure LES calculations have been restricted to simple turbulent flows, predominantly of incompressible free shear layers. Simulations of more practical internal scramjet flow paths have involved moderate hypervelocity conditions using a hybrid LES/RANS schemes, or wall modelled LES. Conducting pure LES of the highly compressible mixing wake at realistic conditions deviates from this approach.

(ii) to investigate how the mixing wake turbulence is altered by the premixing of oxygen with injected fuel and in particular describe the effect this has on the mixing process.

Although the applicability of oxygen enrichment for high altitude scramjet operations has been demonstrated by previous work, its influence upon the various physical phenomena within a scramjet combustor flow field remains unclear. The instantaneous flow fields generated by pure LES allow these physical phenomena to be investigated in greater detail than either experimental or RANS simulation studies can provide. A comparison of the instantaneous LES flow fields generated from pure and oxygen enriched fuel injection is aimed at elucidating key differences between the two cases.

(iii) to compare the mixing characteristics predicted by the RANS and LES numerical methodologies.

There remains a strong reliance in the hypersonic community to use the RANS numerical methodology. As turbulence is completely modelled in RANS, it is important to validate results generated using this approach with experimental or higher fidelity numerical data. This study will provide a direct comparison between the RANS and LES approach and determine if the former method captures all the flow physics predicted by the latter.

1.3 Thesis Outline

The introductory **Chapter One** is followed by:

Chapter Two provides a review on the current body of knowledge regarding scramjet technology, oxygen enrichment, canonical compressible turbulent mixing flows, and previously studies of hypervelocity mixing using large eddy simulations.

Chapter Three presents a simple review of constant dynamic pressure access-to-space trajectories, which highlights the applicability of oxygen enrichment for air-breathing propulsion. This leads into a parametric study of fuelling conditions, using RANS simulations, to better describe the influence oxygen enrichment has on scramjet performance. This includes a description of the RANS numerical methodology and a grid refinement study. The effects oxygen enrichment has upon the compressible flow physics, fuel ignition, and combustion efficiency within a simplified scramjet combustor are detailed. This chapter concludes with a discussion on the predicted turbulence characteristics of the flow through the combustor.

Chapter Four introduces the LES numerical methodology and subsequently the LES results of the pure fuel mixing wake. Overall characteristics of the free-shear turbulence are discussed. Visualisations of the mixing interface and large scale turbulent structures provide new insight into the hypervelocity mixing wake flow field. In addition, a detailed description of the compressible flow features, instabilities and turbulence statistics is provided.

Chapter Five presents the LES results of a mixing wake simulation with oxygen enriched fuel injection. Comparison between mixing characteristics and turbulent statistics are made from two LES simulations. From this comparison, conclusions are drawn regarding the effects of oxygen enrichment upon the mixing wake flow. Comments regarding the suitability of RANS to simulate the hypervelocity mixing wake flow are also detailed.

Chapter Six, the final chapter, summarises the principal findings of this study. Recommendation for future work on the topic of oxygen enrichment are proposed based upon the revealing observations of this study

2 Literature Review

This chapter presents general literature relevant to the current research project according to four principal research fields: 2.1) an overview of current scramjet engine design and proposed use for access-to-space especially in relation to oxygen enrichment; 2.2) previous theoretical studies to characterise turbulent fluid flow; 2.3) experimental observations and derived empirical models relating to simple free-shear turbulence; and 2.4) a review of fundamental computational fluid dynamics concepts, with a discussion of published applications to hypervelocity mixing. Chapters 3, 4, 5 also contain specific literature citations relevant to details of the current research project.

The application of scramjet technology to space access relies on the design of a highly efficient engine that operates over a wide range of flight conditions. The potential benefits of such a system have led to several decades of scramjet research and development. Attempts to develop a complete understanding of the numerous and complex physical phenomena that exist within a operational scramjet engine have driven extensive research into more fundamental science such as compressible turbulent mixing, supersonic combustion, and shock wave-turbulence interactions. Visualisations of these flow features were initially reliant on experimentation, which were used to verify proposed theoretical models and abstractions. In the last few decades, both the availability and power of computational machines has enabled numerical simulations of these phenomena to be performed. This chapter aims to review the major publications that have contributed to the development of scramjet technology and the relevant science which governs its design.

2.1 Supersonic Combustion Ramjets

The scramjet engine is an air-breathing propulsion system which geometrically compresses incoming air-flow to enable fuel-air combustion, whilst maintaining supersonic flow speeds, then expands the flow to convert the liberated chemical energy into kinetic energy. The engine is comprised of four key components: the compression inlet, the isolator, the combustor, and the diverging thrust nozzle. The scramjet concept was pioneered by Weber & MacKay (1958), who investigated the theoretical performance of such an engine. It was found that the scramjet engine out-performed the more conventional ramjet engine at flight Mach numbers greater than 7. In comparison to rockets, scramjets theoretically achieve higher efficiencies by capturing the oxygen necessary for combustion from the atmosphere, rather than carrying it on-board which reduces the space available for cargo (Ferri, et al., 1965). The original experimental evidence of combustion being achieved within a supersonic flow was reported to have occurred in 1959 by Ferri (Ferri, 1973). Scramjet engine development continued through various programs such as: the Hypersonic Research Engine, from 1964 - 1974 at NASA Langley (Andrews & Mackley, 1994); the Supersonic Combustion Ramjet Missile, from 1962 - 1978 at the Applied Physics Laboratory, John Hopkins University (Billig, 1995); and the National Aerospace Plane (Barthelemy, 1989), which was

combined US initiative from 1986 until its cancellation in 1993. The HyShot II experiment, conducted by The University of Queensland in 2002, was the first to achieve supersonic combustion during a flight test (Paull, et al., 2002). This innovative experiment was performed after re-entry following a parabolic flight trajectory launched via a sounding rocket. The scramjet operated between speeds of Mach 7.6 - 8.0. The first successful flight experiments of an airframe integrated, free-flying scramjet propulsion system were performed in 2004 and undertaken by NASA as part of the Hyper-X program. Designated as X-43, the Hyper-X vehicle was accelerated to the pre-defined test condition using a drop-away booster rocket launched from a NASA B-52 carrier aircraft. The vehicle then followed a controlled trajectory using scramjet propulsion after separation from the booster rocket. After an initial failed experiment, the second test maintained Mach 7 for approximately 5 seconds using scramjet propulsion on 27 March 2004. The third test, which occurred on 16 November, managed to achieve a speed of Mach 10 under scramjet power (McClinton, et al., 2005). The X-51 waverider (Hank, et al., 2008), which sustained speeds of Mach 5 for almost 200 seconds, remains the longest duration free-flying scramjet flight test to date. The combustion process which occurs in a typical scramjet engine involves the burning of hydrogen fuel injected into the engine which has mixed with oxygen from the free stream air ingested into the engine via the inlet. This process is depicted in Figure 2.1.

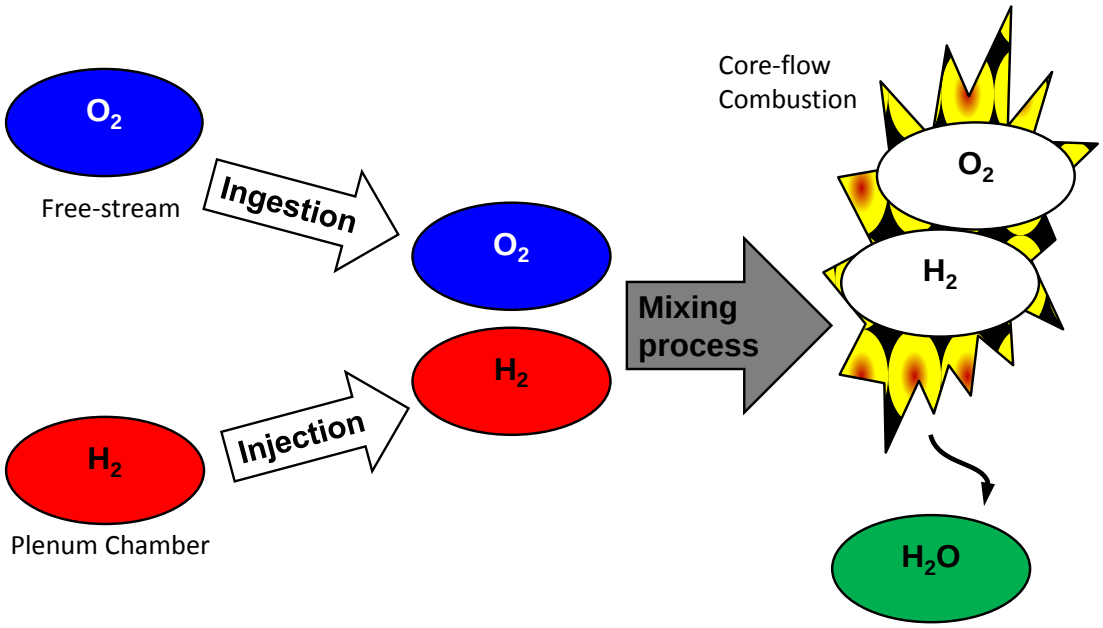

Figure 2.1.: Diagram of combustion process within a typical scramjet engine

Liquid hydrogen is the typical fuel for supersonic combustion research purposes because of its high heating values per unit mass and cooling capacity. Furthermore, its combustion chemistry is simpler to analyse and it has shorter ignition delay times in comparison to hydrocarbon fuels. The fuel equivalence ratio is a design parameter which specifies the amount of fuel available for combustion relative to the amount of oxygen ingested by the engine. For the combustion of hydrogen with oxygen, the fuel equivalence ratio is defined as:

$$\phi_{O_2}^{H_2} = \frac{m_{H_2} / \hat{m}_{H_2} \nu_{H_2}}{m_{O_2} / \hat{m}_{O_2} \nu_{O_2}} \tag{2.1}$$

Where ν_{H_2} and ν_{O_2} are the stoichiometric coefficients of hydrogen and oxygen respectively; $\hat{m}_{H_2}$ and $\hat{m}_{O_2}$ are the molar masses of hydrogen and oxygen respectively; and m_{H_2} and m_{O_2} are the masses of hydrogen and oxygen available for combustion respectively.

This definition can easily be extended to include chemical reactants in a steady state system by substituting the mass quantities with mass flow rates. In the case of a typical scramjet engine, where the ingested stream is of atmospheric air, the fuel equivalence ratio for the combustion of hydrogen is given by:

$$\phi = \frac{1}{2} \frac{\hat{m}_{O_2}}{\hat{m}_{H_2}} \frac{\dot{m}_{H_2}^{inj}}{0.23 \dot{m}^{ing}} \tag{2.2}$$

Where the superscript *inj* reference to injection and *ing* refers to ingestion. Nominal operation of a scramjet engine maximises the mixing of injected fuel with ingested air so as to promote the combustion process necessary for thrust generation. In practice, scramjets are typically mixing limited (Ferri, 1973). However, improving fuel-air mixing can lead to undesirable consequences. For example, greater strain rates in the flow help the mixing process but may cause flame extinction (Curran & Murthy, 2000). In addition, shockwaves have the potential to generate additional turbulence aided mixing but produce undesired total pressure losses. These studies indicate the design of a scramjet combustor must find a delicate balance between these conflicting requirements.

2.1.1 Aero-Vehicle Configurations

Hypersonic flight introduces many coupling effects which make it impossible to design individual engine components in a modular fashion (Heiser & Pratt, 1994). The condition of the air-flow entering the engine is strongly dependent on the altitude, speed and leading edge shape of the vehicle. These authors also showed that obtaining peak performance of a scramjet engine is mandatory to overcome the substantial drag force generated when travelling at hypersonic speeds.

Smart and Tetlow (2009) performed an analysis of a three-stage-to-orbit launch system. The first stage, a solid rocket booster, propelled the system to an altitude of 27.00 km and a flight Mach number of 6.0. The second stage was powered by three REST scramjet engines (Smart, 1999) which operated along a constant 50.0 kPa dynamic pressure trajectory to an altitude of 36.09 km flight speed of Mach 11.55. The third and final stage employed a liquid fuelled rocket to reach Low Earth Orbit (LEO). One of the critical conclusions reported was that the rapid loss of net thrust at high Mach numbers presented a significant challenge for the design of an efficient scramjet propelled space launcher.

2.1.2 Access-to-Space Trajectories

The access-to-space trajectory of an air breathing engine is typically specified with a constant flight dynamic pressure (Olds & Budianto, 1998). Aerodynamic loads are proportional to the dynamic pressure so following a constant dynamic pressure trajectory simplifies the structural and control design of the aero-vehicle. The operable flight envelope of a scramjet engine has a lower limit of 20.0 kPa flight dynamic pressure, where engine performance is adversely affected by a lack of available oxygen (Hunt & Martin, 2000), and an upper limit of 100.0 kPa, where thermal and structural loads become difficult to manage. The free-stream conditions along a specific trajectory are calculated using the U.S Standard Atmosphere model (NASA, 1976) in combination with the fixed flight dynamic pressure. All parameters are considered a function of free-stream (or flight) Mach number, M_∞. The altitude, h_{alt}, trends along an accelerating access-to-space trajectory are shown in Figure 2.2.

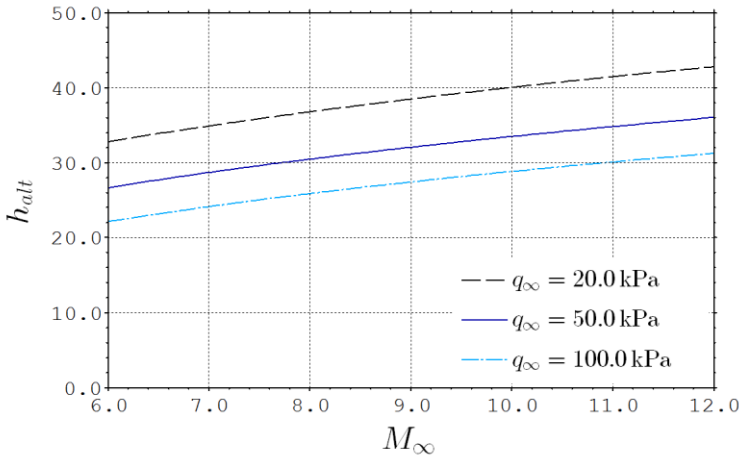

Figure 2.2: Altitude (km) of several accelerating access-to-space trajectories based upon the Standard Atmosphere (NASA, 1976)

2.1.3 Oxygen Enrichment

In order to overcome the previously discussed diminishing thrust at high Mach number and altitude, a technique known as oxygen enrichment has been proposed. Oxygen enrichment introduces a small amount of oxygen into the propellant fuel stream prior to injection into the combustor, providing supplementary oxidiser for combustion with the fuel. This requires oxygen to be stored on-board and integrated into the injection system. One-dimensional numerical analysis of a scramjet engine employing oxygen enrichment (Rudakov & Krjutchenko, 1990) has shown that the additional momentum introduce into the propellant stream is also beneficial for thrust generation. The combustion process which occurs in a scramjet engine utilising oxygen enrichment is slightly more complex than the standard case. The hydrogen pre-mixed with oxygen has the opportunity to combust before the remaining hydrogen can combust with the ingested oxygen, which has the potential to dramatically alter the flow within the combustor. This process is depicted in Figure 2.3.

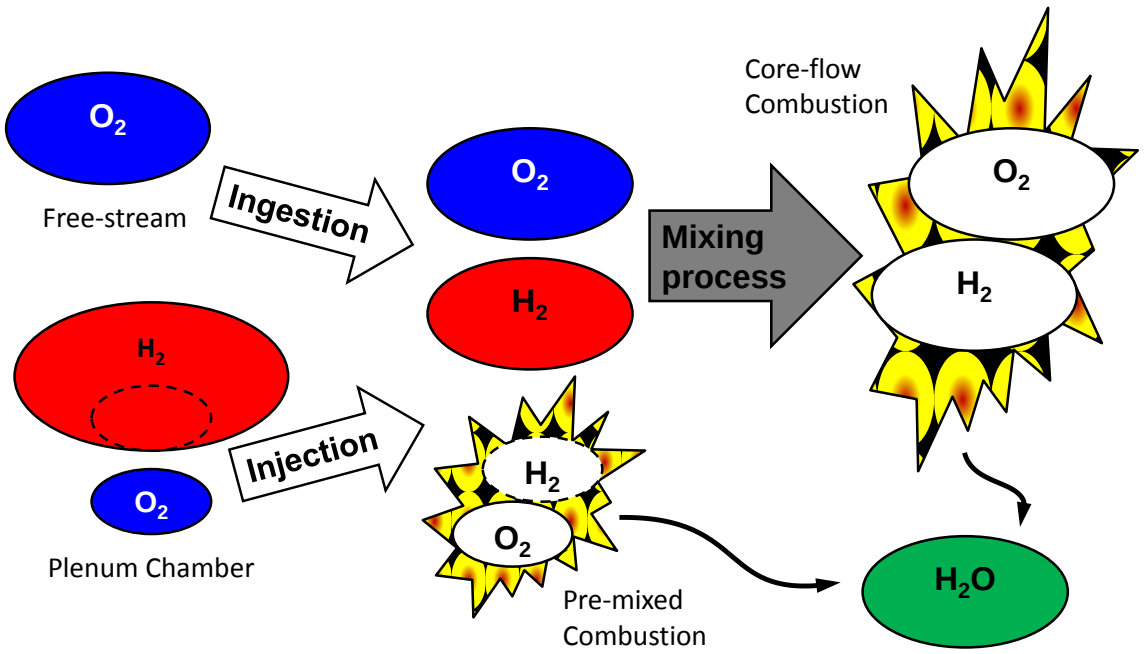

Figure 2.3: Diagram of combustion process within a scramjet engine utilising oxygen enrichment

The enrichment percentage defines the percentage of injected hydrogen which would be consumed in a stoichiometric reaction with the enriching oxygen (Razzaqi & Smart, 2011), expressed as:

$$EP = 2\frac{\hat{m}_{H_2}}{\hat{m}_{O_2}}\frac{\dot{m}_{O_2}^{inj}}{\dot{m}_{H_2}^{inj}} \qquad 2.3$$

A theoretical performance analysis of a restricted class of scramjet powered vehicle (Pike, 1999) indicated that, under their assumptions, oxygen enrichment at high Mach numbers resulted in increased vehicle payload fraction. More recently, an experimental study of oxygen enriched hypervelocity combustion was performed (Razzaqi & Smart, 2011) within the T4 shock tunnel facility at the University of Queensland. The shock tunnel test conditions were chosen to produce pressures entering the model combustor comparable to a Mach 12 Rectangular-to-Elliptical Shape-Transition (REST) engine (Suraweera & Smart, 2009) travelling at $M_\infty = 12.3$ and $q_\infty = 40.2$ kPa. The injection system employed a Ludwieg tube able to supply a near constant flow of hydrogen fuel. Experiments involving oxygen enrichment used an equivalent system to supply a 74.6/25.4 (% by volume) oxygen/nitrogen mixture.

The model utilized is a simplified scramjet engine comprised of: a planar intake, a constant area rectangular duct, an injector strut and a planar expansion surface. A schematic of the experimental model is shown in Figure 2.4.

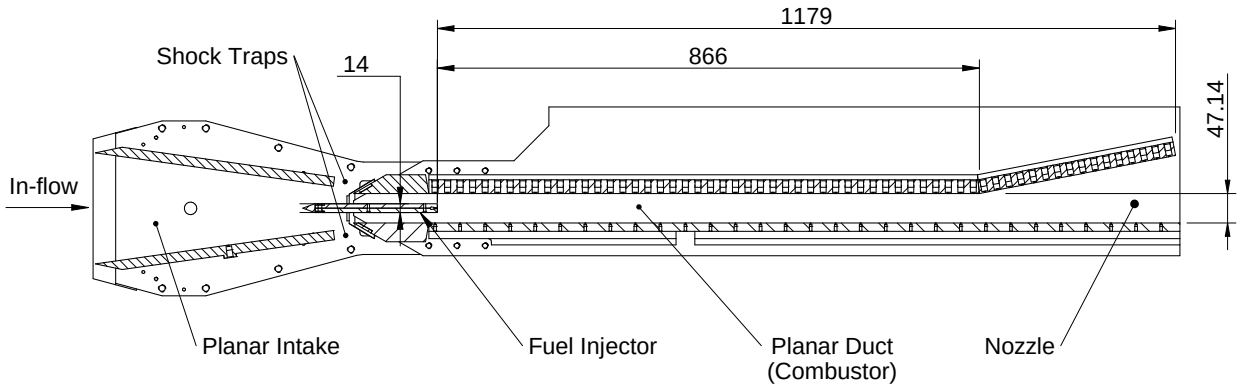

Figure 2.4: Schematic of the experimental model (units in millimeters) (Razzaqi & Smart, 2011)

The planar intake consists of plates angled at 8° to the free stream flow direction and has a span-wise width of 150 mm. The rectangular duct has a cross-sectional area of $h \times w = 47.14 \text{ mm} \times 100 \text{ mm}$ where h is the height and w is the span-wise width of the duct. The duct has a length of $l = 866 \text{ mm}$. The injector strut has a height of 14 mm. The fuel plenum chamber was included in the model. It fed into the rectangular duct via a 1 mm × 100 mm slot located on the backward face of the injector strut. The air flow enters the planar intake from the left after stagnated air with a total specific enthalpy of 7.6 MJ/kg (after being processed by a reflected shock wave) has been expanded by a convergent-divergent nozzle. The nominal shock tunnel condition is approximated with a free-stream Mach number of $M_0 = 5.7$, a static pressure of $p_0 = 6.19 \text{ kPa}$, and a static temperature of $T_0 = 976 \text{ K}$.

The experimental data collected consisted entirely of point measurements of pressure along the model. It was concluded from the observed pressure rise when injecting fuel into the experimental engine that combustion was mixing limited at these flight conditions. Engine performance was derived by fitting the pressure measurements to pressure trends predicted by a one-dimensional cycle analysis (Smart, 2007) employing an empirical combustion model (Heiser & Pratt, 1994).

The core findings of this experimental investigation regarding engine performance were: (i) oxygen enrichment improved the combustion efficiency, (ii) the length to ignite the injected fuel was reduced by oxygen enrichment, (iii) and the specific thrust was increased by oxygen enrichment, but specific impulse decreased. It was also suggested that internal drag forces could be reduced when employing oxygen enrichment as the combustor length could be truncated without adversely affecting the thrust generation of the engine. These conclusions highlight the significant potential oxygen enrichment has to enhance scramjet performance, particularly at altitudes where net thrust becomes marginal. However, due to the limitations of experimental data, only a limited number of fuelling conditions (equivalence ratio and enrichment percentage permutations) were explored and it could not be determined whether the benefit to combustion efficiency goes beyond that expected from the premixed oxygen being completely consumed.

2.2 Turbulent Fluid Motion

The physical phenomena that exists within an operational scramjet engine are complex, including shock-waves, high temperature gas dynamics, and sporadic turbulent motion. Further to this, these phenomena can act in concert to produce additional coupled effects. It is important to develop an understanding of the underling physical elements before tackling the more difficult, realistic flow problem of hypervelocity turbulent mixing. In this section methods of characterising turbulent fluid motion will be discussed.

2.2.1 Scales of Turbulence

Turbulence is a seemingly chaotic state of fluid motion which increases the transport of mass, momentum and energy, aiding the mixing of fluid. Shear forces acting upon the fluid flow induce vorticity giving rise to finite regions of coherent swirling fluid. The formation of these vortical structures, referred to as turbulent eddies, are observed over a range of scales. The largest eddies can be characterised by length and velocities similar to the bulk flow, whereas the smallest eddies exist at scales associated with viscous dissipation. Interaction between neighbouring eddies is virtually guaranteed even for low levels of turbulence. These interactions are usually complex, in

part due to the irregular turbulent topology, and facilitate mass, momentum and energy is transfer between the particular eddies. Despite this, there are well documented similarities in the characteristics of various turbulent fluid flows. The large scale shear force which generates these eddies can be viewed as a source of turbulence energy. Without this source of energy, turbulence will decay. The process of turbulence decay was first documented by Richardson (1922), which he called an energy cascade. This decay process involves the break-up of larger eddies into smaller ones, effectively transferring kinetic energy, which continues until molecular diffusion dissipates turbulent motion into heat.

An apparent result of these turbulent eddies is to generate fluctuations in velocity of the moving fluid. To gain a conceptual understanding of this, consider the velocity component aligned in the *k* Cartesian coordinate, u_k. It is assumed that this velocity can be further decomposed into a steady, component, $\{u_k\}$, and an unsteady component, u_k'', (Reynolds, 1895) via:

$$u_k = \{u_k\} + u_k'' \tag{2.4}$$

The exact mathematical operator for determining these components is not critical for this illustration. The turbulence kinetic energy, based upon turbulent velocity fluctuations, is defined by:

$$k_T = \frac{1}{2} u_k'' u_k'' \tag{2.5}$$

Here, Einstein notation is employed with implied summation over the index *k*. An alternative parameter based upon the turbulent velocity fluctuations is the characteristic turbulence velocity, defined as:

$$u_T = \sqrt{\frac{2}{3} k_T} \tag{2.6}$$

The integral, or inertial, range refers to scales of turbulent motion where large, energy containing eddies dominate the characteristics of the flow. The kinetic energy of an integral scale eddy does not experience significant dissipation due to viscous mechanisms. The Reynolds number based upon the inertial turbulence scale is defined as:

$$\mathrm{Re}_T = \frac{L_T \sqrt{k_T}}{\nu} \qquad 2.7$$

Where L_T is a length that characterises the largest amplitude of turbulent unsteadiness, and ν is the dynamic molecular viscosity. It has been proposed (Prandtl, 1945), based upon earlier dimensional analysis (Taylor, 1935), that the relationship between turbulence energy dissipation and inertial scale turbulence production takes the following form:

$$\varepsilon = C_T \frac{{u_T}^3}{L_T} \qquad 2.8$$

Where C_T is a constant of proportionality commonly prescribed a value of 0.09 in accordance with experimental data. The dissipation range describes turbulent length scales subjected to strong viscous forces that dissipate turbulence kinetic energy into heat. From the turbulence energy cascade theory, Kolmogorov (1941) used dimensional arguments to derive a physical law that describes the smallest scales of turbulent velocity fluctuations. Kolmogorov hypothesised that the smallest scale eddies achieved a Reynolds number of unity before being converted into heat. This work is known as the Universal Equilibrium theory (Kolmogorov, 1941), where the Kolmogorov length scale is defined as:

$$L_\eta = \left(\frac{\nu^3}{\varepsilon} \right)^{\frac{1}{4}} \qquad 2.9$$

The Universal Equilibrium theory is a balance between the production and dissipation of turbulence kinetic energy. Consequently, a greater production of turbulence leads to a greater difference in size between the largest and smallest eddies.

The inertial sub-range exists between the larger scale integral range and the small scale dissipation range. The onset of this range of scales sees a transition from anisotropic, inhomogeneous turbulence to isotropic, homogeneous turbulence. Taylor (1935) proposed for homogeneous, isotropic turbulence that the turbulence energy dissipation rate (per unit volume) could be expressed as:

$$\varepsilon = 15\nu \frac{{u_T}^2}{{L_\lambda}^2} \qquad 2.10$$

The Taylor micro-scale characterises the largest turbulent eddies which can be described as homogeneous and isotropic.

$$L_{\lambda_{kj}} = \sqrt{\left\{u_k'' u_k''\right\} \Big/ \left\{\frac{\partial u_k''}{\partial x_j}\frac{\partial u_k''}{\partial x_j}\right\}} \qquad 2.11$$

The Reynolds number based upon the Taylor micro-scale is defined as:

$$\mathrm{Re}_\lambda = \frac{L_\lambda u_T}{\nu} \qquad 2.12$$

By relating the viscous diffusion of an eddy to thermal diffusion, Batchelor (1959) showed that the smallest scales of turbulent temperature fluctuations may vary from the Kolmogorov scale. This concept extends to turbulent fluctuations of fluid composition, where the Batchelor length represents the smallest scale fluctuations in fluid composition due to turbulent motion and is related to the Kolmogorov length via:

$$L_B = \frac{L_\eta}{\sqrt{Sc}} \qquad 2.13$$

From expression 2.13 it is clear that the Bachelor scale is smaller for diffusion of species with a Schmidt number above unity. In most gaseous flows, the Schmidt number does not deviate substantially from unity.

2.2.2 Turbulence Energy Spectra

Expanding on the notion that a turbulent eddy is region of rotating fluid, the eddy can also be described by a characteristic frequency or wave number. Assuming that turbulence is a superposition of eddies with various frequencies, taking Fourier transform of the turbulent velocity fluctuations will indicate the amplitude, or strength, of eddies associated with a particular frequency

(Pope, 2000). For example, the Fourier transform of a turbulent velocity fluctuations signal taken along spatial direction, x, is given by:

$$\hat{u}_k''(\kappa) = \int_{-\infty}^{+\infty} u_k''(x) e^{-2\pi i \kappa x} dx \qquad 2.14$$

Where $\kappa = \pi / L$ is the wave-number of a eddy of size L. This can be used to construct an energy spectrum of this particular velocity component using:

$$E_k(\kappa) = \hat{u}_k''(\kappa) \, conj\left(\hat{u}_k''(\kappa)\right) \qquad 2.15$$

Where *conj* is the complex conjugate operator. The turbulence kinetic energy spectrum can be determined from the sum of velocity fluctuations spectra using:

$$E_T(\kappa) = \frac{1}{2} E_k(\kappa) \qquad 2.16$$

This energy spectrum is related to the turbulence kinetic energy in the following manner:

$$k_T = \int_0^{\infty} E_T(\kappa) d\kappa \qquad 2.17$$

Kolmogorov (1941) argued that the turbulence energy spectrum within the inertial sub-range is described using:

$$E_T(\kappa) = C_\kappa \varepsilon^{\frac{2}{3}} \kappa^{-\frac{5}{3}} \qquad 2.18$$

Where C_κ is the universal Kolmogorov constant. Combining expression 2.18 with the knowledge of the various scales of turbulence, and respective energy content, it is possible to visualise the hypothetical Richardson energy cascade as an energy spectrum, shown in Figure 4.5.

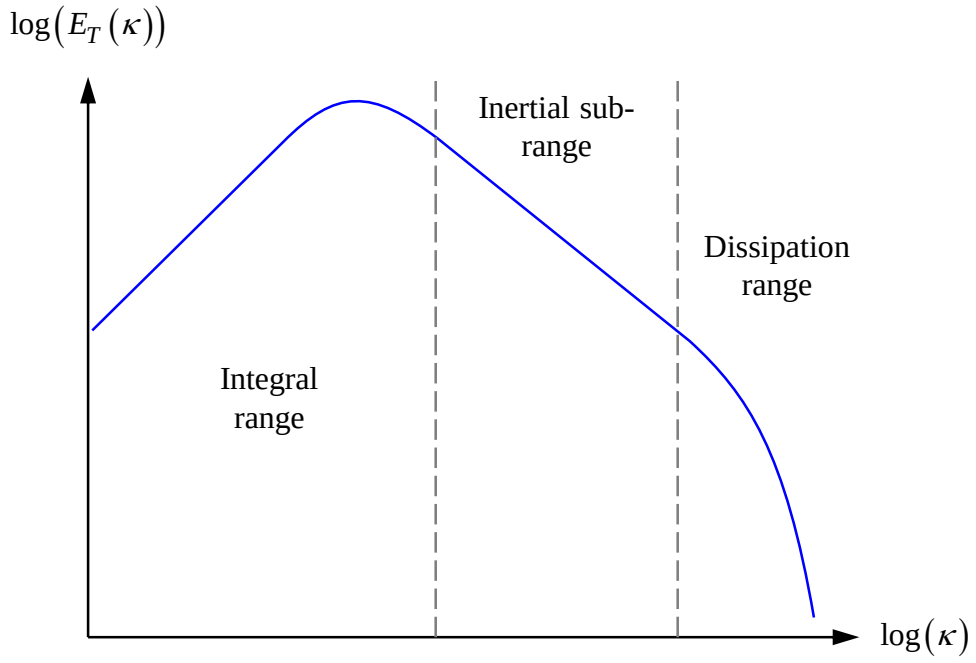

Figure 2.5: Notional turbulence energy spectra as a function of wave-number

2.2.3 Compressibility effects on turbulence

Design of hypersonic aerospace propulsion system must consider the effect compressibility has upon turbulent fluid motion. The relative compressibility of turbulence is related to the intensity of density fluctuations induced by disturbances in pressure (Lele, 1994). More specifically, the material rate of density disturbances generates fluctuations in velocity divergence due to continuity, a process which does not exist in incompressible turbulence (Smits & Dussauge, 2006). The combined effect of density and velocity fluctuations gives rise to turbulent dilatation, where the exchange of turbulent kinetic energy becomes dependent on three physical mechanisms: solenoidal dissipation (incompressible), dilatational dissipation, and pressure dilatation.

The scale at which these thermodynamic perturbations exist influences how the turbulence behaviour changes. Morkovin (1962) hypothesised that the turbulent structure of a boundary layer is not influenced by density fluctuations if these fluctuations are much smaller in magnitude to the mean density. This hypothesis implies compressibility should not affect the energy exchange between eddies of size smaller than the integral length, viewing small scale fluctuation as

isentropic. Bradshaw (1977) made the comment that Morkovin's hypothesis is applicable for wall bounded flows with a free-stream Mach number up to approximately 5.

Although widely used in compressible turbulence modelling, Morkovin's hypothesis essentially only applies to supersonic boundary-layers. Fully resolved direct numerical simulations of compressible turbulence performed by Zeman (1990) identified localised regions of compression, referred to as shocklets, which satisfy the Rankine-Hugoniot relations. The formation of shocklets accounted for a majority of the turbulent dilatational dissipation, which was found to scale linearly with the solenoidal turbulence dissipation (Zeman, 1990; Sarkar, et al., 1991a). In both studies, the proportionality factor was found to be a function of the turbulence Mach number, defined as:

$$M_T = \frac{\sqrt{2k_T}}{a} \qquad 2.19$$

Where a is the local sound speed. Detailed shocklet statistics present within decaying compressible turbulence was documented by Samtaney et al. (2001). This study observed shocklets at length scales larger than the Kolmogorov length, and with a shock strength proportional to $M_T / \sqrt{\mathrm{Re}_\lambda}$. However, numerical simulations (Vreman, et al., 1997; Pantano & Sarkar, 2002) have shown the dilatational term to be negligible and that compressibility directly affects the production of turbulence. This decreased production will be explored in more detail for the most relevant case, shear driven turbulence, in the next subsection.

2.3 Free-shear Turbulence

In order to understand the turbulent fuel-air mixing within a scramjet engine, previous research has sought to represent it as a composite of simpler flows. Canonical flow analogies are instructive as specific physical effects have be isolated, interrogated and subsequently understood. Three major types of free-shear flows have been identified: the mixing layer, the free jet, and the wake. These problems have been elucidated through laboratory experimentation, numerical simulation, and theoretical analysis.

2.3.1 Mixing Layer

The incompressible mixing layer is a turbulent flow generated between two fluid streams moving parallel at difference velocities, shown in Figure 4.2. This velocity difference creates shear between the fluid streams away from any physical boundary and induces a span-wise (out of plane) orientated rotation. Large scale vortices form as a consequence whereby the two streams are entrained and mixing within the region of shear. When both streams are comprised of the same fluid, this flow is generally referred to as a shear layer.

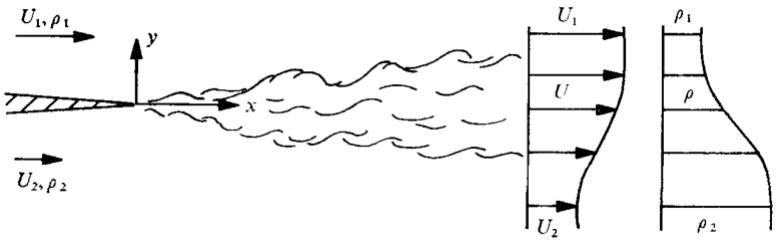

Figure 2.6: Schematic of the canonical turbulent mixing layer (Brown & Roshko, 1974)

The incompressible mixing layer can be characterised using several parameters: the velocity difference $(U_1 - U_2)$, the convective velocity (U_c), and the velocity ratio $(r = U_2 / U_1)$. One of the major differences between the mixing layer and other free shear flows is that the velocity difference remains constant as the flow travels down-stream. The velocity difference, in combination with a length scale, is a standard mixing layer normalisation parameter (Sabin, 1965):

$$U_\delta = U_1 - U_2 \tag{2.20}$$

The vorticity thickness provides an appropriate length scale for non-reacting mixing layers, and is defined as:

$$\delta_\omega = \frac{U_\delta}{\max\left(\frac{\partial U}{\partial y}\right)} \tag{2.21}$$

Accordingly, the characteristic Reynolds number, based upon the vorticity thickness and velocity difference, of a mixing layer is given by:

$$\mathrm{Re}_{\omega} = \frac{\rho U_{\delta} \delta_{\omega}}{\mu} \qquad 2.22$$

Where ρ and μ are the characteristic density and dynamic molecular viscosity respectively. For high Reynolds number mixing layers, the spreading rate was shown to be independent of the Reynolds number and constant in the absence of stream-wise pressure gradients. In situations where the density and viscosity vary between the two parallel streams, the Reynolds number is determined using the average density and viscosity of the two streams. In addition, the density ratio $(s = \rho_2 / \rho_1)$ appears as an additional characteristic parameter of the mixing layer.

Experimental research into the incompressible mixing layer has been an ongoing international effort for many decades. A critical review of mixing layer experimental data conducted by Birch & Eggers (1972) identified several inconsistencies in the then current literature, such as differences in developed and developing turbulence and the role density variations between streams played in mixing layer growth rates. The seminal experimental work of Brown and Roshko (1974) made a significant contribution towards the understanding of how an incompressible mixing layer behaves. Their work focused on the mixing of two parallel streams comprised of different gases in order to isolate density effects from effects of compressibility. Shadowgraph visualisations of the mixing layer, shown in Figure 2.7, highlight that coherent, two-dimensional "roller" vortices dominated the turbulent structure of the shear layer. These span-wise orientated "roller" vortices possess distinct core and braid regions and that, although neither steady in space nor time, persistently appear, disappear and reappear. Comparing various density ratios, it was found that having lighter, slow moving fluid streams mildly reduced the growth rate of the layer. More significantly, the researchers found that supersonic mixing layers experienced large reductions of growth rate seemingly unrelated to the effects of density.

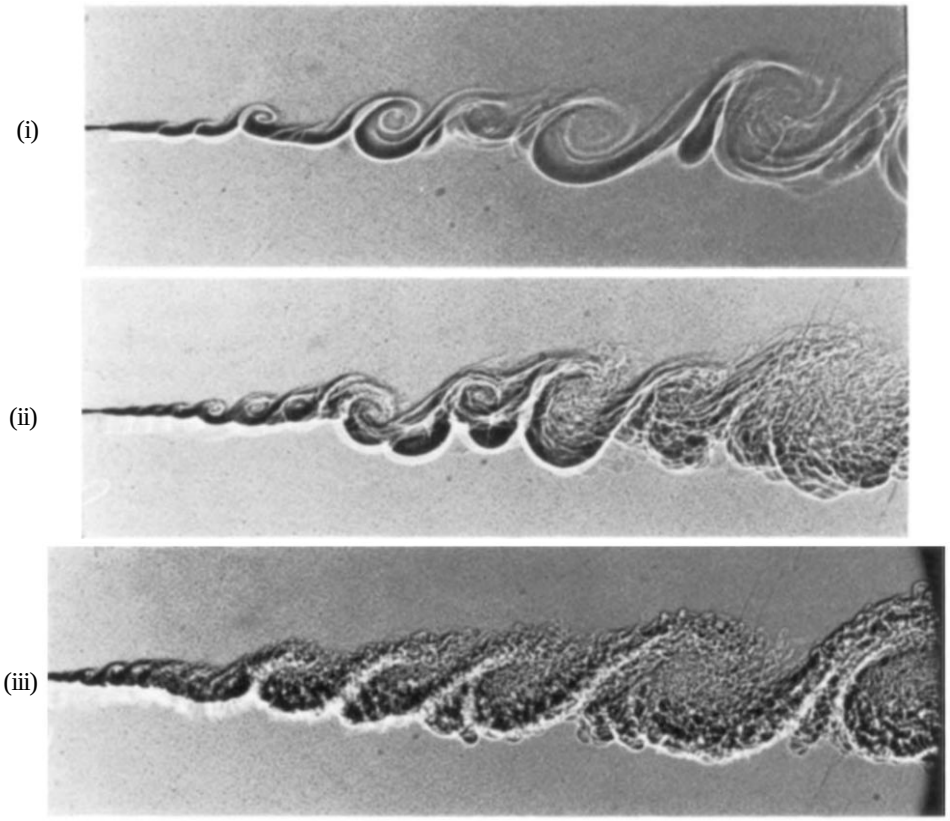

Figure 2.7: Shadowgraphs of the turbulent mixing layer between helium (upper) and nitrogen (lower) with a proprtional Reynolds number of: (i) 20, (ii) 40, and (iii) 80 (Brown & Roshko, 1974)

The observed vortex structures within an incompressible mixing layer, and the potential interactions between such structures, are discussed in detail by Hussain (1986). Vortex pairing, where two vortices approach each other and begin to rotate around a common origin and combine into a single structure (Winant & Browand, 1974), is shown to substantially increase the size of the coherent vortices, leading to greater mixing layer growth and subsequently entrainment rates. Smaller, stream-wise aligned vortices were experimentally observed to wrap around the larger span-wise vortices as these larger vortices began to break-up (Bernal & Roshko, 1986).

The work of Dimotakis (1986) led to a proposed correlation between the density ratio and the spreading rate of a spatially developing, variable density mixing layer, given by:

$$\delta_i'(r,s;x) \approx C_\delta \frac{(1-r)\left(1+\sqrt{s}\right)}{2\left(1+r\sqrt{s}\right)}\left[1-\frac{\left(1-\sqrt{s}\right)/\left(1+\sqrt{s}\right)}{1+2.9(1+r)/(1-r)}\right] \quad 2.23$$

Where C_δ is an empirically derived coefficient with a nominal value of 0.37 (though values between 0.25 - 0.45 are deemed appropriate). Similarity is achieved by choosing an inertial reference frame that moves with the convective velocity of the dominant, large scale eddies within the mixing layer. The stagnation pressures of both streams must be equal in order to produce the observed inflection point of fluid motion between these large span-wise vortices. His model, based upon asymmetric mixing, also characterised shear layer entrainment as a three step process: induction, diastrophy and infusion. Induction is a large scale dynamic process where undisturbed, irrotational fluid is drawn into the mixing layer. The inducted fluid then experiences strain such that viscous forces become dominant and micro-mixing of the two fluid streams occurs. Where the viscous diffusion of momentum and mass are of similar scale, typical for gas-phase shear layers, diastrophy and infusion act concurrently. Unlike previously proposed mixing layer models, Dimotakis considered both the temporal and spatial spreading rate of the mixing layer. The physical behaviour of the incompressible shear layer has become well understood, culminating in the work of Dimotakis (1991). The influences of realistic effects, such as heat release and pressure gradients, upon the mixing layer growth rate are documented. The author concludes that future research should, among other items, seek to understand the role of compressibility upon the mixing layer.

2.3.1.1 The effects of compressibility

It is now established that compressibility rather than density effects are responsible for the mixing layer growth rate reduction (Brown & Roshko, 1974; Bradshaw, 1977). To characterise the compressibility of a mixing layer, Papamoschou and Roshko (1988) proposed the convective Mach number following the work of Bogdanoff (1983). The convective Mach number is defined as the Mach number in a frame of reference moving with the large-scale structures within the mixing layer. The reference sound speed can either be chosen with respect to the faster or slower moving fluid streams via:

$$M_{c,1} = \frac{U_1 - U_c}{a_1} \quad 2.24$$

$$M_{c,2} = \frac{U_c - U_2}{a_2} \tag{2.25}$$

The total convective Mach number is defined as the geometric mean of the both convective numbers. Assuming equivalent ratios of specific heat (γ) for both streams, and that the streams are stagnated isentropically, the total convective Mach number is given by:

$$M_c = \frac{U_\delta}{a_1 + a_2} \tag{2.26}$$

The researchers found that spreading rate reductions of the mixing layer occurred before the flow went supersonic relative to the convective reference frame. For M_c greater than 0.8 it was found that the spreading rate becomes asymptotic to a value approximately one quarter that of the incompressible rate. Dimotakis (1991) derived the following empirical correlation between the ratio of compressible to incompressible mixing layer growth rate and the convective Mach number:

$$\frac{\delta_c'}{\delta_i'}(M_c) = 0.8\,\mathrm{e}^{-3M_c^2} + 0.2 \tag{2.27}$$

Early efforts to characterise the turbulence structures within a compressible mixing layer employed laser Doppler velocimetry (Goebel, et al., 1990; Goebel & Dutton, 1991; Elliott & Samimy, 1990). Increased compressibility of the mixing layer was not found to influence the normalised stream-wise turbulence intensities, but the cross-stream turbulence intensities decreased in accordance with the observed trends in spreading rate (Goebel & Dutton, 1991). This leads to considerable Reynolds normal stress anisotropy with higher compressibility which was attributed to an inviscid exchange of energy rather than an increase in dilatational dissipation proposed by Zeman (1990). Elliott and Samimy (1990) showed that the convective Mach number correlated with decreases in Reynolds stresses and the growth rate of a mixing layer. A direct relationship was found between high compressibility and lower turbulent diffusion of momentum across the layer. Compressible mixing layer turbulent fluctuations were also found to exist within a thinner normalised transverse extent, indicating a lessening dominance of large scale structures. Further analysis determined that less energy was extracted from the mean flow as the large scale structures diminished in size relative to an equivalent incompressible mixing layer.

It was predicted using linear stability theory that convective Mach numbers above 0.6 will alter the principal instability of a free shear from the traditional Kelvin-Helmholtz vortices orientated in the span-wise direction to more complex oblique vortices (Sandham & Reynolds, 1990; Morris, et al., 1990). This conclusion was supported by the three dimension direct numerical simulations of Sandham and Reynolds (1991), where it was found that the traditional span-wise instability is barely evident when the convective Mach number exceeds unity. Three-dimensional instability, principally aligned in the stream-wise direction, became the dominant wave form where the convective Mach number exceeded unity.

Clemens and Mungal (1992; 1995) visualised the compressible planar mixing layer using a planar laser Mie scattering (PLMS) technique. Even at high Reynolds numbers, distinct span-wise core and braid structures, similar to the incompressible mixing layer structure, were observed at convective Mach numbers less than approximately 0.50. A break-down of the apparent span-wise coherence into three-dimensional structures occurred at $M_c = 0.62, \ \& \ 0.79.$ Samimy, et al. (1992) observed that the characteristic large-scale structures tend to be span-wise oblique at a convective Mach number of 0.86.

The high fidelity numerical simulations of uniformly sheared compressible flow performed by Sarkar (1995) deduced that the normalised growth rate of turbulence kinetic energy was proportional to thickness growth rate of the layer. This stabilisation, namely reduction in the turbulence kinetic energy production, was attributed to less Reynolds shear stress anisotropy. In effect, a less efficient conversion of turbulence kinetic energy into productive Reynolds shear stress occurs at high levels of compressibility. The relative turbulent dissipation was found to marginally increase with compressibility, but this effect was found to be small relative to the less efficient turbulence production mechanism. Although dilatational effects were observed to constitute as much as 20% of the turbulence kinetic energy transport, there did not appear to be a direct correlation between dilatation and reduced growth rates. Vreman et, al. (1996) performed high fidelity numerical simulations of mixing layers with a range of convective Mach numbers. Similar reductions in turbulence production were reported, symptomatic of a reduced correlation between pressure and strain fluctuations which affected the evolution of the Reynolds shear stress. This result was confirmed by the mixing layer simulations of Pantano & Sarkar (2002).

The choice of convective velocity is not always unique and flow complexities introduce uncertainty in the idealised approach of determining its value. An alternative parameter used to determine compressibility effects upon a supersonic mixing layer was proposed by Slessor et al. (2000):

$$\Pi_c = \max\left(\sqrt{\gamma_i - 1}\,\frac{a_1 + a_2}{a_i}\right) M_c \qquad 2.28$$

This compressible scaling factor assumes an adiabatic conversion between kinetic and thermal energy, rather than assuming the turbulent eddies generate a convective stagnation point isentropically. The collapse of experimentally determined compressible mixing layer growth rates is reported to be marginally improved when plotted against this compressibility parameter, where curve-fitting yields the following empirical relationship:

$$\frac{\delta_c'}{\delta_i'}(\Pi_c) \simeq \left(1 + 4\Pi_c{}^2\right)^{-0.5} \qquad 2.29$$

A compilation of experimentally derived spreading rates of mixing layers with various convective Mach numbers is shown in Figure 2.8.

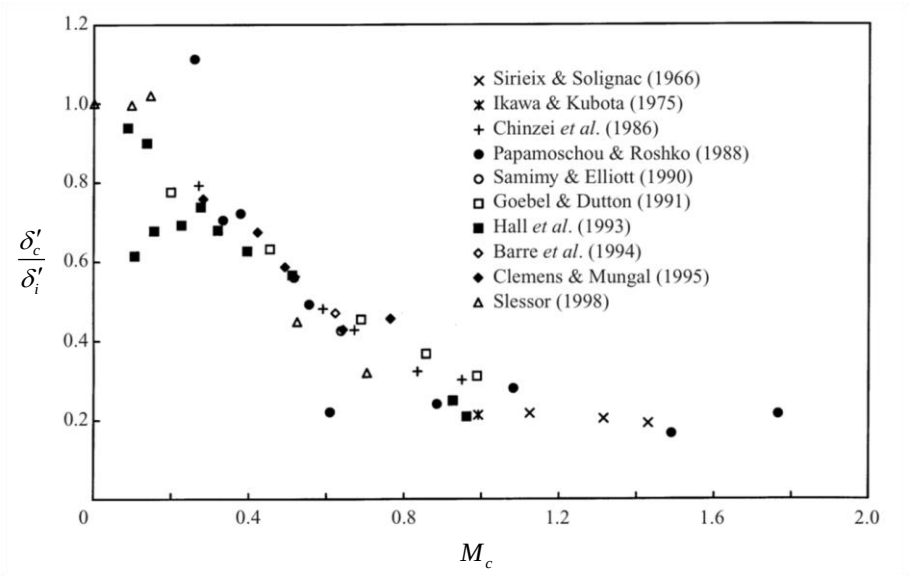

Figure 2.8: Growth rate of the compressible shear layer trend with convective Mach number (Slessor, et al., 2000)

2.3.2 Wake Flow

The wake which forms behind bluff bodies is another canonical turbulent flow that has received the interest of the fluid dynamics research community. It is well documented that the incompressible wake flow undergoes several vortex shedding regimes (Roshko, 1993) as the Reynolds number, based upon the free-stream and transverse size of the bluff body, increases. At very low Reynolds numbers, below 49, the incompressible wake remains steady as two symmetric recirculation regions form behind the bluff body. Above a Reynolds number of 50, the wake becomes unstable. The pioneering experimental and analytical work of von Kármán (1911; 1912) was instrumental in developing the current understanding of the unstable wake flow vortex dynamics. His work showed, except in one unique case, that the two rows of counter-rotating vortices were unstable. Attempts to describe the near-field vortex shedding event which evolves into the von Kármán vortex sheet was undertaken by Gerrard (1966). As one recirculation region grows into a vortex, the shear layer generated by the opposite flow separation is drawn across the wake and prevents further vorticity generation. The reaction to this by the opposite recirculation region leads to the oscillatory vortex shedding. The vortex shedding frequency is characterised by the non-dimensional Strouhal number, given by:

$$\mathrm{St} = \frac{fL}{U} \qquad 2.30$$

Where f is the shedding frequency, L is a characteristic length (taken as the diameter in the case of cylindrical wakes), and U is a characteristic velocity typically taken from the free-stream. Experimental measurements of Roshko (1954) found that two-dimensional, laminar vortex shedding occurred for Re = 40 - 150. This regular periodic shedding evolves from instabilities within the recirculation regions. Stream-wise vortex pairs begin to form between Re ~ 190 to 260 as the initial span-wise vortices experience deformation. At the upper end of this regime, the span-wise vortices experience dislocation at scales much larger than the vortex diameter. Above Re 260, the smaller vortices, which form due to the break-down of the large, span-wise aligned vortices, become increasingly disordered and three-dimensional. The Kelvin-Helmholtz instabilities of the shear layers which form at the point of separation begin to dominate the near-field flow for Re = 1×10^3 to 2×10^5. Formation of the von Kármán vortex sheet remains apparent down-stream as

the shear-layer structures quickly break-down. Visualisations of wake flows at various Reynolds numbers are shown in Figure 2.9. The critical transition occurs for $Re \sim 2\times10^5$ where the base suction drastically reduces as the separation undergoes asymmetric reattachment to one side of the body. The Supercritical wake regime occurs when separation reattachment occurs symmetrically. Up to this point, the boundary-layer which forms around the body remains laminar before separation which allowed coherent structures to form. For $Re \sim 1\times10^6$, or the post-critical regime, turbulent transition of the boundary is expected before separation. Within this regime, the behaviour of the wake is strongly influenced by the turbulent boundary-layer. Despite this, there is experimental evidence that vortex shedding persists (Roshko, 1961). A review of these wake flow regimes, specifically focussing on the three-dimensional vortex dynamics of cylinder wakes, was published by Williamson (1996).

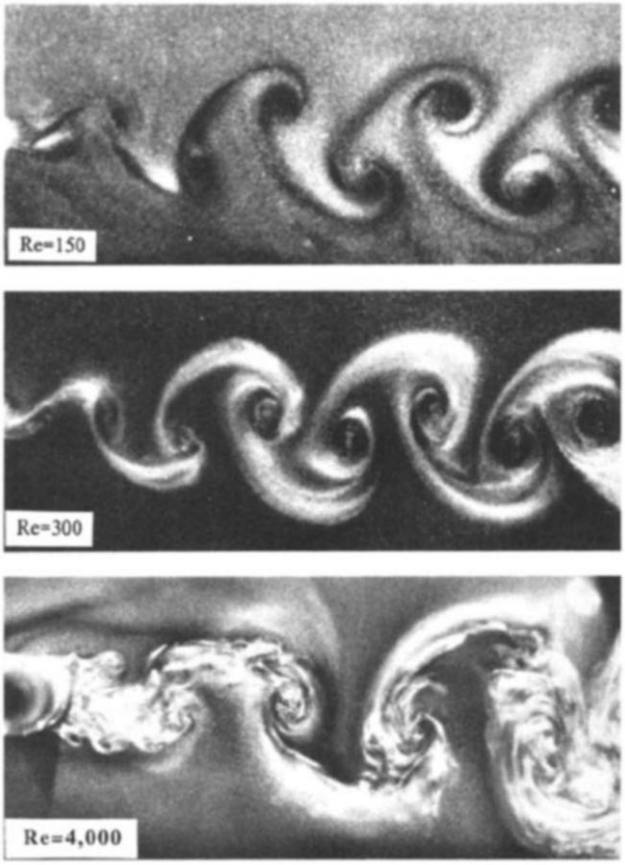

Figure 2.9: Aluminium flake visualisations of laminar and turbulent incompressible wake vortex sheets (Williamson, 1996)

2.3.2.1 Mixing Wake Flow

The mixing wake refers to the down-stream flow generated by injecting fluid into the wake that forms behind a free-stream immersed body. The near-field is characterised by the free-stream, the injected jet stream, and the wake the forms between these streams. The two fluid streams meet further down-stream to form a mixing layer. Unlike the canonical mixing layer, which experiences a constant shearing velocity difference, the near-field wake will generate a momentum deficit between the free and jet streams. The magnitude of this deficit is dependent on the conditions of both these streams. The flow will eventually behave as wake in the far-field if the momentum flux of the injected stream is less than that of the free-stream. Conversely, jet flow occurs is the far-field if the momentum flux of the injected stream is greater than that of the free-stream

Weinstein, et al. (1956) developed an algebraic model based upon a similarity solution of the governing fluid equations to determine the mean velocity profiles of an incompressible, self-similar mixing wake flow. This assumed momentum diffusion can be described by a Gaussian function. Weinstein's model primarily characterises the mixing wake with the ratio of jet to free-stream velocity, in addition to an empirical spreading coefficient, just as the velocity ratio is the primary descriptor of an incompressible shear layer. Attempts to correct the model for compressibility effects using the Howarth transformation failed to accurately predict experimental data (Casey, 1990). By employing the compressible scaling parameter from mixing layer theory, which is a function of the convective Mach number, the model was able to match the experimentally determined mixing wake growth-rate, but not the integrated width. As this model assumes self-similarity, it is not appropriate for the prediction of near-field turbulent motion, nor regions where shock-waves interact with the mixing layer.

The introduction of a wake component within compressible mixing layers was studied by Zhuang & Dimotakis (1995). The authors performed a linear, inviscid stability analysis upon mean-velocity profiles which represented near-field shear flows with an imbedded detached boundary-layer. The wake momentum deficit introduces another instability mode in addition to the strong and weak supersonic modes present in a typical compressible mixing layer. Larger wakes were found to reverse the oblique instability evolution predicted for highly compressible shear layers such that the two-dimensional instability dominates in a similar manner to the incompressible mixing layer.

2.4 Computational Fluid Dynamics

Computational Fluid Dynamics (CFD) is a subject devoted to solving the Navier-Stokes set of differential equations using a numerical methodology. Solving the exact Navier-Stokes equations numerically, with a discretisation capable of resolving all physical scales, is referred to as Direct Numerical Simulation (DNS). The DNS approach requires all the scales of turbulent motion to be resolved, from the integral scale down to the molecular dissipation scale. Scaling arguments shows that a DNS appropriate computational grid scales with the integral Reynolds number to the power of 9/4. This requirement is computationally prohibitive for most practical flows, where the integral Reynolds number is greater than 1.0×10^4. When attempting to simulate such flows, there are various alternative approaches which involve finding the solution to a modified version of the Navier-Stokes equations.

The Reynolds Averaged Navier-Stokes (RANS) simulations simply aim to determine the mean field of the desired fluid flow. This is achieved by solving a different set of differential equations which govern the evolution of the mean flow field. This technique greatly reduces the computational expense of the simulation. The main caveat with this approach is that the effects of all unsteady fluid motion must be modelled, rather than resolved.

Intermediate unsteady simulations such as Large Eddy Simulation (LES) and Detached Eddy Simulation (DES) strike a balance between the DNS and RANS methodologies. For these techniques, the large, energy containing turbulent motion is resolved whereas the smaller turbulent motions, which are expected to be near universal, are modelled using an analytic sub-grid scale (SGS) model. The major distinction between LES and DES is in regards to simulating the turbulence generated near viscous walls. In such regions, the smaller scale turbulent motion is most energetic and a more sophisticated turbulence model is required to capture the physical processes. The SGS models used in typical LES fail to capture this. Blending between the sgs model for free shear turbulence and a RANS turbulence model for wall-bounded turbulence circumvents this deficiency and is the basis of DES.

The work contained within this thesis utilises only two of the aforementioned methodologies, those being RANS and LES. The remainder of this section is devoted to describing RANS and LES techniques in further detail.

2.4.1 Reynolds Averaged Navier-Stokes Simulations

The Reynolds Averaged Navier-Stokes (RANS) equations are derived by performing an ensemble average of the constitutive equations of fluid dynamics. This ensemble average, also referred to as the Reynolds operator, is generally described by:

$$\langle \phi \rangle (\mathbf{x},t) = \int_{-\infty}^{+\infty} \phi(\mathbf{x},t) P(\phi) d\phi \qquad 2.31$$

Where $P(\phi)$ is the probability density function (likelihood) of a particular realisation of ϕ instantaneously existing at a given location within a particular flow field. The ensemble Reynolds operator commutes with temporal and spatial differentiation. The improper integral can be numerically approximated using a discrete number of realisation of ϕ by the following:

$$\langle \phi \rangle (\mathbf{x},t) = \frac{1}{\mathrm{N}} \sum_{i=1}^{\mathrm{N}} \phi^{(i)}(\mathbf{x},t) \qquad 2.32$$

The ambition is that a sufficiently large number, N, of realisations, $\phi^{(i)}$, are taken such that the result becomes invariant to further increasing to the number of realisations and representative of the total realisation population. This requirement is referred to as the convergence criteria.

For compressible fluid flows, where fluctuations in density must be considered, it is advantageous to utilise a density weighted ensemble average. In response to Morkovin's hypothesis, Favre (1965) proposed an alternative density weighted operator, which is related to the Reynolds operator by:

$$\{\phi\}(\mathbf{x},t) = \frac{\langle \rho\phi \rangle}{\langle \rho \rangle} \qquad 2.33$$

The advantage of this operator is that variations in density do not lead to additional terms appearing in the compressible form of the Reynolds averaged conservation of mass equation. Triple product terms involving density fluctuations in the compressible momentum and higher order product terms in the energy transport equation are also avoided. In effect, this mathematical notation treats momentum, rather than velocity, as the principal dependent variable (of time and space) from which velocity can be derived. Of course, if Morkovin's hypothesis applies then the difference between Reynolds and Favre averaged quantities, such as velocity, should remain small. Smit & Dussauge (2006) have shown for a compressible adiabatic boundary-layer flow that these differences are less than 1.5%.

2.4.1.1 Reynolds Decomposition

Reynolds decomposition (Reynolds, 1895) represents a variable as the sum of a mean component and fluctuating component, given by:

$$\phi = \langle \phi \rangle + \phi' \tag{2.34}$$

From this definition, the Reynolds average of a fluctuating component is identically zero:

$$\langle \phi' \rangle = \langle \phi - \langle \phi \rangle \rangle = 0 \tag{2.35}$$

Decomposition of an unsteady term into Favre-averaged and fluctuating components is given by:

$$\phi = \{\phi\} + \phi'' \tag{2.36}$$

It is important to note that the Reynolds and Favre fluctuating components are not equivalent, except in the trivial case where the Reynolds and Favre averaged components are equal. This results in the following inequality:

$$\langle \phi'' \rangle = \langle \phi - \{\phi\} \rangle = \langle \phi \rangle - \{\phi\} \neq 0 \tag{2.37}$$

These decomposition techniques can be extended to provide a statistical description of the Navier-Stokes equations. The steady terms are determined using the mean primitive variables of the flow (such as mass density, components of velocity, static pressure, and chemical species mass

fractions), and the unsteady terms are simply the difference between the instantaneous term and the steady term. As a benign example, the advection of mass density simply becomes:

$$\frac{\partial}{\partial x_j}\left(\rho u_j\right) = \frac{\partial}{\partial x_j}\left(\langle\rho\rangle\{u_j\}\right) + \frac{\partial}{\partial x_j}\left(\rho u_j - \langle\rho\rangle\{u_j\}\right) \tag{2.38}$$

By taking the Reynolds-average of expression 2.38 and noting the definition of a Favre-Reynolds averaged variable, it is clear that the last term on the right hand side becomes zero:

$$\begin{aligned}\left\langle\frac{\partial}{\partial x_j}\left(\rho u_j\right)\right\rangle &= \left\langle\frac{\partial}{\partial x_j}\left(\langle\rho\rangle\{u_j\}\right) + \frac{\partial}{\partial x_j}\left(\rho u_j - \langle\rho\rangle\{u_j\}\right)\right\rangle \\ &= \frac{\partial}{\partial x_j}\left(\left\langle\langle\rho\rangle\{u_j\}\right\rangle\right) + \frac{\partial}{\partial x_j}\left(\left\langle\rho u_j\right\rangle - \langle\rho\rangle\{u_j\}\right) \\ &= \frac{\partial}{\partial x_j}\left(\langle\rho\rangle\{u_j\}\right)\end{aligned} \tag{2.39}$$

A more significant outcome of describing the governing equations in this form is the case of linear momentum advection, given by

$$\frac{\partial}{\partial x_j}\left(\rho u_i u_j\right) = \frac{\partial}{\partial x_j}\left(\langle\rho\rangle\{u_i\}\{u_j\}\right) + \frac{\partial}{\partial x_j}\left(\rho u_i u_j - \langle\rho\rangle\{u_i\}\{u_j\}\right) \tag{2.40}$$

Taking the Reynolds average of the above expression yields the following result:

$$\begin{aligned}\left\langle\frac{\partial}{\partial x_j}\left(\rho u_i u_j\right)\right\rangle &= \left\langle\frac{\partial}{\partial x_j}\left(\langle\rho\rangle\{u_i\}\{u_j\}\right) + \frac{\partial}{\partial x_j}\left(\rho u_i u_j - \langle\rho\rangle\{u_i\}\{u_j\}\right)\right\rangle \\ &= \frac{\partial}{\partial x_j}\left(\left\langle\langle\rho\rangle\{u_i\}\{u_j\}\right\rangle\right) + \frac{\partial}{\partial x_j}\left(\left\langle\rho u_i u_j\right\rangle - \left\langle\langle\rho\rangle\{u_i\}\{u_j\}\right\rangle\right) \\ &= \frac{\partial}{\partial x_j}\left(\langle\rho\rangle\{u_i\}\{u_j\}\right) + \frac{\partial}{\partial x_j}\left(\langle\rho\rangle\left(\{u_i u_j\} - \{u_i\}\{u_j\}\right)\right)\end{aligned} \tag{2.41}$$

The kernel of the last differential term on the right is identified as a Reynolds stress, τ_{ij}, and shows that not all unsteady terms average to become identically zero. Applying the Reynolds operator to

the complete Navier-Stokes equations, which are defined in Appendix A1, yields the following set of mean field evolution equations:

$$\frac{\partial}{\partial t}\left(\langle\rho\rangle\right)+\frac{\partial}{\partial x_j}\left(\langle\rho\rangle\{u_j\}\right)=0 \tag{2.42}$$

$$\frac{\partial}{\partial t}\left(\langle\rho\rangle\{u_i\}\right)+\frac{\partial}{\partial x_j}\left(\langle\rho\rangle\{u_i\}\{u_j\}+\langle p\rangle\delta_{ij}-\langle\sigma_{ij}\rangle\right)=-\frac{\partial}{\partial x_j}\left(\tau_{ij}\right) \tag{2.43}$$

$$\begin{aligned}\frac{\partial}{\partial t}\left(\langle\rho\rangle\{e_t\}\right)+\frac{\partial}{\partial x_j}\left(\langle\rho\rangle\{e_t\}\{u_j\}+\langle p\rangle\{u_j\}\right) &= -\frac{\partial}{\partial x_j}\left(q_{T,j}-\langle\sigma_{jk}u_i''\rangle+\frac{1}{2}\langle\rho u_i''u_i''u_j''\rangle\right)\\ +\frac{\partial}{\partial x_j}\left(\langle q_j\rangle-\langle\sigma_{jk}\rangle\{u_k\}\right) &\quad -\frac{\partial}{\partial x_j}\left(\tau_{kj}\{u_k\}\right)\end{aligned} \tag{2.44}$$

$$\frac{\partial}{\partial t}\left(\langle\rho\rangle\{Y_{S_i}\}\right)=\frac{\partial}{\partial x_j}\left(\langle\rho\rangle\{Y_{S_i}\}\{u_j\}+\langle J_{S_i j}\rangle\right)=-\frac{\partial}{\partial x_j}\left(J_{T,S_i j}\right) \tag{2.45}$$

Where the mean total internal energy is defined as:

$$\{e_t\}=\{e\}+\frac{1}{2}\{u_k\}\{u_k\}+\{k_T\} \tag{2.46}$$

The terms on the right hand-side of equations 2.43, 2.44, and 2.45 are mean coupled unsteady terms. These correlated unsteady terms must be modelled in order to close the Reynolds averaged Navier-Stokes equations as they cannot be determined from the mean field nor can they be trivialised.

2.4.1.2 Turbulence Modelling

Turbulence modelling seeks to close the Reynolds-averaged Navier-Stokes equations using a combination of statistics, empirical correlations, and dimensional analysis. The principal focus of the turbulence model is to formulate an expression for the Reynolds stress tensor, τ_{ij}. The Boussinesq eddy-viscosity approximation (Boussinesq, 1877) is commonly used in the modelling of

turbulence, which considers turbulent momentum transport in a similar fashion to molecular momentum transport. This results in the following expression for the Reynolds stress:

$$\tau_{ij} = -\mu_T \left[\left(\frac{\partial \{u_i\}}{\partial x_j} + \frac{\partial \{u_j\}}{\partial x_i} \right) - \frac{2}{3} \frac{\partial \{u_k\}}{\partial x_k} \delta_{ij} \right] + \frac{2}{3} \langle \rho \rangle \{k_T\} \delta_{ij} \qquad 2.47$$

Rather than a molecular viscosity, the Reynolds stress tensor comes from the multiplication of the mean strain of the flow with a eddy viscosity μ_T, approximated to be a scalar value. This formation also ensures that the sum of the normal Reynolds stresses is equal to twice the turbulence kinetic energy, which is expected by definition. However, implementing equation 2.47 introduces an explicit dependence on both the mean turbulence kinetic energy and the eddy viscosity.

The most direct approach for closing the turbulence model is to derive an evolution equation for the eddy viscosity and ignore the contribution of the turbulence kinetic energy to both the total internal energy and the normal Reynolds stresses. A popular example of this is the Spalart-Almaras (SA) one-equation model (Spalart & Allmaras, 1992). More rigorous modelling accounts for the turbulence kinetic energy in the RANS equations, whereby its evolution, for a compressible flow, is given by:

$$\begin{aligned} \frac{\partial}{\partial t}\left(\langle \rho \rangle \{k_T\} \right) + \frac{\partial}{\partial x_j}\left(\langle \rho \rangle \{k_T\} \{u_j\} \right) = \langle \rho \rangle \tau_{ij} \frac{\partial \{u_i\}}{\partial x_j} - \langle \rho \rangle \{\varepsilon\} \\ + \frac{\partial}{\partial x_j}\left(\langle \sigma_{ij} u_i'' \rangle - \frac{1}{2} \langle \rho u_i'' u_i'' u_j'' \rangle - \langle p' u_i'' \rangle \right) \\ - \langle u_i'' \rangle \frac{\partial \langle p \rangle}{\partial x_i} + \left\langle p' \frac{\partial u_i''}{\partial x_i} \right\rangle \end{aligned} \qquad 2.48$$

Several of the terms in equation 2.48 have already been introduced into the RANS equations set, such as the molecular diffusion and turbulent transport of $\{k_T\}$ which appears in the total internal energy evolution equation. These terms are typically modelled using a gradient diffusion expression (Wilcox, 2006) of the form:

$$\langle \sigma_{ij} u_i'' \rangle - \frac{1}{2} \langle \rho u_i'' u_i'' u_j'' \rangle = \left(\mu + \frac{\mu_T}{\sigma_k} \right) \frac{\partial \{k_T\}}{\partial x_j} \qquad 2.49$$

Where σ_k is a model constant. Pressure diffusion is almost universally ignored due to a lack of information. The pressure work term is an artefact of Favre-averaging and usually trivialised as it only become significant when the Morkovin hypothesis breaks down. Models for the pressure dilatation have been proposed by Zeman (1990), Sarkar et al (1991a), and Wilcox (1992), among others, which view the term as a function of turbulence Mach number. The validity of these model remains questionable as discussed in section 2.2.3. With an expression for the turbulence kinetic energy now formulated, it must now be related back to the eddy viscosity. This can be achieved in a variety of ways by appealing to dimensional arguments, yielding:

$$\mu_T \sim \rho L_T \sqrt{k_T} \tag{2.50}$$

$$\mu_T \sim \frac{\rho {k_T}^2}{\varepsilon} \tag{2.51}$$

$$\mu_T \sim \rho \frac{k_T}{\omega_T} \tag{2.52}$$

Where L_T is a characteristic turbulence length scale, ε is the turbulence dissipation rate, and ω_T is the turbulence specific dissipation rate. Closure of the model is achieved by defining a transport equation for one of the three newly introduced parameters. The most common formulations are the standard $k_T - \varepsilon$ model (Launder & Sharma, 1974), Wilcox's $k_T - \omega_T$ model (Wilcox, 1998; Wilcox, 2008), and Menter's SST model (Menter, 1994). The models are referred to as two equation models as they introduce two additional evolution equations into the RANS equations set. The remaining correlated unsteady terms, namely the turbulence heat flux and the turbulence scalar diffusion, have an assumed gradient diffusion form:

$$q_{T,j} = -\frac{\mu_T}{\mathrm{Pr}_T} \frac{\partial \{h\}}{\partial x_j} \tag{2.53}$$

$$J_{T,S_i j} = -\frac{\mu_T}{Sc_T} \frac{\partial \{Y_{S_i}\}}{\partial x_j} \tag{2.54}$$

Where Pr_T is the turbulence Prantl number and Sc_T is the turbulence Schmidt number. Both are assumed constant scalar values which are tuned to match empirical data.

2.4.2 Large Eddy Simulation

The concept of Large Eddy Simulation (LES) is to resolve only the large, energy containing scales. The small scales need only be modelled. The technique was first applied to incompressible turbulent fluid problems by meteorologists (Smagorinsky, 1963; Deardorff, 1970). The formal LES equations are derived by applying a filter to the instantaneous Navier-Stokes set of differential equations (Leonard, 1974). The LES filter is equivalent to a convolution integral using a filter kernel:

$$\bar{\psi}\left(\mathbf{x},t;\Delta_c\right)=\int G\left(\mathbf{x}-\mathbf{x}';\Delta_c\right)\psi\left(\mathbf{x}',t\right).d\mathbf{x}' \qquad 2.55$$

Where $G\left(\mathbf{x}-\mathbf{x}';\Delta_c\right)$ represents a filter kernel, and Δ_c is the sub-grid cut-off length scale. The filter should attenuate high frequency (small scale) turbulence which exist at scales smaller than a prescribed cut-off scale Δ_c. A kernel filter which is independent of time and absolute position is referred to as homogeneous and is commutative with temporal and spatial differentiation. The Favre-filter (Favre, 1965) is a density weighed filter, similar to the Favre-Reynolds operator, and is related to the LES filter operator in the following manner:

$$\tilde{\psi}\left(\mathbf{x},t;\Delta_c\right)=\frac{\overline{\rho\psi}}{\bar{\rho}} \qquad 2.56$$

Applying the LES filter to the Navier-Stoke equations yields the following set of resolved field evolution equations:

$$\frac{\partial}{\partial t}\left(\bar{\rho}\right)+\frac{\partial}{\partial x_j}\left(\bar{\rho}\tilde{u}_j\right)=0 \qquad 2.57$$

$$\frac{\partial}{\partial t}\left(\bar{\rho}\tilde{u}_i\right)+\frac{\partial}{\partial x_j}\left(\bar{\rho}\tilde{u}_i\tilde{u}_j+\bar{p}\delta_{ij}-\tilde{\sigma}_{ij}\right)=-\frac{\partial}{\partial x_j}\left(\tau_{ij}^{sgs}\right) \qquad 2.58$$

$$\frac{\partial}{\partial t}\left(\bar{\rho}\tilde{e}_t\right)+\frac{\partial}{\partial x_j}\left(\bar{\rho}\tilde{e}_t\tilde{u}_j+\bar{p}\tilde{u}_j+\tilde{q}_j-\tilde{\sigma}_{jk}\tilde{u}_k\right)=-\frac{\partial}{\partial x_j}\left(q_j^{sgs}+D_j^{sgs}\right) \quad 2.59$$

$$\frac{\partial}{\partial t}\left(\bar{\rho}\tilde{Y}_{S_i}\right)=\frac{\partial}{\partial x_j}\left(\bar{\rho}\tilde{Y}_{S_i}\tilde{u}_j+\bar{J}_{S_i j}\right)=-\frac{\partial}{\partial x_j}\left(J_{S_i j}^{sgs}\right) \quad 2.60$$

The time evolution of the resolved fields, by nature of the filtering operation, does not contain all the information of the turbulent flow dynamics. The ambition of LES is to replicate statistical information, such as the mean or variance, of the physical quantities being simulated (Pope, 2004). The explicit dependence of the filtered terms upon the sub-grid cut-off length is commonly ignored, a choice referred to as implicit LES. The implicit dependence on the cut-off length comes from the sub-grid terms, which aim to dissipate fluctuations in the filtered terms at scales below the prescribed cut-off scale. Discretisation of the computational domain also acts to implicitly box filter the constitutive equations, with the filter width equivalent to twice the geometric mean of the local cell size. However, the exact form of the filter kernel is not known when using implicit LES due to a coupling between the residual scale model and the discretised resolved field.

Consideration should be given to the commutative error introduced when an inhomogeneous filter is applied to the governing equations. This problem was studied by Ghosal and Moin (1995) who found that additional terms, which have second order significance with respect to Δ_c, should be included in the equations if discretisation is done using a high-order numerical scheme.

2.4.2.1 Sub-grid Scale Models

The additional terms which appear on the right-hand side of the transport equations are generated from filtering the Navier-Stokes equations and represent: the sub-grid scale turbulent stresses τ_{ij}^{sgs}, the sub-grid scale turbulent heat flux q_j^{sgs}, the sub-grid scale turbulent diffusion D_j^{sgs}, and the sub-grid scale turbulent scalar flux $J_{S_i j}^{sgs}$, where these terms are defined as:

$$\tau_{ij}^{sgs}=\bar{\rho}\left(u_i u_j-\tilde{u}_i\tilde{u}_j\right) \quad 2.61$$

$$q_j^{sgs} = \bar{\rho}\left(h_t u_j - \tilde{h}_t \tilde{u}_j\right) \quad 2.62$$

$$D_j^{sgs} = \frac{\bar{\rho}}{2}\left(u_j u_j u_k - u_j u_j \tilde{u}_k\right) \quad 2.63$$

$$J_{S_i j}^{sgs} = \bar{\rho}\left(Y_{S_i} u_j - \tilde{Y}_{S_i} \tilde{u}_j\right) \quad 2.64$$

These sub-grid terms are not strictly a function of only the resolved terms and must be modelled. In a similar vein to RANS, the most important modelled terms in LES are the sub-grid scale turbulent stresses. These stresses were initially computed using functional models, namely the eddy-viscosity assumption, which focuses on dissipating turbulence kinetic energy correctly. This leads to the following relationship:

$$\tau_{ij}^{sgs} - \frac{1}{3}\tau_{kk}^{sgs}\delta_{ij} = -2\mu^{sgs}\tilde{S}_{ij} \quad 2.65$$

Where μ^{sgs} is the sub-grid scale eddy viscosity and $\tilde{S}_{ij}$ is the resolved strain-rate tensor. The first model of this kind was developed by Smagorinsky (1963), which for compressible flow defines the sgs eddy viscosity as:

$$\mu^{sgs} = \bar{\rho}\left(C_S \Delta_c\right)^2 \sqrt{2\tilde{S}_{ij}\tilde{S}_{ij}} \quad 2.66$$

Where the Smagorinsky constant, C_S, has values between 0.1 - 0.2 depending on the simulated turbulence. It was found that excessive turbulence energy dissipation generated by the model led to inaccuracies when simulating laminar regions experiencing mean shear (Germano, et al., 1991). To rectify this deficiency, a dynamic eddy viscosity model was proposed by Germano (1992), which replaced the Smagorinsky constant with a variable coefficient, C_d, dependent on the local turbulent structure of the flow. This technique introduces another filter operator, or test-filter. Two symmetric tensors are generated by applying various permutations of the LES filter and test-filter to the non-linear advection term which generates the sgs turbulent stress tensor. These tensors can then be used to determine C_d (Lilly, 1992) using the Germano identity. To prevent numerical instability, averaging of tensor products over the homogeneous flow directions is necessary. A compressible

extension of this sub-grid closure model was proposed by Martin et al. (2000), who investigated the numerous additional sub-grid terms generated due to the energy transport of variable density fluids.

The need to simulate flows without a homogeneous direction, and improve the physical representation of the sgs turbulence gave rise to structural sgs models. One approach is to decomposed the sgs turbulent stresses into Leonard, cross, and Reynolds components. Each component is then expressed as a Taylor expansion of the filtered velocity (Clark, et al., 1979). However, this method was found to be numerically unstable (Vreman, et al., 1995). A dynamic structural approach is to consider a model for the sgs turbulence kinetic energy and relate this to the various components of the sgs stresses. An example of this is the model of Pomraning & Rutland (2002), who proposed a transport equation for the sgs turbulence kinetic energy. A physical rationalisation that the sgs turbulence could consist of stretched vortices was proposed by Misra & Pullin (1997). The orientation of these vortices could be determined from the resolved field. This model was extended to include the turbulent diffusion of a passive scalar by Pullin (2000). This work culminated in a complete sgs turbulence model including the effects of compressibility (Kosovic, et al., 2002). Details of this model are discussed in a subsequent section.

2.4.2.2 Hypervelocity LES Simulations

Early compressible LES were limited to canonical turbulent flows confined within simple geometries. The temporally developing shear layer has been investigated Vreman, et al. (1997). Foysi & Sarkar (2010) performed LES of temporally developing mixing layer at various convective Mach numbers ranging from 0.3 to 1.2. The ambition of this work was to demonstrate LES can capture the self-similar evolution of highly compressible mixing layers. The authors reported grid spacing two orders of magnitude larger than Kolmogorov scale and negligible resolved dissipation relative to the sub-grid scale model dissipation. The characteristic mixing layer Reynolds number ranged between 705 and 20,000. Increased anisotropy of the Reynolds stress correlated with reduced layer growth rates with increasing convective Mach number. These simulations confirmed the experimental observations that, for convective Mach numbers above 0.6, the dominant vortical structures of the mixing layer became smaller and stretched in the stream-wise direction. Smaller, more three-dimensional turbulent eddies consequently reduces pressure-strain correlations which suppresses turbulence production. It is reported that the pressure-strain must be accounted for when

considering the Reynolds stress transport. Excellent agreement with experimental (Bell & Mehta, 1990) and DNS (Pantano & Sarkar, 2002) results was reported.

Performing pure LES of an internal scramjet flow path is very difficult due in part to the complex geometries and viscous boundary-layers that develop. A review of the various strategies to overcome these difficulties is presented by Piomelli (2008). The simplest approach is to apply a wall function in grid cells adjacent to viscous wall boundaries that obeys the logarithmic law of the wall. An alternative method is to use a hybrid LES/RANS methodology where, in addition to solving the LES equations, the RANS equations are solved in near-wall regions of the flow. A blending function is then used to transition between the RANS (in the near-wall region) and LES (in the prescribed free-stream region) solutions. This approach was first proposed by Spalart, et al. (1997). Additional difficulties arise when attempting to simulate reactive flows using LES, which are twofold: computational costs increase due to the extra transport equations introduced by simulating intermediate chemical species, and turbulence-chemistry interactions at the sub-grid scale can be prominent (Pope, 1990).

LES simulations of internal scramjet engine flow paths typically replicate ground or flight supersonic combustion experiments. This is done so that simulation results can be validated against experimental data. The reactive flow through a model scramjet experimentally tested at the Institute of Chemical Propulsion of the DLR, German Aerospace Center (Waidmann, et al., 1995) has received the interest of several computational researchers. The combustor is comprised of an initial constant area duct, which then diverges at a constant 3° angle 100 mm down-stream of the entrance. A wedge-shaped centre-body, which is 32 mm in length with a 6° half angle, is positioned on the symmetry plane of the up-stream constant area section. Slightly pre-heated air at a temperature of 340 K and a pressure of 100 kPa enters the combustor travelling at a Mach number of 1.96. The Reynolds number based upon these conditions and the strut base is $\sim 2.5 \times 10^5$. Hydrogen was injected at a temperature of 250 K and at the speed of sound via 15 holes in the base of the strut, each with a diameter of 1.0 mm. Fuel equivalence ratios ranged between 0.034 and 0.136 over the experimental testing. A schematic of the combustor is shown in Figure 2.10.

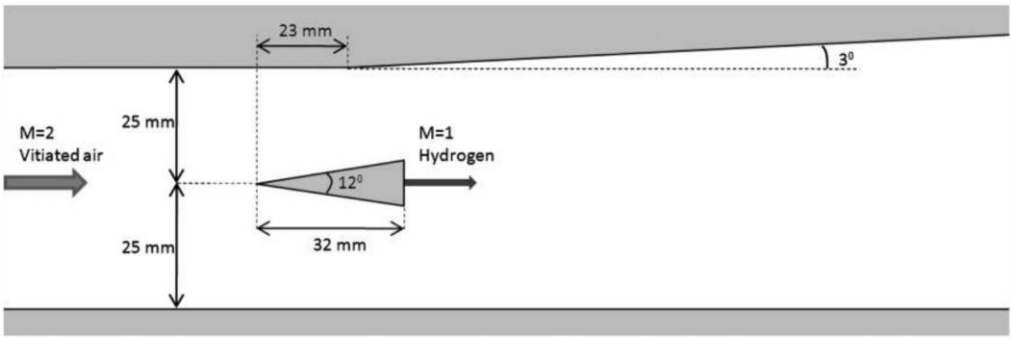

Figure 2.10: Schematic of the DLR scramjet combustor (Génin & Menon, 2010) .

Berglund & Fureby (2007) were the first to simulate the experiment using LES by employing a wall model. The combustion of hydrogen was modelled using both a one and two equation flamelet model. Two computational grids consisting of approximately 3.2 and 6.4 million cells were used, with cell clustering around the wedge and wake. Visualisations of the supersonic wake reveal the boundary-layers which form on the intrusive wedge detach at its base and form highly compressible shear layers. Three discernible regions of the flow are identified: a near-field induction zone, a transitional zone dominated by large coherent Kelvin-Helmholtz structures and volumetric change due to heat release, and a turbulent combustion zone. Generally, good agreement with experimental data is reported. Minor discrepancies were noted in the mean stream-wise velocity profiles and the growth rate of the wake, where volumetric expansion due to heat release is under predicted in the transitional region.

Genin and Menon (2010) avoided modelling the boundary-layers which formed within the experimental combustor by treating the boundaries as slip (inviscid) walls. A hybrid numerical scheme was used that switches between: a MUSCL-type interpolation in regions where flow discontinuities are detected, and an extension of the low numerical dissipation McCormack scheme away from flow discontinuities. Chemical reactions were modelled using an assumed laminar seven-step mechanism. A grid size similar to that of Berglund & Fureby (2007) study was employed. Several comments are made that the down-stream wake flow exhibit a combination of Kelvin-Helmholtz instabilities, consistent with a shear layer, and a von Kármán vortex sheet. These generate three-dimensional vortical structures that govern the observed mixing between injected fuel and captured air.

A hybrid LES/RANS methodology was employed by Potturi & Edwards (2014) to simulate this experiment. The stated major aim of the study was investigate the predictive capabilities of various modelling and algorithmic variations. This included variations of: grid topology, flux reconstruction techniques, chemical reaction models, sub-grid turbulence chemistry interaction model, and laminar/turbulent in-flows. Two grids were used: the first grid consisted of approximately 12.6 million cells, and the second grid consisted of approximately 20.3 million cells by having addition grid resolution around the injector walls. To accurately simulate the shock structure within the combustor, it was found that non-uniformities must be considered. A Synthetic Eddy Method (SEM) was also used to generate turbulent boundary-layer in-flow profiles. The SEM enhanced near-field turbulent mixing and improved predictions of the flame structure. This improvement still failed to predicted the attached flame observed in the experiments. Comparative visualisations of compressible flow features observed during the simulation with the experiment are shown in Figure 2.11.

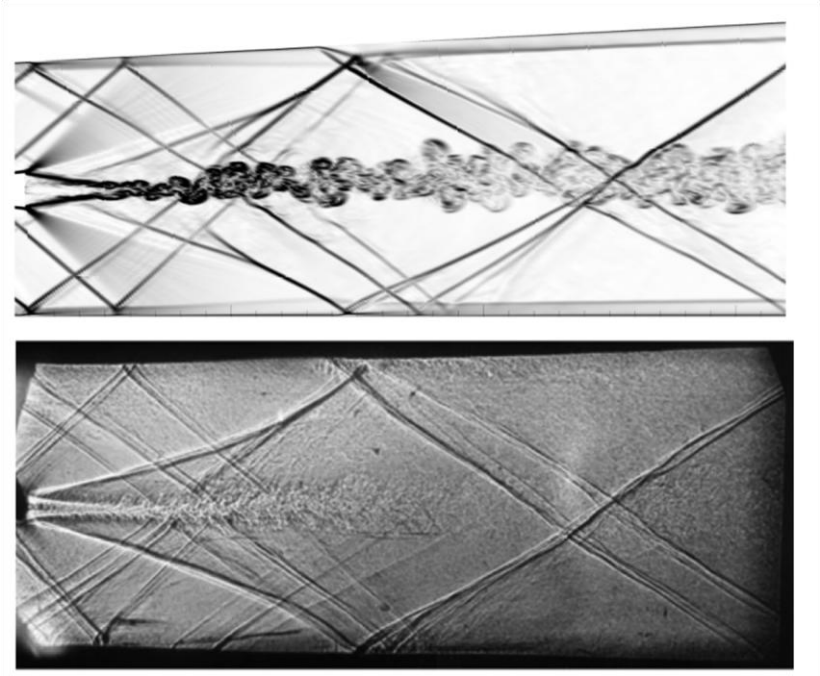

Figure 2.11: Instantaneous density-gradient contours taken for (top to bottom): i) the hybrid RANS/LES simulation, and ii) experimental schliren photograph (Potturi & Edwards, 2014).

The wall function LES methodology has also been combined with finite-rate chemistry models to simulate reactive flows within the National Aerospace Laboratory of Japan's supersonic combustor (Berglund, et al., 2010). Vitiated air flow enters a constant area duct with a velocity of 1449 m/s, a temperature of 830 K, and a pressure of 34.2 kPa. The duct begins to diverge just behind a strut injection, which supplies supersonic $(M = 2.5)$ gaseous hydrogen via two rows of injectors. The integral Reynolds number of the wake, based upon the incoming vitiated air flow condition and strut height, is ~55,000. Two computational grids were used to simulate the flow: (i) a coarse grid with 2.5 million cells, and (ii) a fine grid with 8.5 million cells. The authors report fair agreement with experimental results, shown in Figure 2.12, and conclude that a seven-step reaction mechanism is required so that transport of radical intermediates can be accounted for.

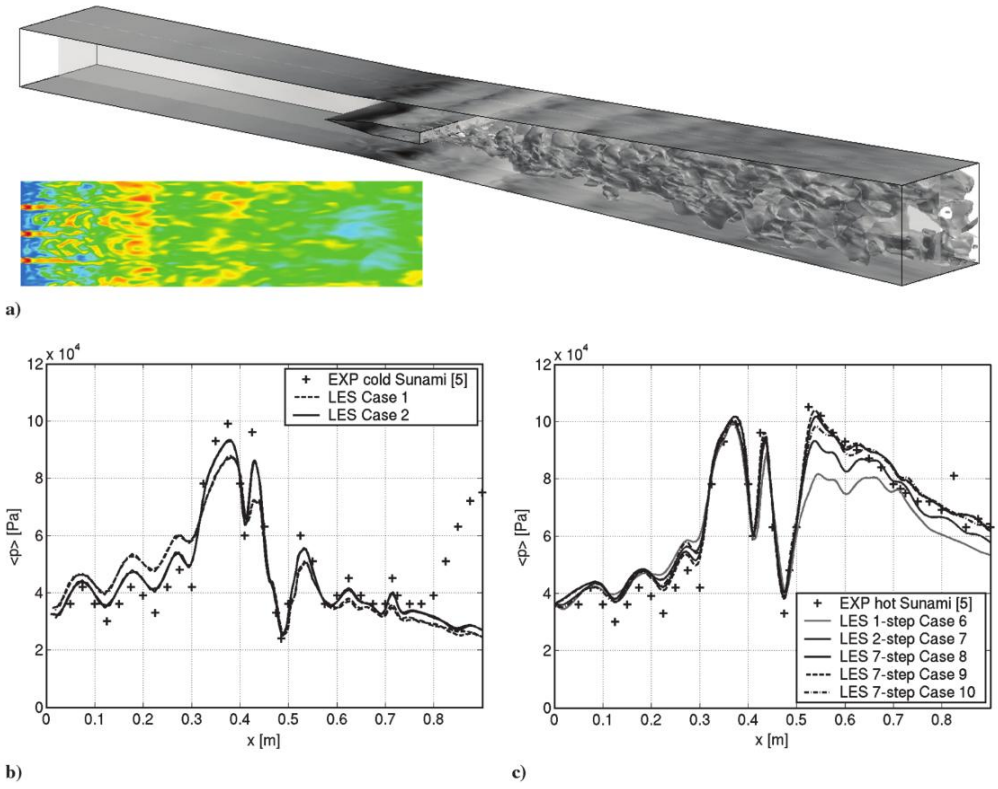

Figure 2.12: Comparison of pressure: a) perspective view of the pressure distribution on the upper and lower strut walls and an iso-surface of temperature (1400 K), and time averaged wall pressure distributions along the lower combustor wall for b) inter H2 injection, and c) combustion (Berglund, et al., 2010)

This methodology was also used to simulate the supersonic reactive flows within the HyShot II scramjet combustor during ground testing in the High Enthalpy Shock Tunnel Göttingen (Fureby, et al., 2011; Chapuis, et al., 2013). The HyShot II combustor is a constant area planar duct with a row of port hole injectors that face normal to the bottom duct wall surface. Two test conditions were simulated: a low and high altitude case. For the high altitude experimental test of the engine, equivalent to a flight Mach number of 7.3 at an altitude of 33.0 km, the nominal combustor in-flow conditions were: a velocity of 1800 m/s, a temperature of 1500 K, and a pressure of 57 kPa. The hydrogen fuel was injected at a sonic speed, a cold temperature of 250 K, and at a low fuel equivalence ratio of 0.43. The authors found that the formation of vortices in the far-field were markedly different between the two altitude cases. The horse-shoe vortices, which formed around the injected fuel, meet and distort to produce spiral vortices in the low altitude case. Conversely, longitudinal vortices with little span-wise interaction formed in the high altitude case. The generation of these longitudinal vortices was attributed to a reduction in heat release and subsequent decline in baroclinic torque generation.

The hybrid RANS/LES method has been used Simon et al. (2007) to simulated the wake generated behind an axisymmetric body immersed in a supersonic free-flow $(M = 2.46)$, shown in Figure 2.13. The Reynolds number based upon the free-stream conditions and axisymmetric trailing edge diameter is 2.9×10^6. The authors noted that an apparent turbulent feedback mechanism was promoted by the recirculation region just behind the axisymmetric body. Two hypotheses were put forward to describe this feedback mechanism, suggesting that either: pressure waves emanating from the initial shear layer are trapped inside the recirculation region leading to a resonant phenomenon, or that the development of an absolute instability generates self-sustaining oscillations in the recirculation region. It was argued that the latter scenario was more likely based upon the findings of Sandberg & Fasel (2006).

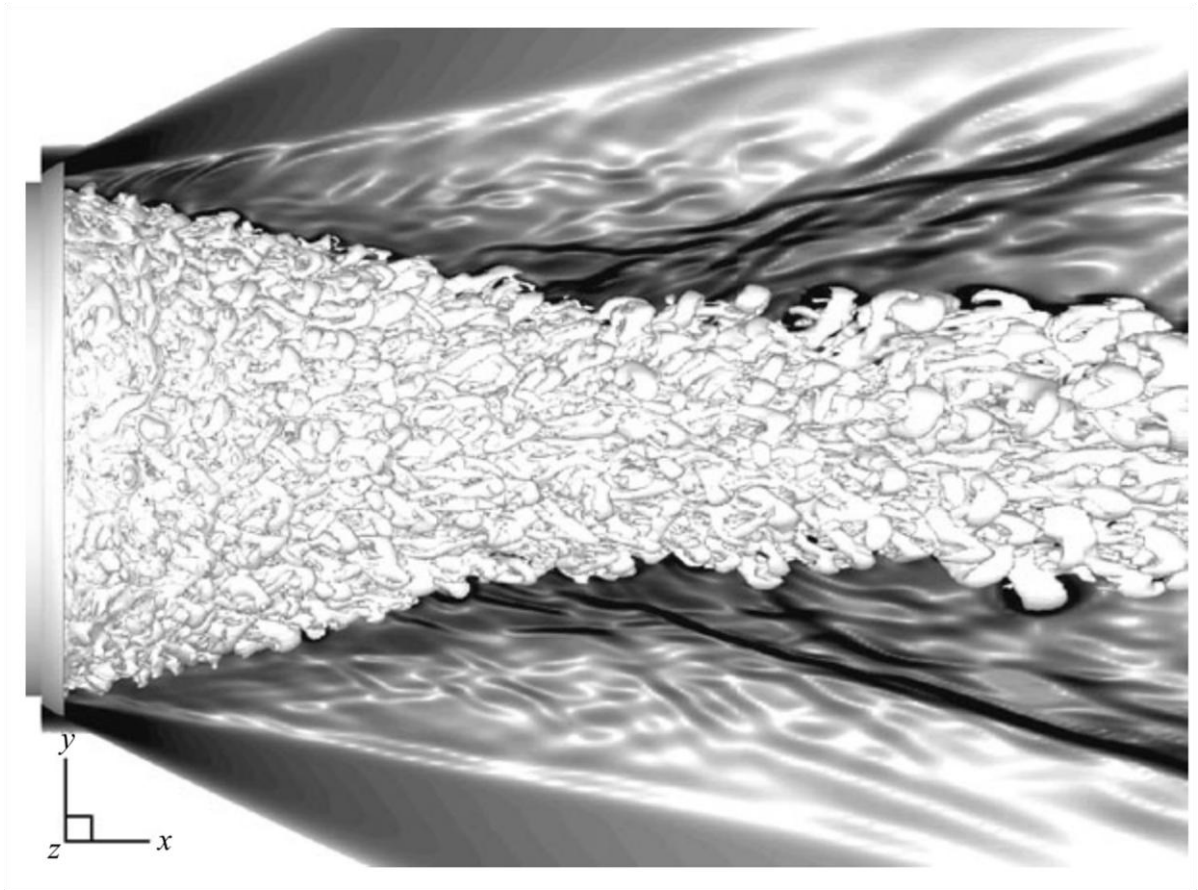

Figure 2.13: Instantaneous iso-surface of the Q criterion superimposed upon contours of the static density gradient magnitude (Simon, et al., 2007).

Other scramjet engine configurations have also been investigated using LES. Experiments of wall normal injection via circular porthole into M = 1.6 cross-flow (Santiago & Dutton, 1997) have been simulated using a hybrid RANS/LES methodology (Peterson & Candler, 2010; Kawai & Lele, 2010). Peterson & Candler have also investigated low-angle porthole injection into M = 2.0 cross-flow (2011) and the internal flow path of an inlet fuelled axisymmetric scramjet (Peterson, et al., 2013) visualisations of which are shown in Figure 2.14.

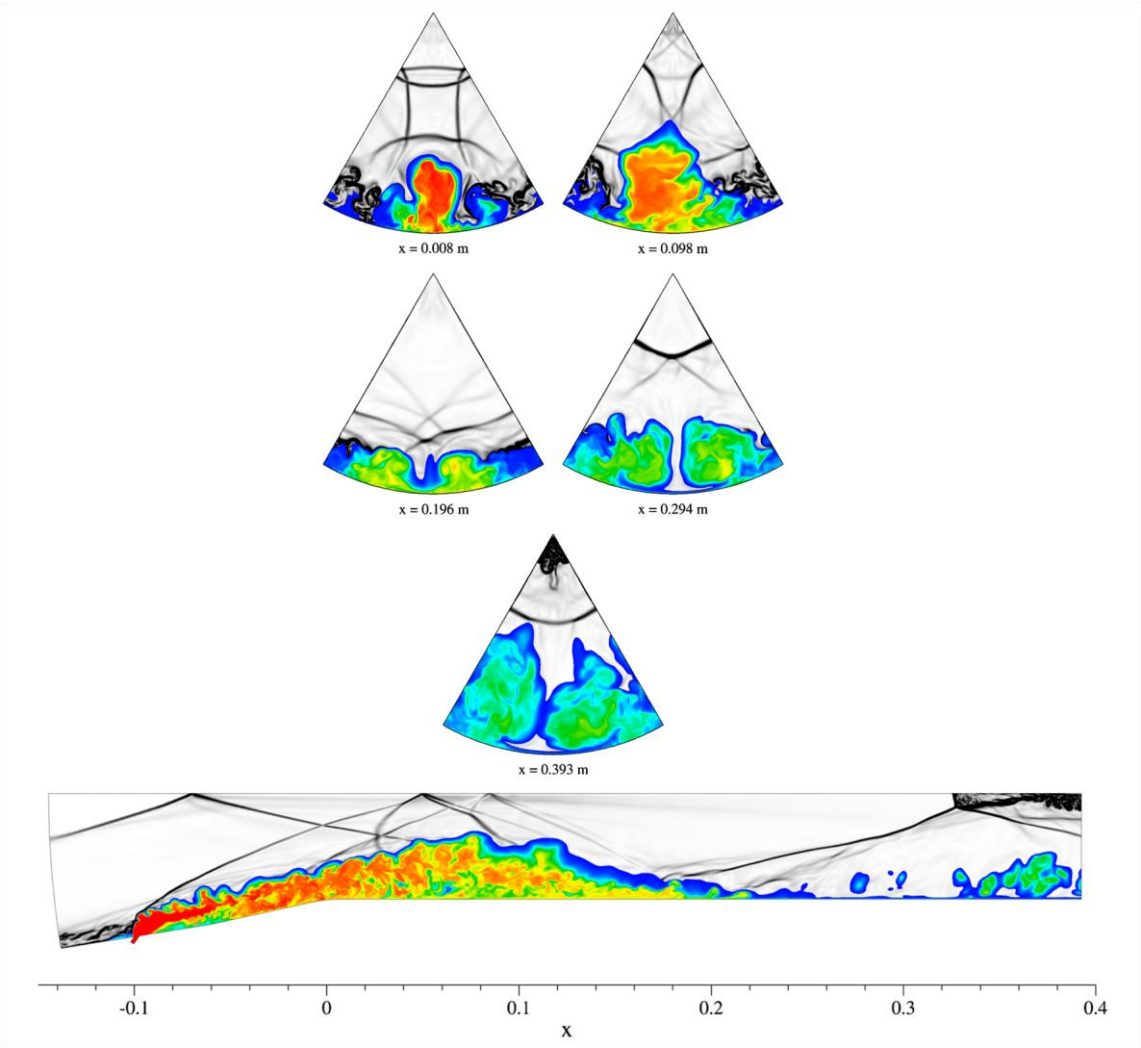

Figure 2.14: Cross-sectional contour plots of hydrogen mole fraction within an inlet fuelled scramjet engine (Peterson, et al., 2013)

2.5 Conclusions

The current literature indicates that oxygen enrichment is a potential enabling technology for high altitude, high speed operation of scramjet propulsive systems. There is, however, a lack of understanding regarding this technology at a fundamental fluid dynamics level. Numerous experimental and numerical studies have been undertaken, providing insight into the characteristics of canonical compressible turbulent flows, but these do not holistically address the more complex flow physics within a high speed scramjet engine. The hypervelocity planar mixing wake has yet to be investigated using high fidelity simulation. Previous publications have demonstrated that numerical techniques now exist to accomplish this and that there is significant interest from the research community.

3 Preliminary Simulations

This chapter begins with an analysis of the captured mass flow rate trends along an accelerating constant dynamic pressure trajectory in section 3.1. The results of this analysis provide further context to the interest in oxygen enrichment. Following this analysis is section 3.2, a description of the RANS numerical methodology employed to further study the effects of oxygen enrichment. Section 3.3 presents the simulated compression of hypersonic flow by a planar intake. The chapter culminates with a parametric study of a simplified scramjet combustor operating at various fuelling conditions with and without oxygen enrichment contained in section 3.4.

The benefits of oxygen enrichment outlined in Chapter 2 come at the cost of decreasing the chemical energy that can potentially be liberated per unit mass of stored propellant (fuel and on-board oxygen). Thus utilizing oxygen enrichment along portions of an access-to-space trajectory where vehicle net thrust is already high would not be advantageous. However, activating oxygen enrichment and additional fuel injection at the end of the trajectory where net thrust would otherwise tend to zero could boost net thrust back to useful levels, permitting the air-breathing stage to operate up to a significantly higher speed and altitude. Carrying a small tank of oxygen on-board for the purposes of enrichment at high altitudes can then be viewed as the cost of utilizing atmospheric oxygen for longer. The goal of the preliminary simulations is to provide a more detailed analysis of how enriching fuel with oxygen alters the high altitude performance of a scramjet engine. A matrix of fuelling conditions will be investigated to extend knowledge of oxygen enriched performance beyond the limited range of the experimental investigation (Razzaqi & Smart, 2011). Ultimately, a design study such as that conducted by Smart and Tetlow (2009) is required to determine how to optimally use oxygen enrichment and whether this results in a higher payload fraction for the rocket-scramjet-rocket system than utilizing a larger third stage. To facilitate such future design studies, a predictive model of combustion efficiency will be formulated in this thesis as a function of the fuel equivalence ratio and an oxygen enrichment parameter.

3.1 Trajectory Analysis

The appeal of oxygen enrichment becomes more apparent when considering the mass capture of air by a scramjet engine as it travels along an access-to-space trajectory. To investigate the trend of air mass capture with flight Mach number, first consider the definition of flight dynamic pressure:

$$q_\infty = \frac{1}{2}\rho_\infty {U_\infty}^2 \tag{3.1}$$

Where ρ_∞ is the free-stream static density and U_∞ is the flight speed, or incoming free-stream velocity magnitude using the vehicle centre of mass as an inertial frame of reference. Using the

ideal gas law and relationship between velocity magnitude and Mach number allows an alternative form of the flight dynamic pressure:

$$q_\infty = \frac{\gamma}{2} p_\infty M_\infty{}^2 \tag{3.2}$$

Where γ is the ratio of specific heat capacities and p_∞ is the free-stream static pressure. An expression for the free-stream inertial momentum as a function of dynamic pressure and static density can be formulated from the flight dynamic pressure definition, given by:

$$\rho_\infty U_\infty = \sqrt{2q_\infty}\sqrt{\rho_\infty} \tag{3.3}$$

The free-stream flow is processed by a forebody shock before being ingested by the engine. For the purposes of this illustration, this forebody shock will represented by a planar oblique shock, shown in Figure 3.1.

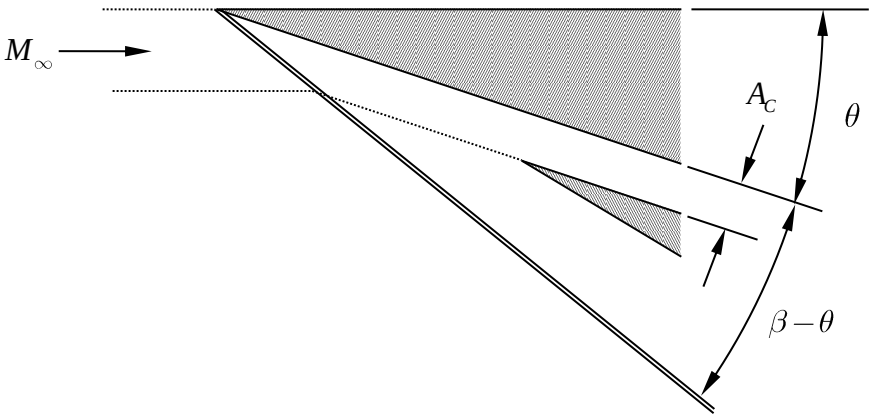

Figure 3.1: Schematic of the idealised flow upstream of the scramjet engine

The oblique shock wave compresses the incoming free-stream, reducing the cross-sectional area of a stream-tube (constant mass flux) of fluid as it passes through. The ratio of the free-stream cross-sectional area over the post-shock stream cross-sectional area of a given stream-tube of fluid flow can be determined using continuity (mass conservation):

$$\frac{A_\infty}{A_C} = \frac{\rho_C U_C}{\rho_\infty U_\infty} = \frac{\sin(\beta)}{\sin(\beta-\theta)} \tag{3.4}$$

The angle β can be computed by iteratively solving the following simultaneous equations, derived from inviscid oblique shock relations for a mixture of ideal gases with temperature dependent heat capacities:

$$\tan(\beta) = \cot(\theta)\left(\frac{\sec(\theta)}{\psi_1} - 1\right) \tag{3.5}$$

$$f(T_C) = (\psi_2 T_\infty - T_C)R - 2\frac{\psi_2}{\psi_2 + 1}\left(h(T_\infty) - h(T_C)\right) = 0 \tag{3.6}$$

Where,

$$\psi_1 = \sqrt{2\frac{h(T_\infty) - h(T_C)}{{M_\infty}^2 \gamma(T_\infty) R T_\infty} + 1}$$

$$\psi_2 = \frac{\tan(\beta-\theta)}{\tan(\beta)}$$

The ingested mass flow rate of the scramjet engine can be approximated using the conditions behind the forebody shock:

$$\begin{aligned} \dot{m}_C &= \rho_C U_C A_C \\ &= \rho_\infty U_\infty A_C \frac{A_\infty}{A_C} \end{aligned} \tag{3.7}$$

Substituting the oblique shock relationship and definition of dynamic pressure into the mass flow rate expression yields:

$$\dot{m}_C = \left(\sqrt{2q_\infty} A_C\right)\sqrt{\rho_\infty}\frac{\sin(\beta)}{\sin(\beta-\theta)} \tag{3.8}$$

Variations in the capture area of the inlet behind the forebody shock due to flow spillage are considered small. Under these conditions, the bracketed term remains constant for the duration of the flight. A similar substitution can be made to determine an expression for the Reynolds number of the flow behind the forebody shock, given by:

$$\begin{aligned} \mathrm{Re}_C &= \frac{\rho_C U_C L}{\mu_C} \\ &= \left(\sqrt{2q_\infty} L\right) \frac{\sqrt{\rho_\infty}}{\mu_C} \frac{\sin(\beta)}{\sin(\beta-\theta)} \end{aligned} \qquad 3.9$$

For a fixed geometry scramjet, the integral length scales remain constant for the duration of the flight, ensuring that the bracketed terms remain constant. An aero-vehicle with a forebody angle of 6°, following a constant 50.0 kPa dynamic pressure trajectory, will experience a 26.5% reduction in air mass capture when travelling from Mach 6.0 to 12.0, see Figure 3.2. In addition, the Reynolds number of the flow entering the scramjet engine will have almost halved over the same period.

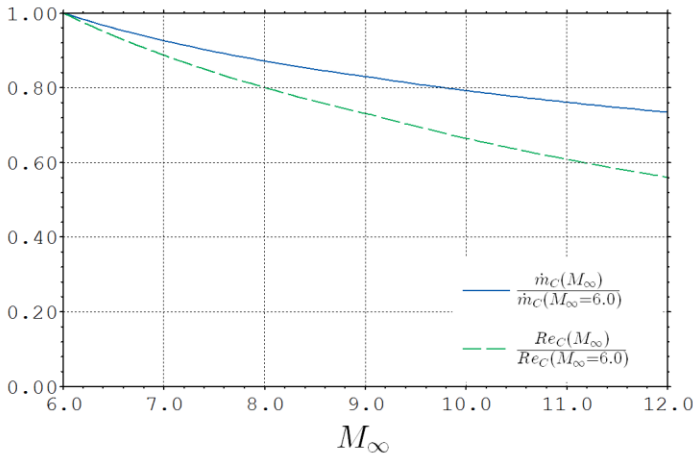

Figure 3.2: Normalised mass flow rate and Reynolds number of the captured flow.

It is clear from this analysis that travelling along an accelerating constant dynamic pressure trajectory will result in decreasing captured mass flow rate of air and a reduction in captured flow Reynolds number. Both of these trends are a result of the decreasing inertial momentum of the air flow entering the scramjet engine, a somewhat surprising outcome given the flight speeds of the vehicle.

The potential to produce thrust decreases as a consequence of the reduced air capture. However, the drag that must be overcome does not decrease. Additionally, the residence time of the air within the engine decreases as the vehicle accelerates to the high speeds associated with high altitude flight along a constant dynamic pressure trajectory. The shorter length of time available for the combustion process to complete implies that the engine will operate less efficiently at these higher speeds and altitudes. These observations indicate that a method for both supplementing the captured atmospheric air and increasing the efficiency of scramjets at high altitudes will be of significant benefit. The reduction in Reynolds number is further exacerbated by increases in viscosity due to the strengthening of shock waves generated within the engine at higher altitudes. Pressure dilatational effects, which act to reduce turbulence kinetic energy production, will also become significant within a scramjet engine at higher altitudes. The only physical mechanisms which can combat all of these factors acting to reduce the turbulent intensities is potentially larger shearing velocity gradients and baroclinic torque generation.

3.2 RANS Numerical Methodology

A RANS numerical methodology has been selected to investigate the effects pre-mixing oxygen with hydrogen fuel has upon combustion within an idealised scramjet engine. This method has been selected as various fuelling cases can be executed without consuming large amounts of computational resources. This study employs the RANS implementation contained within version 6.1.0 of NASA's Viscous Upwind aLgorithm for Complex flow Analysis (VULCAN) code.

3.2.1 Vulcan Solver

The VULCAN is a structured, finite-volume code that solves the Favre Reynolds-averaged Navier-Stokes equations (White & Morrison, 1999). The code can simulate two and three dimensional flows on multi-block structured grids by solving cell-centred integral forms of the Reynolds-averaged Navier-Stokes (RANS) equations. Inviscid fluxes were calculated using the third order upwind-biased Monotone Upstream-centred Scheme for Conservation Laws (MUSCL, $\kappa=1/3$) utilising Edward's Low Dissipation Flux Split scheme as the approximate Riemann solver. Viscous

fluxes were evaluated using second-order central differences. Temporal advancement of the unsteady equations in pseudotime towards a steady-state solution was achieved using the Diagonalised Approximate Factorization (DAF) scheme. The Courant-Friedrichs-Lewy (CFL) number was ramped from 0.1 to 2.5 over one thousand iterations. The fluid is modelled as a mixture of thermally perfect gases obeys empirically derived 3-interval 9-coefficient caloric curve fits, for temperatures between 200 K and 20,000 K (McBride, et al., 1993). The combustion of hydrogen was modelled using the 9 species and 18 finite rate reactions developed at NASA Langley (Drummond, 1988). The molecular viscosity and thermal conductivity of an individual species are both calculated using Sutherland's law. The molecular viscosity and thermal conductivity of the mixture of chemical species was calculated using Wilke's law and Wassajewa's law respectively. Turbulence is modelled using the Wilcox $k_T - \omega_T$ formulation (Wilcox, 1998). The transport of turbulence kinetic energy is governed by the following differential equation:

$$\frac{\partial}{\partial t}\left(\langle\rho\rangle\{k_T\}\right)+\frac{\partial}{\partial x_j}\left(\langle\rho\rangle\{k_T\}\{u_j\}\right)=\tau_{ij}\frac{\partial\{u_i\}}{\partial x_j}-\beta^*\langle\rho\rangle\{k_T\}\omega_T + \frac{\partial}{\partial x_j}\left(\left(\mu+\frac{1}{2}\frac{\langle\rho\rangle\{k_T\}}{\omega_T}\right)\frac{\partial\{k_T\}}{\partial x_j}\right) \tag{3.10}$$

Where β^* is a model parameter which, when applying a compressible correction (Wilcox, 1992), is given by:

$$\beta^* = 0.09 f_{\beta^*}\left(1+1.5\max\left(0,\langle M_T\rangle^2-0.25^2\right)\right) \tag{3.11}$$

The auxiliary functions are given by:

$$f_{\beta^*} = \frac{1+680\chi_k{}^2}{1+400\chi_k{}^2} \tag{3.12}$$

$$\chi_k = \max\left(0,\frac{1}{\omega_T{}^3}\frac{\partial k_T}{\partial x_j}\frac{\partial \omega_T}{\partial x_j}\right) \tag{3.13}$$

The transport of the turbulence specific dissipation rate is governed by the following differential equation:

$$\frac{\partial}{\partial t}\left(\langle\rho\rangle\omega_T\right)+\frac{\partial}{\partial x_j}\left(\langle\rho\rangle\omega_T\left\{u_j\right\}\right)=\frac{13}{25}\frac{\omega_T}{\{k_T\}}\tau_{ij}\frac{\partial\{u_i\}}{\partial x_j}-\beta\langle\rho\rangle{\omega_T}^2 + \frac{\partial}{\partial x_j}\left(\left(\mu+\frac{1}{2}\frac{\langle\rho\rangle\{k_T\}}{\omega_T}\right)\frac{\partial\omega_T}{\partial x_j}\right) \tag{3.14}$$

Where β is another model parameter given by:

$$\beta=0.072\,f_\beta \tag{3.15}$$

The auxiliary functions are given by:

$$f_\beta=\frac{1+70\chi_\omega}{1+80\chi_\omega} \tag{3.16}$$

$$\chi_\omega=\left|\frac{\Omega_{ij}\Omega_{jk}S_{ki}}{\left(0.09\omega_T\right)^3}\right| \tag{3.17}$$

The turbulence viscosity and turbulence dissipation rate can be determined using the following dimensional arguments:

$$\mu_T=\langle\rho\rangle\frac{\{k_T\}}{\omega_T} \tag{3.18}$$

$$\varepsilon=\beta^*\{k_T\}\omega_T \tag{3.19}$$

Turbulent transport of mass is computed using the local species mass fraction gradients in combination with the modelled eddy viscosity by assuming a constant turbulence Schmidt number of 0.50. Similarly, the turbulence transport of heat flux is computed using the local gradient in static temperature and the modelled eddy viscosity with an assumed constant turbulence Prandtl number of 0.90. This turbulence model has been shown to reasonably predict turbulent mixing of a supersonic coaxial jet (Cutler & White, 2001; Baurle & Edwards, 2010).

3.2.2 Computational Grid

The experimental model of Razzaqi & Smart (2011) represented a simplified scramjet engine comprised of: a planar intake, a constant area rectangular duct, an injector strut and a planar expansion surface. The geometry of this model, excluding the expansion ramp, has been employed in these preliminary simulations. In addition, the simulations are performed using two computational grids: a planar intake grid, and a duct grid. These grids were generated using the commercial software package Pointwise version 17.1R1 (2012) . The numerical grid of the planar intake was constructed to determine the flow conditions entering the rectangular duct and is shown in Figure 3.3.

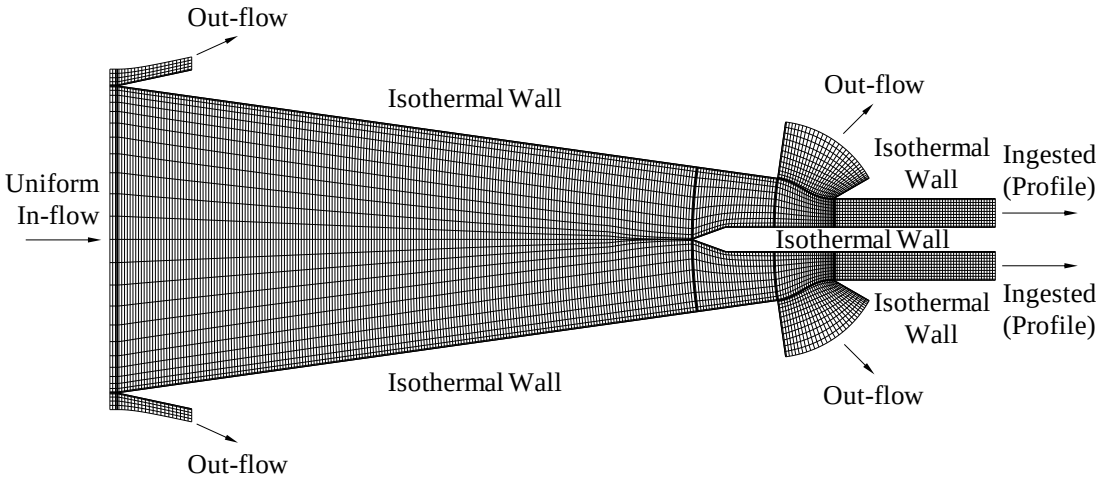

Figure 3.3: Planar intake numerical model (mesh coarsened by a factor of 8 in each direction)

The flow enters the planar intake domain from the left and was modelled as a uniform free stream of air at the nominal shock tunnel conditions. The inflow turbulence intensity and turbulence to molecular viscosity ratio were set to 0.01 and 0.10, respectively. The free-stream is then compressed by two symmetrically converging plates that form a wedge. Wall boundaries were modelled as 300 K isothermal walls where the flow solution was solved to the wall. The aspect ratio of grid cells clustered around these boundaries was constrained to not exceed 500. Outflow boundaries used zero-order extrapolation of all variables. The domain was initialized by extending the conditions entering domain up to the leading edge of the injection strut. Beyond this point, the

condition was initialized with a different condition determined by isentropically compressing the inflow to the cross-sectional area entering the duct.

Shock traps are positioned in such a way as to prevent the shock waves which form at the leading edges of these plates, as well as those generated by the centre-body leading edge, from entering the duct. This results in only a fraction of the captured air mass being ingested into the duct. To estimate the discretization error, a grid convergence study was performed using the methodology presented by Roache (1997). This involved analysing the mass flow rate entering the duct on three planar intake grids with varying refinement. This parameter was chosen as it is used to determine the injected flow conditions and is strongly dependent on the manner in which the shock waves and boundary-layers that form within the intake domain direct the flow towards the multiple out-flow boundaries. A summary of the study is provided in Table 3.1.

Table 3.1: Grid convergence study of the planar intake model

Grid	Normalized Grid Spacing	Total Number of Cells	max y^+	$\dot{m}_C$ kg/s
Fine	1	638,976	0.54	0.670
Medium	2	159,744	1.24	0.665
Coarse	4	39,936	3.23	0.650

The study found an order of convergence equal to 1.56 with a grid convergence index (Roache, 1997) between the medium and fine grid of 0.49%. The Richardson extrapolated value of the ingested mass flow rate was found to be 0.673 kg/s. Note that the tabulated maximum normalised wall distance, y^+, represents the distance between the wall and the nearest adjacent cell centre measured in wall units.

The numerical grid of the rectangular duct used to analyse the performance of different fuelling conditions is shown in Figure 3.4. This rectangular duct section has a height of $h = 47.14$ mm and a length of $l = 866$ mm or $l = 18.37h$.

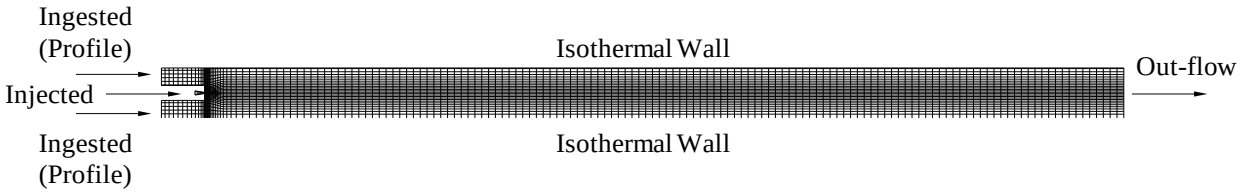

Figure 3.4: Rectangular duct numerical model (mesh coarsened by a factor of 16 in each direction)

The inflow profiles which enter the planar duct domain from the left were obtained from the outflow profile of the intake simulation at the equivalent grid resolution. The injected fuel mixture entered the domain via the modelled plenum chamber, travelling at a subsonic speed and with a stagnation temperature of 300 K. The injected mass flow rate and species mass fraction were determined from the desired fuelling condition. The pressure in the plenum chamber is always sufficient to cause sonic flow at the injector exit. The turbulence parameters of the injected inflow, wall boundaries and outflow boundaries were modelled in an equivalent manner to those of the planar intake simulation. Initialization of this domain for the no-fuel case involved extending the profile conditions entering the domain to the backward face of the injection strut step. Beyond this point, conditions were set by isentropically expanding the profile flow to the new cross-sectional area of the duct. Initialization of the domain for fuelled conditions interpolated the no-fuel solution on to the computational domain.

A grid convergence study was performed by analysing the total heat release due to combustion within the rectangular duct on three grids with varying refinement. A summary of this study is provided in Table 3.2.

Table 3.2: Grid convergence study of the planar duct model

Grid	Normalised Grid Spacing	Total Number of Cells	max y^+	$\int Q_{release}$ kW
Fine	1	1,078,292	0.62	725
Medium	2	269,568	1.41	718
Coarse	4	67,392	3.67	652

Using the total heat release due to combustion, the study found the apparent order of convergence to be 3.12 with a grid convergence index between the medium and fine grid of 0.17%. The Richardson extrapolated value of the total heat release was found to be 726 kW. All succeeding numerical results were obtained from simulations using the medium grid.

3.3 Planar Intake RANS Simulations

The purpose of the planar intake simulation was to accurately determine the condition at which the air flow enters the planar duct. It is possible to visualise the compressible flow features that form within the intake using the simulation results.

3.3.1 Compressible Flow Features

The air-flow entering the planar intake travels at hypersonic speeds, leading to a highly compressible flow field. Contour plots of the static density gradient magnitude help to visualise the shock waves generated from wedge leading edges as well as the expansion fans generated by the trailing edges of the wedge and the corners of the centre-body. These features are clearly visible in in Figure 3.5.

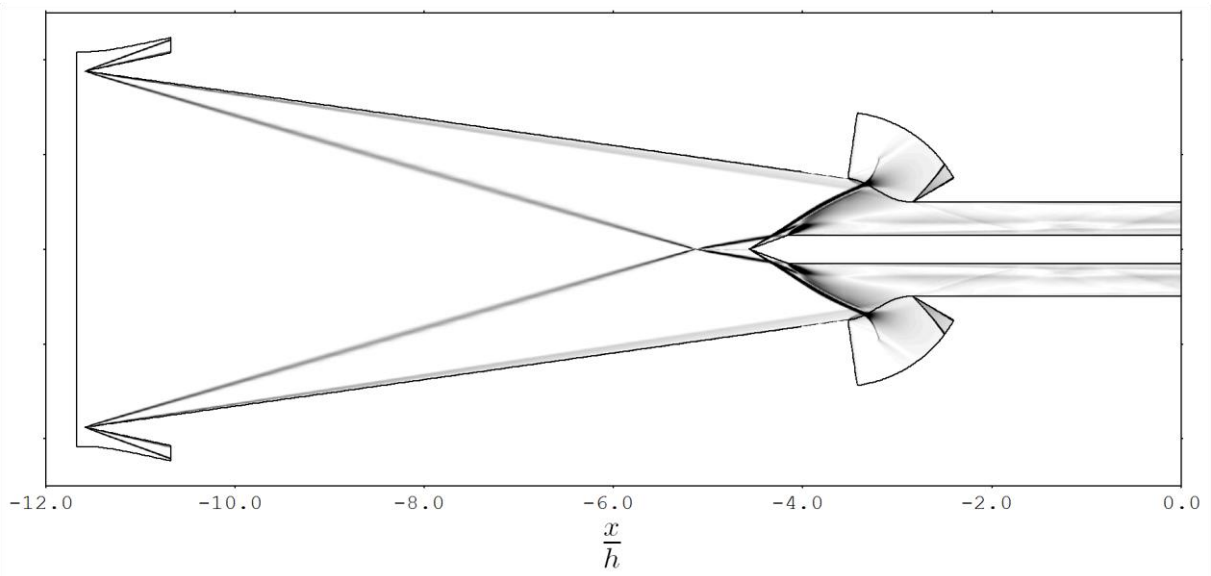

Figure 3.5: Static density gradient magnitude contour of the flow through the planar intake

The oblique shocks produced by the leading edges of both the planar intake and the injection strut exit the engine through the shock traps (see Figure 3.5), which was the intention of the design. This allows the flow entering the duct (combustor) to be relatively uniform, disturbed only by weak oblique shocks generated from the leading edge of the duct wall and expansion waves originating from the injection centre-body. The flux conserved one-dimensional flow properties entering the duct were $M_c = 3.37$, $p_c = 41.5$ kPa ,and $T_c = 2140$ K .

3.4 Rectangular Duct RANS Simulations

Multiple simulations of the flow through the duct, each with difference fuelling conditions, were performed. Compressible flow features will be presented and described. Engine performance parameters such as ignition length and combustion efficiency are determined from these simulations. Trends in combustion efficiency with the various fuelling conditions are reported. Finally, several comments regarding the turbulence characteristics of the flow through the duct are made which includes a comparison between pure fuel injection and oxygen enriched fuel injection.

3.4.1 Compressible flow features

Most of the flow travels through the planar duct at supersonic speeds, giving rise to compressible flow features such as expansion fans that are generated from the trailing centre-body edges, and shock waves where the cross-streams meet behind the centre-body. It is also possible to identify the mixing interface between the injected fuel and the ingested air. Figure 3.6 shows the static density gradient magnitude of the flow downstream of the point of injection for three representative fuelling conditions with: (i) no injection, (ii) pure fuel injection, and (iii) oxygen enriched fuel injection.

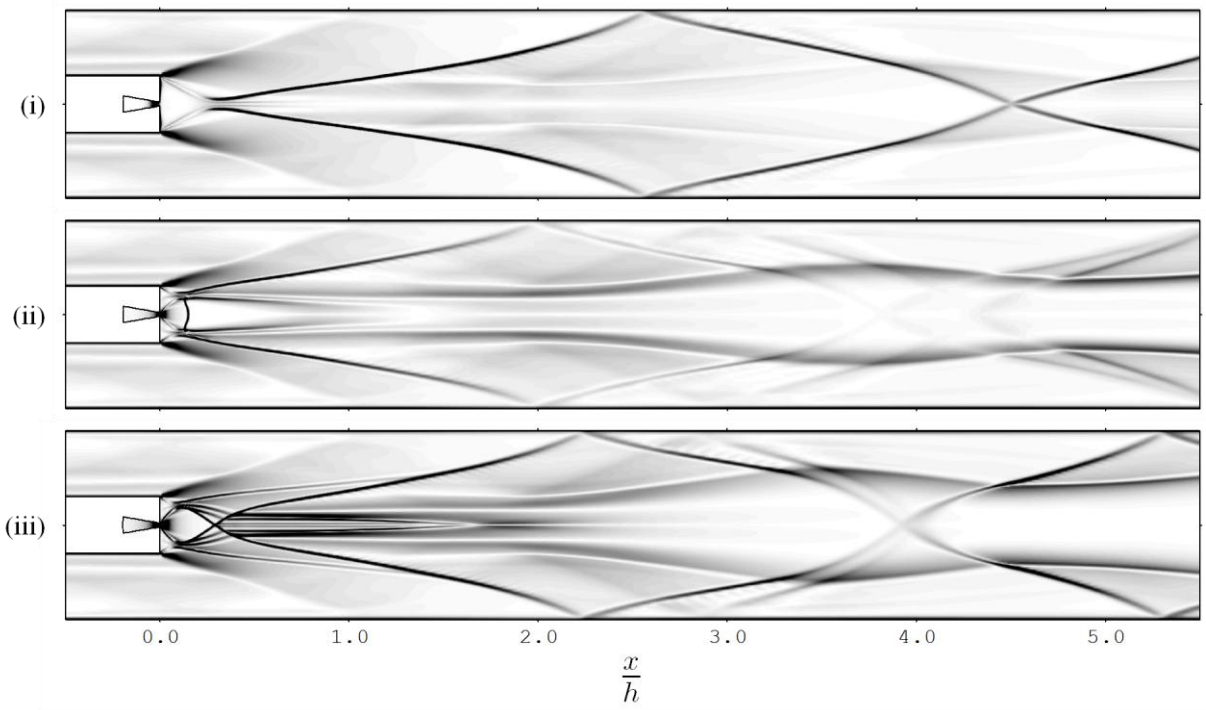

Figure 3.6: Contours of static density gradient magnitude (top to bottom): (i) $\phi = 0.0$ $EP = 0.0\%$, (ii) $\phi = 1.0$, $EP = 0.0\%$, and (iii) $\phi = 1.0$, $EP = 10.0\%$

The injection strut boundary-layers detach at its base to form an initial shear layer between the ingested air flow and the re-circulating fluid behind the strut. Figure 3.6 clearly shows the expansion fans originating from the downstream corners of the strut that deflect the ingested air flow into the lower pressure wake behind the injection strut. These expansion fans are subsequently reflected from the duct walls, thus they interact with the injector wake and modify its properties at downstream locations. This process can most clearly be seen occurring near *x/h* = 2 in Figure 3.6.

For the case with no injection, shown in Figure 3.6 (i), the ingested air flow is straightened by oblique recompression shock waves when it reaches the duct centreline. The oblique shocks are then reflected by the duct walls multiple times to form the clearly visible shock train.

For cases with fuel injection, the sonic fuel mixture injected at the base of the injection strut is highly underexpanded, thus it rapidly expands into the relatively low pressure re-circulating flow abutting the rear faces of the strut. This expansion is halted when the fuel jet meets the ingested flow. At this point, the ingested air flow is straightened by oblique recompression shocks while two distinct flow structures can form in the fuel depending on the stagnation pressure of the injected flow. For lower injected stagnation pressures, a Mach disk forms to instantly alleviate the pressure gradient between the injected flow and the ingested flow, shown in Figure 3.6 (ii). Higher injected stagnation pressures cause an oblique shock pattern to form, shown in Figure 3.6 (iii). Both flow features produce a small subsonic region downstream of where the flow is re-directed in a stream-wise direction.

For cases with fuel injection, mixing layers subsequently form between the redirected ingested air flows and the fuel jet. The Mach disk solution usually occurs when regular reflection of the oblique shocks at the centreline is not possible. The oblique recompression shocks that form to redirect the air flow are subsequently reflected from the walls to generate the shock pattern evident downstream of the injector strut. These shocks interact with the mixing layers multiple times, altering their properties each time. When the oblique shock structure occurs in the fuel jet, Figure 3.6 (iii) shows that an additional pair of recompression shocks are directed into the air streams. These originate from the initial meeting point of the expanding jet and ingested streams.

3.4.2 Ignition

Experimental studies have suggested that one of the benefits of oxygen enrichment is to reduce the ignition length (Razzaqi & Smart, 2011). Ignition signals that the process of combustion has begun. It is defined to have occurred where the net rate of atomic hydrogen production per unit time is at a maximum (Nicholls, et al., 1963):

$$x_{ign} = x \Rightarrow \max\left(\dot{\xi}_H\left(x\right)\right) \qquad 3.20$$

Ignition was not directly measured in the experiments using this definition, but inferred from the combustion induced pressure rise. It is therefore instructive to examine whether the simulations, in which species production rates are available, confirm the benefits inferred from the experimental data. Figure 3.7 shows contour plots of the net formation rate of atomic hydrogen for three fuelling cases: (i) stoichiometric fuelling relative to the ingested oxygen ($\phi = 1.0$) with no oxygen enrichment ($EP = 0.0\%$, $\dot{m}^{inj} = 0.0194$ kg/sec), (ii) fuel rich ($\phi = 1.4$) with no oxygen enrichment ($EP = 0.0\%$, $\dot{m}^{inj} = 0.0271$ kg/sec) and (iii) stoichiometric fuelling relative to the ingested oxygen $\phi = 1.0$ with addition oxygen enrichment ($EP = 15.0\%$, $\dot{m}^{inj} = 0.0424$ kg/sec). Stream-wise trends of the cross-stream maximum formation rate are also shown to clarify variations between the three cases.

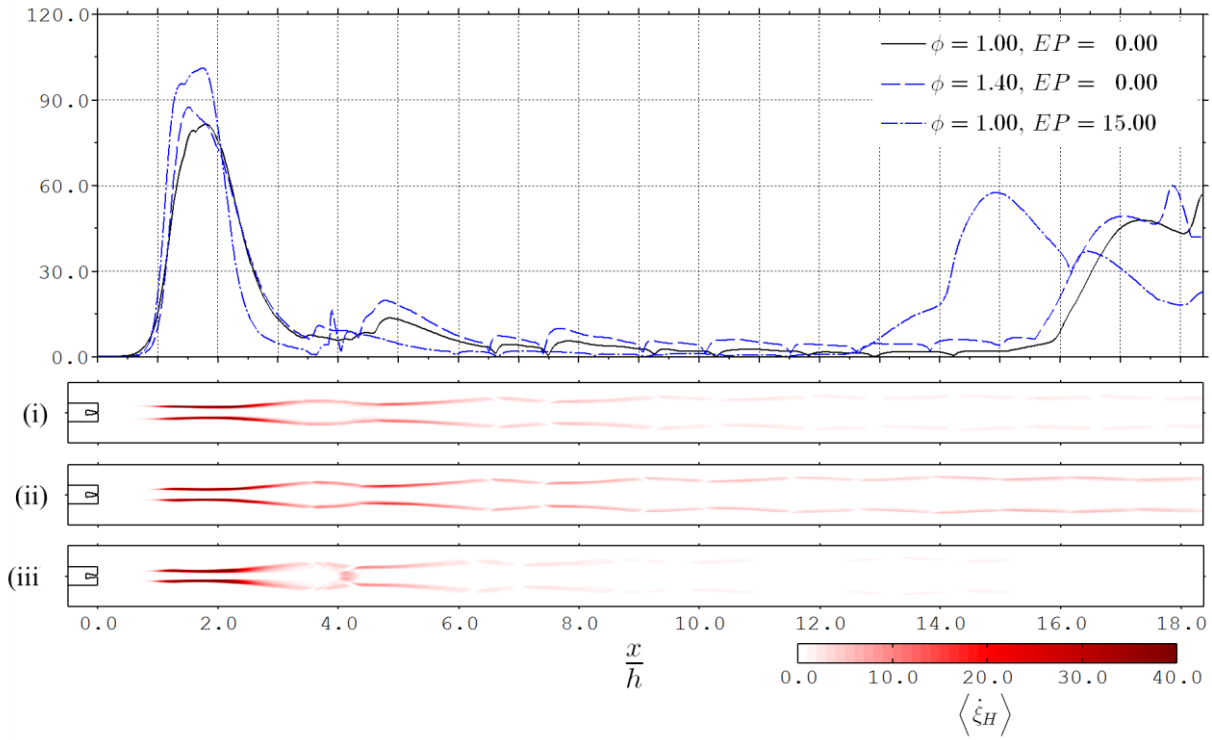

Figure 3.7: Net production rate of atomic hydrogen (kg/(m^3.s)) cross-stream maximum trends with stream-wise location and contours with (top to bottom): (i) $\phi = 1.0$, $EP = 0.0\%$, (ii) $\phi = 1.4$, $EP = 0.0\%$, and (iii) $\phi = 1.0$, $EP = 15.0\%$.

Comparing Figure 3.7 with Figure 3.6, it can be seen that ignition occurs in the centre of the mixing layer, where the mixture is closest to stoichiometric, in a hot region between the recompression shocks and the reflected expansion fans. It is observed that the point of ignition remains relatively constant at approximately 1.9 duct heights downstream of the injection point for all simulated cases. Ignition does move upstream slightly for the enriched case, but this decrease in ignition length is not significant relative to the length of the duct. Neither varying fuel equivalence ratio nor enrichment percentage induces significant shifts of the ignition location. We postulate that the simulated insensitivity of the ignition length to fuelling conditions is due to the very high temperatures in the combustor, which are discussed in the next subsection, causing rapid ignition following the formation of the fuel-air mixing layers.

3.4.3 Combustion Efficiency

Increasing combustion efficiency is a primary driver of scramjet combustor design and one of the main claimed benefits of oxygen enrichment. Here we thoroughly examine the effects of oxygen enrichment on combustion efficiency in our simulations, comparing overall results to experimentally derived values where possible. Water is the terminal product of hydrogen combustion. One definition of combustion efficiency is the ratio of the mass flow rate of water through the combustor at a given stream-wise location over that expected if all available fuel is combusted, which is defined as:

$$\eta_c\left(x\right) = \frac{\widehat{m}_{H_2}}{\widehat{m}_{H_2O}} \frac{\dot{m}_{H_2O}\left(x\right)}{\dot{m}_{H_2}^{inj}} \tag{3.21}$$

This definition does not require the complex derivation used to analyze experimental combustion efficiency (Razzaqi & Smart, 2011), which are reliant solely on pressure measurements taken along the duct wall. The combustion efficiencies achieved along the duct for varying fuelling conditions are shown in Figure 3.8.

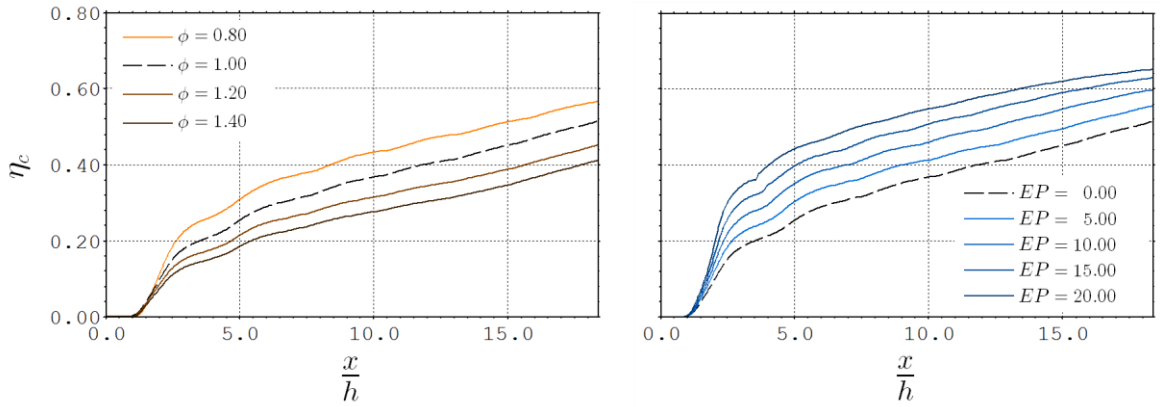

Figure 3.8: Combustion efficiency against x/h (left to right): (i) $EP = 0.0\%$, and (ii) $\phi = 1.0$.

Combustion efficiency is shown to decrease with increasing fuel equivalence ratio but rises with increasing enrichment percentage. Linearly increasing combustion efficiency trends with axial location indicate mixing limited combustion (Heiser & Pratt, 1994), which becomes apparent approximately six duct heights downstream from the point of injection for all cases. Combustion appears to remain mixing limited for all non-enriched cases shown in Figure 3.8 (i). The rate at which mixing limited combustion occurs does not seem to be influenced by the fuel equivalence ratio. This indicates that increasing the equivalence ratio simply causes a greater mass flow of unmixed fuel between the mixing layers, with little effect on the rate of mixing. Figure 3.8 (ii) shows that enriching fuel with oxygen causes significantly higher combustion efficiencies to be achieved between two to six duct heights downstream of injection when compared to the fuel-only case. Combustion remains mixing limited throughout the duct for enrichment percentages of less than 15% and a fuel equivalence ratio of unity. In contrast, higher enrichment percentages demonstrate asymptotic behavior in combustion efficiency as the flow approaches the exit of the duct, $x = 18.37h$, This characteristic is mostly likely attributed to the high static temperatures within the duct, shown in Figure 3.9.

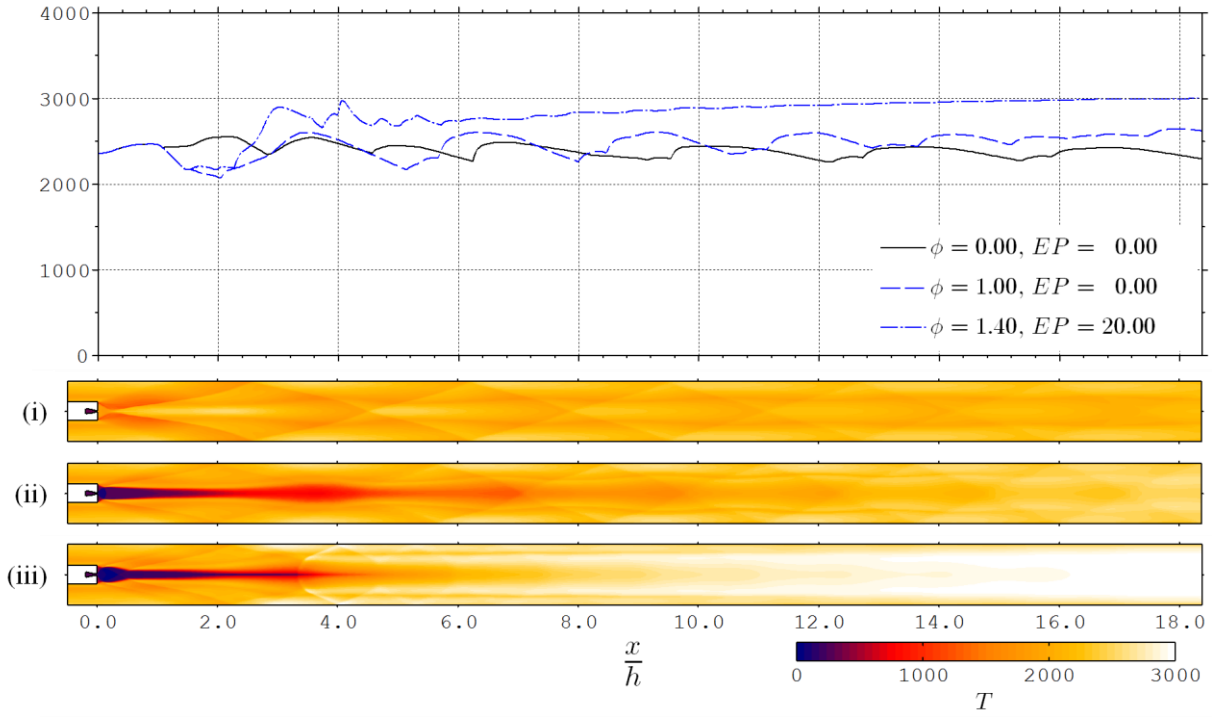

Figure 3.9: Static temperature (K) cross-stream maximum trends with stream-wise location and contours with (top to bottom): (i) $\phi = 0.0$, $EP = 0.0\%$, (ii) $\phi = 1.0$, $EP = 0.0\%$, and (iii) $\phi = 1.4$, $EP = 20.0\%$

.

The injection of cold fuel and oxygen initially reduces the span-wise averaged temperature of the flow in the duct but heat released from combustion raises temperatures to as high as 3000 K for highly enriched cases (e.g. Figure 3.9 (iii)). As approximately 35% of water will dissociate at these conditions, this limits combustion efficiency as defined in this study to values less than 0.65, thus the engine studied here does not fully illustrate the benefits of oxygen enrichment for enrichment percentages greater than 10%.

Now that the trends in combustion efficiency along the duct have been identified, we will examine the benefits of oxygen enrichment upon combustion efficiency for the full matrix of simulated fuelling conditions at two discrete locations: (i) halfway along the duct, $x = 9.19h$, where combustion efficiency does not exhibit product dissociation limited behaviour, and (ii) at the exit of the duct, $x = 18.37h$, where combustion efficiency may be product dissociation limited at high enrichment percentages. These results are shown in Figure 3.10.

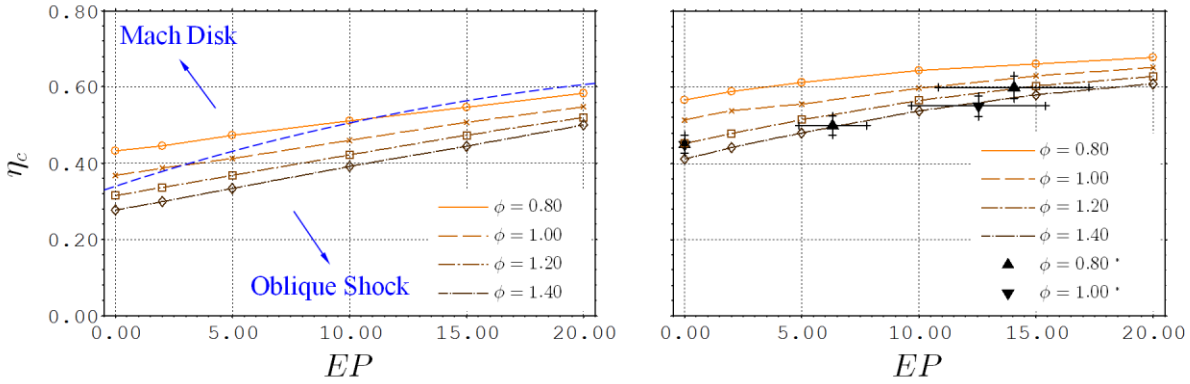

Figure 3.10: Combustion efficiency against EP (left to right): (i) $x = 9.19h$, and (ii) $x = 18.37h$ where * refers to experimental data (Razzaqi & Smart, 2011).

It is observed that combustion efficiency increases linearly with enrichment percentage at $x = 9.19h$. At this location, the static temperature effects have not begun to limit the formation of water. However, these effects are clearly evident in the trends of combustion efficiency with enrichment percentage at $x = 18.37h$. These curves appear to asymptote towards combustion efficiencies of 0.65 as predicted. These trends compare reasonably well to the experimentally derived values shown in Figure 3.10 (ii) despite differing definitions of combustion efficiency, the exclusion of injected nitrogen, ignoring three-dimensional effects and simulating with nominal shock tunnel conditions.

Interestingly, Figure 3.10 shows that the change between the two distinctly different near field flow structures (see Figure 3.5) caused by varying the injected mass flow rate has no visible impact on the combustion efficiency trends. Examination of the mixing layer just downstream of these near field flow structures indicates why the combustion efficiency is insensitive to the change. For this analysis, the spatial growth-rate theory of Slessor et al. (2000) has been applied to the mixing layer just downstream of the near field flow structure. According to this theory, the compressible mixing layer growth rate is given by:

$$\delta_c' \approx 0.36\left[\frac{(1-r)\left(1+\sqrt{s}\right)}{2\left(1+r\sqrt{s}\right)}\right]\left[1-\frac{\left(1-\sqrt{s}\right)\left(1+\sqrt{s}\right)}{1+2.9(1+r)(1-r)}\right]\left(1+4\Pi_c{}^2\right)^{-0.5} \qquad 3.22$$

Where r is the velocity ratio of the slow moving (injected) stream over the fast moving (ingested) stream, s is the corresponding density ratio and Π_c is a compressibility parameter, given by:

$$\Pi_c = \max_i \left(\sqrt{\gamma_i - 1} \frac{a_1 + a_2}{a_i} \right) M_c \qquad 3.23$$

Where ΔU is the velocity difference across the mixing layer. The mixing layers which develop approximately one duct height downstream of injection for a Mach disk flow field ($\phi = 1.0$ and $EP = 2.0\%$) and an oblique shock flow field ($\phi = 1.0$ and $EP = 5.0\%$), with similar fuelling conditions, have been selected to investigate the influence of the near field flow structure upon the growth rate of the mixing layer. The Mach disk flow field has a velocity ratio of $r \sim 0.20$, a density ratio of $s \sim 0.62$, and a compressibility parameter of $\Pi_c \sim 1.78$ which yields a compressible mixing layer growth-rate of $\delta_c' \sim 0.077$. The oblique shock flow field has a velocity ratio of $r \sim 0.26$, a density ratio of $s \sim 1.22$, and a compressibility parameter of $\Pi_c \sim 1.76$ which yields a compressible mixing layer growth-rate of $\delta_c' \sim 0.078$. These calculations show that the mixing layer growth rate does not vary significantly with respect to the different near field flow structure despite notable variations in the density and velocities ratios. From this, it can be inferred that the mixing of fuel and ingested air are not strongly dependent on the near field flow structure for the conditions under investigation.

Predicting trends in combustion efficiency with respect to the enrichment percentage would facilitate the implementation of oxygen enrichment into scramjet trajectory studies. Consequently, a bilinear surface representing combustion efficiency as a function of fuel equivalence ratio and enrichment percentage has been fit to combustion efficiency, given by:

$$\eta_c(\phi, EP) = c_0 + c_1(\phi - 1) + c_2 EP + c_3(\phi - 1) EP \qquad 3.24$$

The coefficients (c_0 – c_3) have been evaluated at $x = 9.19h$ as this data does not include the product dissociation limiting influence of high temperatures, giving a better representation of oxygen enrichments influence on combustion efficiency. Values for these coefficients are given in Table 3.3:

Table 3.3: Combustion efficiency surface fit coefficients

x/h	c_0	c_1	c_2	c_3
9.19	3.6371×10^{-1}	-2.5567×10^{-1}	8.7437×10^{-3}	5.7370×10^{-3}

This trend surface has a coefficient of determination (R^2) of 0.9954 and can be used to estimate the multiplicative benefit of oxygen enrichment on the combustion efficiency of an arbitrary scramjet combustor, denoted the Combustion Enhancement Factor (*CEF*), in the following way:

$$CEF = \frac{\eta_c(\phi, EP)}{\eta_c(\phi)} = \left[1 + \frac{c_2 + c_3(\phi - 1)}{c_0 + c_1(\phi - 1)} EP\right] \qquad 3.25$$

The *CEF* predicts a linear increase in combustion efficiency with enrichment percentage, where the slope is determined by the surface fit coefficients and is a function of fuel equivalence ratio. It should be noted the considered engine has relatively low combustion efficiencies. Subsequently, this predictive trend cannot be applied to engines which achieve combustion efficiencies near unity without employing oxygen enrichment. The *CEF* generated from the above surface fit for a variety of equivalence ratios is shown in Figure 3.11.

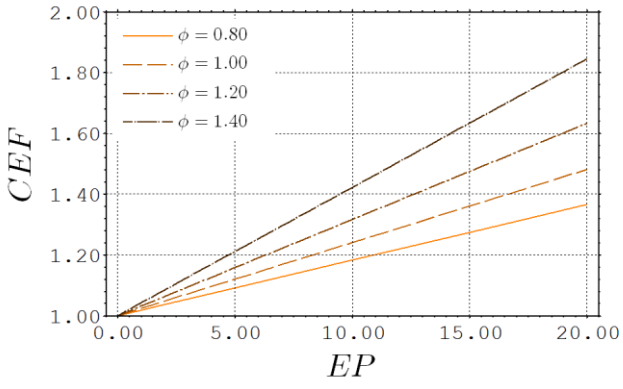

Figure 3.11: Combustion Enhancement Factor against *EP*.

The introduction of enriching oxygen means that there are now two sources of oxygen for the combustion process: oxygen homogeneously mixed with fuel prior to injection, where the fuel is in

stoichiometric excess; and combustion between residual fuel and oxygen within the ingested air. "Premixed combustion" is a term used hereinafter to conceptually isolate combustion which hypothetically involves only enriching oxygen and fuel. In practice, both aspects of combustion may occur simultaneously. It is reasonable to assume that, for relatively low enrichment percentages, the enriching oxygen and the stoichiometric equivalent amount of fuel will react to completion within the duct. Accordingly, a modification to the combustion efficiency definition is proposed which excludes the premixed combustion component from the total combustion, defined as:

$$\eta_c^{OxEn}(x) = \frac{\eta_c(x) - EP}{1 - EP} \tag{3.26}$$

This parameter elucidates the percentage of the residual fuel (fuel not consumed by premixed combustion) which has mixed and combusted with the ingested oxygen. If premixed combustion is the only source for the observed improvements in overall combustion efficiency, then the proposed modified combustion efficiency will be either constant or decreasing with increasing enrichment percentage. However, Figure 3.12 shows an additional improvement with enrichment percentage that was not noted in earlier studies (Razzaqi & Smart, 2011).

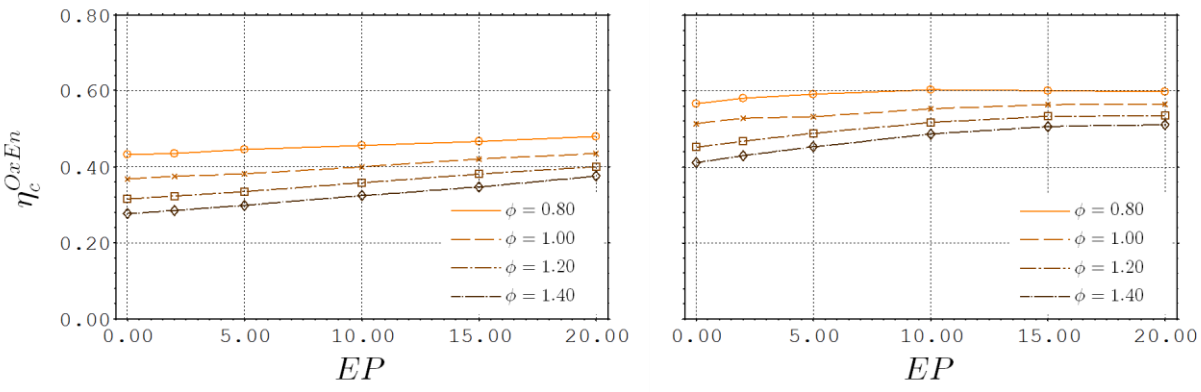

Figure 3.12: Oxygen enrichment modified combustion efficiency against *EP* (left to right): (i) $x = 9.19h$, and (ii) $x = 18.37h$.

It is postulated that the physical mechanism for improved combustion efficiency between the injected fuel and the ingested airflow is mixing enhancement due to two factors: increasing shear

and density ratio across the mixing layer. Due to the increased average molecular weight of the injected oxygen-fuel mixture with enrichment percentage, the speed of sound decreases leading to a slower injected flow at the sonic injector exit. This creates a stronger velocity gradient across the mixing layers, which drives the production of turbulence. Thus the levels of turbulence kinetic energy in the mixing layers increase with enrichment percentage, as shown in Figure 3.13.

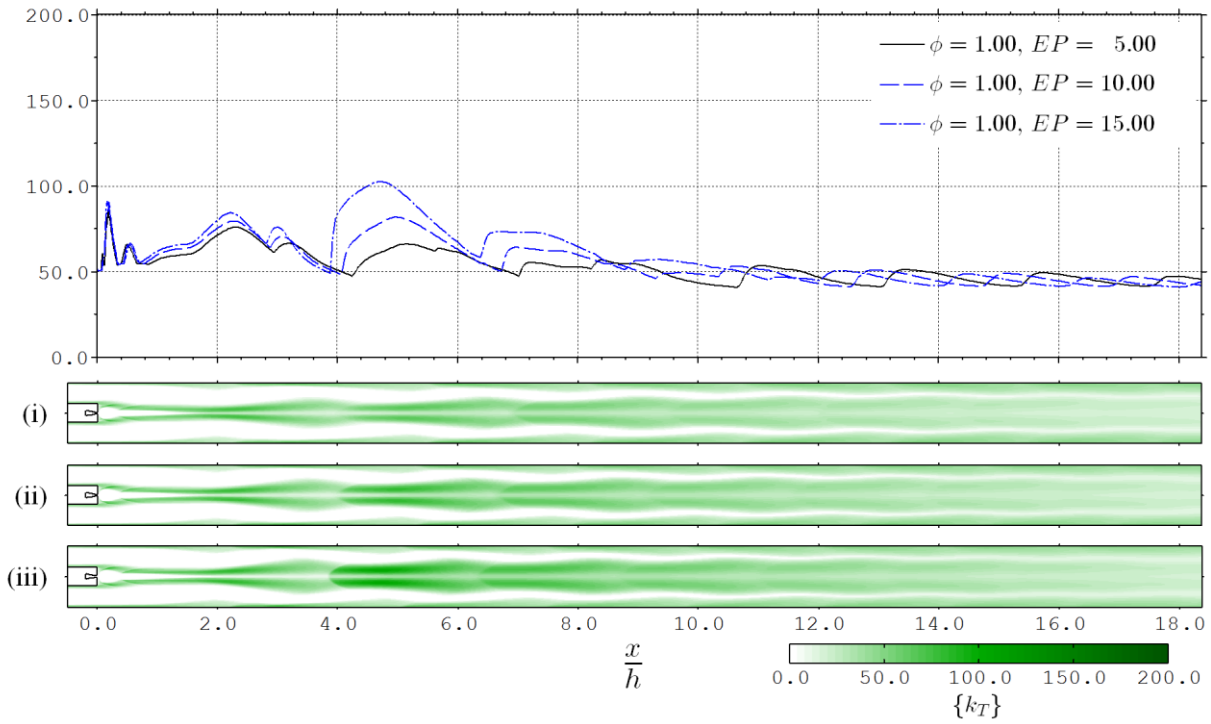

Figure 3.13: Turbulence kinetic energy (kJ/kg) cross-stream maximum trends with stream-wise location and contours with (top to bottom): (i) $\phi = 1.0$, $EP = 5.0\%$, (ii) $\phi = 1.0$, $EP = 10.0\%$, and (iii) $\phi = 1.0$, $EP = 15.0\%$.

The increase in turbulence kinetic energy is most prominent between 4-5 duct heights downstream of injection, following the passage of the reflected recompression shock through the mixing layers. This, combined with the other local maxima in turbulence kinetic energy following wave interactions, illustrates the strong influence of the wave structure on the properties of the mixing layer. It is observed that increasing the enrichment percentage from 5.0% to 15.0% causes the peak turbulence kinetic energy to be amplified by more than 50%, resulting in a substantial increase in the mixing rate.

The reduced injectant velocity with enrichment percentage not only creates a stronger shear between the ingested and injected flows but due to conservation of mass, the density of the injected flow increases. Secondly, additional enriching oxygen increases the injected mass flow rate, further increasing the injectant density. This resulting increase in density ratio with enrichment percentage, combined with the increasing shear, causes the mixing layer growth rates to be enhanced by oxygen enrichment according to the mixing layer growth rate equation 3.22. For example, at $x \sim 4h$, for: $\phi = 1.0$, the predicted mixing layer characteristics are: $r \sim 0.63$, $s \sim 0.45$, $\Pi_c \sim 0.76$, and $\delta' \sim 0.039$ for $EP = 5.0\%$; $r \sim 0.53$, $s \sim 0.55$, $\Pi_c \sim 0.94$ and $\delta' \sim 0.048$ for $EP = 10.0\%$; and $r \sim 0.35$, $s \sim 0.69$, $\Pi_c \sim 1.26$ and $\delta' \sim 0.067$ for $EP = 15.0\%$. The improved mixing between the fuel and the ingested air leads directly to the residual fuel being combusted more efficiently in the model considered here.

3.4.4 Turbulence Scaling

Having concluded that oxygen enrichment promotes the combustion of fuel with ingested oxygen due to enhanced turbulence production, there is now motivation to investigate the turbulence characteristics of the flow as predicted by the turbulence model. This can be done by calculating approximations of the various scales of turbulence using the modelled turbulence parameters. The scales of interest include the turbulence integral scale, the Taylor micro-scale, and the Kolmogorov scale. The turbulence scales generated by pure fuel injection, $\phi = 1.0$ and $EP = 0.0\%$, and moderately enriched fuel injection, $\phi = 1.2$ and $EP = 10.0\%$, are compared to the case where no fluid is injected, $\phi = 0.0$ and $EP = 0.0\%$. These cases provide insight into the effect of injecting fluid into a supersonic wake and how the turbulence characteristics are altered.

The turbulence integral Reynolds number gives an indication of current turbulence intensity, where greater values signify that larger amounts of turbulence have been produced up to this point. Using the $k_T - \omega_T$ model, the turbulence Reynolds number can be calculated using:

$$\mathrm{Re}_T = \frac{\langle \rho \rangle}{\langle \mu \rangle} \frac{\{k_T\}}{\omega_T} \qquad 3.27$$

Contour plots and stream-wise trends of turbulence Reynolds number for three aforementioned cases are shown in Figure 3.14.

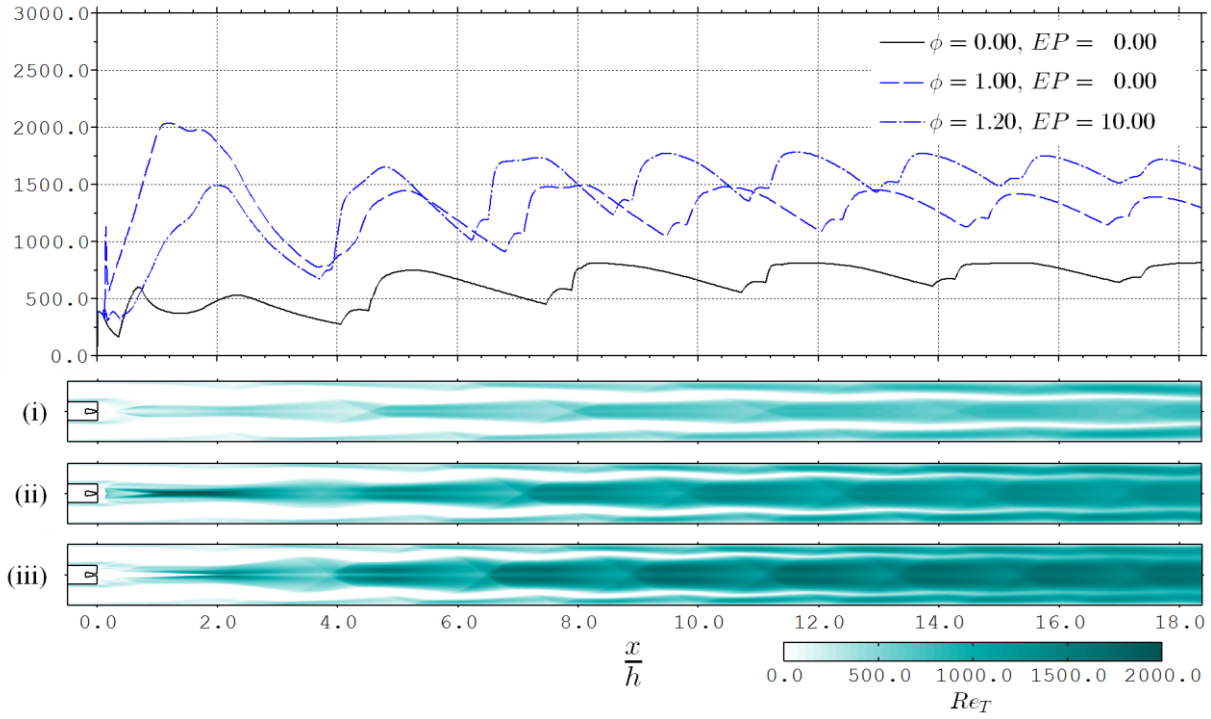

Figure 3.14: Turbulence Reynolds number cross-stream maximum trends with stream-wise location and contours with (top to bottom): (i) $\phi = 1.0$, $EP = 0.0\%$, (ii) $\phi = 1.0$, $EP = 5.0\%$, and (iii) $\phi = 1.2$, $EP = 10.0\%$.

The modelled turbulence predicts that fluid injection into the centre-body wake greatly increases the turbulence Reynolds number of the initial mixing layers which develop between $x \sim 1.0h - 4.0h$. The wake naturally generates a turbulence Reynolds number between 200 - 500 ($\phi = 0.0$ and $EP = 0.0\%$) in this region. Injection of pure fuel develops near symmetric mixing layers with a maximum Re_T of ~2000 at $x \sim 1.0h.$, whereas the injection of oxygen enriched fuel ($\phi = 1.2$ and $EP = 10.0\%$) exhibits a maximum Re_T of ~1500 at $x \sim 2.0h$. The difference in turbulence Reynolds number between the two previous cases is attributed to the varying recompression of the injected stream: Mach disk ($\phi = 1.0$ and $EP = 0.0\%$) versus oblique shock waves ($\phi = 1.2$ and $EP = 10.0\%$). This is confirmed by the other simulated cases. The turbulence Reynolds number decreases in regions where reflected expansion fans intersect the mixing wake. This reduction is far

more extreme in the pure fuel case. Shock-turbulence interactions increase the turbulence Reynolds number for all three cases. This increase is most notable in the oxygen enriched case, where the reflected recompression shock first interacts with the mixing wake at $x = 4.0h$, as Re_T increases beyond the previous upstream maxima. Oxygen enrichment appears to promote greater turbulence production due to shock-turbulence interactions by strengthening the reflected recompression shock - indicated by the interaction occurring further upstream in comparison to the pure fuel case. The turbulence Reynolds number of the oxygen enriched case remains greater than that of the pure fuel case downstream of the first shock-turbulence interaction. Subsequent shock interactions are less effective at stimulating turbulence within the mixing wake. The turbulence Reynolds number of the wake flow ($\phi = 0.0$ and $EP = 0.0\%$) roughly asymptotes to a value of ~800 downstream, the pure fuel injection asymptotes to a value of ~1300, and the enriched fuel injection asymptotes to a value of ~1700.

The modelled turbulence dissipation (Equation 3.19) can be combined with Taylor's expression for homogeneous turbulence dissipation (Equation 2.10) to derive an expression for the Taylor length, given by:

$$L_\lambda = \sqrt{\frac{10}{\beta^* \omega_T} \frac{\langle \mu \rangle}{\langle \rho \rangle}} \qquad 3.28$$

The resultant Taylor lengths for three cases are shown in Figure 3.16. Without injection, the smallest Taylor length scales in the region just behind the centre-body are governed by the boundary-layer that detaches from the upper and lower walls of the centre-body. Once the two ingested streams meet, $x \sim 0.3h$, the minimum Taylor length is ~0.5 mm. There is a nearly linear increase in this length as the flow travels downstream, reaching a maximum of ~2.3 mm at $x \sim 4.0h$.. The Taylor length then drops to ~1.6 mm due to the reflected shock wave interaction with the wake turbulence. Subsequent shock-turbulence interactions are not as significant and a mild increase in the minimum Taylor length as the flow travels downstream culminates in a final value of ~3.3mm. The injection of both pure fuel and oxygen enriched fuel is predicted to generate turbulence with Taylor lengths behind the centre-body of ~0.1 mm. The formation of mixing layers results in an initially slow increase of the Taylor length until $x \sim 2.0h$. The mixing wake then

experiences expansion and the Taylor length increases to a value of ~1.9 mm as a consequence. Overall, the length slowly increases for both injection cases, slightly affected by reflected shock wave and expansion fan interactions, until the exit of the duct where $L_\lambda \sim 4.0$ mm.

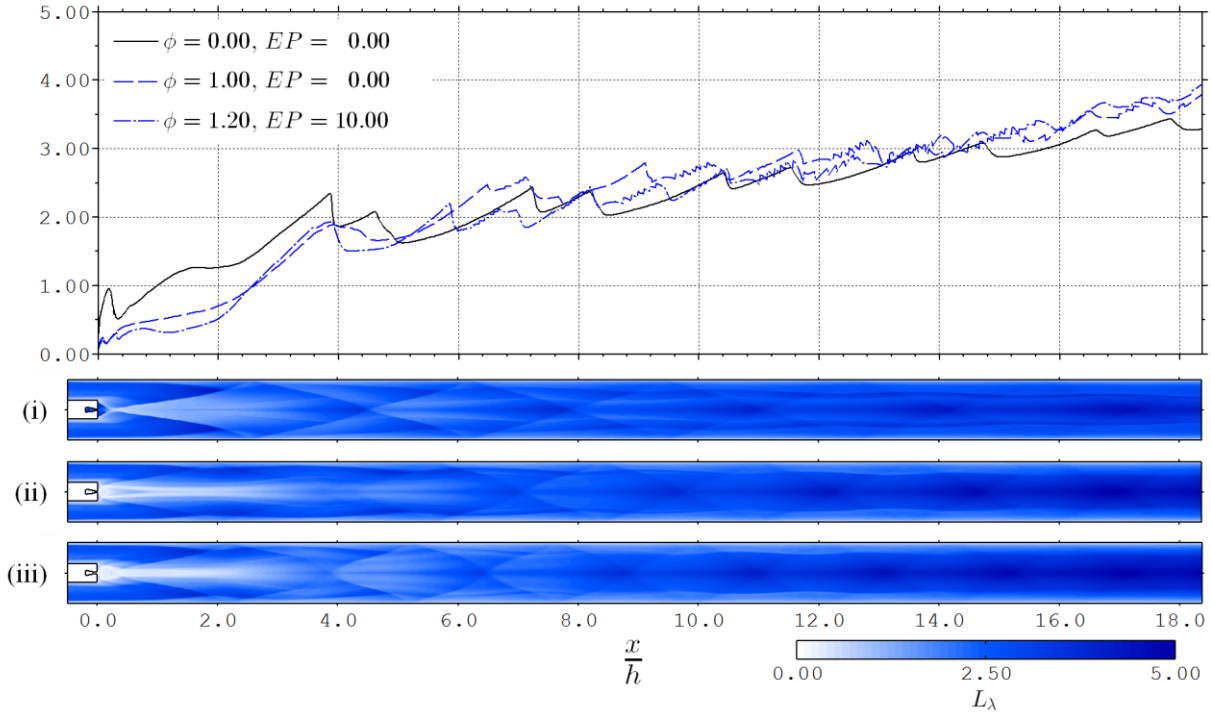

Figure 3.15: Taylor length (mm) cross-stream minimum trends with stream-wise location and contours with (top to bottom): (i) $\phi = 1.0$, $EP = 0.0\%$, (ii) $\phi = 1.0$, $EP = 5.0\%$, and (iii) $\phi = 1.2$, $EP = 10.0\%$.

The Reynolds number associated with the Taylor length, shown in Figure 3.16, is defined as:

$$\mathrm{Re}_\lambda = \frac{\langle \rho \rangle L_\lambda}{\langle \mu \rangle} \sqrt{\frac{2}{3}\{k_T\}} \qquad 3.29$$

The wake flow turbulence is characterised by a Taylor Reynolds number of ~200. Expansion and shock wave interactions with the free turbulence have a mild influence on Re_λ, which gradually trends to ~220 by the exit of the duct. As with the turbulence Reynolds number, pure fuel injection achieves a larger initial peak in Re_λ of ~400 when compared to oxygen enriched fuel injection

where $\mathrm{Re}_\lambda \sim 340$. Stream-wise trends of the Taylor Reynolds number for these two cases are very similar to the trends of the turbulence Reynolds number.

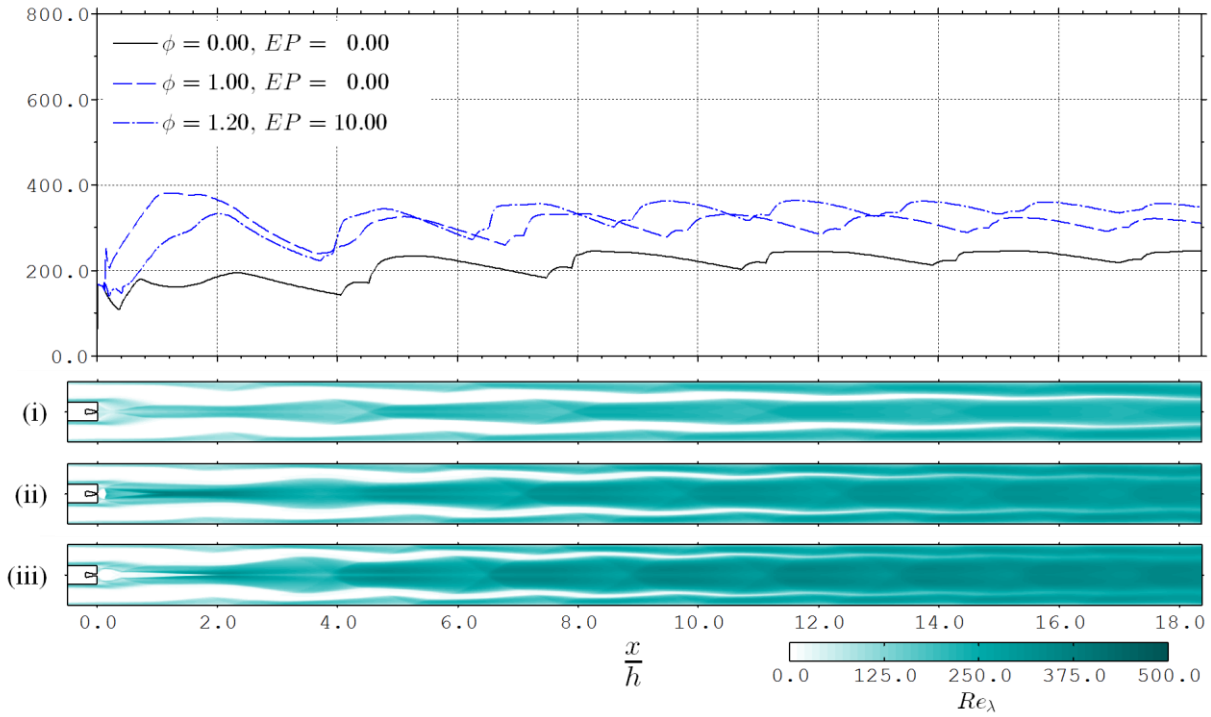

Figure 3.16: Taylor Reynolds number cross-stream maximum trends with stream-wise location and contours with (top to bottom): (i) $\phi = 1.0$, $EP = 0.0\%$, (ii) $\phi = 1.0$, $EP = 5.0\%$, and (iii) $\phi = 1.2$, $EP = 10.0\%$.

The turbulence model can also be used to estimate the Kolmogorov length, shown in Figure 3.17, given by:

$$L_\eta = \left(\frac{\langle \mu \rangle^3}{\langle \rho \rangle^3} \frac{1}{\varepsilon} \right)^{\frac{1}{4}} \qquad 3.30$$

The near field is characterised by a minimum Kolmogorov length of ~50.0 μm without injection, and ~10 μm with injection. The difference in near field Kolmogorov length between the various fuelling conditions is marginal. The expansion of the mixing wake correlates with an increase in the length such that $L_\eta \sim 100$ μm for no injection, and $L_\eta \sim 60$ μm for both injection cases at $x \sim 4.0h$.

The first shock-turbulence interaction causes a small decrease in the length but overall, there is a increasing stream-wise trend where, in all cases, $L_\eta \sim 120\ \mu m$ by the exit of the duct.

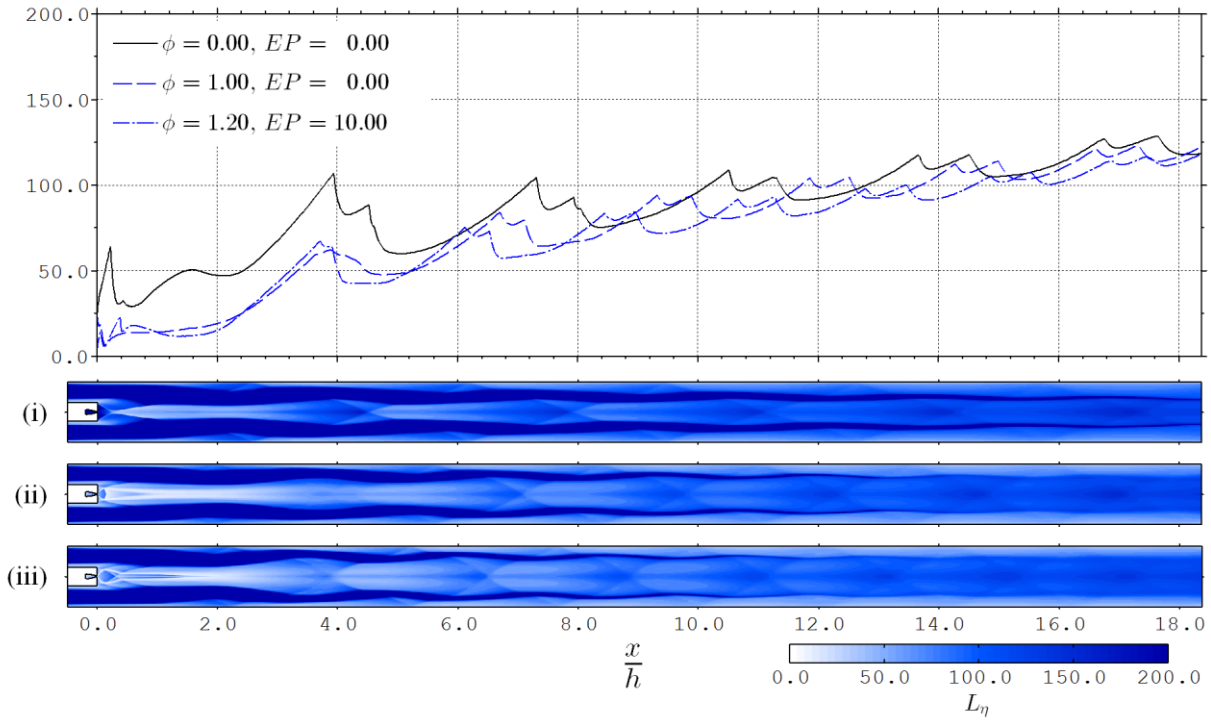

Figure 3.17: Kolmogorov length (μm) cross-stream minimum trends with stream-wise location and contours with (top to bottom): (i) $\phi = 1.0$, $EP = 0.0\%$, (ii) $\phi = 1.0$, $EP = 5.0\%$, and (iii) $\phi = 1.2$, $EP = 10.0\%$.

In regions of free turbulence, the ratio of Taylor length to Kolmogorov length varies between 30 and 35. Wilcox (2006) suggests that this ratio should be in excess of 70 for modelled turbulence to exhibit a well-defined sub-inertial range. This truncation of turbulent scales, in combination with the compressible nature of the flow, indicates that the turbulence generated within the duct is unlikely to obey Kolmogorov's universal equilibrium theory and form a well-defined inertial sub-range. Given this result, there is strong motivation to verify the presented conclusions regarding oxygen enrichment, which are based on changes in modelled turbulence characteristics, using higher fidelity numerical techniques that resolve the turbulent fluid motion.

4 Large Eddy Simulation with Pure Fuel Injection

This chapter begins with a section, 4.1, that presents material relating to the Large Eddy Simulation of the hypervelocity mixing wake with pure fuel injection, beginning with an outline of the LES numerical methodology, including grid sizing and boundary conditioning. This is followed by section 4.2 relating to the execution of the simulation detailing the temporal evolution of statistical quantities. An overall assessment of the mixing wake is provided in section 4.3. More detailed analysis of the flow physics is reported in section 0 and conclusions are presented in 4.5.

The preliminary RANS simulations indicate that enriching fuel with oxygen is beneficial to mixing of fuel and captured air. However, the ability of RANS to accurately simulate compressible free shear flows is currently debatable. RANS has been shown to reasonably predict certain free shear turbulent flows (Cutler & White, 2001), after model parameters have been tuned to match experimental data. In contrast, compressibility corrections applied to RANS simulations have been shown to encounter difficulty in replicating experimental results derived from the free shear mixing layer (Barone, et al., 2006) and that these corrections may fail to model important physical aspects of compressible turbulence such as the baroclinic effect (Aupoix, 2004). It is therefore necessary to verify the findings of the previously reported RANS simulations of the mixing wake flow using a higher fidelity method, in this case Large Eddy Simulation.

4.1 LES Numerical Methodology

The aim of the following work is to investigate the hypervelocity mixing wake from the preliminary RANS simulations using a high fidelity LES methodology. The latter methodology utilises the Virtual Test Facility 2 code which includes: an Adaptive Mesh Refinement (AMR) technique, a hybrid numerical scheme designed for compressible flow simulation, and the stretched vortex sub-grid scale mode. There are several key differences between the previous study and the following simulation. In order to isolate the physical mechanisms which influence the mixing of fuel and air, finite-rate chemistry was suppressed. In addition, a laminar in-flow was simulated to isolate the natural turbulence characteristics of the mixing wake flow from up-stream influences. This requirement leads to the upper and lower duct walls to be artificially modelled as zero shear stress walls (slip walls), rather than walls with viscous shear (no-slip walls). The stream-wise extent of the planar duct simulated using LES is slightly more than half the full extent of the previous RANS simulations. This was done to make the computation practicable. The final deviation from the preliminary simulations was a slight truncation of the transverse extent of the computational domain to allow for cubic grid cells.

4.1.1 Virtual Test Facility Solver

The Virtual Test Facility 2 (VTF2) methodology performs time-explicit finite volume integration of the compressible LES equations (Chapter 2) on a block-structured Cartesian mesh. A structured adaptive mesh refinement (SAMR) algorithm (Pantano, et al., 2007) suited to this hyperbolic system of differential equations is utilised. The refinement of the mesh, or grid, is governed by two conditions: i) the detection of flow discontinuities using the Lax-Wendroff entropy method (Lax & Wendroff, 1960) with a residual characteristic wave threshold of 0.02 (Lombardini, 2008), and ii) the detection of hydrogen mass fraction gradients greater than 5.0×10^2 kg/(kg.m). It is worth noting that the adaptive mesh will not maintain a homogeneous filter, causing the filter and differential operators to no longer commute. However, the errors generated from mesh adaption should remain unsubstantial if the filter width variations are small in comparison to the local cell size.

Fluxes are calculated using a hybrid Tuned Centre-Difference (TCD) - Weighted Essentially Non-Oscillatory (WENO) scheme (Hill & Pullin, 2004). The TCD scheme is second-order accurate, tuned to minimise commutative errors (Ghosal, 1996), that produces zero-numerical-dissipation whereas the upwind WENO scheme does produce non-trivial amounts of numerical dissipation. The activation of WENO is governed only by the detection of flow discontinuities, using the equivalent Lax-Wendroff residual characteristic wave threshold of the SAMR. It is undesirable to activate WENO in regions of species composition gradients as this would add non-physical numerical dissipation which may adversely affect the simulated mixing process. Sub-grid closure is achieved using the compressible extension of the stretched-vortex model (Kosovic, et al., 2002), where the stretched vortex sub-grid terms are given by:

$$\tau_{ij}^{sgs} = \bar{\rho} k_T^{sgs} \left(\delta_{ij} - e_i e_j \right) \tag{4.1}$$

$$\begin{aligned} q_j^{sgs} + D_j^{sgs} &= \frac{1}{2} \bar{\rho} \Delta_c \sqrt{k_T^{sgs}} \left(\delta_{kj} - e_k e_j \right) \frac{\partial \tilde{h}}{\partial x_k} \\ &= \frac{\Delta_c \tau_{kj}^{sgs}}{2\sqrt{k_T^{sgs}}} \frac{\partial \tilde{h}}{\partial x_k} \end{aligned} \tag{4.2}$$

$$J_{S_i j}^{sgs} = \frac{1}{2}\bar{\rho}\Delta_c\sqrt{k_T^{sgs}}\left(\delta_{kj} - e_k e_j\right)\frac{\partial \tilde{Y}_{S_i}}{\partial x_k} = \frac{\Delta_c \tau_{kj}^{sgs}}{2\sqrt{k_T^{sgs}}}\frac{\partial \tilde{Y}_{S_i}}{\partial x_k} \quad 4.3$$

Where e_i is the sub-grid vortex axis which is assumed to align with resolved scale vorticity, Δ_c is the sub-grid cut-off length and k_T^{sgs} is the sub-grid turbulence kinetic energy, which can be determined from:

$$k_T^{sgs} = \int_{\kappa_c}^{\infty} E_T\left(\kappa\right)d\kappa \quad 4.4$$

The sub-grid cut-off wave-number is related to the cut-off length via $\kappa_c = \pi/\Delta_c$. The integrand of equation 4.4 is determined from the shell summed sub-grid energy spectrum of a Lundgren spiral vortex (Lundgren, 1982), given by:

$$E_T\left(\kappa\right) = \mathscr{K}_0\varepsilon^{\frac{2}{3}}\kappa^{-\frac{5}{3}}\exp\left(-\frac{2\kappa^2\nu}{3|\tilde{\alpha}|}\right) \quad 4.5$$

Where $\mathscr{K}_0$ is the Kolmogorov pre-factor, ε is the turbulence kinetic energy dissipation rate, and $\tilde{\alpha}$ is the axial strain rate along the sub-grid vortex axis. The resolved scale, second order velocity structure function can be used to calculate the following parameter (Voelkl, et al., 2000):

$$\mathscr{K}_0\varepsilon^{\frac{2}{3}} = \frac{\tilde{F}_2\left(\Delta_c;\mathbf{x}\right)}{4\Delta_c\int_0^{\pi} s^{-\frac{5}{3}}\left(1-\frac{\sin\left(s\right)}{s}\right)ds} \quad 4.6$$

Local evaluations of the structure function are estimated using the following discrete spherical average (summation of *j* and *k*):

$$\tilde{F}_2\left(\Delta_c;\mathbf{x}\right) = \frac{1}{6}\left(\left(\delta_j^{+}\tilde{u}_k\right)^2 + \left(\delta_j^{-}\tilde{u}_k\right)^2\right) \quad 4.7$$

Where the discrete differencing of velocity component $\tilde{u}_i$, taken in direction *j*, is defined as:

$$\delta_j^{\pm}\tilde{u}_i = \tilde{u}_i\left(\mathbf{x} \pm \mathbf{d}_j\Delta\right) - \tilde{u}_i\left(\mathbf{x}\right) \qquad 4.8$$

Where $\mathbf{d}_j$ is a unit vector aligned direction *j* and Δ is the local grid spacing. The stretched vortex model can also be used to estimate the fluid composition variance due to its structural basis. The mixing of different chemical species at the sub-grid scales assumes a winding of the fluid induced by the stretched vortices (Pullin & Lundgren, 2001). The thermodynamic properties, molecular viscosity, and thermal conductivity were calculated in an equivalent manner to the preliminary simulations. The mass diffusivity was calculated by assuming a constant Schmidt number between chemical species. These calculations are described in Appendix A1.

4.1.2 Computational Grid

The LES computations were performed on a three-dimensional adaptively refined Cartesian grid based upon the planar duct of the experimental model used by Razzaqi (2011), shown in Figure 4.1. The grid extends from the backward face of the intrusive centre-body to a distance $L_x = 470.0$ mm downstream in the stream-wise direction (*x*). The transverse, or cross-stream (*y*), and span-wise (*z*) extent of the domain are $h = 47.0$ mm and $L_z = 50.0$ mm respectively. Note the subtle deviation of the LES duct height from the experimental configuration, where $h = 47.14$ mm. This was done so that the computational domain could be discretised into at base grid of equal sized cubic cells suitable for high fidelity numerics. Subsequent refinements to this grid due to SAMR gives rise to variations in grid density and is discussed further in section 4.1.2.1.

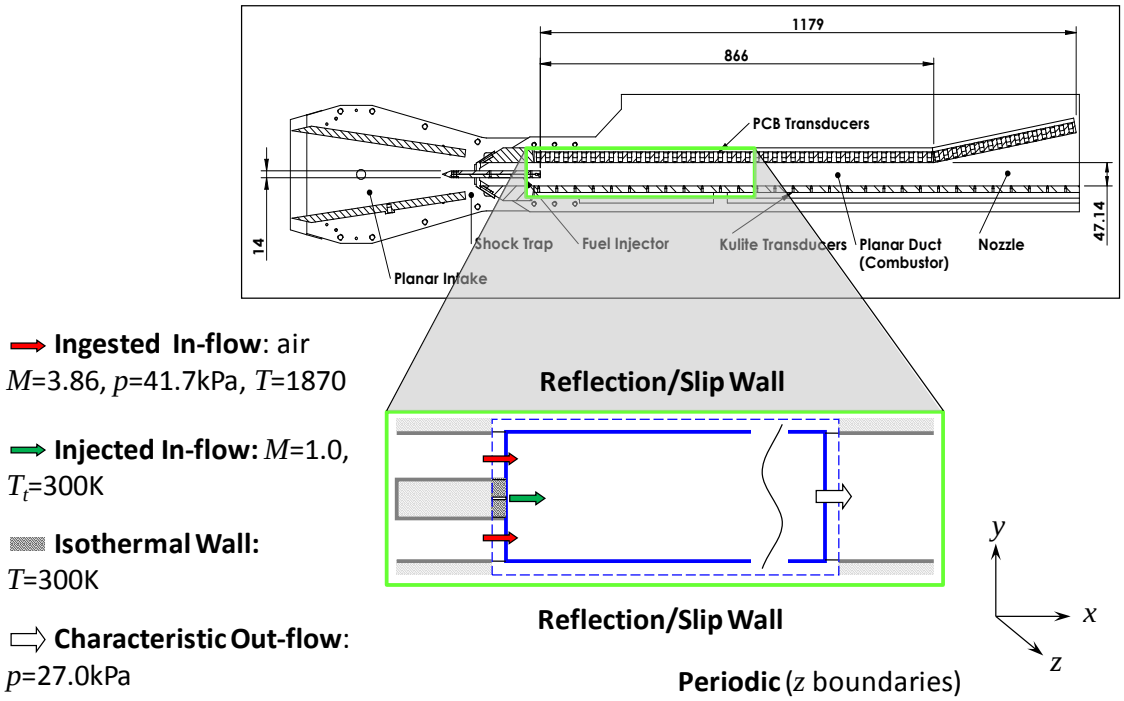

Figure 4.1: Computational Domain and Boundary Condition Schematic

The length of the grid was truncated to 10 duct heights. The rationale for this decision was twofold: i) the preliminary RANS simulations indicated that the important physical features of the experimental fluid flow occurred within this length, and ii) the computational expense of performing LES of the entire planar duct would be prohibitive. Practical simulations of the entire duct flow would also have to address the predicted interaction between the boundary-layer and free shear turbulence, combustion kinetics, and dissociative thermo-chemical effects.

4.1.2.1 Grid Sizing Estimation

It is crucial to choose a grid size that will resolve a sufficient amount of the turbulence to obtain accurate LES results whilst remaining computationally tractable. For high Reynolds number free turbulence flows, which are expected to form a well-defined inertial sub-range, an appropriate grid spacing, Δ, choice lies between the turbulence integral length and the Taylor length ($L_\lambda < \Delta < L_T$). The turbulence integral length is commonly taken directly from the geometry of the flow. There are several techniques for determining the Taylor length, with the simplest using scaling arguments (Dimotakis, 2000) and the integral Reynolds number of the intended flow simulation. A more localised method uses the modelled turbulence parameters from a RANS simulation of the intended

flow to predict the variations in Taylor length scale throughout the computational domain. However, previous RANS simulations identified that the inertial sub-range of the mixing wake may be dramatically truncated (Chapter 3), which suggests conservative grid spacing should be chosen to ensure unique physics are resolved rather than incorrectly modelled. In this context, it was considered appropriate that the grid spacing for the following work should obey the following inequality:

$$\Delta \leq L_{\lambda} \tag{4.9}$$

Unlike a fixed structured mesh, where the total number of grid cells is determined before the simulation is executed, the eventual size of an adaptive mesh is not immediately apparent. It is important to estimate the ultimate size of an adaptive mesh to ensure that the chosen base grid spacing, and allowable refinement, does not produce a computationally exhaustive simulation. The local grid spacing can be viewed as the inverse of the local linear grid density. Constraining the local grid spacing to be equal in all Cartesian coordinates allows the grid density to be expressed as:

$$\frac{dN}{dV} = \frac{1}{\Delta^3} \tag{4.10}$$

By allowing continuous variation of the grid spacing, the grid size can be determined by integrating equation 4.10 whilst satisfying the equality of expression 4.9. Integration over the mixing wake domain yields:

$$N = L_z \int_0^{L_x} \int_{-h/2}^{h/2} \frac{1}{{L_{\lambda}}^3} \, dydx \tag{4.11}$$

The difficulty in generating the proposed grid is that cell sizes cannot vary continuously. The VTF2 AMR algorithm sub-divides a base grid cell by a specified refinement factor, RF . This refinement can be performed recursively. It is disadvantageous to sub-divide a base grid cell more than three to four times as reductions in grid size due to adaption typically do not offset the additional computational overheads of solving on multiple grids. The choice of refinement factor should avoid dramatic changes in grid cell size, preferably resulting in even/integer division of the base cell. A

refinement factor of $RF = 2$ was prescribed for the mixing wake simulation based upon the aforementioned considerations. In all cases of refinement, grid cells remain cubic.

Another consideration is that the grid cell vertices must match the various boundary condition edges being applied to the simulation. To match the injector slot, strut backward face, and ingested in-flow boundaries, the maximum cell spacing must be $\Delta_{\max} = 0.5$ mm. This spacing requires a base computational grid of size 940 × 94 × 100. The minimum grid spacing can be determined using:

$$\Delta_{\min} = \Delta_{\max} RF^{\left\lfloor \log_{RF} \frac{\min(L_\lambda)}{\Delta_{\max}} \right\rfloor} \tag{4.12}$$

Where $\lfloor \ \rfloor$ represents the rounding of a value to the nearest integer less than that value. For the mixing wake simulation, it was found that $\Delta_{\min} = 62.5\ \mu$m with a total of four grid levels including the base grid. The minimum spacing would constitute a uniform grid of more than 4.5 billion cells. The local grid spacing can subsequently be found using:

$$\Delta = \begin{cases} \Delta_{\min} RF^{\left\lfloor \log_{RF} \frac{L_\lambda}{\Delta_{\min}} \right\rfloor} & L_\lambda < \Delta_{\max} \\ \Delta_{\max} & L_\lambda \geq \Delta_{\max} \end{cases} \tag{4.13}$$

In regions of refinement, the VTF2 calculates a solution using both the refined and parent grid cells. The overlapping grid is accounted for using:

$$\frac{dN}{dV} = \frac{RF^3 \Delta^{-3} - \Delta_{\max}{}^{-3}}{RF^3 - 1} \tag{4.14}$$

The grid spacing generated from the preliminary RANS results using equation 4.13 is shown in Figure 4.2 (i). Substituting equation 4.13 into equation 4.14 and integrating yields a modest total grid size estimate of 10.5 million cells. Resolving discontinuities within the flow, namely shock waves, is another consideration when utilising adaptive mesh refinement. Shock waves are apparent in regions of flow that exhibit high levels of compression (negative divergence of velocity). This can be achieved with the following modified definition of the local grid spacing:

$$\Delta = \begin{cases} \Delta_{\min} & \dfrac{\partial u_k}{\partial x_k} < -1.0 \times 10^5 \\ \Delta & \dfrac{\partial u_k}{\partial x_k} \geq -1.0 \times 10^5 \end{cases} \qquad 4.15$$

In addition, large gradients in fluid composition must also be well resolved:

$$\Delta = \begin{cases} \Delta & \left| \dfrac{\partial Y_{S_k}}{\partial x_k} \right| \leq 50.0 \\ \Delta_{\min} & \left| \dfrac{\partial Y_{S_k}}{\partial x_k} \right| > 50.0 \end{cases} \qquad 4.16$$

The modified grid spacing provided by equation 4.15 and 4.16 is shown in Figure 4.2 (ii). The total grid size is estimated to be 485 million cells, which would be a prohibitively expensive computation. The generation of a more manageable grid size can be achieved by restricting the allowable number of recursive cell divisions in specific regions of the domain. As the smallest Taylor lengths only exist near the laminar in-flow, three successive cell refinements are only permitted by base cells adjacent to the in-flow boundary. Two successive cell refinements are permitted for base cells with a centroid between 0 and 2 duct heights downstream from the in-flow boundary, and a single refinement is permitted for base cells with a centroid between 0 and 5 duct heights downstream from injection. The restricted grid spacing is shown in Figure 4.2 (iii), which produces an estimated 35.4 million cell grid. The resultant grid is predicted to resolve the Taylor micro-scale everywhere and provide at least one level of refinement around shocks until after the first shock-wake interaction is completed.

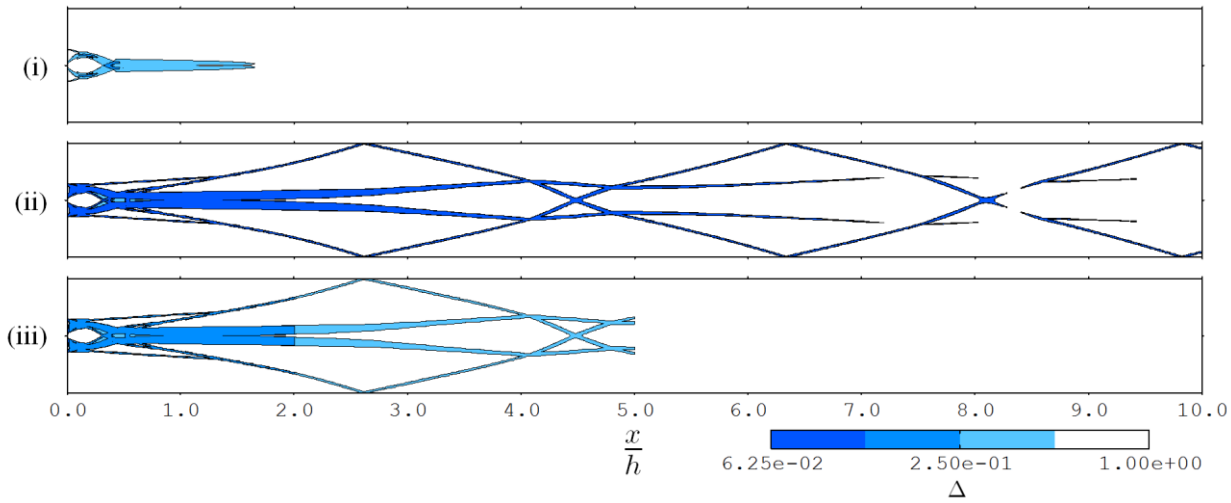

Figure 4.2: Contour of the LES grid spacing using: i) Taylor length, ii) Taylor length and flow discontinuities, and iii) restricted Taylor length and flow discontinuities

4.1.2.2 Sub-Grid Scale Cut-off

The appropriate choice of sub-grid scale cut-off length, Δ_c, requires finding a balance between better resolved flow physics and numerical error. The cut-off length is inherently related to the grid spacing. A larger cut-off length relative to the grid spacing reduces numerical errors but also reduces the resolvable turbulent scales. Conversely, a cut-off length of similar size to the grid spacing increases the physical resolution of the simulation but may also increases numerical errors to non-trivial amounts (Pope, 2004). For certain combinations of numerical schemes and sub-grid models, it has been shown that numerical errors are negligible where the cut-off length is at least four times larger than the grid spacing (Chow & Moin, 2003). Ensuring the cut-off length remains sufficiently larger than the grid spacing locally is especially important for dissipative schemes, where variations at the grid scale will be highly diffuse. For low numerically dissipative scheme however, allowing the cut-off length to reach parity with the grid spacing should produce acceptable numerical errors (Pope, 2004).

For this simulation, the sub-grid scale cut-off length is computed by linearly interpolating between the minimum permissible cell lengths at 0, 2, and 5 duct lengths downstream from injection. This ensures the sub-grid scale cut-off length is greater than or equal to the local cell size in all regions

were the AMR is active whilst avoiding large discontinuities in resolved and sub-grid quantities. The cut-off wave-number associated with the base grid cell is $\kappa_c = 2000\pi$.

4.1.3 Boundary Conditions

The in-flow conditions are prescribed with a uniform free-stream and a laminar boundary-layer profile so that all turbulence generated within the computational domain occurs as a consequence of the natural instabilities of the mixing wake flow. The outflow plane was modelled as a characteristic boundary so as to avoid artificial acoustic feedback. The upper and lower boundaries of the simulation were modelled as reflective slip walls, and the out-of-plane boundaries were modelled as a periodic extension. The details of each of these boundary conditions follow.

4.1.3.1 Ingested In-Flow Conditions

The ingested in-flow profile is prescribed to have a uniform free-stream with a 1.17 mm thick laminar boundary-layer on the strut. The uniform ingested free-stream conditions are described with: Mach number $M = 3.857$; static temperature $T = 1867$ K, and static pressure $p = 41.72$ kPa. The fluid composition of the ingested flow is 0.77 by mass gaseous nitrogen and 0.23 by mass gaseous oxygen. The Reynolds number based upon the injector strut height and the ingested free-stream conditions is 55,650.

By comparing the preliminary RANS simulation results of the previous chapter to the empirical relationship derived by He & Morgan (1994), the boundary layers which form on the top and bottom surfaces of the injection strut were considered laminar. The laminar boundary-layer profile was calculated using the self-similar Illingworth-Levy transformed compressible laminar boundary-layer equations with temperature dependent specific heat and transport coefficients (Appendix A1). The non-dimensionalised stream-wise velocity and static temperature profiles are found by solving a boundary value problem of the following coupled ordinary differential equations:

$$\frac{d^3 f}{d\eta^3} = -\left(\left(\frac{T_e}{\mu}\frac{d\mu}{dT} - \frac{1}{g}\right)\frac{dg}{d\eta} + \frac{f}{C}\right)\frac{d^2 f}{d\eta^2} \qquad 4.17$$

$$\frac{d^2 g}{d\eta^2} = -\left(\left(\frac{T_e}{\lambda}\frac{d\lambda}{dT} - \frac{1}{g}\right)\frac{dg}{d\eta} + \Pr\frac{f}{C}\right)\frac{dg}{d\eta} - \frac{\Pr}{c_p}\frac{U_e^{\,2}}{T_e}\left(\frac{d^2 f}{d\eta^2}\right)^2 \qquad 4.18$$

Where,

$$\frac{df}{d\eta} = \frac{U}{U_e}, \quad g = \frac{T}{T_e}, \quad C = \frac{1}{g}\frac{\mu}{\mu_e}, \quad \Pr = \frac{\mu c_p}{\lambda}$$

An appropriate assumption for simulations of an impulse facility test, which only operator for several milliseconds, is to consider the centre-body wall temperature constant at 300 K and apply the following boundary conditions:

$$\eta = 0: \quad \frac{df}{f\eta} = 0, \quad g = \frac{300}{T_e}$$

$$\eta \to \infty: \quad \frac{df}{f\eta} = 1, \quad \frac{d^2 f}{f\eta^2} = 0, \quad g = 1$$

A piecewise polynomial approximation of the solution to the boundary-value problem was implemented into the definition of the in-flow profile. The boundary condition employs characteristic wave cancellation (Rudy & Strikwerda, 1980) including viscous terms (Poinsot & Lele, 1992) in regions where the boundary-layer is subsonic to ensure acoustic waves are not reflected back into the domain.

4.1.3.2 Injected In-Flow Conditions

The injected in-flow represents a sonic choked flow of pure gaseous hydrogen exiting the 1.0 mm planar slot with a total temperature of 300 K (cold propellant injection). The in-flow profile is comprised of a uniform free-stream with an upper and lower laminar boundary-layer of thickness 0.25 mm. The definition of the injected in-flow is completed by specifying the fuelling condition; in this case an equivalence ratio $\phi = 1.0$, and an Enrichment Percentage $EP = 0.0\ \%$. This results in the following free-stream condition: a Mach number $M = 1.0$; static temperature $T = 248.9$ K and static pressure $p = 248.6$ kPa. The boundary-layer profile was determined in an equivalent manner

to the ingested stream, using the aforementioned conditions. As with the ingested in-flow, characteristic wave cancellation was employed.

4.1.3.3 Centre-body Backward Face

The remaining sections of the upstream boundary, which represent the backward face of the instrusive centre-body, have been modelled as a no-slip, isothermal wall with a static temperature of 300 K. This condition is imposed using a ghost fluid method (Laney, 1998). The properties of the fluid within the ghost cells are equivalent to their in-domain reflections, except static density which is adjusted to match the prescribed temperature.

4.1.3.4 Out-Flow Conditions

Although the mean out-flow of the mixing wake simulation is expected to be supersonic, localised regions of flow may exit the domain at sub-sonic speeds. To ensure that no acoustic waves are propagated back into the computational domain, corrupting the simulation, a characteristic out-flow condition was applied at the downstream boundary (Poinsot & Lele, 1992). This condition requires the specification of a far-field static pressure; a value of 27.0 kPa was prescribed for this simulation based upon the preliminary RANS results.

4.1.3.5 Reflective Boundary

Both cross-stream normal boundaries are modelled as reflective slip walls. This imposes a method of images type flow condition using ghost cells that extend beyond the computational domain. The fluid contained within these ghost cells are prescribed equivalent properties to the in-domain reflection, except the component of momentum normal to the boundary which is reversed.

4.1.3.6 Periodic Boundary

The span-wise normal boundaries employed a periodic condition, which enforced mass, momentum, and energy fluxes exiting one of these boundaries to enter the other. This condition acts as a high-pass filter on the flow, which can impose non-physical constraints on the simulation. For this reason, it is important to ensure the span-wise extent of the domain is of sufficient size so that no energy containing turbulence is obscured by the periodic condition.

4.2 LES Execution

The simulation was initialised with the ingested flow free-stream condition throughout a majority of the grid. To prevent artificially larger gradients during the simulation start-up, the flow conditions of grid cells located within 0.1 duct heights of the backward face of the centre-body are linearly interpolated between the ingested flow free-stream condition and a 300 K stagnant flow at the boundary. In addition, the mass flow rate of the injected stream was initially zero and linearly increased to the nominal value after 1.0 μs of simulated time.

Injected fluid requires approximately 200 μs to traverse the extent of the computational domain (470mm, 10 duct heights). Hence, a nominal flow through time is defined as $t_c = 2.0 \times 10^{-4}$ s. The simulation was executed for 1.0 ms, or 5 nominal flow through times, with approximately 14,000 explicit time steps. During simulation, the average size of the AMR grid was 71 million grid cells. This is a significant reduction in size when compared to a uniform grid refined by a factor of 4, which would exceed 565 million grid cells. At each base cell vertex, 2001 truncated data samples were taken during the simulation at a sampling frequency of 2 MHz in order to calculate statistical properties of the flow field. The total computational time of the simulation was slightly above 400,000 CPU hours. The complete solution set was saved every 10 simulated microseconds (0.07% of the entire solution data) and required a total 2.2 TB of disk storage. The sheer amount of data generated from this LES calculation highlights the importance of maximising the potential usefulness of the saved data by performing a priori analysis using cheaper computational methods.

The grid adaption and regions of active WENO behind the in-flow boundary are shown in Figure 4.3 (ii), and compared to the static density gradient magnitude in Figure 4.3 (i). There are several regions downstream where shock waves interact with the turbulent mixing interface which has the undesirable potential to activate WENO. Fortunately, the TCD scheme was sufficiently stable in these regions so minimal numerical dissipation is generated. Visualisations of the grid adaption and active WENO of the entire computational domain at several instances are compared to the static density gradient in Figure 4.4. There a several circumstances where weak shock waves form around the visible edge of the mixing wake. These weak shocks do not have the strength to activate WENO and discernible, albeit very small, oscillations in density gradient are apparent nearby. The

frequency of these oscillations, equivalent in scale to the local grid spacing, suggests that these oscillations are numerical. These oscillations quickly dissipate away from the emanating shock.

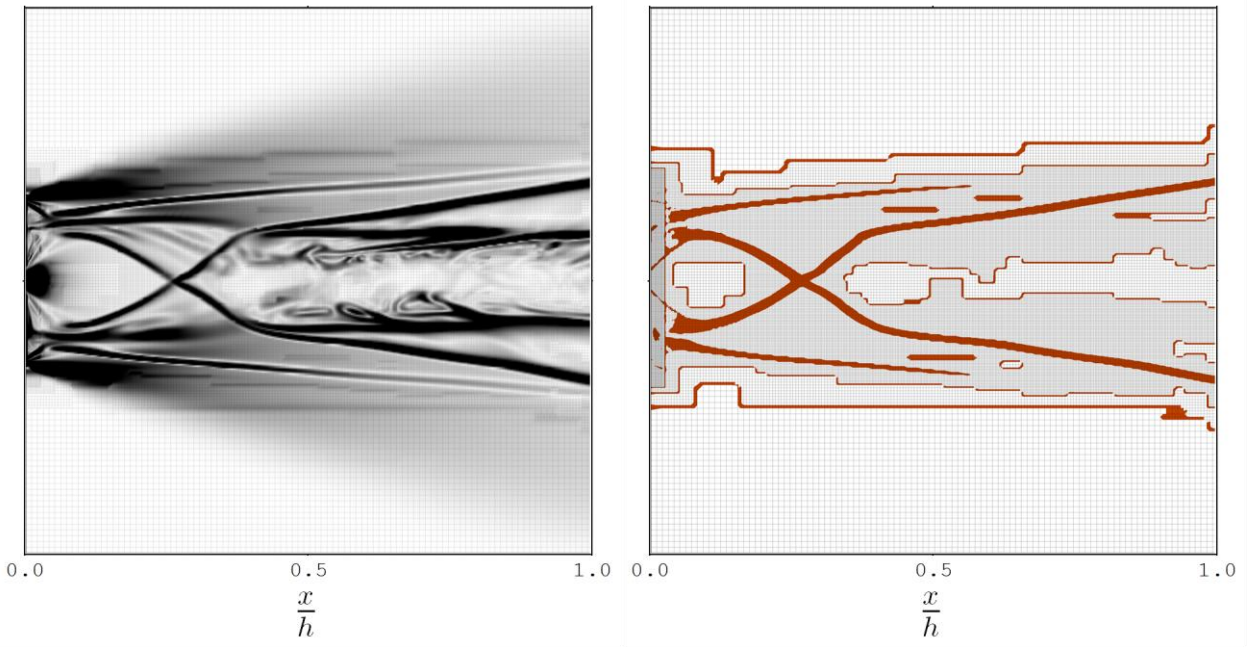

Figure 4.3 Visualisation of the adaptive grid just downstream of injection, taken at the instant $t = 4.0t_c$, superimposed onto (left to right): i) contours of static density gradient magnitude within the near field , and ii) regions of active WENO shaded in brown

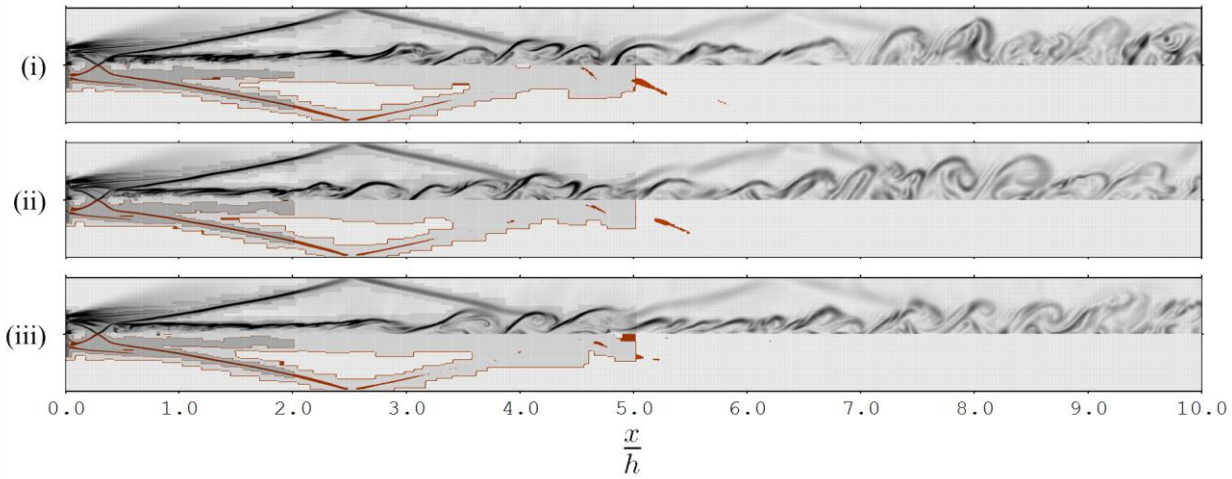

Figure 4.4 Visualisation of the entire adaptive grid superimposed on contours of static density and active WENO taken at the instant (top to bottom): i), $t = 3.0t_c$, ii) $t = 4.0t_c$, and iii) $t = 5.0t_c$

4.2.1 Statistical Convergence

It is important to define a Reynolds operator in order to determine the mean flow field and hence a statistical description of the simulated turbulence. For this work, the Reynolds operator is given as a time average defined by:

$$\langle \psi \rangle_t^{t+\Delta t} \left(\mathbf{x}_k \right) = \frac{1}{\Delta t} \int_t^{t+\Delta t} \psi \left(\mathbf{x}_k, \zeta \right) d\zeta \tag{4.19}$$

Where ψ is a simulated physical quantity, t is the time at which averaging can commence, and Δt is the time averaging window. For numerical simulations, which can only provide discrete evaluations of a given quantity; integration is approximated using the trapezoidal method. As the boundary conditions are held steady throughout the simulation, it is expected that the simulated fluid flow will tend towards a statistically stationary state. As such, the upper bound of integration is prescribed to be the final simulation time, t_∞. The lower bound should be chosen to maximise the time averaging window without including transient flow effects caused by flow establishment from the initial conditions. An appropriate choice can be made by observing the different results of averaging a simulated physical quantity when varying the lower bound of integration. This leads to defining the cumulative average residual as:

$$\epsilon_{\langle \psi \rangle_t^{t_\infty}} \left(\mathbf{x}_k \right) = \langle \psi \rangle_{t_i}^{t_\infty} \left(\mathbf{x}_k \right) - \langle \psi \rangle_{t_{i+1}}^{t_\infty} \left(\mathbf{x}_k \right) \tag{4.20}$$

Where t_i is the simulation time at which the i^{th} statistical sample is taken. The difference between successive simulated time samples is 0.5 μs. Taking the difference of the cumulative average, starting from the final simulation time and moving backward in time, will produce a monotonically decreasing trend if the simulated physical quantity being averaged has achieve a steady state; transient effects will cause this difference, or residual, in cumulative averaging to increase. Time-averaging of steady quantities is least sensitive to the lower integration bound selection when the cumulative average residual takes on an initial local minimum. Fluctuations of the cumulative average residual calculated at a particular domain location can be significant, making it difficult to determine this minimum. In addition, the cumulative average of a physical quantity at a single

location may not be representative of the cumulative average taken at other locations within the computational domain. By determining the Euclidean norm (l^2-norm) of several cumulative average residuals, taken at multiple locations, one finds a single parameter which both represents the more general behaviour of averaging the entire flow field and provides a clearer minimum in cumulative averaging residual. Subsequently, the Euclidean cumulative average residual is defined as:

$$\left\| \epsilon_{\langle \psi \rangle} \right\|_2 = \sqrt{\frac{1}{N_k} \sum_{k=1}^{N_k} \epsilon_{\langle \psi \rangle_t^{t_\infty}} \left(\mathbf{x}_k \right)^2} \qquad 4.21$$

The statistical convergence of the mixing wake flow has been analysed using the: static density (Figure 4.5), stream-wise velocity (Figure 4.6), static pressure (Figure 4.7), and the stream-wise momentum advection in the stream-wise direction (Figure 4.8). The final simulation time is 5.0 flow through times. The Euclidean norm was calculated using 89,395 unique locations, homogeneously distributed throughout the computational domain. The Euclidean cumulative average residual was normalised by the initial Euclidean cumulative average residual value.

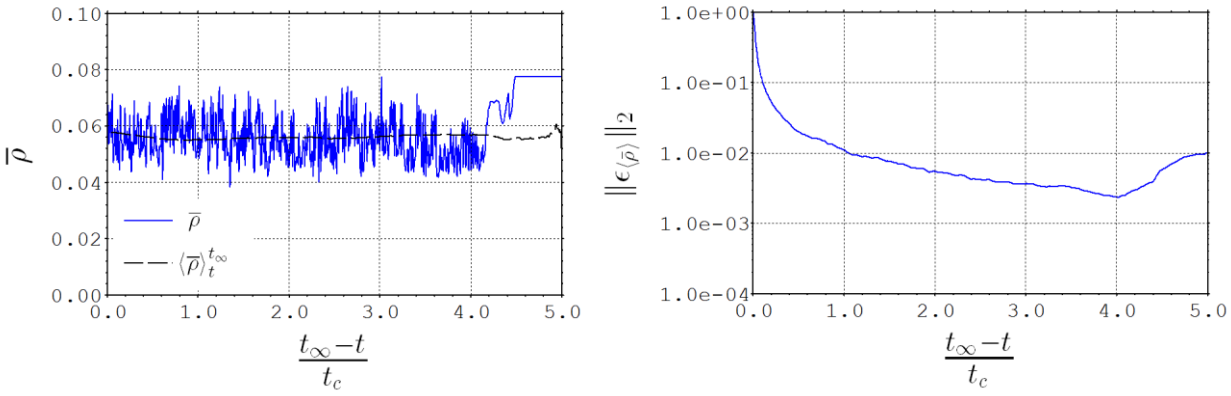

Figure 4.5 (left to right): i) Trends in instantaneous and cumulative time-averaged (from time t to $5.0t_c$) static density (kg/m^3) with time at $x = 9.0h$, $y = 0.0$, and $z = 0.0$, and ii) the l^2-norm of the cumulative time-average residual of the static density field

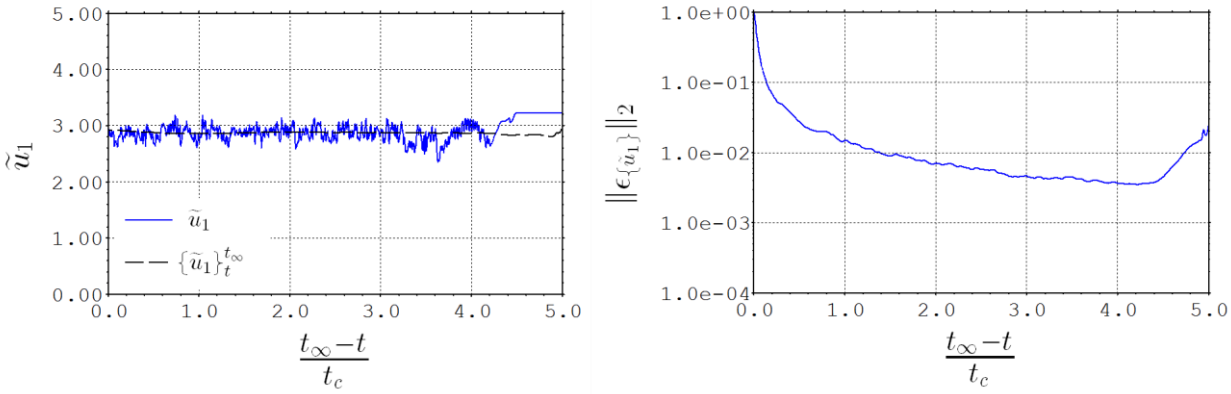

Figure 4.6 (left to right): i) Trends in instantaneous and cumulative time-averaged (from time t to $5.0t_c$) stream-wise velocity (km/s) with time at $x = 9.0h$, $y = 0.0$, and $z = 0.0$, and ii) the l^2-norm of the cumulative time-average residual of the stream-wise velocity field

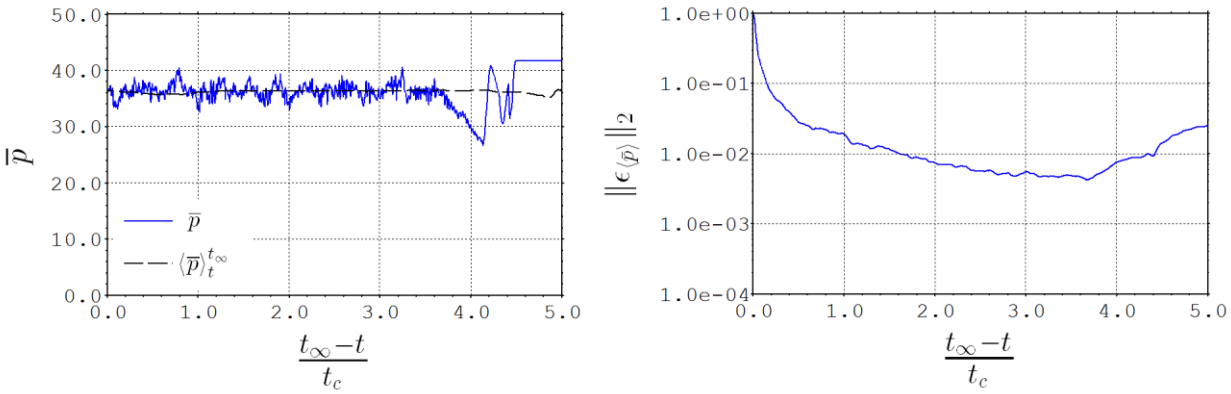

Figure 4.7 (left to right): i) Trends in instantaneous and cumulative time-averaged (from time t to $5.0t_c$) static pressure (kPa) with time at $x = 9.0h$, $y = 0.0$, and $z = 0.0$, and ii) the l^2-norm of the cumulative time-average residual of the static pressure field

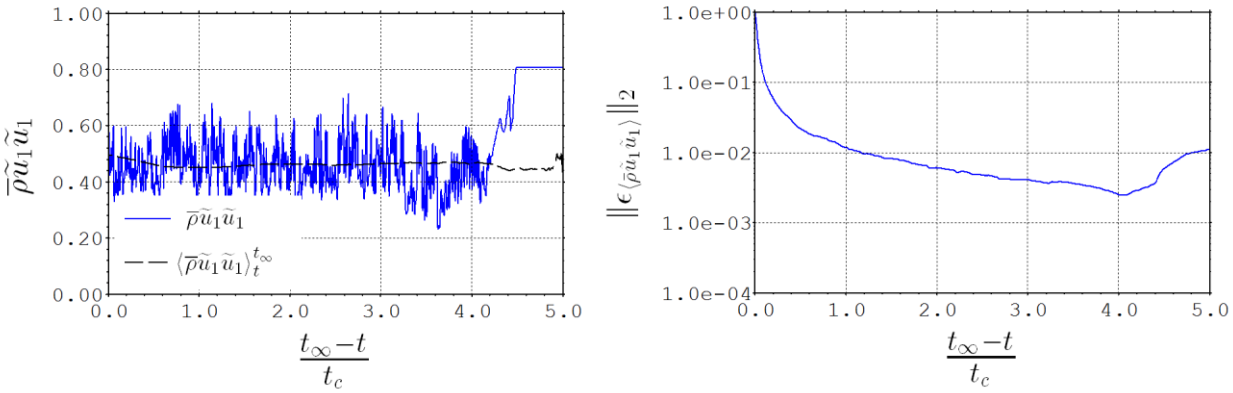

Figure 4.8 (left to right): i) Trends in instantaneous and cumulative time-averaged (from time t to $5.0t_c$) stream-wise momentum advection (MPa) in the stream-wise direction with time at $x = 9.0h$, $y = 0.0$, and $z = 0.0$, and ii) the l^2-norm of the cumulative time-average residual of the static pressure field

The Reynolds averaged static pressure was found to be most sensitive to the transient flow establishment. These transient flow features were found to influence the Reynolds average static pressure if the lower bound of integration was set below $t = 1.5t_c$. The Euclidean norm of the cumulative average residuals was shown to decrease by at least two orders of magnitude, relative to the initial residual, for each of the investigated quantities. This was deemed sufficient to report statistical convergence of the simulated quantities, defining the Reynolds operator as:

$$\langle\psi\rangle = \frac{1}{3.5t_c}\int_{1.5t_c}^{5.0t_c}\psi(\mathbf{x},\zeta)\,d\zeta \qquad 4.22$$

4.3 Overall Flow Structure

Contour plots of the instantaneous static density gradient, shown in Figure 4.9 at three difference instances, help to visualise the dynamics of the major compressible flow features of the mixing wake as well as that of the mixing interfaces between the fuel and air. The character of the mixing wake undergoes several dramatic changes as the flow travels downstream. Initially, the mixing wake is dominated by rapidly expanding injected and ingested fluid streams behind the injection strut. Symmetric mixing layers form where the injected and ingested streams meet and recompression shock waves are generated. These mixing layers are then accelerated towards the injected core flow before experiencing recompression due to a shock wave interaction. These mixing layers continue to develop parallel and symmetrically opposed after being processed by the recompression shock waves.

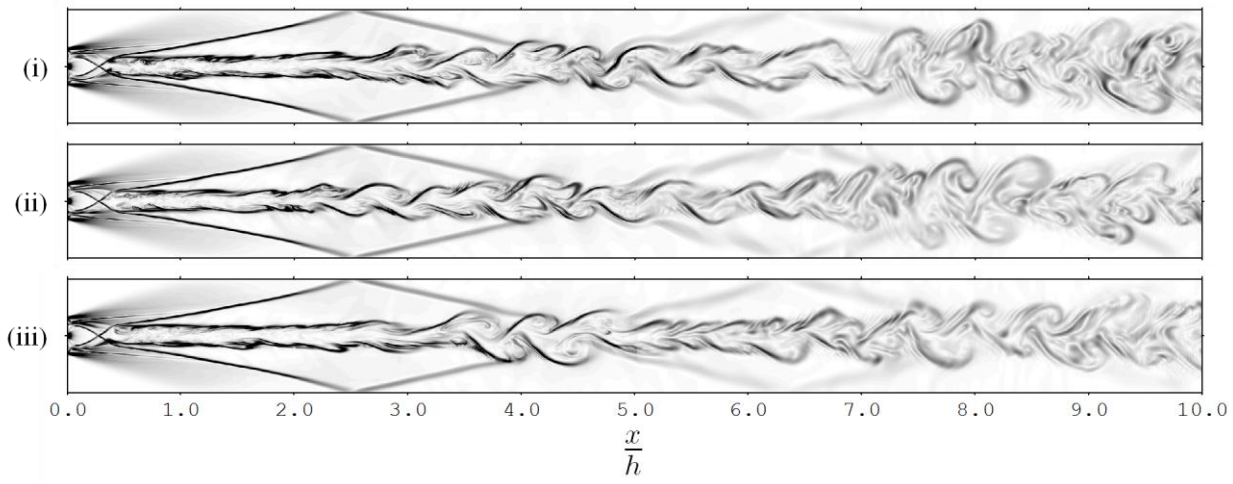

Figure 4.9: Span-wise normal $(z = 0.0)$ contours of static density gradient magnitude taken at the instant: (i) $t = 3.0t_c$, (ii) $t = 4.0t_c$, and (iii) $t = 5.0t_c$.

The turbulent structure of the mixing wake can be observed in Figure 4.10, where an iso-surface of the second invariant of the velocity gradient tensor (indicating regions of the flow experiencing greater rotation than shear) help to distinguish the dominant vortical structures within a flow field (Chong, et al., 1990). Distinct near stream-wise vortices dominate the turbulent structure of the initial mixing layers. The mixing wake then undergoes a transition at $x \sim 3.0h$, where larger scale

stream-wise and span-wise distortions of the wake begin to grow. From these waves, span-wise coherent counter rotating vortices evolve into what shall hereinafter be referred to as a rolling-up of the wake. During this roll-up, the initial stream-wise structures persist but are wrapped around the larger structures. Continuing down-stream, the recompression shock waves reflect off the upper and lower duct boundaries and interact with the fuel plume at $x \sim 4.0h$, causing a contraction in the transverse extent of the mixing wake. Subsequently, the wake roll-up is compressed and a pile-up of vortices occurs. By $x \sim 5.5h$ Growth of the span-wise coherent vortices recommences. Break-up of these coherent vortices into smaller, more three-dimensional vortices is evident at the flow nears the exit of the computational domain. In order to better characterise the mixing wake flow, Further examination of the mixing wake one-dimensional free shear parameters, turbulence statistics, and mixing and entrainment properties is given in subsections 4.3.1 - 4.3.3 respectively.

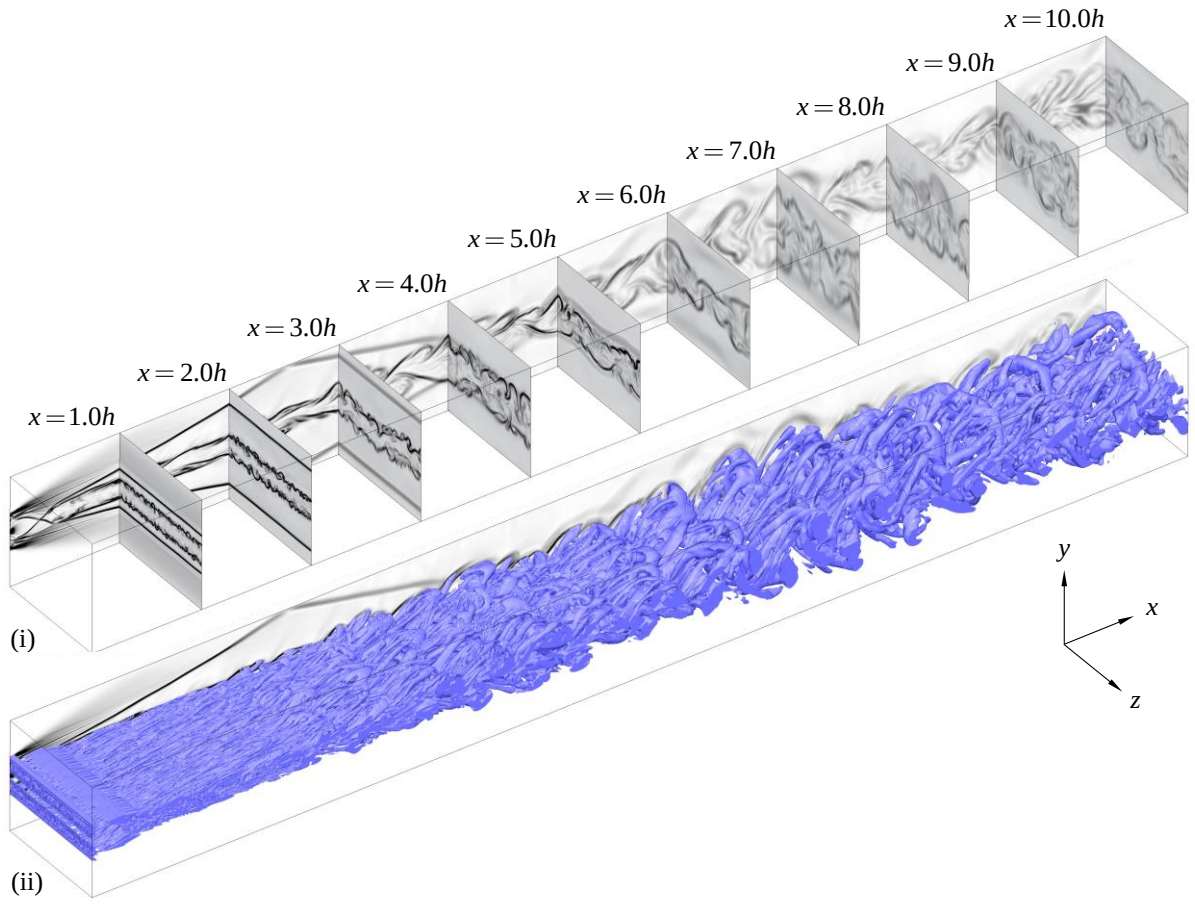

Figure 4.10: Visualisations taken at the instant $t = 4.0t_c$ of: (i) Stream-wise normal contours of static density gradient magnitude, and (ii) constant second invariant of the velocity gradient tensor.

4.3.1 Shear Layer Properties

At this point, it is instructive to describe the mixing wake flow using simple free-shear layer parameters. They become effective descriptors of the flow once the symmetric mixing layers form, at approximately 0.4 duct heights downstream from injection. Determining such quantities first requires defining the mixing wake transverse extent. There are several methods for calculating this parameter, such as the vorticity thickness or kinetic energy thickness (Bradshaw, 1981). For this work, we define the edge of the mixing wake to exist where the mean fluid composition is 1.0% by mass of hydrogen.

$$y_{+\delta} = y \Rightarrow \left\{Y_{H_2}\right\}(x, y > 0) = 0.01, \quad y_{-\delta} = y \Rightarrow \left\{Y_{H_2}\right\}(x, y < 0) = 0.01$$

$$\delta(x) = y_{+\delta} - y_{-\delta} \tag{4.23}$$

The mean "free-stream" injected condition of the flow is taken along the symmetry plane, and the mean "free-stream" ingested condition is taken outside the defined mixing wake extent where the cross-stream gradient of the stream-wise velocity is sufficiently small. Taking these conditions, a one-dimensional description of the mixing wake can be made with the: transverse extent δ, velocity ratio r, density ratio s, and convective Mach number M_c. These parameters are shown in Figure 4.11. The free shear parameters offer little insight into the dynamics of the near field, which cannot be simply represented as two parallel moving streams with differing properties. The formation of recompression shock waves also have a dynamic effect on the development of the mixing layers up to $x = 1.0h$, most notably on the density ratio.

Near uniform, parallel streams exist between $x = 1.0h$ and $x = 2.0h$. Correspondingly, the velocity ratio, density ratio, convective Mach number, and spreading rate of the wake remain effectively constant over this distance. The velocity ratio across the symmetric mixing layers is ~0.38, corresponding to the high levels of shear between the initial meeting of ingested and injected streams. The density ratio is ~0.55, lower than unity due to the different compositions of the two streams. The theoretical incompressible spreading rate based upon the aforementioned velocity and density ratios is ~0.15 (Dimotakis, 1986). A reduced density ratio across an incompressible shear layer causes a weak retardation of the spreading rate, according to the model of Dimotakis (1986).

However, this effect is small in comparison to the highly compressible effects associated with a convective Mach number of ~1.0. Theoretical compressible spreading rates are predicted to be ~0.037 using the model of Dimotakis (1991), and ~0.069 using the model of Slessor, et al. (2000). The measured spreading rate of the wake in this region is ~0.025, markedly less than any of the theoretical predictions. The formation, structure, and growth of the initial, highly compressible mixing layers are explored further in section 4.4.1. It is also worth noting that the mixing wake thickness does not well represent the thickness of the initial mixing layers but rather the thickness of the fuel plume. The thickness of each mixing layer is better characterised by the vorticity thickness, δ_ω, which at $x = 1.0h$ is approximately $0.050h$. The Reynolds number based upon this vorticity thickness, Re_ω, is ~7,200. By $x = 2.0h$, $\delta_\omega \sim 0.076h$ and $\mathrm{Re}_\omega \sim 10,600$, which produces a growth rate of ~0.026 - similar to the measured spreading rate based upon the wake thickness.

The wake roll-up event causes a dramatic increase in the mixing wake growth rate, upwards of ~0.17 (more than a factor of seven increase). For comparison, the growth rate of an incompressible wake flow can be determined using the empirical correlations of Sreenivasan and Narasimha (1982), yielding the following expression:

$$\delta'_{iw0.5}(r;x) = \frac{0.298 + 0.099(1-r)}{1.627 + 0.688(1-r)}(1-r) \qquad 4.24$$

Where $\delta'_{iw0.5}$ is the half-velocity width growth rate of the incompressible wake. The growth rate of the full transverse extent (0.99-velocity width) of an incompressible wake, which is a fairer comparison to the calculated mixing wake growth rates, can be determined by assuming a self-similar wake velocity profile (White, 2006), which yields $\delta'_{iw0.99} = 2.5778\delta'_{iw0.5}$. This results in a theoretical incompressible wake growth rate of ~0.16 at $x = 3.0h$, which compares well with the rolling-up mixing wake growth rate. The shearing velocity difference between the two streams rapidly decreases and the convective Mach number drops to a nearly incompressible value of 0.45 by $x = 4.0h$. The density ratio shows only a mild increase due to the wake roll-up. Details of the wake roll-up event and transition to near incompressible flow will be discuss in section 4.4.2.

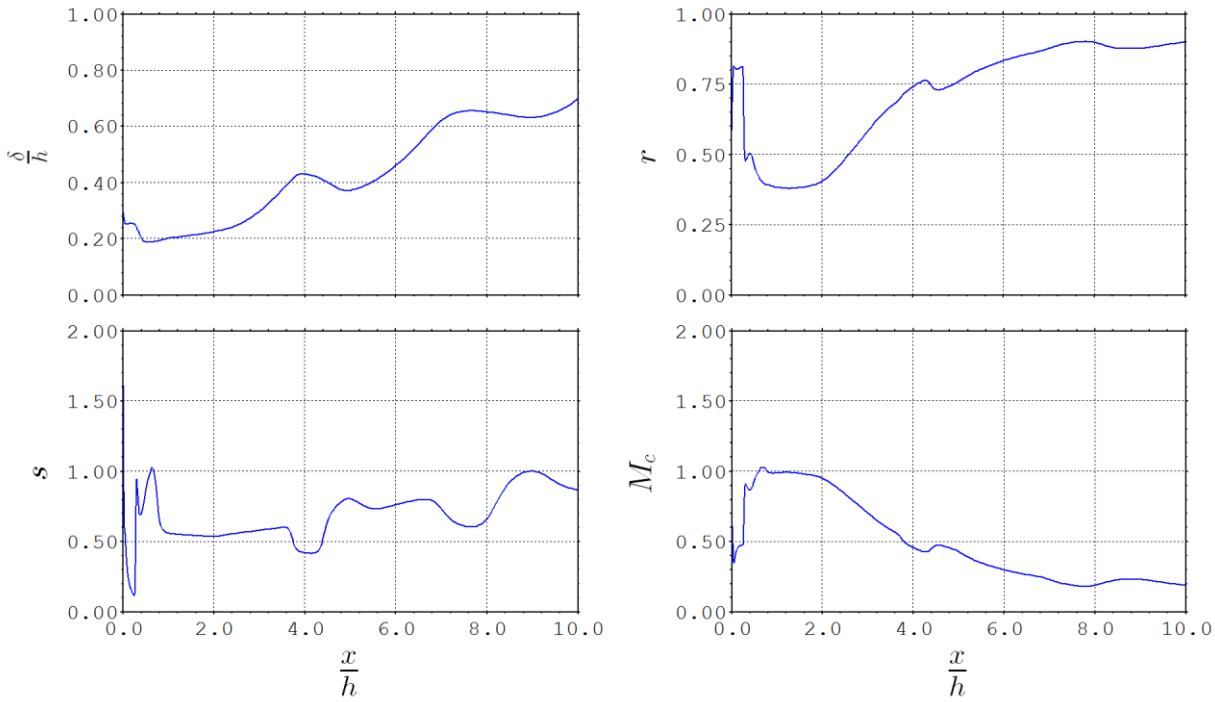

Figure 4.11: Shear layer properties of the mixing wake (clockwise from top left): transverse extent normalised by the duct height, velocity ratio, convective Mach number, and density ratio.

The upward trend in spreading rate reverses to the point of moderate contraction where the reflected shock first interacts with the mixing wake. The velocity ratio and convective Mach number also display a reverse trend, albeit slight. In contrast, the density ratio exhibits a dramatic rise towards unity across the shock interaction. The wake roll-up then recommences at $x = 5.0h$ and the growth rate returns to its pre-shock value of ~0.17. The theoretical incompressible wake growth rate at this location is ~0.07 due to the reduced velocity difference between the core stream and outer streams. The discrepancy between the calculated and empirically derived growth rates at this location highlights the influential variable density, and compositional effects between the core and outer streams upon the mixing wake growth rate. The second shock interaction, beginning at $x = 7.0h$, influences the mixing wake more weakly over a longer distance. More extensive analysis of the shock interaction with the wake flow is provided in section 4.4.3. To facilitate this exploration, and that of the initial mixing layers and the wake roll-up, we first report key turbulence statistics of the flow.

4.3.2 Turbulence Statistics

In turbulent fluid flow, it is useful to provide a statistical description of the fluid fluctuations, such as the mean turbulence kinetic energy, Reynolds stresses and correlations of velocity fluctuations. From these statistics, the scales of turbulence can be inferred, specifically the Taylor micro-scale, as well as sources of instability within the flow. Comments on the resolution of the turbulence kinetic energy due to grid discretisations are also made based upon these statistical quantities.

As previously mentioned, the turbulence kinetic energy is a key parameter in describing the behaviour of turbulent fluid motion. For LES, the total turbulence kinetic energy is the summation of the resolved and sub-grid scale contributions, given by:

$$\tilde{k}_T = k_T^{res} + k_T^{sgs} \tag{4.25}$$

The resolved turbulence kinetic energy, as the name implies, can be calculated directly from fluctuations in the resolved flow velocity components. The Favre averaged turbulence kinetic energy, determined using the averaging technique described in 4.2.1, of the mixing wake is shown in Figure 4.12. Contained within this figure are mean turbulence kinetic energy stream-wise trends of the cross-stream maximum $(\max)$ and the centre-line $(y = 0.0)$ values at a given stream-wise location.

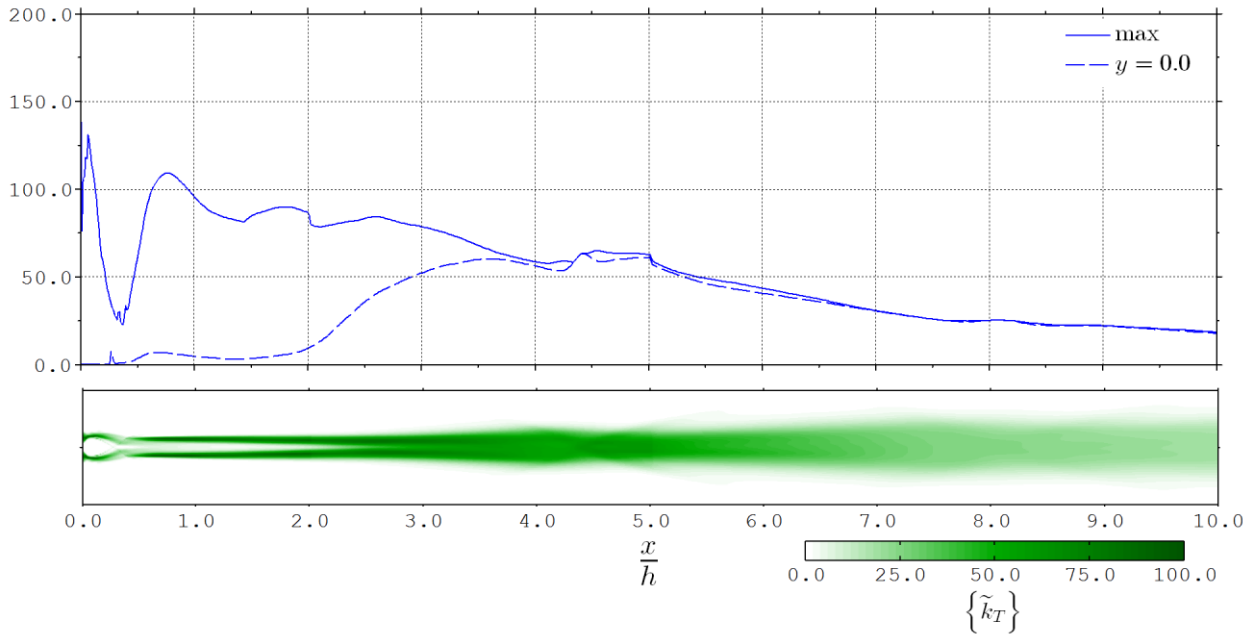

Figure 4.12: Favre averaged turbulence kinetic energy (kJ/kg) trends with stream-wise location and contour.

The initial peak in turbulence kinetic energy just downstream of injection is somewhat deceptive. The entire recirculation region exhibits a degree of large scale unsteadiness which cannot be readily classified as turbulent motion. Following this peak, the observed sharp decrease in turbulence kinetic energy is less likely the result of turbulent dissipation but rather moving beyond the closure of the recirculation regions that contain the fluctuations. The maximum Favre averaged turbulence kinetic energy achieved within the initial mixing layer is 105 kJ/kg at approximately 0.8 duct heights downstream from injection. The cross-stream maximum turbulence kinetic energy levels slowly decrease to a value of 60 kJ/kg $x = 4.2h$. At this point the reflected recompression shock interaction occurs with a modest 10% increase in the turbulence energy.

A dramatic increase in the levels of turbulence kinetic energy along the plane of symmetry, Figure 4.12, coincides with the visible change in turbulent behaviour of the wake. This suggests that the onset of wake roll-up appears intrinsically related to the initial interactions between the two turbulent mixing layers. Investigating the contribution of the three normal Reynolds stresses to the turbulence kinetic energy provides further insight into interaction between the initial mixing layers, where: the stream-wise Reynolds normal stress shown in Figure 4.13., the cross-stream Reynolds

normal stress shown in Figure 4.14, and the span-wise Reynolds normal stress shown in Figure 4.15.

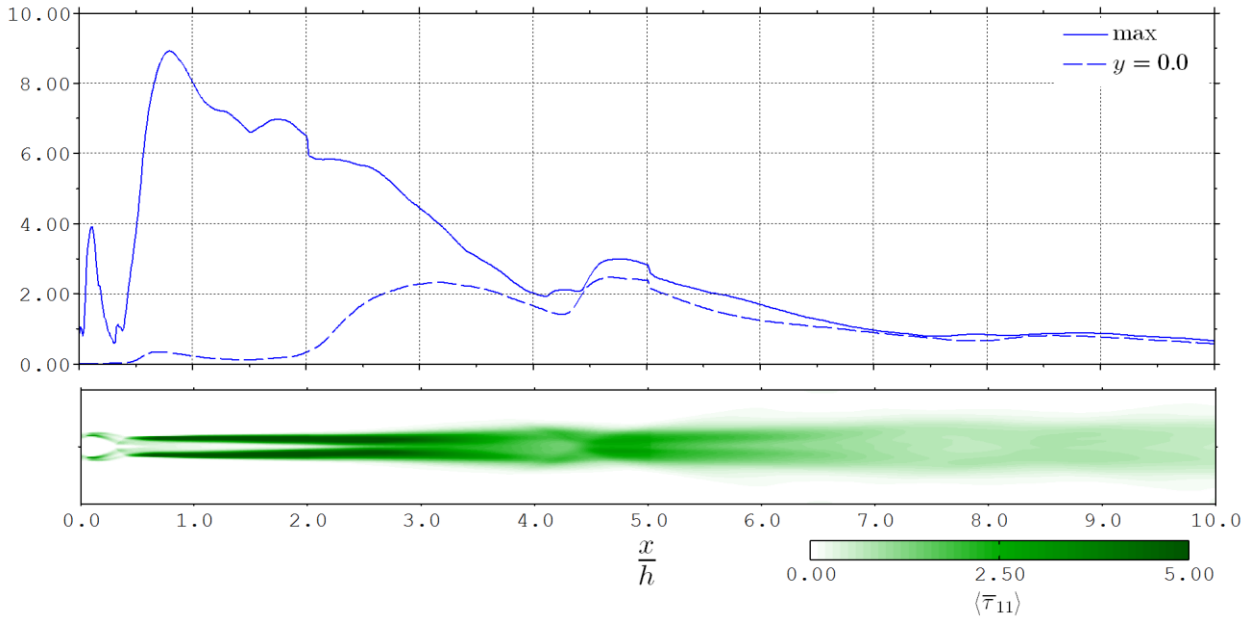

Figure 4.13: Reynolds averaged stream-wise Reynolds normal stress (kPa) trends with stream-wise location and contour.

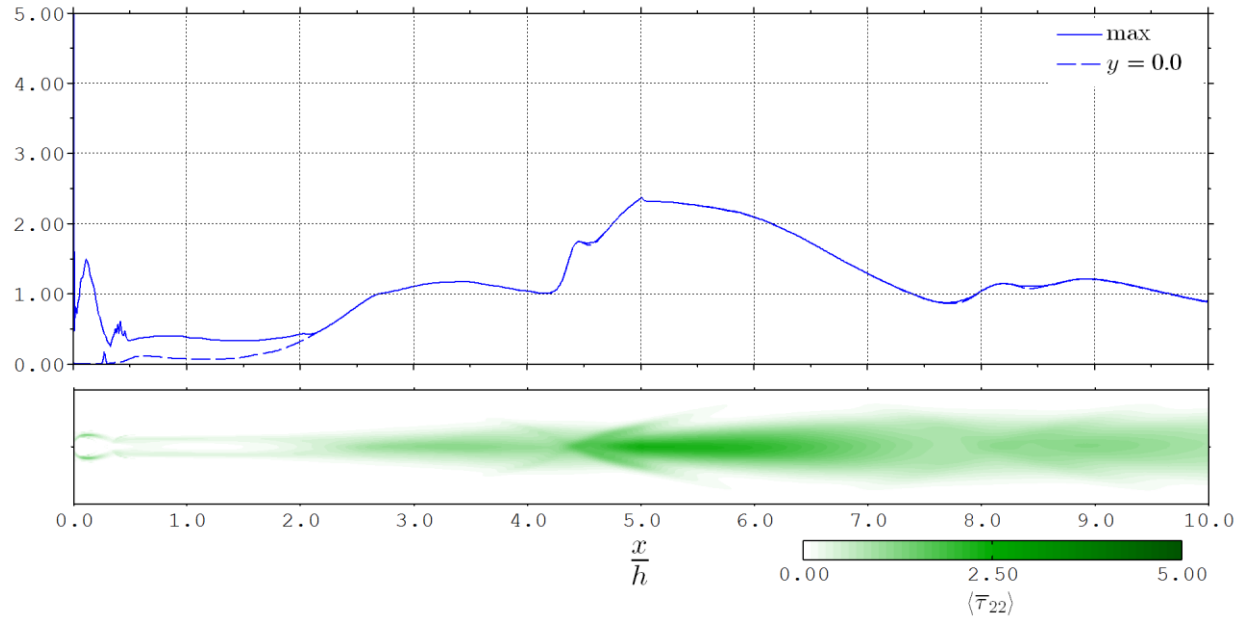

Figure 4.14: Reynolds averaged cross-stream Reynolds normal stress (kPa) trends with stream-wise location and contour.

The peak stream-wise Reynolds normal stress occurs at $x = 0.8h$, which correlates with the peak in turbulence kinetic energy. At its peak, this component of Reynolds stress is almost an order of magnitude greater than the other local normal Reynolds stresses. The cross-stream maximum stress displays a dramatic decrease after this location and parity with the other normal Reynolds stresses is achieved by $x = 4.0h$. The primary shock-turbulence interaction does not stimulate the stream-wise velocity fluctuations greatly.

The cross-stream Reynolds normal stress is initially the least significant normal Reynolds stress. Its stream-wise trend remains effectively constant during the early stage development of the symmetric mixing layers. This invariance ceases when the centre-line stress becomes the peak cross-stream stress at $x = 2.0h$, and the stress increases substantially within half a duct height. This is a key observation. It has been reported that turbulence within a shear layer experiences a reduction in the cross-stream Reynolds normal stress due to compressibility effects (Sarkar, 1995). It has been suggested that this reduction may account for the slow growth rate of highly compressible shear layers. The stresses presented here corroborate this assertion. Referring back to the convective Mach number of the mixing layer, Figure 4.11, the growth of cross-stream Reynolds normal stress appears directly related to falling compressibility. The influence of the reflected recompression shock interaction with the turbulent mixing wake upon this Reynolds stress is most pronounced. The primary shock interaction at $x = 4.3h$ enhances the cross-stream Reynolds normal stress by a factor of ~2.2, and increase which results in this stress becoming the dominant Reynolds stress. By this stage, the convective Mach number has dropped to a near-incompressible value of ~0.5. The cross-stream Reynolds stress reaches a peak value of 2.4 kPa at $x = 5.0h$, after which it follows a reducing trend down-stream until a modest amplification by the second turbulence-shock interaction. It is clear that the primary shock-turbulence interaction simulates the turbulent velocity fluctuations in the cross-stream direction.

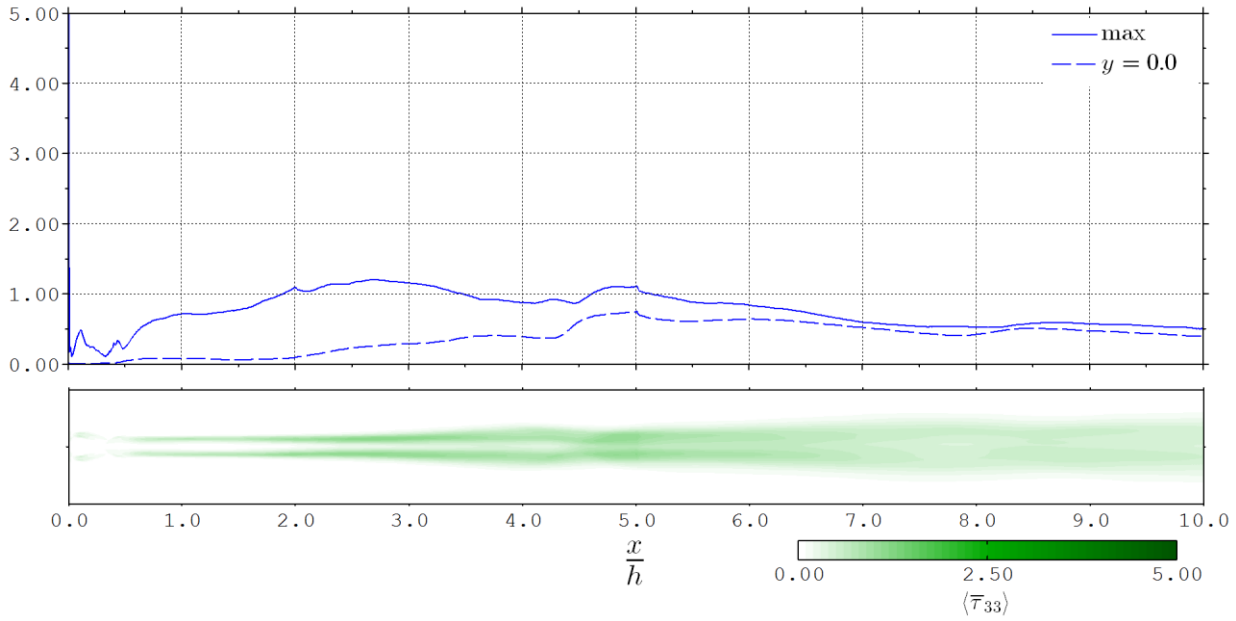

Figure 4.15: Reynolds averaged span-wise Reynolds normal stress (kPa) trends with stream-wise location and contour.

The span-wise Reynolds normal stress is least sensitive to features such as the wake instability or the shock-turbulence interactions. The span-wise turbulent fluctuations are the slowest to be transported into the core of the fuel plume. It is clear that the normal Reynolds stresses are distinctly anisotropic, suggesting that the mixing wake turbulence has not become fully developed within the computational domain. Turbulent momentum transport through the shear layer is observed through the Reynolds shear stress, shown in Figure 4.16. There is a sudden increase in the Reynolds shear stress at $x = 4.5h$ due to the primary shock-turbulence interaction. Turbulent scalar transport through the mixing layer is observed in Figure 4.17. As turbulence transports stream-wise momentum towards the centre of the wake, hydrogen is transported towards the ingested stream. The turbulence transport of hydrogen pre-dominantly occurs slightly further away from centre of the wake in comparison to the cross-stream turbulence momentum transport. The wake roll-up and first shock-turbulence interaction stimulate the cross-stream turbulent transport of hydrogen that is otherwise diminishing with stream-wise distance.

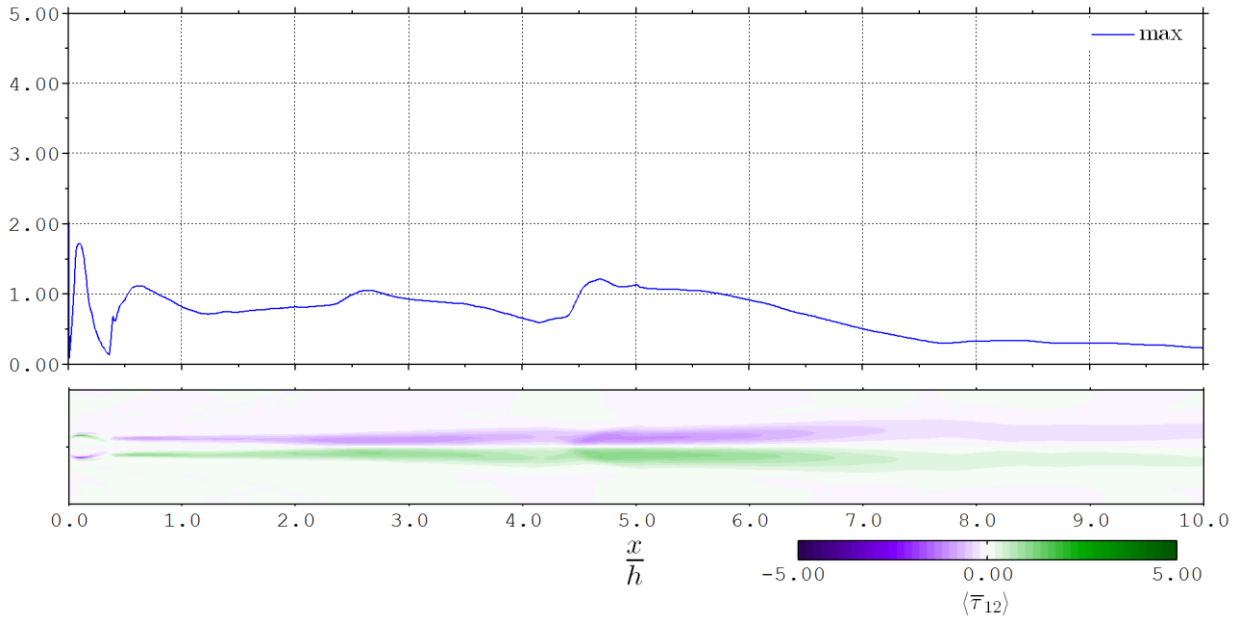

Figure 4.16: Reynolds averaged Reynolds shear stress (kPa) trends with stream-wise location and contour.

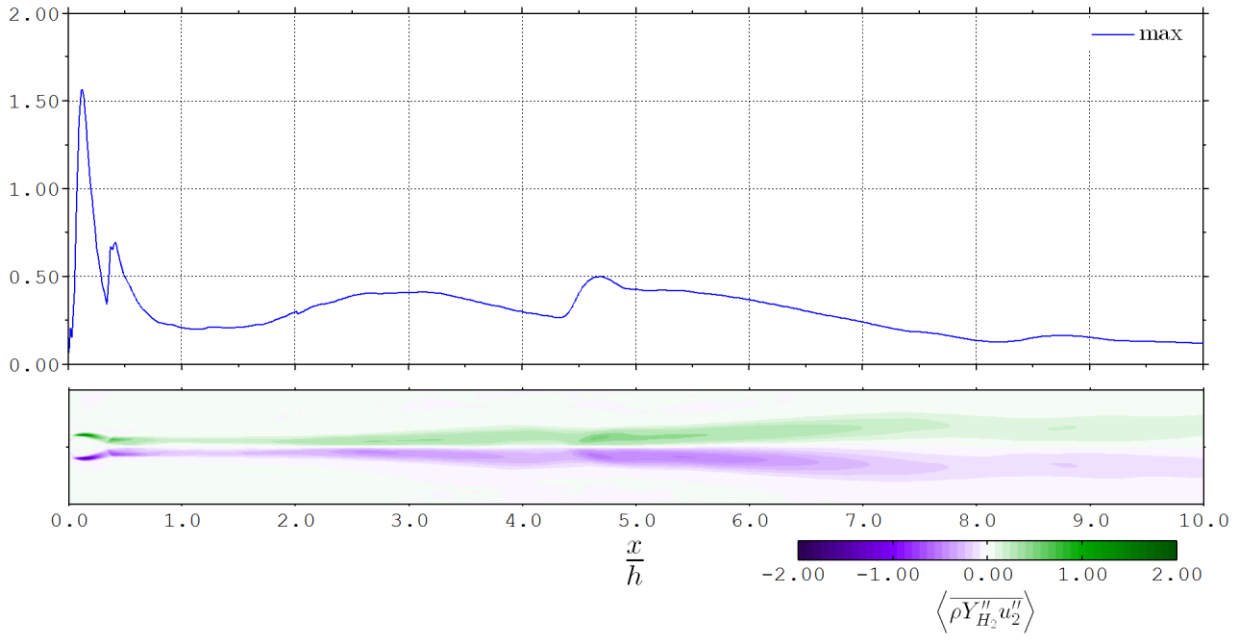

Figure 4.17: Reynolds averaged turbulence cross-stream flux of hydrogen (kg/(m^2.s)) trends with stream-wise location and contour.

4.3.2.1 Turbulence Resolution

An important aspect of LES verification is to ensure that the turbulence kinetic energy is sufficiently resolved. This is dependent on grid quality. It has been proposed that the sub-grid turbulence model must contribute less than 20.0% towards the total turbulence kinetic energy for well resolved LES (Pope, 2004). Consequently, a turbulence resolution metric measuring the ratio of sub-grid scale turbulence kinetic energy to the total turbulence kinetic energy has been defined as:

$$\theta_{k_T} = \frac{k_T^{sgs}}{k_T^{sgs} + k_T^{res}} \tag{4.26}$$

The resolution metric indicates completely resolved turbulence with a value of 0, and fully modelled turbulence (equivalent to RANS) with a value of 1. Ensuring the turbulence resolution metric remains below 0.2 instantaneously and locally within the computational domain is a taxing constraint. It appears that such a constraint would effectively require a DNS appropriate grid refinement. However, achieving an average turbulence resolution metric, shown in Figure 4.18, of less than 0.2 was found to be tractable.

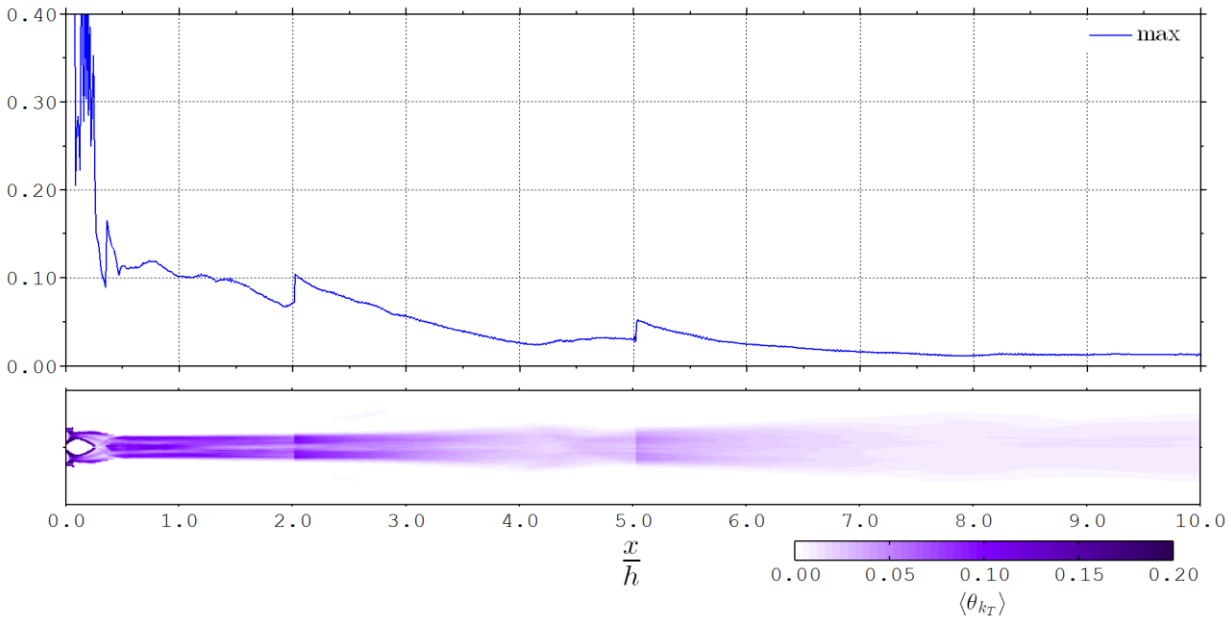

Figure 4.18: Reynolds averaged turbulence resolution metric trend with stream-wise location and contour.

Despite achieving an average turbulence resolution metric less than 0.2 throughout a majority of the domain, there are small yet notable jumps in turbulence kinetic energy at locations were the grid resolution changes at $x = 2.0h$ and $x = 5.0h$ (see Figure 4.12). This indicates that some of the resolved turbulence kinetic energy lost by increasing the grid size is not fully recovered by the sub-grid scale model. A review of the turbulence kinetic energy dissipation allows this anomaly to be investigated further. The turbulence dissipation resolution metric, which measures the ratio of sub-grid scale turbulence kinetic energy dissipation to the total turbulence kinetic energy dissipation, is defined as:

$$\theta_{\varepsilon} = \frac{\varepsilon^{sgs}}{\varepsilon^{sgs} + \varepsilon^{res}} \tag{4.27}$$

Even well resolved LES will predominantly rely on the sub-grid scale contribution of total turbulence energy dissipation, as dissipation occurs at the smallest scales of turbulence. In the current simulation, the resolved turbulence kinetic energy dissipation rate is of an equivalent order to the sub-grid contribution, evident in Figure 4.19, which gives another strong indication that the turbulence is well resolved.

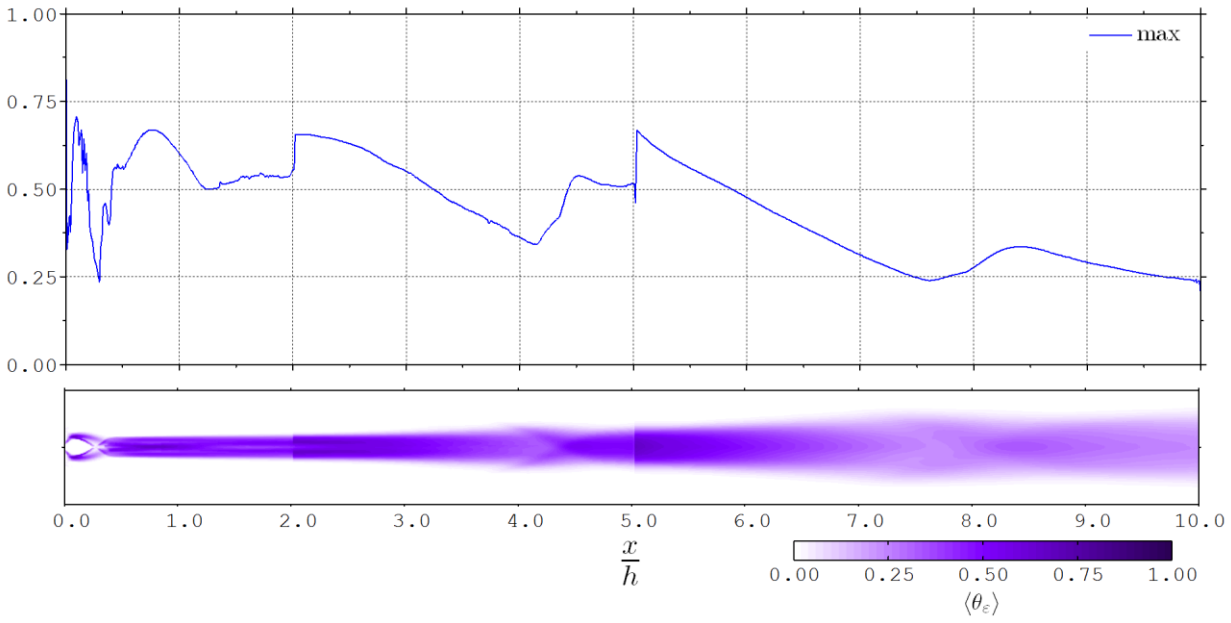

Figure 4.19: Reynolds averaged turbulence dissipation resolution metric trend with stream-wise location and contour.

This can be confirmed by calculating the Kolmogorov length using the total turbulence energy dissipation and comparing it to the sub-grid scale cut-off length, the ratio of which is shown in Figure 4.20. The sub-grid scale cut-off length is found to be no more than ten times larger than the Kolmogorov length for a majority of the domain. Based upon summarised experimental data of developed turbulence (Chapman, 1979; Saddoughi & Veeravalli, 1994), it is estimated that viscous dissipation influences eddies up to 50 times larger than the Kolmogorov length (Dimotakis, 2000). This further strengthens the suggestion that turbulence scales are resolved well into the dissipation range and that the mixing wake turbulence is not yet fully developed, and hence is difficult to model.

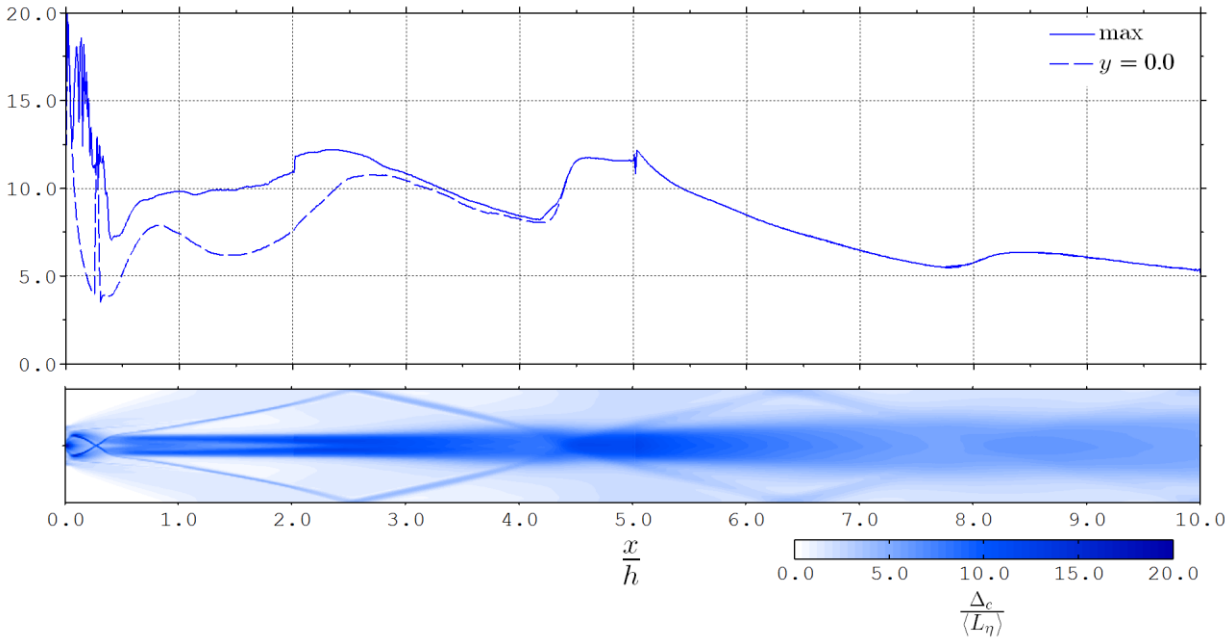

Figure 4.20: Ratio of sub-grid scale cut-off length to Kolmogorov length trend with stream-wise location and contour.

4.3.2.2 Energy Spectra

Turbulence energy spectra can be calculated by performing a Fast Fourier Transform of the temporal evolution of velocity fluctuations. These spectra are then smoothed by performing an average along the homogenous, span-wise direction which is shown in Figure 4.21. As expected, the lack of observable large scale structure in the near-field visualisations correlates with no clear peak in turbulence kinetic energy $(x = 1.06h)$. The turbulence in this region does appears to obey the Kolmogorov constant power law spectrum of -5/3, despite the short distance travelled by the flow. This may simply be coincidence, or that the initial span-wise disturbance rapidly evolves into full developed turbulence. Just down-stream, at $x = 1.91h$, a maximum in turbulence kinetic energy has formed with an associated frequency of 110 kHz. Applying Taylor's hypothesis, the wavelength associated with this frequency is 11.6 mm. This wavelength roughly corresponds to the distortions seen in previous visualisations of the mixing wake (Figure 4.10). Distinct maxima in down-stream turbulence energy spectra prevail at near identical frequencies, including an apparent invariance to influences of the first shock-turbulence interaction. It seems reasonable to conclude that this frequency is related to the fundamental instability of the wake flow. The Strouhal number based upon this instability frequency and the centre-body height of 14.0 mm is 0.467. Applying Taylor's hypothesis again at $x = 8.09h$, where the fuel core has been accelerated by the faster moving ingested streams, results in a wavelength of 26.4 mm. The choice of domain width, 50.0 mm, seems appropriate based upon this calculation. The presence of a developed inertial sub-range, with a Kolmogorov like spectra, begins to form after the onset of wake roll-up although over a small range of frequencies. At $x = 8.09h$, the inertial sub-range exists between 120 kHz and 230 kHz. The decreasing power slope above these frequencies is indicative of turbulence undergoing viscous dissipation. The energy spectra turn-up at the highest frequencies is conducive of aliasing errors. These minor alias errors are well documented (Hill, et al., 2006; Matheou, et al., 2010) and are symptomatic of the stretch vortex model. To clarify, this sub-grid scale model does not perform explicit filtering of the solution.

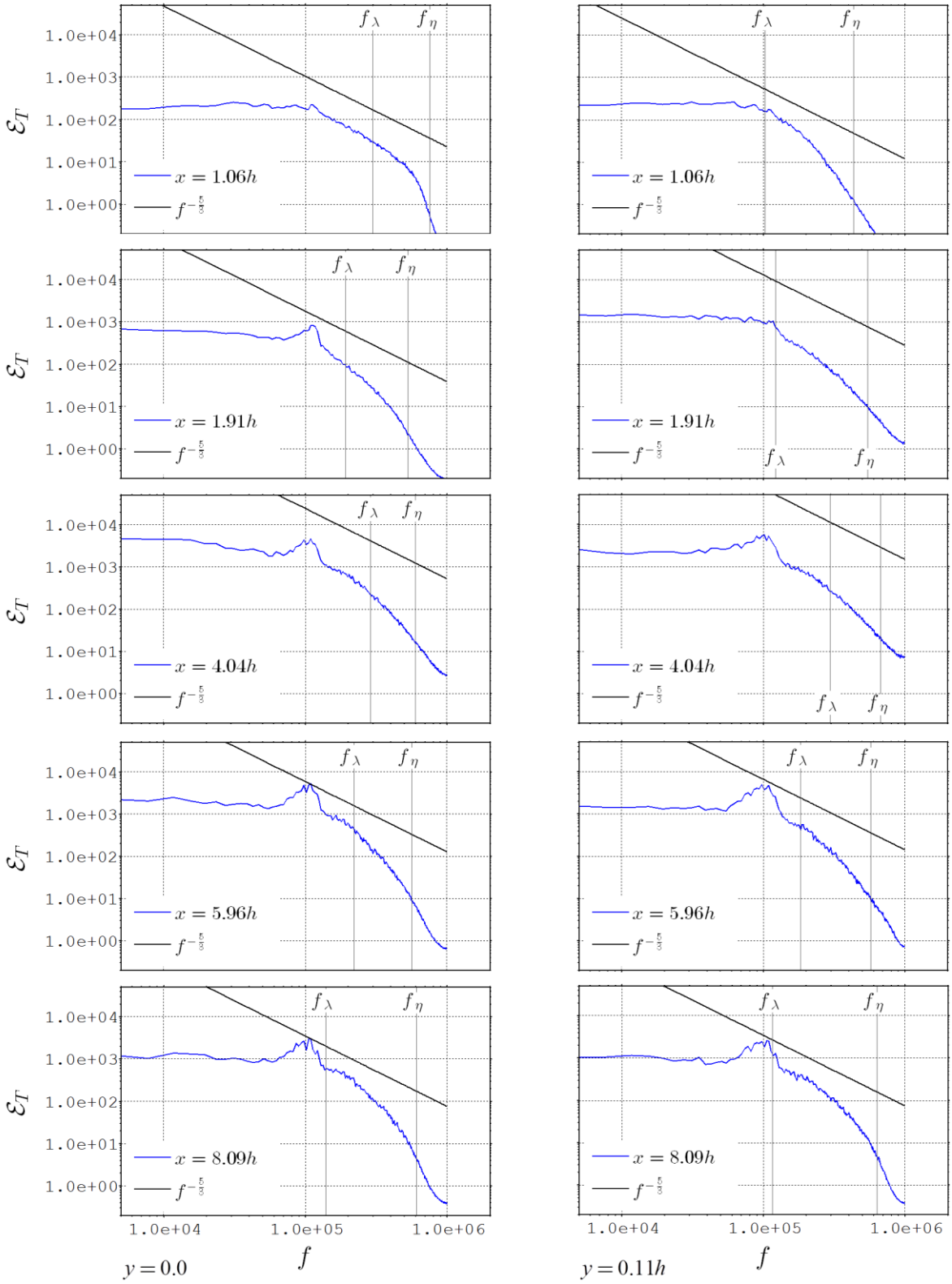

Figure 4.21: Logarithmic turbulence energy spectra trend with frequency (Hz) taken at (left to right): (i) $y = 0.0$, and (ii) $y = 0.11h$

4.3.3 Mixing and Entrainment

The effectiveness of a combustor in mixing reactants dictates many of the performance parameters of a scramjet engine. Effective mixing involves all the reactants being entrained into a region of turbulence such that the diffusion of these chemical species can occur at a much faster rate than would otherwise take place in a laminar flow. The vortical structures generated by turbulent fluid motion act to dramatically increase the interfacial surface between the various regions rich in only one reactant. The mixing dynamics within a given flow field can be elucidated by visualising the mixing interface, where reactants achieve perfect stoichiometry, as shown in Figure 4.22. Previously mentioned flow features can be seen in the stoichiometric mixture iso-surface, such as: the initially symmetric mixing layers, the wake roll-up, and the vortex pile-up. One key difference is that the stoichiometric mixture iso-surface exhibits a greater degree of span-wise coherence in comparison to the second invariant of the velocity gradient tensor. This indicates that the smaller scale vortical structures are forming within the fuel plume, rather than at the fuel-air interface.

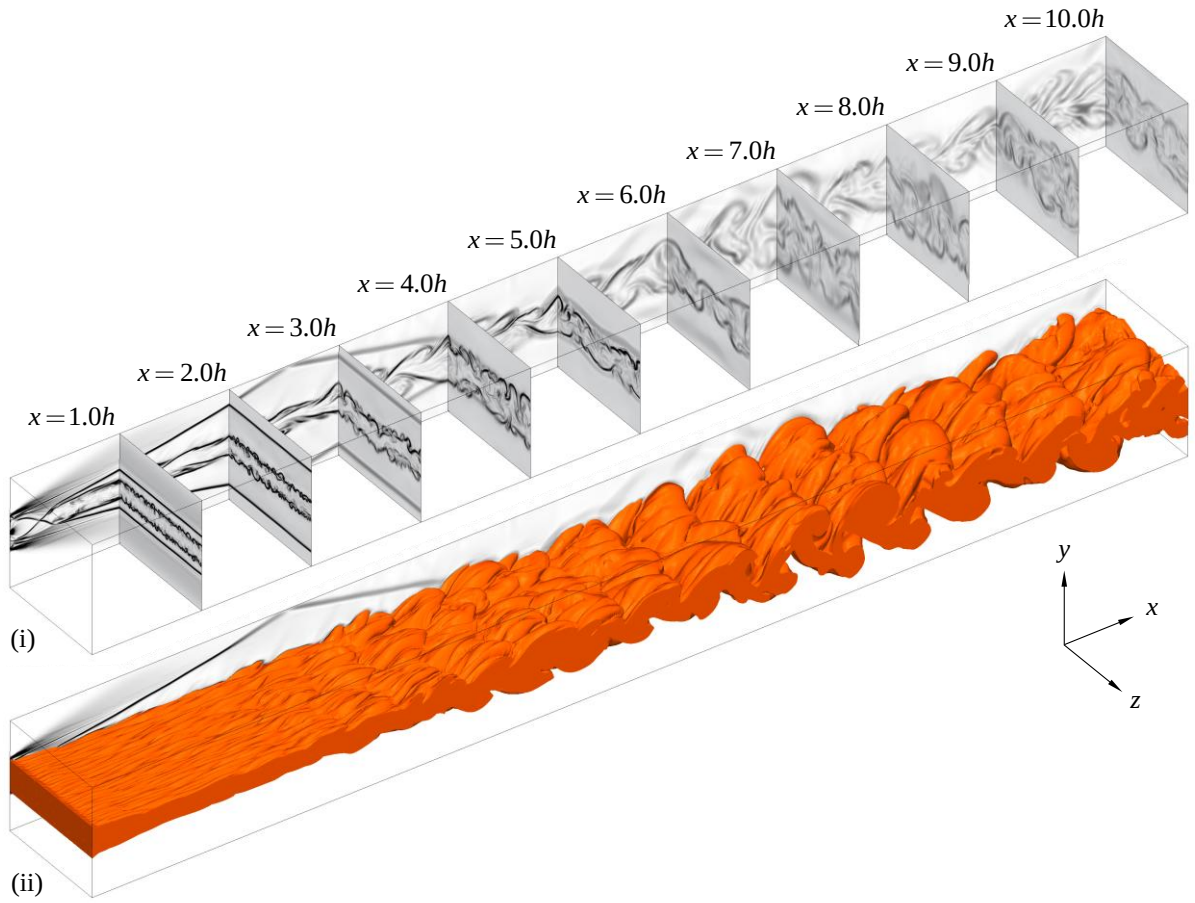

Figure 4.22: Stream-wise normal contours taken at the instant $t = 4.0t_c$ of: (i) static density gradient magnitude, and (ii) stoichiometric mixture iso-surface.

4.3.3.1 Mixing Efficiency

One metric used to determine how well reactants are mixed within the combustor is the mixing efficiency. A convenient scale of mixing efficiency has a value of: i) 0.0 if at least one of the reactants is not present, and ii) 1.0 if all the reactants present would be consumed by completing the chemical reaction. The most common definition of mixing efficiency of a particular reactant species, within a dynamic system, is the ratio of local absolute mass flow rate of the reactant species that would be consumed by completing a chemical reaction to the local mass flow rate of the reactant species.

$$\eta_{R_i}^{mix} = -\frac{\Delta\dot{m}_{R_i}^{\rightarrow}}{\dot{m}_{R_i}} \equiv -\frac{\Delta\dot{n}_{R_i}^{\rightarrow}}{\dot{n}_{R_i}} \tag{4.28}$$

Where R_i represents the i^{th} reactant species and "$\rightarrow$" represents the completion of a chemical reaction. The negative sign takes into account that reactant species are consumed rather than produced by a stoichiometric chemical reaction. The mass flow rates can be calculated by integrating the flux of mass over a cross-sectional area of the fluid flow:

$$\begin{aligned} \dot{m}_{R_i} &= \int d\dot{m}_{R_i} \\ &= \int_A \dot{m}''_{R_i}.dA \\ &= \int_A Y_{R_i}\rho u_j \hat{n}_j.dA \end{aligned} \tag{4.29}$$

Where $\hat{n}_j$ is the *j*-Cartesian component of the unit vector normal to the local surface of integration. The absolute mass flow rate of the reactant species that would be consumed by completing a chemical reaction is calculated using:

$$\begin{aligned} -\Delta\dot{m}_{R_i}^{\rightarrow} &= -\int \Delta d\dot{m}_{R_i}^{\rightarrow} \\ &= \int_A -\Delta\dot{m}''^{\rightarrow}_{R_i}.dA \\ &= \int_A \alpha_{R_i}\rho u_j \hat{n}_j.dA \end{aligned} \tag{4.30}$$

For this work, the reaction of interest is the combustion of hydrogen with oxygen to produce water. The chemical reaction stoichiometry of hydrogen - oxygen combustion is given by:

$$\nu_{H_2}H_2 + \nu_{O_2}O_2 \rightleftharpoons \nu_{H_2O}H_2O \tag{4.31}$$

Where the stoichiometric coefficients are: $\nu_{H_2} = -2$, $\nu_{O_2} = -1$, and $\nu_{H_2O} = 2$. The stoichiometric coefficient of a chemical species is effectively the constant rate of change of moles of that species caused by the progress of a given chemical reaction. It is advantageous to define a parameter which

represents the change of moles of each chemical species as the reaction progresses to completion, given by:

$$\Delta dn_{H_2}^{\rightarrow} = dn_{H_2}^{\rightarrow} - dn_{H_2} \tag{4.32}$$

The change of moles of each chemical species caused by completing the chemical reaction, referred to as the extent of the reaction, is limited by the entire consumption of the most lean reactant. It follows that the extent of the reaction is given by:

$$\begin{aligned} \Delta d\left(n/\nu\right)^{\rightarrow} &= \min\left(\frac{0-dn_{H_2}}{\nu_{H_2}}, \frac{0-dn_{O_2}}{\nu_{O_2}}\right) \\ &= \min\left(-\frac{dn_{H_2}}{\nu_{H_2}}, -\frac{dn_{O_2}}{\nu_{O_2}}\right) \end{aligned} \tag{4.33}$$

In perfect stiochiometry, all the reactants are entirely consumed and the following equality holds:

$$\Delta d\left(n/\nu\right)^{\rightarrow} = -\frac{dn_{H_2}}{\nu_{H_2}} = -\frac{dn_{O_2}}{\nu_{O_2}} \tag{4.34}$$

The resultant change of moles of each chemical species by completing the chemical reaction is determined by scaling the extent of the reaction with the rate of consumption of each respective chemical species, for hydrogen this is given by:

$$\Delta dn_{H_2}^{\rightarrow} = dn_{H_2}^{\rightarrow} - dn_{H_2} = \nu_{H_2} \Delta d\left(n/\nu\right)^{\rightarrow} \tag{4.35}$$

The resultant change of mass of hydrogen by completing the chemical reaction can be computed with the knowledge of the molar mass, given by:

$$\Delta dm_{H_2}^{\rightarrow} = \hat{m}_{H_2} \Delta dn_{H_2}^{\rightarrow} \tag{4.36}$$

The fraction of change of mass of hydrogen by completing the chemical reaction to the local amount of hydrogen mass is given by:

$$\frac{\Delta dm_{H_2}^{\rightarrow}}{dm_{H_2}} = \min\left(1, \frac{\hat{m}_{H_2}\nu_{H_2}}{\hat{m}_{O_2}\nu_{O_2}}\frac{dm_{O_2}}{dm_{H_2}}\right) \tag{4.37}$$

For convenience, the follow parameter is introduced:

$$\alpha_{O_2}^{H_2} = \frac{\hat{m}_{H_2}\nu_{H_2}}{\hat{m}_{O_2}\nu_{O_2}} \tag{4.38}$$

Rewriting the fraction of change of mass of each reactant species by completing the chemical reaction to the amount of respective reactant mass gives:

$$\frac{\Delta dm_{H_2}^{\rightarrow}}{dm_{H_2}} = \min\left(1, \alpha_{O_2}^{H_2}\frac{Y_{O_2}}{Y_{H_2}}\right) \tag{4.39}$$

Finally, it is possible to calculate the α parameter required to compute the absolute mass flow rate of hydrogen that would be consumed by completing the chemical reaction, given below:

$$\alpha_{H_2} = \min\left(Y_{H_2}, \alpha_{O_2}^{H_2}Y_{O_2}\right) \tag{4.40}$$

Hereinafter, the following simplified syntax is used for brevity:

$$\dot{m}''_{mix} = -\Delta\dot{m}''^{\rightarrow}_{H_2}, \quad \eta_{mix} = \eta_{H_2}^{mix}$$

The regions of flow where effective mixing is taking place can be identified from visualisations of the mass flux of mixed hydrogen, which is shown in Figure 4.23 and Figure 4.24. The instantaneous mass flux of well mixed hydrogen reveals how distinct and stratified the initial mixing layers remain until the advent of wake roll-up. Even when span-wise coherent undulations do start to form, a core of poorly mixing hydrogen remains until the shock interaction. The shock interaction immediately promotes mixing within this fuel rich core. Ingested oxygen continues to be entrained once the roll-up process resumes. The breaking up of larger vortical structures into smaller ones is apparent as the flow nears the domain exit, but slightly fuel rich regions still persist. The second shock interaction does not appear to stimulate mixing in the same profound way as the first.

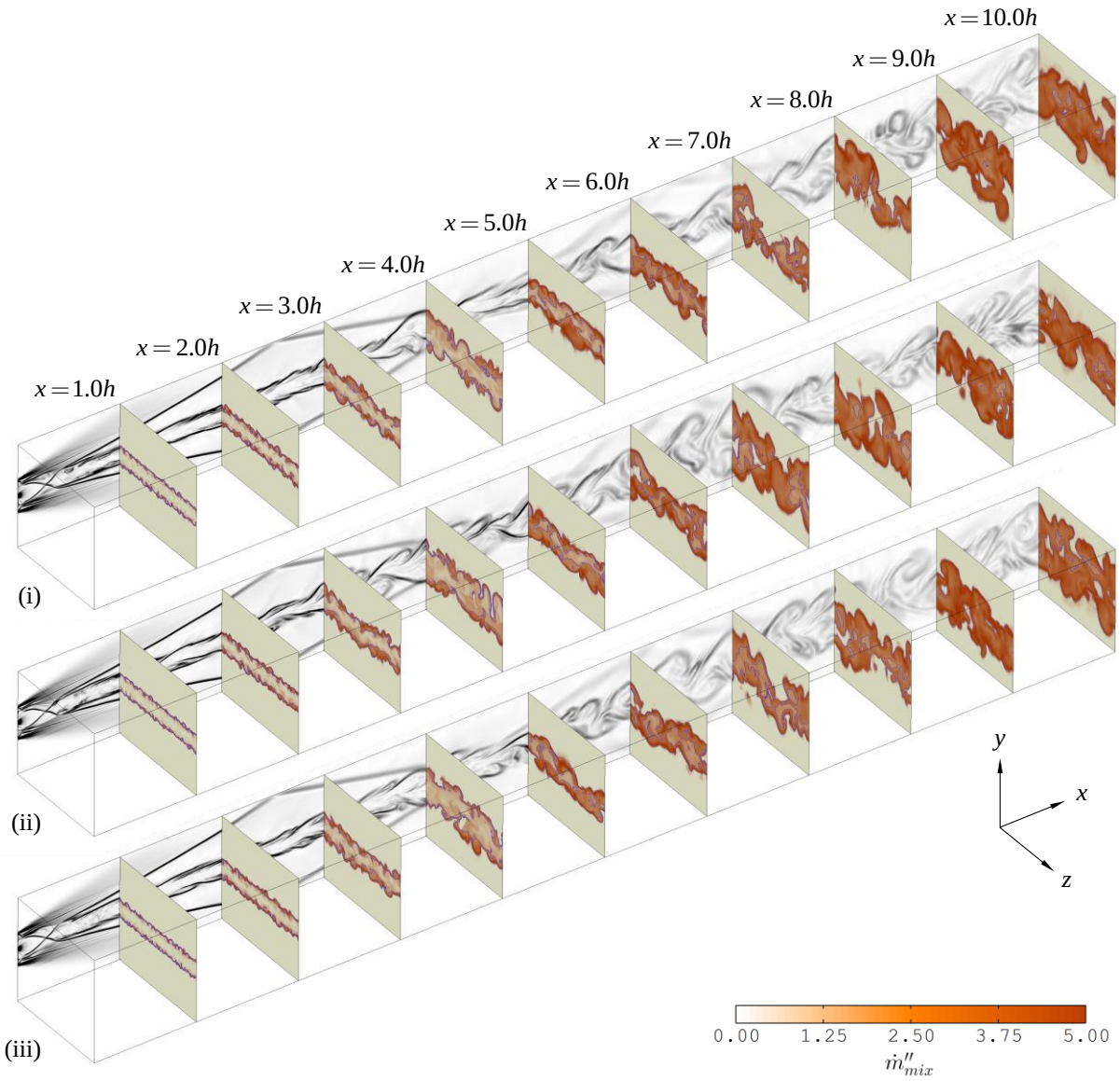

Figure 4.23: Stream-wise normal contours of well mixed hydrogen mass flux (kg/(m^2.s)) taken at the instant: (i) $t = 3.0t_c$, (ii), $t = 4.0t_c$, and (iii) $t = 5.0t_c$.

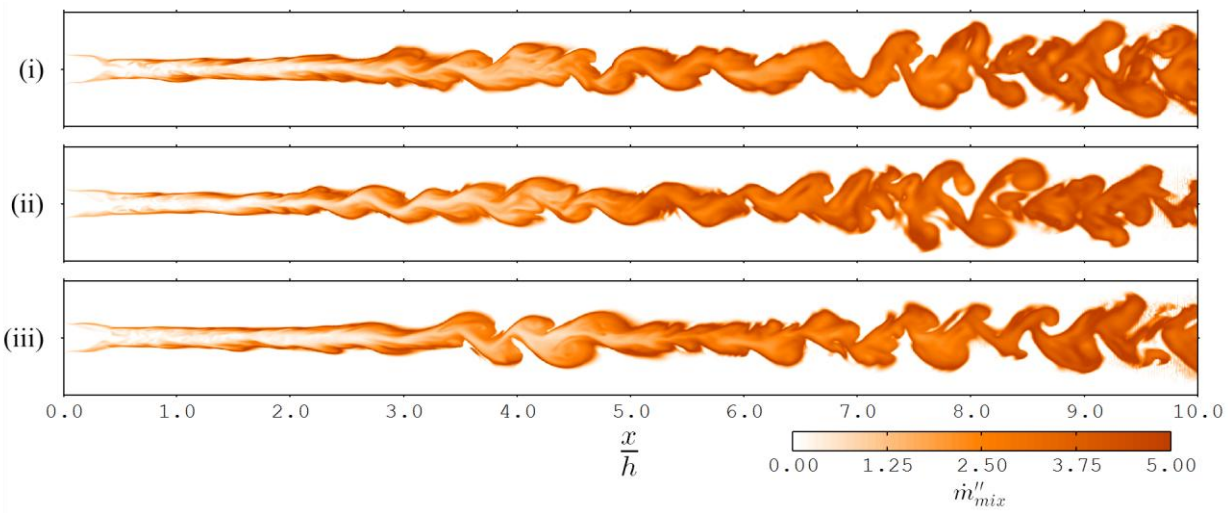

Figure 4.24: Span-wise normal contours of well mixed hydrogen mass flux (kg/(m^2.s)) taken at the instant: (i) $t = 3.0t_c$, (ii), $t = 4.0t_c$, and (iii) $t = 5.0t_c$.

The entrained mass flow rate of ingested oxygen into the mixing wake was calculated by integrating the mass flux of oxygen containing within the area defined by extending the transverse extent of the mixing wake across the span-wise extent of the domain (p109), given by:

$$\begin{aligned} \dot{m}_{O_2}^{ent} &= \int H\left(\frac{\delta}{2} - |y|\right) d\dot{m}_{O_2} \\ &= \int_A H\left(\frac{\delta}{2} - |y|\right) \dot{m}''_{O_2}.dA \\ &= \int_A H\left(\frac{\delta}{2} - |y|\right) Y_{O_2} \rho u_j \hat{n}_j.dA \end{aligned} \qquad 4.41$$

Where $H(\,)$ is the Heaviside function. There is little value in calculating the entrainment of hydrogen into the wake, as all the fuel is initially injected into the plume. The entrainment fraction of oxygen into the mixing wake, again employing a simplified syntax for brevity, is determine using the following:

$$\eta^{ent} = \frac{\dot{m}_{O_2}^{ent}}{\dot{m}_{O_2}} \qquad 4.42$$

The mean mixing and entrainment characteristics also help to describe the performance of the mixing wake, shown in Figure 4.25. Determination of the mixing efficiency and entrainment fraction requires knowledge of the unfiltered mass fractions. Sub-grid scale variations of mass fraction can be estimated using a Dirichlet probability distribution (for multiple chemical species flows) that matches the local mean and variance within each grid cell (Matheou, et al., 2010). This distribution can subsequently be used to determine expected values of arbitrary functions of mass fraction, such as the local mass flux. Considering the sub-grid scale mass fraction variance was found to reduce the mixing efficiency by approximately ~1.0% in comparison to neglecting this variation. Calculation of the Reynolds averaged entrainment fraction and mixing efficiency did not include the effect of sub-grid scale mass fraction variance due to its small contribution and the computational requirements of performing numerical quadrature in each cell over all time samples.

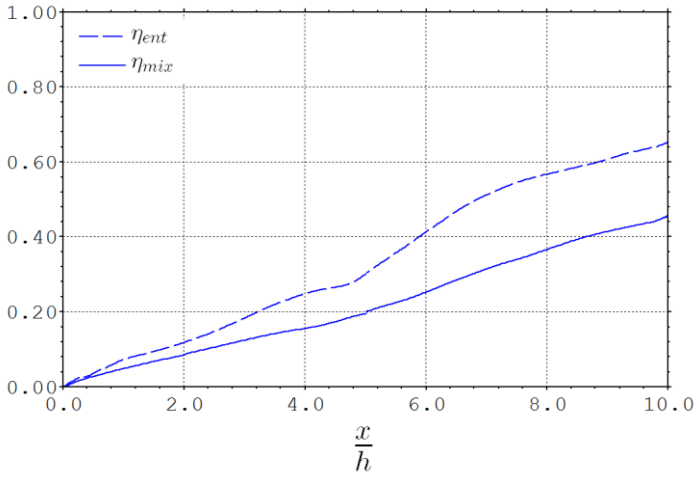

Figure 4.25: Trends of Reynolds averaged entrainment fraction and mixing efficiency with stream-wise location (pure fuel injection only).

The dynamics of the near field entrains approximately 10% of the ingested oxygen into the mixing wake by $x = 1.0h$. The rate of oxygen entrainment then drops as the compressible mixing layers begin to form. This shows that, despite achieving the highest levels of turbulence kinetic energy, the initial mixing layers are ineffective at drawing oxygen into the fuel plume. There is a clear increase in the oxygen entrainment rate where the wake begins to roll-up, at three duct heights downstream from injection. This trend reverses as the transverse extent of the wake experiences contraction due to the shock-turbulence interaction; a local minimum in the mean entrainment rate is observed at

$x \sim 5.0h$. A distinct boost to the entrainment rate occurs just downstream of the first shock-turbulence interaction where the wake roll-up process recommences. The influence of the second shock interaction is modest. The average percentage of ingested oxygen contained within the mixing wake by the end of the computational domain is ~65%.

The initial mean mixing of hydrogen and oxygen is quite low as a consequence of the poor entrainment achieved by the initial mixing layers. Of the oxygen mass that has been entrained into the initial shear layers, approximately 74% is well mixed. More interesting is the apparent invariance of the mixing rate upon the onset of the wake roll-up. Whilst the entrainment rate increases, the percentage of entrained oxygen mass that is well mixed decreases to ~63% by $x \sim 4.0h$. As mixing occurs at much smaller scales than that of the wake roll-up, it seems that the break-down of generated turbulence is not well established. The rate of mixing is enhanced where the reflected shock passes through the mixing wake, which correlates with the Reynolds shear stress trend. The percentage of entrained oxygen mass that is well mixed also increases to ~67% by the shock interaction. Recommencement of the wake roll-up causes this percentage to again decrease, to a overall minimum of 57% at $x = 6.8h$, before the large turbulent eddies begin to break-down and promote mixing. The mixing rate remains effectively constant downstream of this point until the end of the domain, whereby ~46% of the injected fuel is well mixed with oxygen and 64% of the entrained oxygen mass is well mixed with fuel.

4.4 Local Flow Structure

Previous observations of the mixing wake have identified general characteristics of the mixing wake and broad correlations between the mean turbulent statistics, entrainment, and mixing trends. One of the advantages of LES is that these correlations can be explored in greater detail by interrogating the instantaneously resolved flow physics. This section provides a description of the flow physics governing the local behaviour of the mixing wake as it develops.

4.4.1 Near Field Flow Structure

The ingested stream enters the computational domain as a supersonic fluid stream with a subsonic laminar boundary-layer. The expansion fans produced by the corner between the inlet and backward facing walls of the intrusive centre-body, shown in Figure 4.26, quickly accelerate the laminar boundary-layer into the supersonic regime as well as increasing the maximum ingested stream Mach number to ~4.0. The injected stream enters the computational domain as an under-expanded jet travelling at a sonic speed. Expansion fans generated by the corner between the convergent injector geometry and the backward facing wall of the intrusive strut accelerate the injected stream to a maximum Mach number of ~4.5.

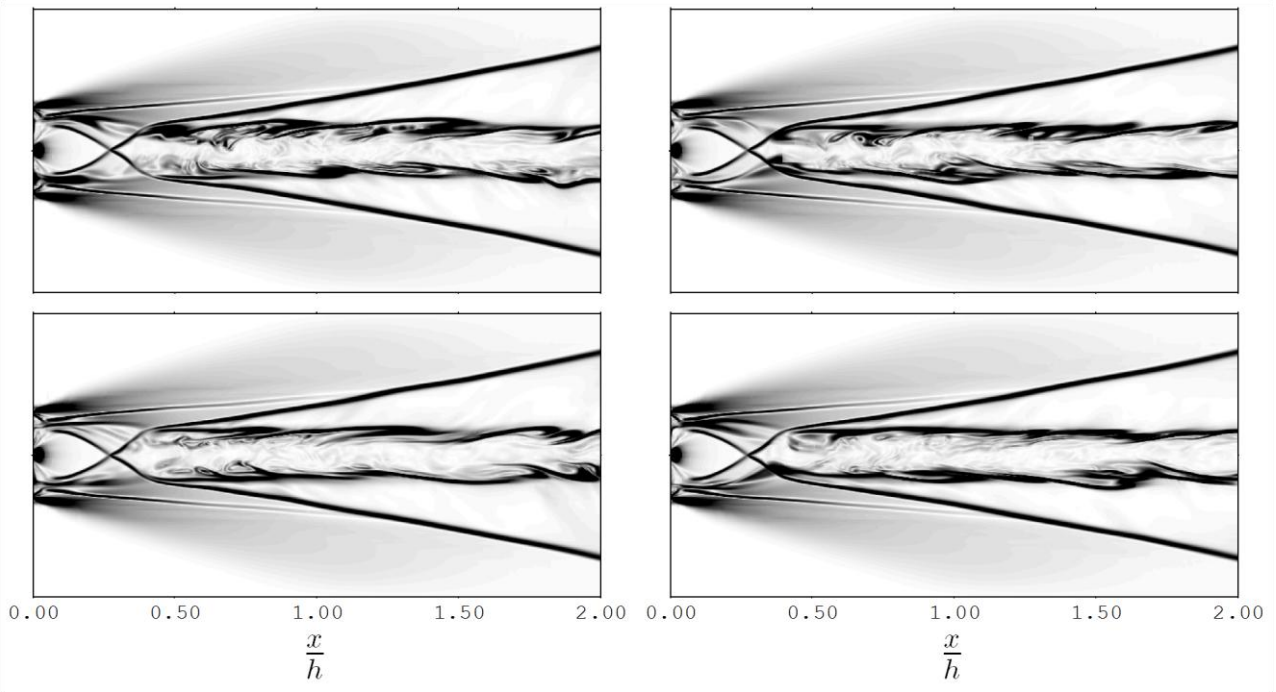

Figure 4.26: Span-wise normal contours of static density gradient magnitude within the near field taken at the instant (clockwise from top left): i) $t = 2.0t_c$, ii), $t = 3.0t_c$, iii) $t = 5.0t_c$, and iv) $t = 4.0t_c$.

A recirculation region forms between the expanding ingested stream, injected stream, and the backward facing wall of the centre-body, shown in Figure 4.27. The perturbed detached laminar boundary-layer, and its symmetric partner transition into a mixing layer where the ingested and injected streams meet. Small amounts of down-stream fluid enter the recirculation region by means of a reverse flow which forms between the meeting point of the expanding ingested and injected streams. This reverse flow generates a momentum deficit which imprints a small wake component onto the mixing layer profile. Contraction of the over-expanded injected stream pulls this slower moving fluid towards the slightly faster moving fuel core flow. The subsequent shear accelerates the slower fluid and alleviates the momentum deficit whilst the fuel core experiences mild deceleration. This is evident in the continuing decline of the velocity ratio between $x = 0.3h$ and $x = 1.0h$ (Figure 4.11) as the ingested flow stream-wise velocity remains effectively constant. Small, high frequency disturbances generated by the initial shear of the expanding laminar boundary layer are fed back into the recirculation region due to this reverse flow. Consequently, the recirculation region becomes highly perturbed, which can be seen at $x = 0.01h$ in Figure 4.28, and imprints significant stream-wise perturbations on the edges of the expanding ingested and injected

streams. This feed-back process provides the source of disturbances within the simulated flow and is highly sensitive. It is suspected that slight numerical error generated due to the adaptive mesh refinement was sufficient to produce the initial disturbances of the flow as no perturbations to the in-flow conditions were applied.

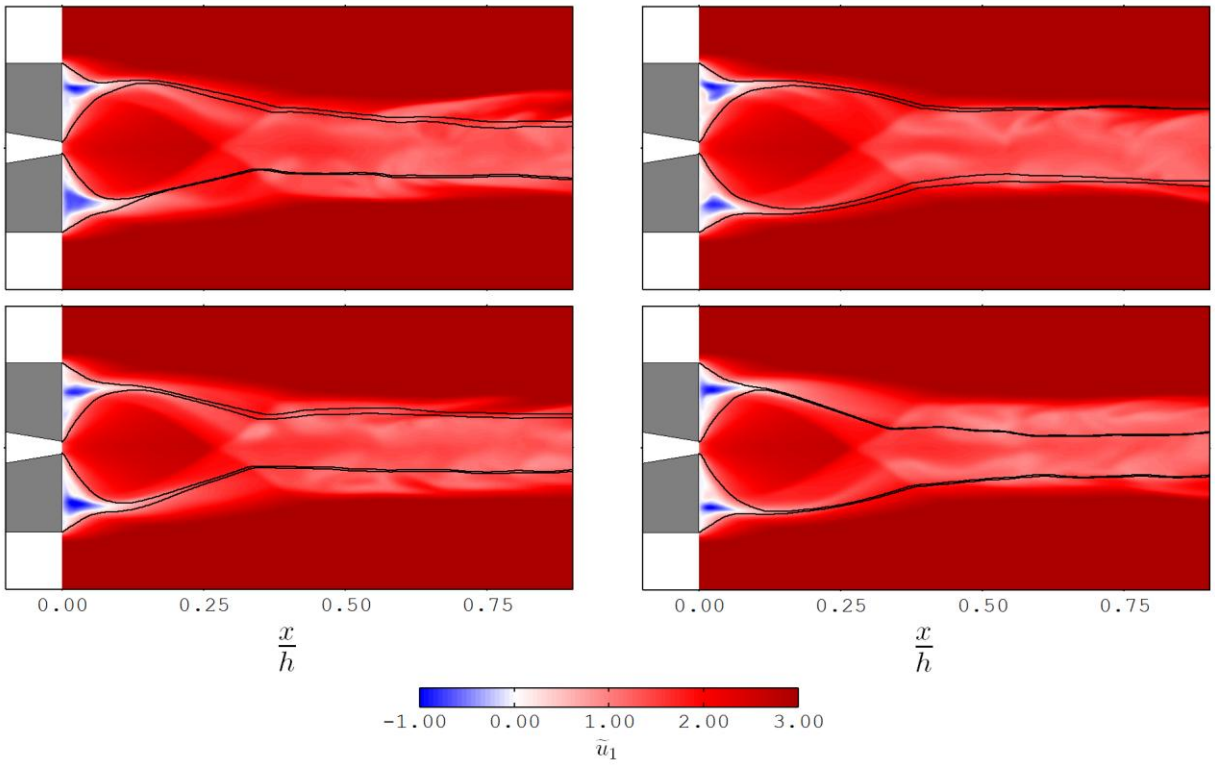

Figure 4.27: Span-wise normal contours of stream-wise velocity (km/s) behind the centre-body, with superimposed streamlines, taken at the instant (clockwise from top left): i) $t = 2.0t_c$, ii), $t = 3.0t_c$, iii) $t = 5.0t_c$, and iv) $t = 4.0t_c$.

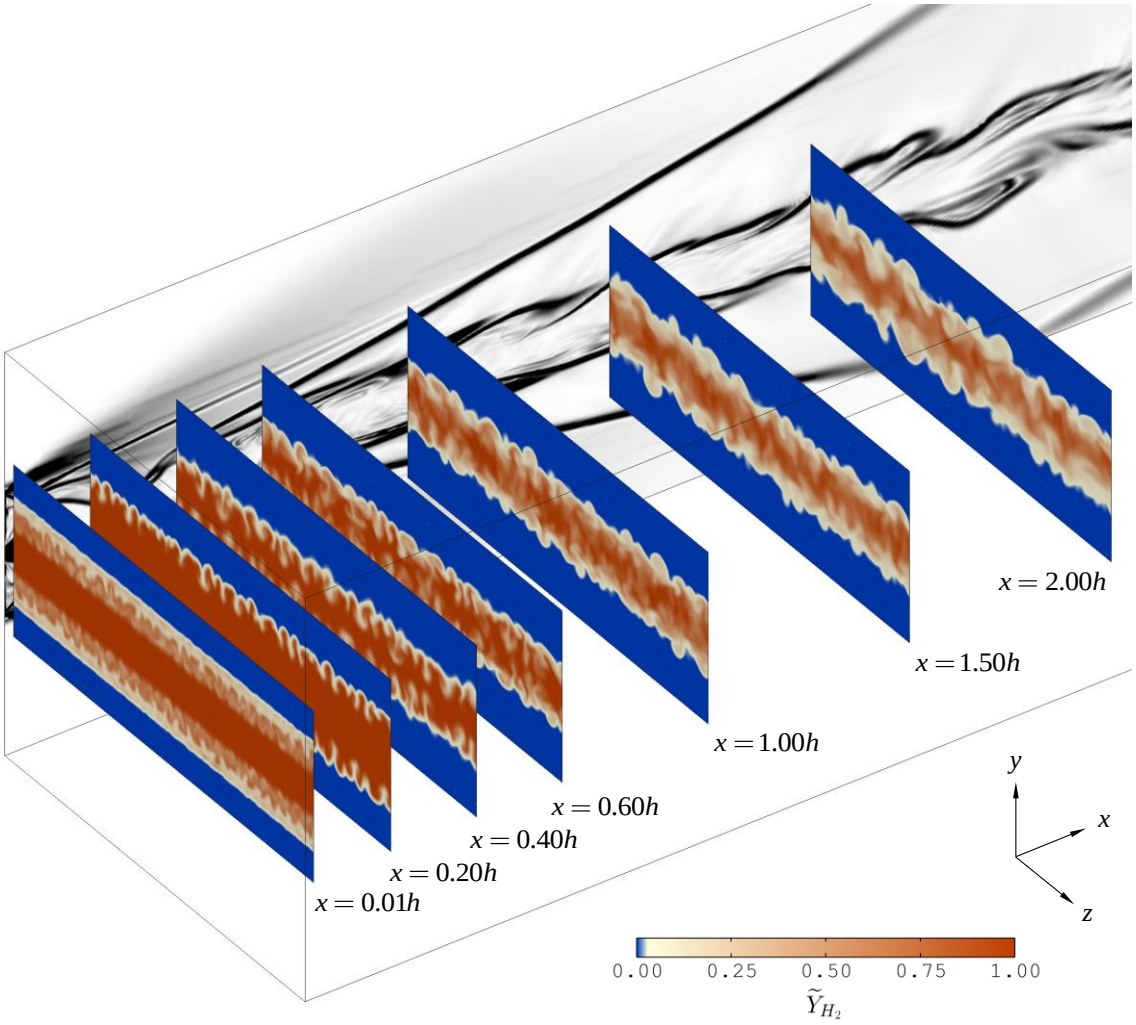

Figure 4.28: Stream-wise normal contours of hydrogen mass fraction within the near field taken at the instant $t = 4.0t_c$.

The span-wise organised corrugation of the mixing interface is dramatically enhanced by the interaction with expansion fans originating from the edges of the injection slot, evident by comparing the first two cross-sections shown in Figure 4.29. This transverse stretching of the large scale structures that define the mixing interface, observed as an increase in the span-wise disturbance amplitude, due to the action of a planar expansion fan is consistent with the experimental study of Smith & Dutton (2001). Given the directions and strength of the density gradient due to this corrugation of the mixing interface, and the pressure gradient induced by the expansion fans, misalignment of the pressure and density gradient causes a generation of vorticity due to the action of baroclinic torque:

$$\frac{1}{\rho^2}\frac{\partial \rho}{\partial x_j}\frac{\partial p}{\partial x_k}\epsilon_{ijk} \qquad 4.43$$

Where ϵ_{ijk} is the Levi-Civita tensor. This process excites the Richtmyer-Meshkov instabilities (Richtmyer, 1960; Meshkov, 1969) within the thin mixing layer. The mushroom shaped corrugation of the mixing interface at $x = 0.20h$, seen in Figure 4.29, is indicative of the such flow instability.

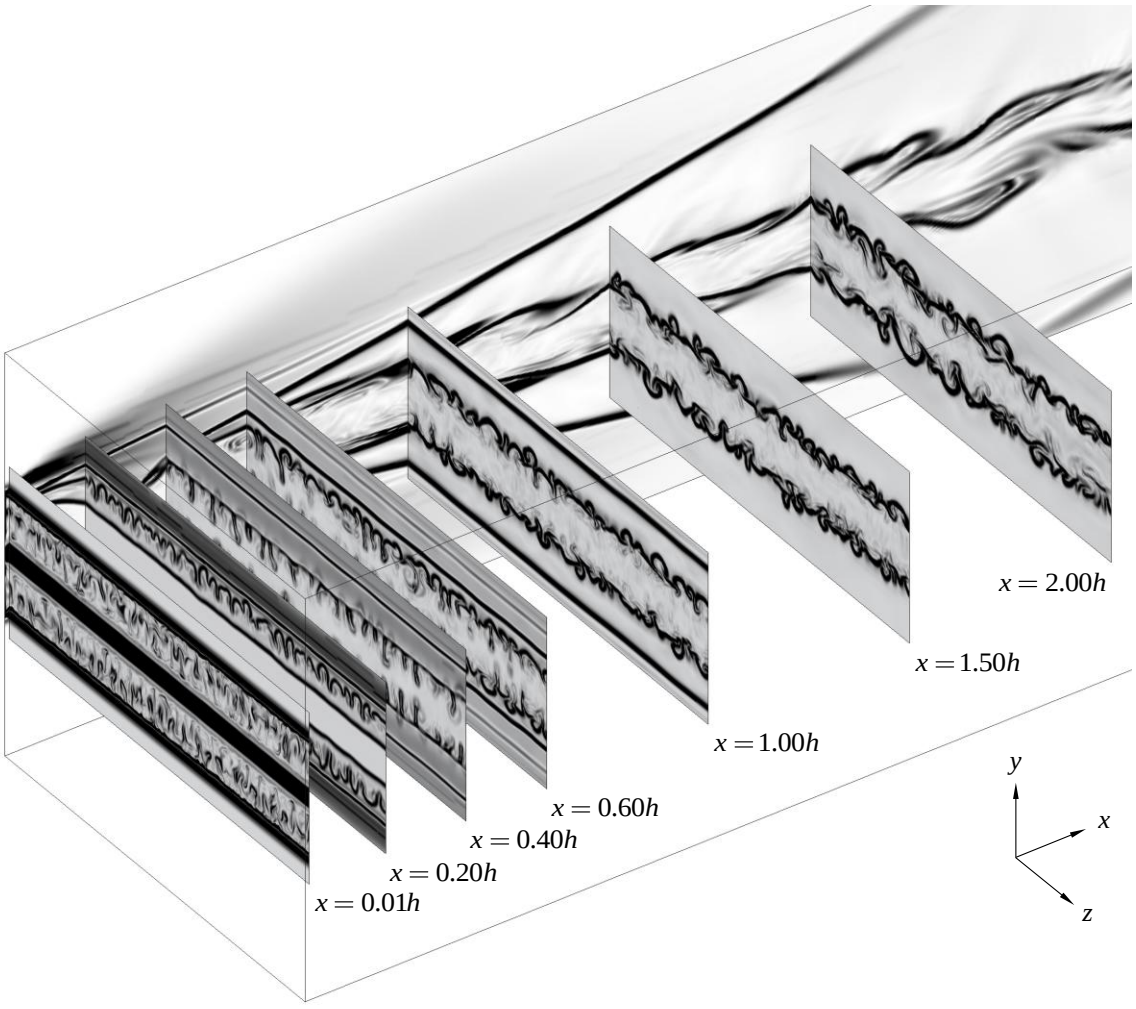

Figure 4.29: Stream-wise normal contours of static density gradient magnitude within the near field taken at the instant $t = 4.0t_c$.

The static pressure of the expanded fuel stream is notably lower than that of the ingested air at their meeting point. As a consequence, two oblique recompression shock waves are produced on either side of the mixing layer formation (for both top and bottom). One of the recompression shock waves is directed away from the plane of symmetry with a relatively weak strength. The other recompression shock wave is substantially stronger and directed towards the plane of symmetry. The strong recompression shock intersects the plane of symmetry at approximately 0.3 duct heights downstream from the point of injection.

The mushroom-shaped intrusions of ingested air into the fuel stream continue to be stretched due to expansion, almost reaching the fuel core. However, the stronger recompression shock wave then interacts with the mixing interface, generating vorticity directionally opposed to vorticity previously induced from expansion, shown in Figure 4.30. This interaction causes a phase inversion of the instability. It appears that this phase inversion presses the dominant mushroom-shaped intrusions of air into thin slivers at $x = 0.40h$. In contrast, the well-established smaller scale fluctuations contained within a thin mixing region are enhanced by the shock interaction. The mushroom-shapes re-emerge after the recompression shock wave has passed through the interface, at $x = 0.60h$. Both mixing layers are re-aligned parallel by the shock interaction.

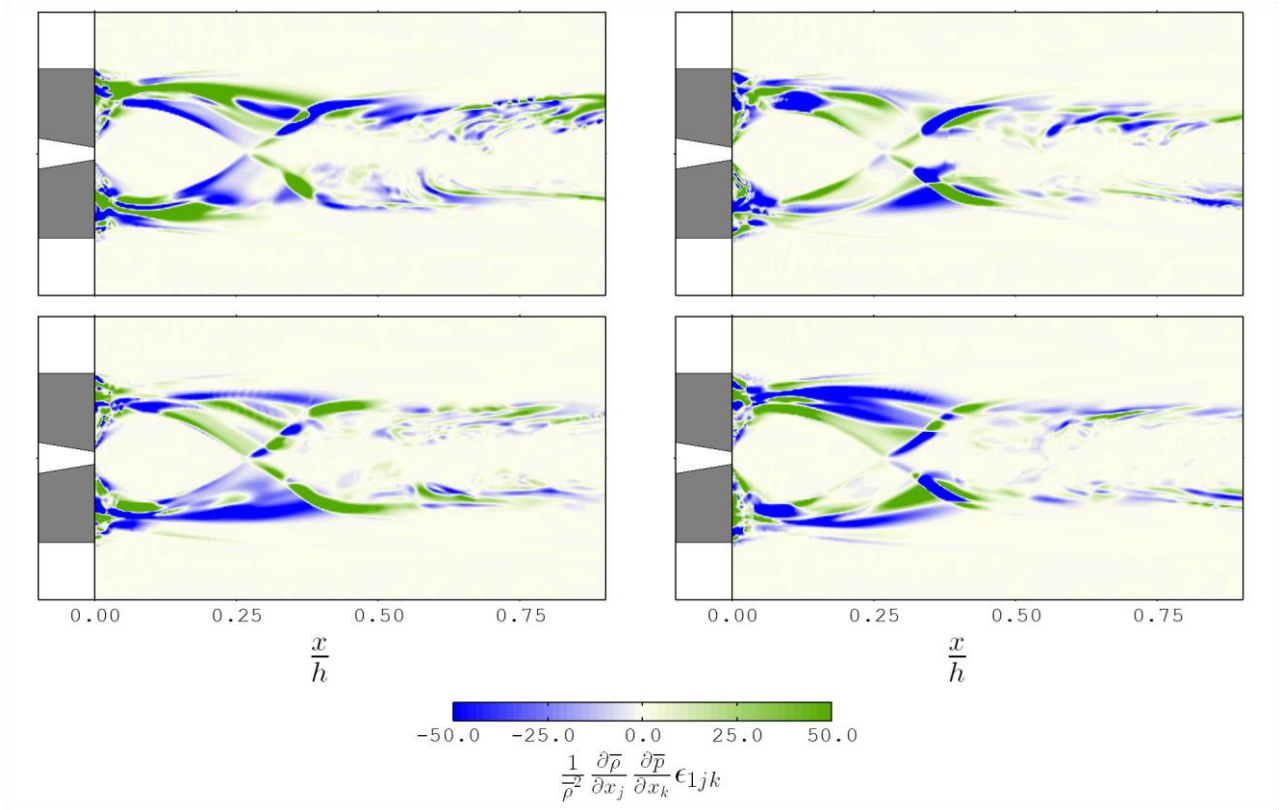

Figure 4.30: Span-wise normal contours of stream-wise baroclinic torque (GHz/s) behind the centre-body taken at the instant (clockwise from top left): i) $t = 2.0t_c$, ii), $t = 3.0t_c$, iii) $t = 5.0t_c$, and iv) $t = 4.0t_c$.

Vortex tubes with near stream-wise alignment can be observed in the second invariant of the velocity tensor, Figure 4.10. These vortex tubes are tightly spaced across the mixing-layer forming a distinct vortex sheet. Interactions between neighbouring vortex tubes cause topological irregularities in the vortex sheet; however, excursions into the high-speed stream of ingested air do not appear. These vortex tubes are most likely an evolution of the inherent instability of local shearing, influenced by the previous Richtmyer-Meshkov instability. This is consistent with the work of Sandham and Reynolds (1990; 1991), who showed by using linear theory and direct numerical simulation, that the dominant instability of a mixing layer shifts from a span-wise to a stream-wise orientation with increasing compressibility. They used linear stability theory to investigate the amplification rate ω_i of waves that propagated at various angles $\theta = \text{atan}\ \beta/\alpha$, where α and β are the wave numbers associated with stream-wise and span-wise orientated disturbances, and convective Mach numbers, depicted in Figure 4.31. An angle $\theta = 0°$ is associated

with a span-wise alignment, whereas an angle $\theta = 90°$ represents a stream-wise alignment. According to this correlation and the calculated convective Mach number of the initial mixing layers being ~1.0, the dominant instability is expected to be at an angle 55° towards stream-wise alignment.

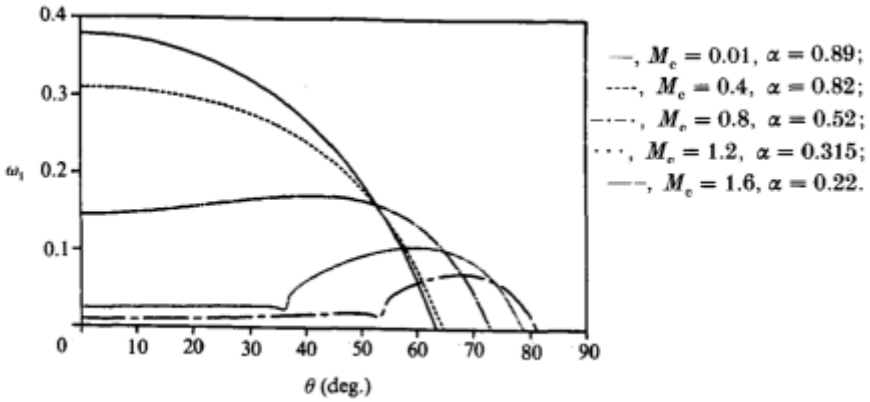

Figure 4.31: Trend in temporal inviscid linear growth rate ω_i with wave angle θ for several convective Mach numbers M_c (Sandham & Reynolds, 1991).

Another key feature of compressible mixing layers is the formation of eddy shocklets (Lee, et al., 1991). These shocklets form where localised turbulent fluctuations decelerate the fluid motion from supersonic to subsonic. In such an event, the flow experiences a high level of compression, or negative velocity divergence. Instantaneous visualisation of velocity divergence focused on the initial mixing layer, shown in Figure 4.32, clearly shows weak shocks originating from the mixing interface and travelling into the ingested stream. The observed shocklets consistently originate from the edge of the mixing wake being directed away from the symmetry plane. The strength of these shockets is quite varied, but tends to weaken whilst travelling downstream. These eddy shocklets enhance pressure fluctuations which produce non-trivial pressure dilatational effects that influence the production of turbulence kinetic energy. Simulations performed by Lee et al. (1991) and Samtaney et al. (2001) observed eddy shocklets where the turbulence Mach number is above ~0.4. The turbulence Mach number for the mixing wake flow, shown in Figure 4.33, sits just below this threshold with a maximum value of 0.39.

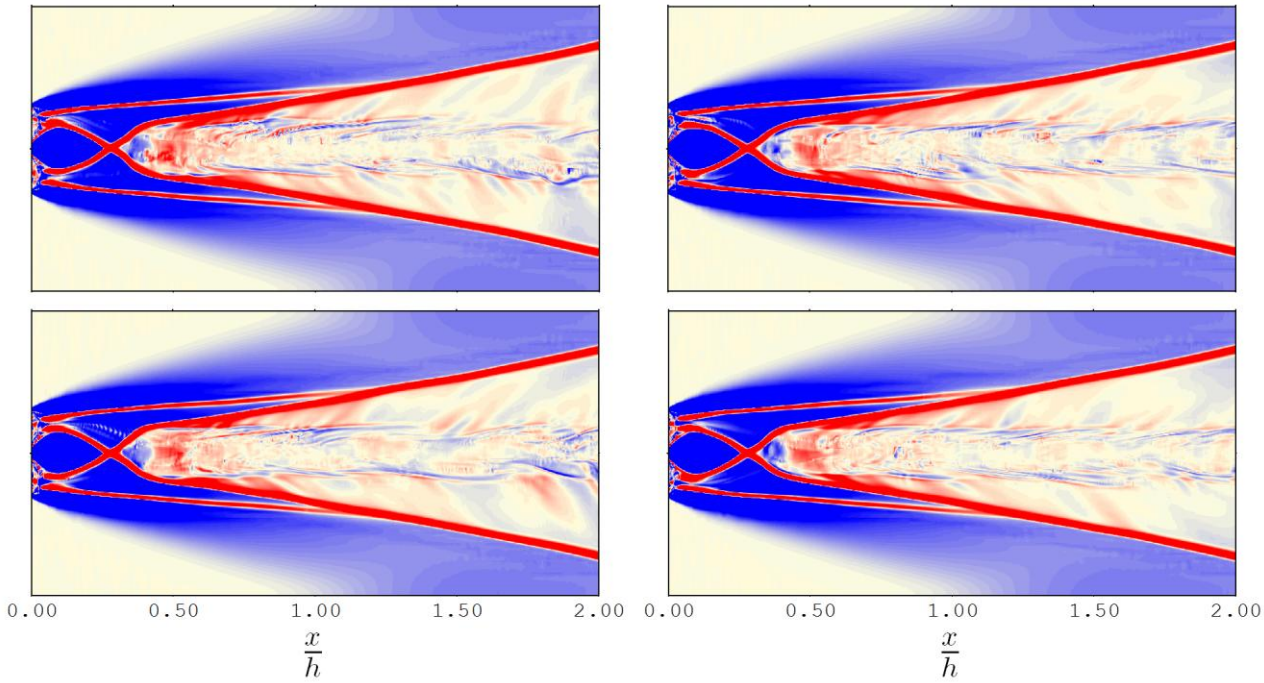

Figure 4.32: Span-wise normal contours of velocity divergence within the near field taken at the instant (clockwise from top left): i) $t = 2.0t_c$, ii), $t = 3.0t_c$, iii) $t = 5.0t_c$, and iii) $t = 4.0t_c$

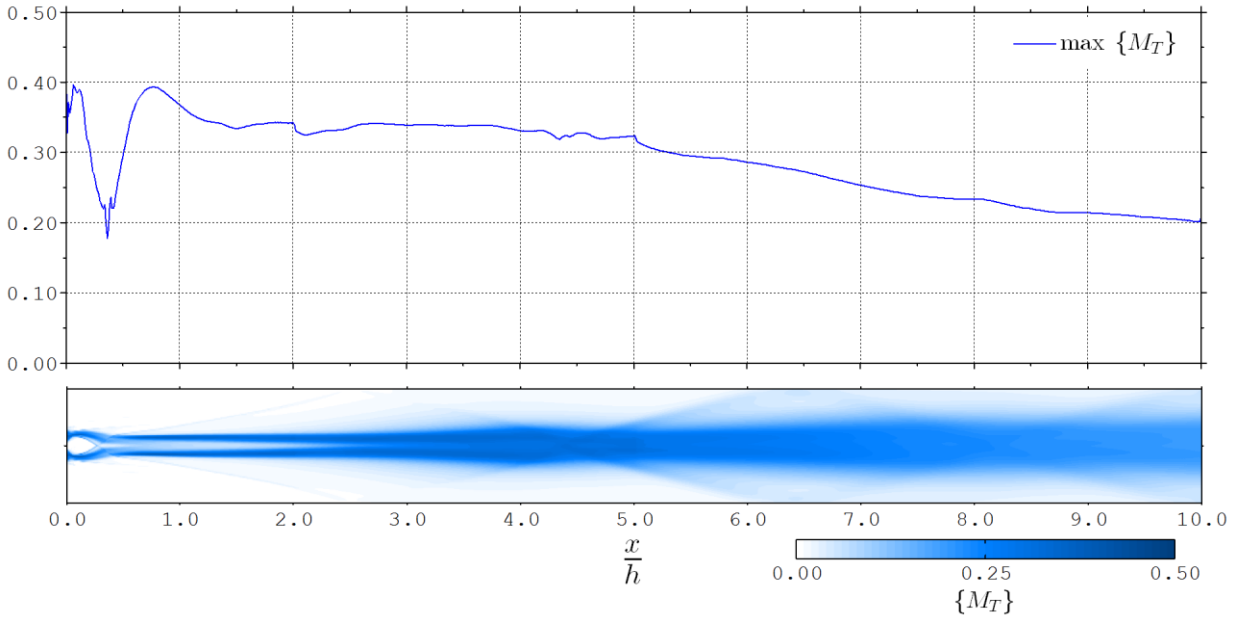

Figure 4.33: Faver-Reynolds averaged turbulence Mach number trend with stream-wise location and contour.

4.4.2 Wake Transition

A distinct change in behaviour of the most dominant vortical structures occurs at approximately 3.0 duct heights downstream from injection. Upstream of this location, the turbulence appears well contained within two thin, symmetrically opposed layers. Downstream of this location, larger vortices being to form and protrude into the ingested stream coupled with larger intrusions of ingested air into the fuel plume. These larger vortices exhibit motions similar in behaviour to neighbouring vortices which gives the turbulence an observable span-wise coherence which resembles a von Kármán vortex sheet.

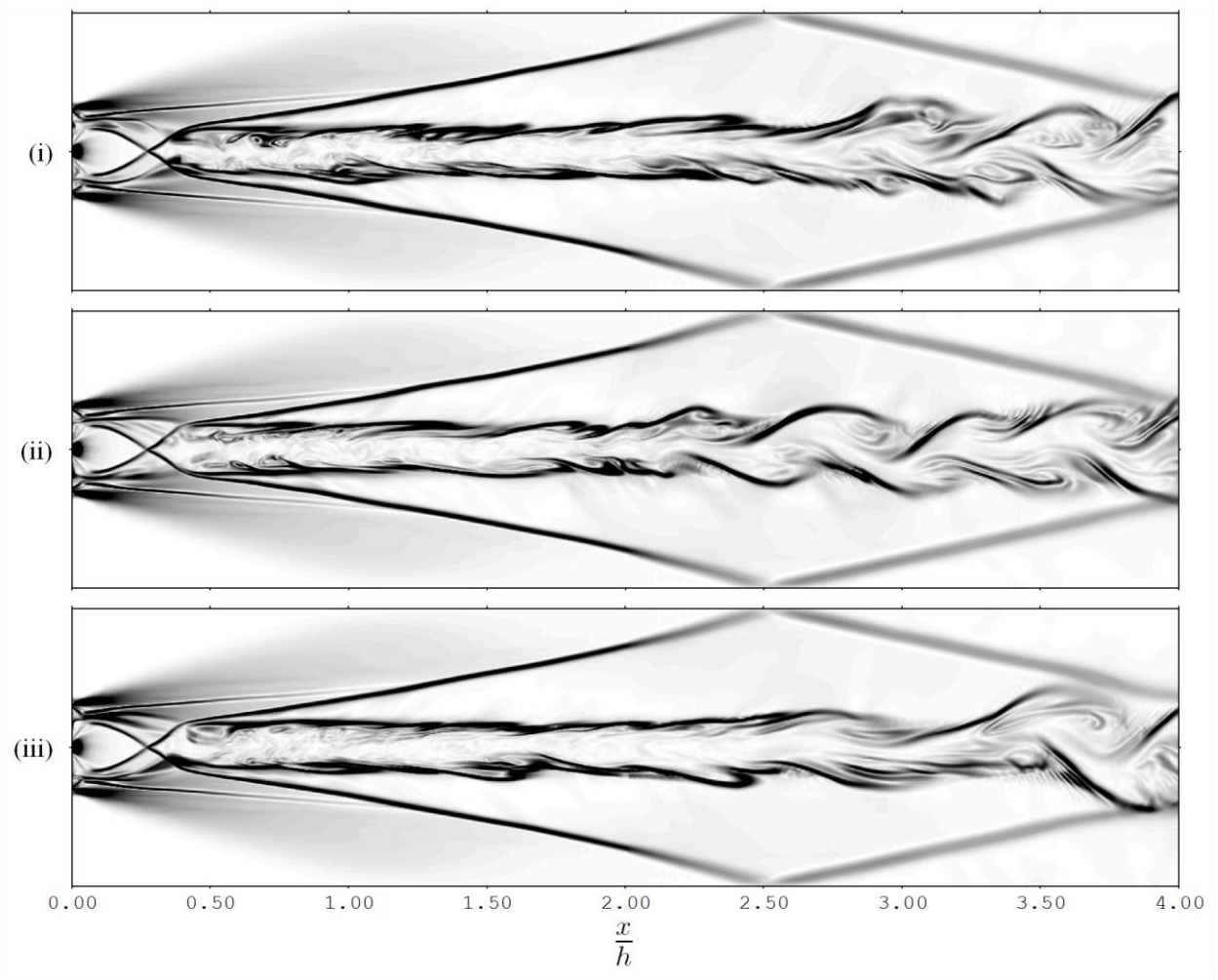

Figure 4.34: Span-wise normal contours of static density gradient magnitude taken at the instant: i) $t = 3.0t_c$, ii), $t = 4.0t_c$, and iii) $t = 5.0t_c$

This wake roll-up is distinctly different to vortex pairing, where two co-planar vortices are drawn together, rotating about a common origin (Hussain, 1986). Incipient cross-stream distortion of the entire fuel plume can be observed in Figure 4.34 as early as $x = 2.0h$. The scale of these distortions are significantly larger in comparison to the now well established stream-wise orientated fluctuations, and rapidly intensify, causing initially wavy patterns to coalesce into distinct, counter rotating vortex cores connected with a thinner braid section. The exact seeding location of this transitional process is intermittent, but guaranteed within 3.0 duct heights downstream from injection. Though coherent, the shape of the vortex cores can be irregular, making the distinction between wavy distortion and vortex-braid structures difficult, further illustrating the transitional nature of this turbulent process.

Before the wake begins to roll-up, a well-defined core of near pure fuel is evident between the two mixing layers exhibiting high frequency span-wise disturbances. As the wake rolls-up, span-wise waves with a lower frequency and greater amplitude than the near-field span-wise waves form to produce a three-dimensional distortion of the mixing interface, shown in Figure 4.35. Roll-up also dissipates fuel away from the injected core flow, evident in Figure 4.36.

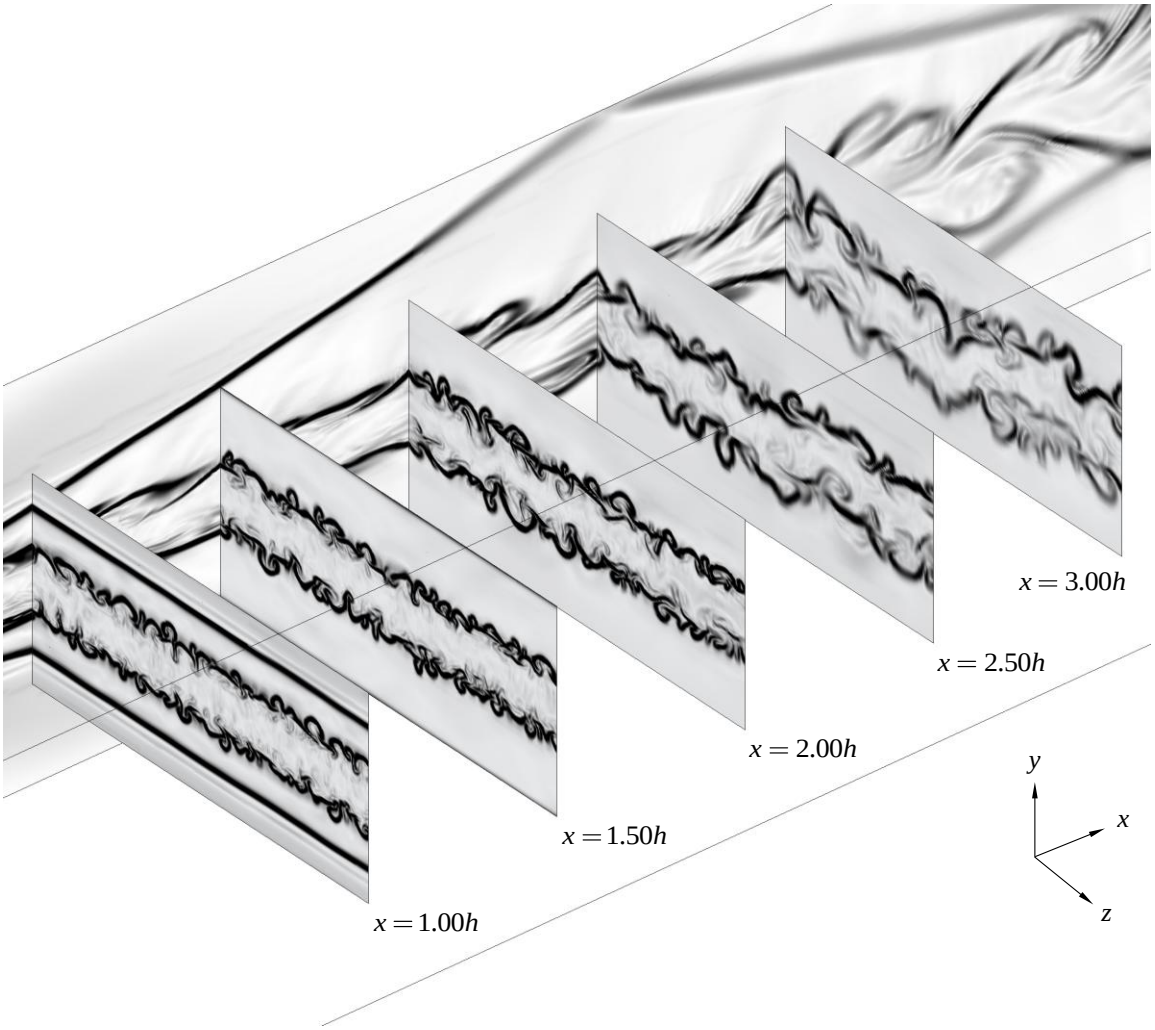

Figure 4.35: Stream-wise normal contours of static density gradient magnitude of the mixing layers at the instant $t = 4.0t_c$

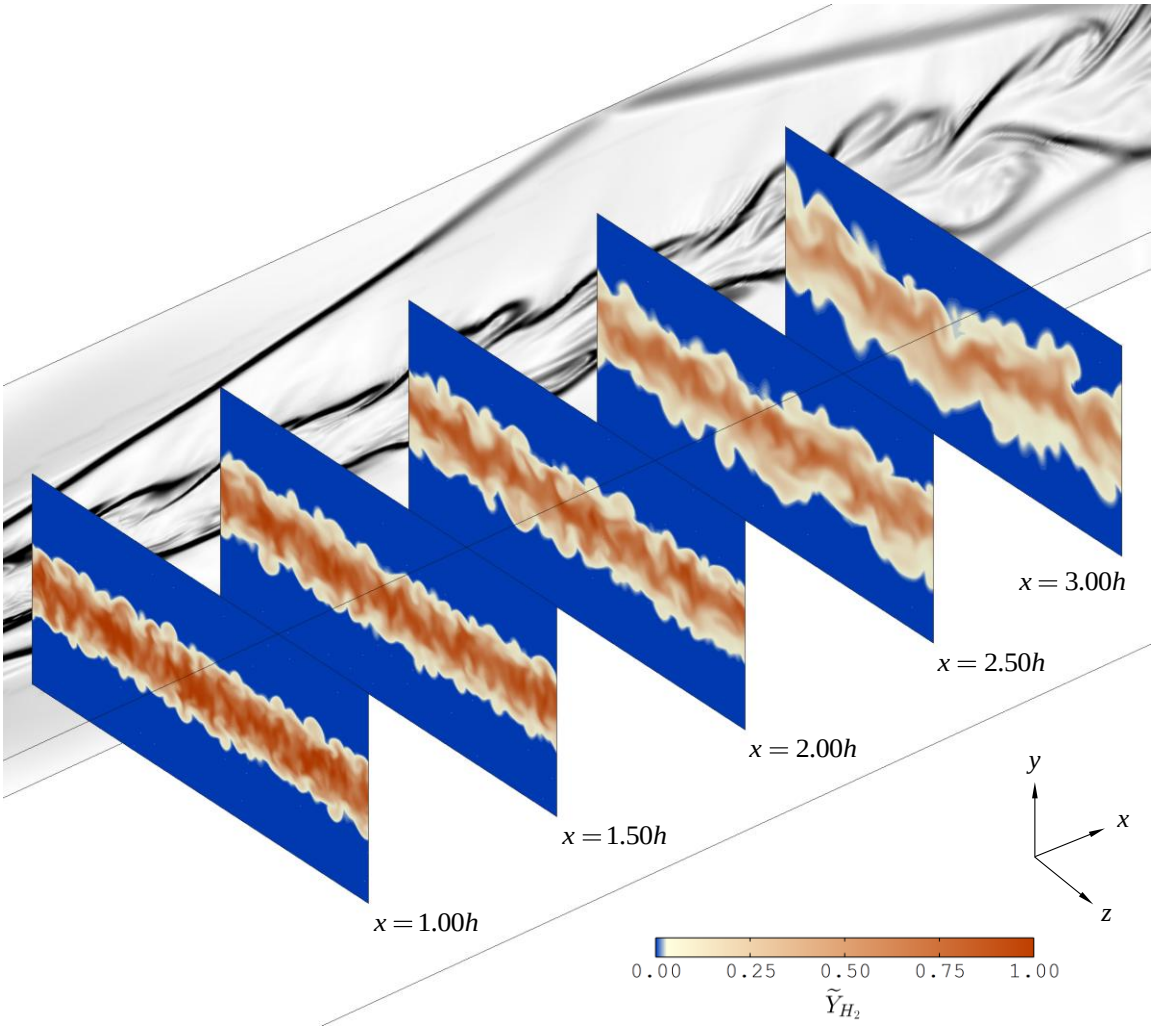

Figure 4.36: Stream-wise normal contours of hydrogen mass fraction of the mixing layers taken at the instant $t = 4.0t_c$

Self-similarity is not demonstrated by the mean velocity and density profiles, shown in Figure 4.37, which gives further evidence that the developing large scale eddies are not yet experiencing full turbulent break-down. The influence of the recirculation regions on the mean velocity profile can be seen at $x = 1.0h$, where slightly slower moving fluid appears just away from the symmetry plane. The mean density profile is described using the Atwood number, which is defined as:

$$A_t = \frac{\langle \overline{\rho} \rangle - \rho_2}{\rho_1 - \rho_2} \qquad 4.44$$

The Atwood number profiles show that density gradients across the mixing layers are further displaced than the velocity gradients, another sign of poor entrainment of oxygen into the fuel core flow.

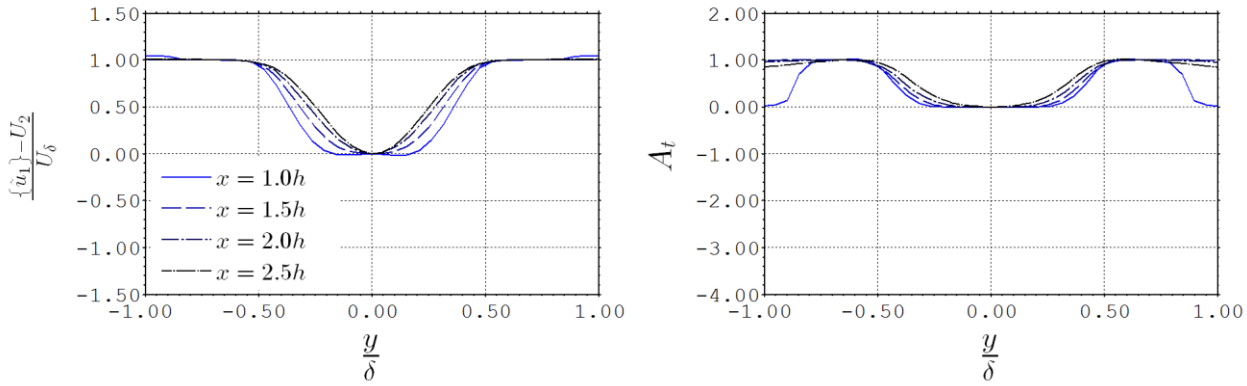

Figure 4.37:Normalised mean stream-wise velocity (left) and Atwood number (right) cross-stream profiles during the wake transition.

That the wake roll-up behaves similarly to a von Kármán instability driven flow indicates this transitional turbulent behaviour is more a feature of the wake rather than the symmetric mixing layers. However, it appears the onset of vortex shedding relies on "communication" between the symmetric mixing layers. This is apparent in the stream-wise normal Reynolds stress profiles, shown in Figure 4.38, normalised by the mean density and shearing velocity difference squared, which is the principal turbulence stress in this region of the flow. The profile taken at $x = 2.0h$ illustrates that there is effectively no mean turbulent stresses along the plane of symmetry. This is no longer the case at $x = 2.5h$ where the stream-wise normal Reynolds stress is non-trivial. The other Reynolds stresses remain small but have begun to develop. This location coincides with the onset of wake roll-up. The transitional nature of this process is also apparent in the mean span-wise vorticity, shown in Figure 4.39. There is a obvious inflection in the span-wise vorticity upstream of the wake roll-up that disappears by $x = 2.0h$.

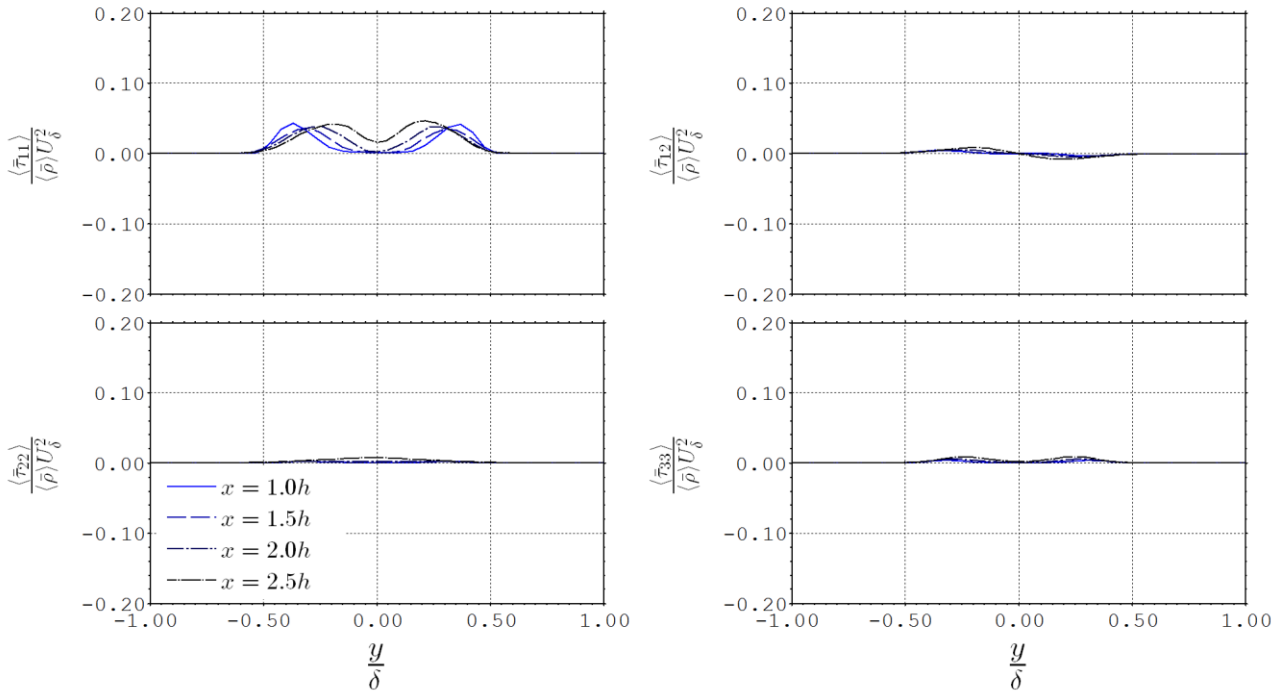

Figure 4.38: Normalised mean Reynolds stresses cross-stream profiles during the wake transition.

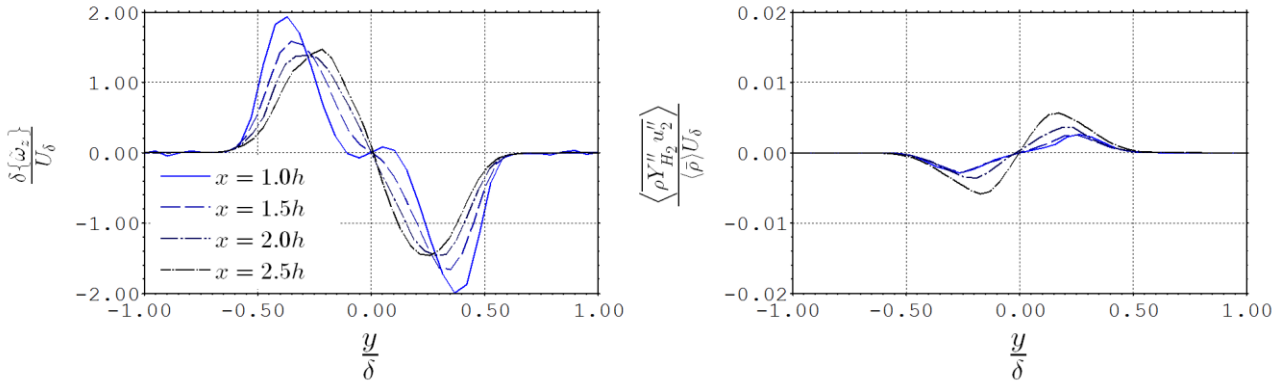

Figure 4.39: Normalised span-wise vorticity (left) and turbulence hydrogen diffusion (right) cross-stream profiles during the wake transition.

4.4.3 Shock-Turbulence Interactions

After interacting with the mixing layer, the stronger recompression shock wave is realigned with a more acute angle relative to the plane of symmetry. The strong recompression shock wave and its weak symmetric partner coalescence at approximately 1.0 duct heights downstream from the point of injection. The combined recompression shock wave remains relatively undisturbed until its

reflection by the upper (or lower) computational boundary at 2.5 duct heights downstream from injection. After reflection, the recompression shocks ultimately interact with the mixing region approximately 4.0 duct heights downstream of injection. This interaction will be referred to as the primary shock-turbulence interaction. This interaction causes a remarkable change in the wake roll-up. Just as the reflected shock waves begin to pass through the edges of the mixing layer, the vortex cores are progressively pressed together hereinafter referred to as a vortex pile-up. Not only do the vortices exist in closer proximity, but their shape becomes highly irregular with the interconnecting braids occasionally indistinguishable. This undulation is smaller in scale but greater in intensity in comparison to the previously formed vortex cores. The transverse extent of the mixing wake visibly contracts as the shock wave continues to pass through the turbulent fluid.

The wake flow turbulence is stimulated by the shock-turbulence interaction via the generation baroclinic torque. This helps to effectively mix the air previously entrained by the wake roll-up. Based upon the mean pressure and density gradients, the shock-shear interaction will produce vorticity aligned in the span-wise direction. Surprisingly, the profiles of mean span-wise vorticity during this interaction, shown in Figure 4.40, do not depict much enhancement. It is reasonable to expect vorticity is also generated in the stream-wise and cross-stream directions as the fuel-air interface is highly disturbed. Enhancement of these components of vorticity will occur at smaller scales and promote better mixing.

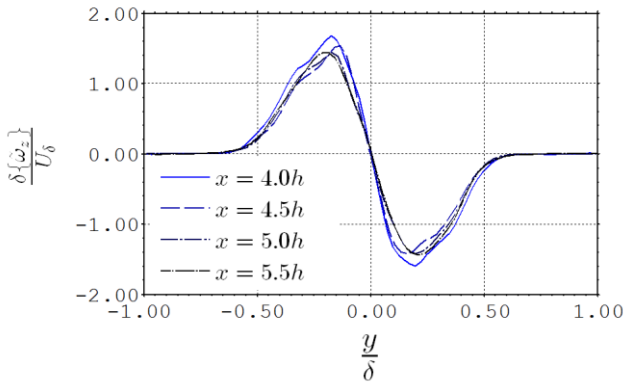

Figure 4.40: Normalised mean span-wise vorticity cross-stream profiles during the primary shock-turbulence interaction.

The recompression shock wave experiences a "scattered" refraction as it passes through the turbulent wake. A large oscillation of the mixing interface topology causes the reflected recompression shock interaction to occur at a range of stream-wise locations. In addition, the irregular mixing interface causes the reflected recompression shock to be refracted at a range of angles. The second interaction of the reflected recompression shock with the mixing wake only has a marginal effect on the turbulence behaviour. This is predominately due to the previously mentioned "scattered" refraction of the recompression shock when it first interacts with the wake flow.

4.4.4 Dominant Wake Field

The span-wise coherent turbulent structures re-emerge just down-stream of the primary shock-turbulence interaction although smaller three-dimensional eddies remain superimposed. The larger eddies quickly grow in size and the mean stream-wise velocity and density both start to develop a self-similar profile, shown in Figure 4.41.

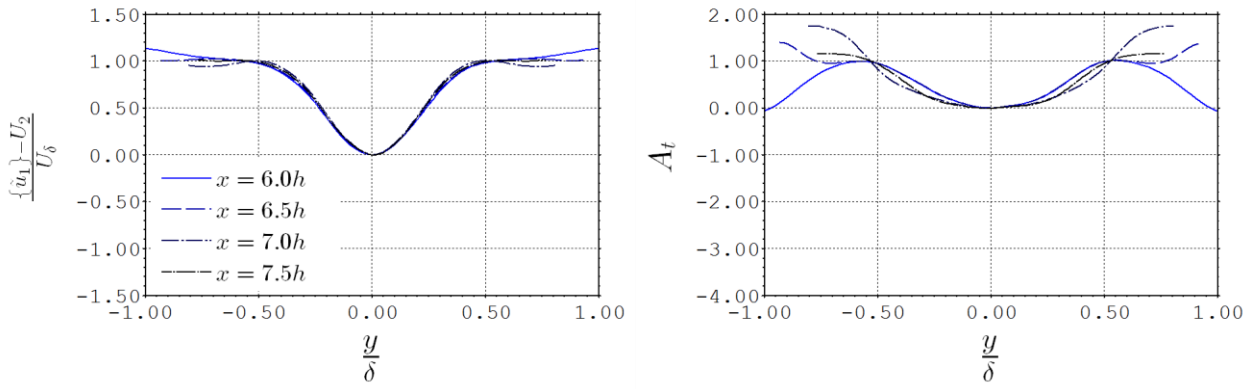

Figure 4.41: Mean stream-wise velocity (left) and Atwood number (right)cross-stream profiles proceeding the primary shock-turbulence interaction

In contrast to the profiles taken during the wake transition, where the stream-wise normal Reynolds stress was dominant, all the normal Reynolds stress (Figure 4.42) have similar magnitudes indicating that the break-down of eddies is occurring. Some degree of anisotropy remains however, signalling that this break-down is not yet fully developed. The maximum transverse stream-wise and span-wise Reynolds stresses are yet to appear at the centre of the profile, as is the case with the

cross-stream normal Reynolds stress. The normalised Reynolds shear stress show a near collapse of profiles.

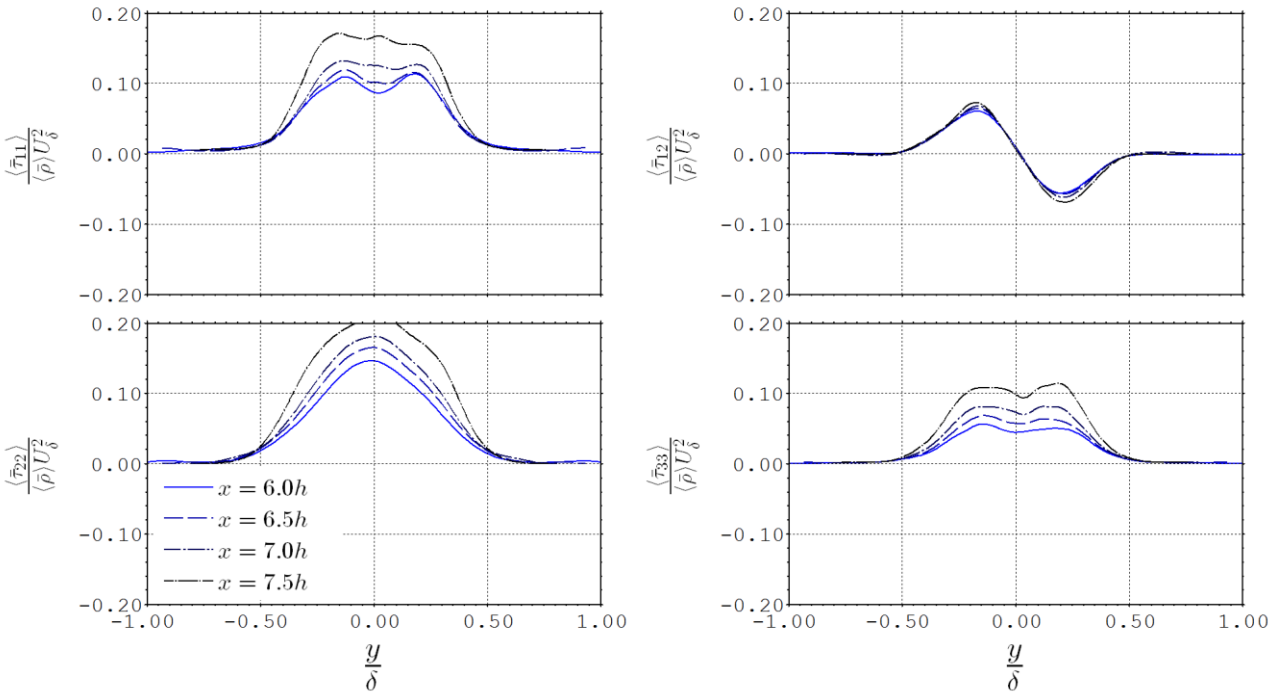

Figure 4.42: Mean Reynolds stress cross-stream profiles proceeding the primary shock-turbulence interaction

4.5 Conclusions

In summary, LES of the mixing wake flow produced several intriguing findings. The symmetrically opposed mixing layers which initially form between the fuel and air streams are strongly influenced by the instabilities of the recirculating flow. Compressible effects play a major role in reducing the cross-stream turbulent fluctuations within these mixing layers and causing the dominant instability to produce vortices of close to stream-wise alignment. The observed growth rate of these mixing layers in this highly compressible region is lower than those predicted theoretically, and substantially lower to that of an equivalent incompressible mixing layer. However, the effects of compressibility dramatically reduce as the flow travels down-stream, allowing the natural instability of the wake to cause an interaction between the turbulent mixing layers and form span-wise

coherent structures. Consequently, the growth rate and ingested oxygen entrainment of the mixing wake is greatly amplified. The primary shockwave interaction with the turbulent wake flow further enhances the initially suppressed cross-stream turbulent fluctuations. This interaction does not appear to be the stimulus of wake roll-up as span-wise coherent structures are observed several duct heights up-stream. The overall levels of turbulence kinetic energy did not clearly correlate with the mixing rate of fuel and air. A correlation is observed between the entrainment rate of air into the mixing wake and the intensity of the cross-stream turbulent fluctuations. Near-field mixing appears to be limited by the entrainment rate, where as far field mixing is more limited by lack of fully developed small scale turbulence.

5 Large Eddy Simulations with Oxygen Enriched Fuel Injection

Large Eddy Simulation results of the hypervelocity mixing wake with oxygen enriched fuel injection are presented in this chapter. Details regarding the modified boundary conditions and computational execution of this simulation are presented in section 5.1. A comparison of the overall characteristics of the oxygen enriched mixing wake to the pure fuel mixing wake is provided in section 5.2. Differences in the local flow structure between the two cases are discussed in section 5.3. The ability of RANS to replicate the LES results is reported in section 5.4 and several concluding remarks are made in section 5.5.

After discussing the Large Eddy Simulation of the pure fuel mixing wake flow in the previous chapter, attention is given to the case of oxygen enriched fuel injection. The intent of this work is to investigate whether oxygen enrichment does produce benefits to fuel-air mixing as was noted in the preliminary RANS study.

5.1 LES Execution

The LES of oxygen enriched fuel injection employs essentially the same numerical method that was used in Chapter 4. The injected in-flow boundary condition was modified to include oxygen enrichment. As in the case with pure fuel injection, the injected in-flow represents a sonic choked flow exiting the 1.0 mm planar slot with a total temperature of 300 K (cold propellant injection). Only the fuelling condition was varied, with an equivalence ratio $\phi = 1.11$, and an Enrichment Percentage $EP = 10.0\ \%$. This fuelling condition maintains global stoichiometry of the injected hydrogen with the sum of ingested and injected oxygen. The resultant injectant free-stream condition is defined by: a Mach number $M = 1.0$; static temperature $T = 248.9\ \mathrm{K}$ and static pressure $p = 379.2\ \mathrm{kPa}$. The fluid composition of the ingested flow is 0.56 by mass gaseous hydrogen and 0.44 by mass gaseous oxygen. The boundary-layer profile was modified to match the oxygen enriched in-flow condition.

The simulation was initialised in the same manner as the pure fuel injection simulation. As before, the injected stream is ramped up from no injection to sonic injection over a simulated period of 1.0 μs. The flow through time is assumed to be 200 μs. The total simulated time was 1.0 ms which required approximately 14,000 explicit time steps. The average size of the AMR grid was 72 million grid cells, which is a slight increase over the pure fuel injection LES case. The total computational time of the simulation was approximately 450,000 CPU hours. Solution data was saved in an equivalent manner to the pure fuel injection case.

5.2 Overall Flow Structure

It is of interest to determine how injecting oxygen enriched hydrogen alters the general behaviour of the mixing wake. Comparisons to the pure fuel case will be made throughout the analysis of the oxygen enriched fuel injection simulation. The compressible flow features will be considered first, shown in Figure 5.1.

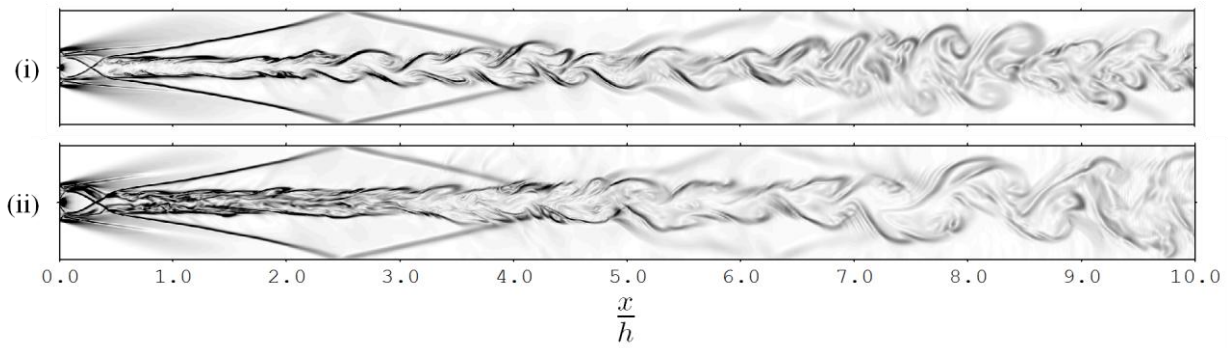

Figure 5.1: Span-wise normal $(z = 0.0)$ contours of static density gradient magnitude taken at the instant $t = 4.0t_c$ with: (i) $\phi = 1.0$ and $EP = 0.0\%$, and (ii) $\phi = 1.11$ and $EP = 10.0\%$.

The oxygen enriched fuel injection case exhibits all the compressible features present in the fuel only injection case, including: the supersonic expansion of the injected stream, and the formation of oblique recompression shock waves that travel downstream. The first observable difference between the two cases is that the density gradients just behind the centre-body are intensified by oxygen enrichment. In addition, the location at which the recompression shock waves are reflected by the upper and lower boundaries moves slightly upstream in the oxygen enriched case. This indicates that these recompression waves are slightly stronger than those of the pure fuel case. However, these changes are relatively minor.

The visible mixing interface undergoes a more dramatic change of character. The wake structure of the pure fuel case generates two distinct and symmetric mixing layers after recompression of the injected stream. It seems that the expansion and subsequent recompression of the injected stream generates several stratified interfaces in the case of oxygen enriched fuel injection. The outer interfaces resemble those of the pure fuel case, but the inner interfaces generate perturbations that

exist right throughout the fuel plume almost directly after recompression. These internal interfaces reduce in magnitude as the flow travels downstream and cease to be observed by approximately three duct heights down-stream from injection. This can be observed in Figure 5.2.

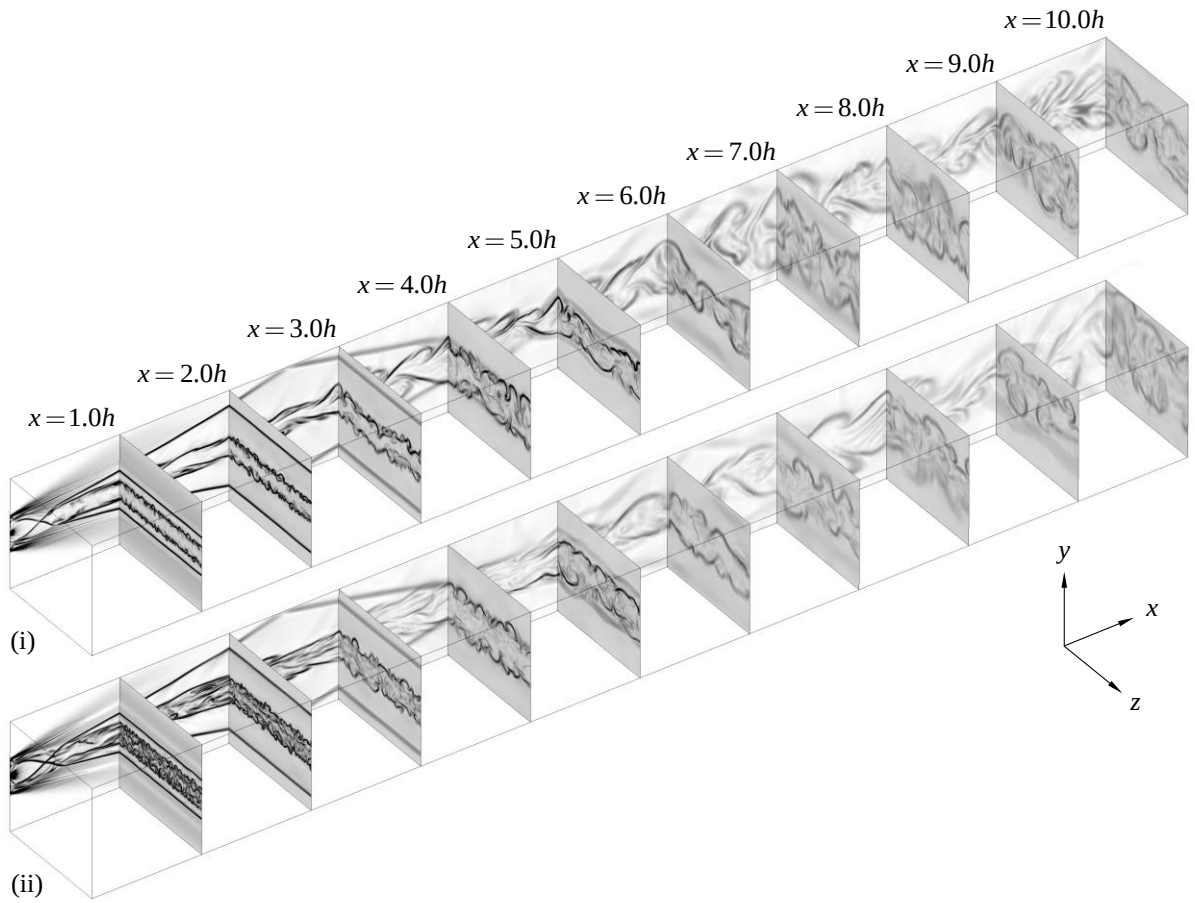

Figure 5.2: Stream-wise normal contours of static density gradient magnitude taken at the instant $t = 4.0t_c$ with: (i) $\phi = 1.0$ and $EP = 0.0\%$, and (ii) $\phi = 1.11$ and $EP = 10.0\%$.

Oxygen enriched fuel injection also appears to delay the wake roll-up onset. The span-wise coherent vortices observed in the pure fuel case at $x = 3.0h$ are not observed in the enriched case. The stream-wise correlation of the mixing interface at this location is also less pronounced in the enriched case. The occurrence of wake roll-up is not visible in the oxygen enriched fuel injection case until after the first shock-turbulence interaction. Once formed, the frequency at which the wake rolls-up is markedly less. The predominant vortex structures that form within the mixing wake are shown in Figure 5.3. An immediately observed effect of oxygen enrichment is the amplification of

the stream-wise aligned corrugation of the mixing interface that forms where the injected and ingested streams meet. The previously documented stream-wise aligned vortices which dominate the structure of the parallel mixing layers are also apparent in the oxygen enriched case. The delayed formation of large span-wise coherent vortices is also evident, where span-wise coherent structures still appear to be developing as the flow exits the domain. These coherent structures have broken-up into a sporadic ensemble of vortices by this stage in the contrasting pure fuel case.

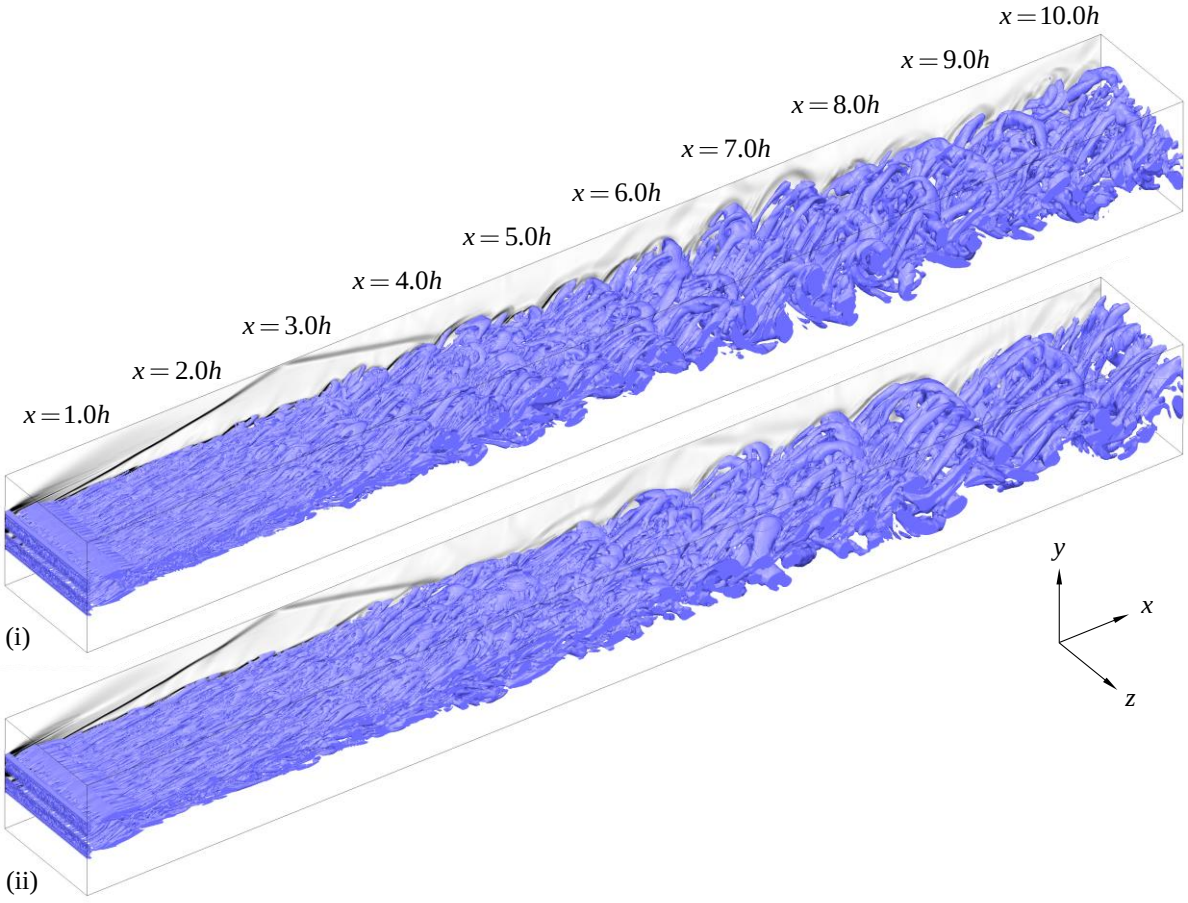

Figure 5.3: Surfaces of constant second invariant of the velocity gradient tensor taken at the instant $t = 4.0t_c$ with: (i) $\phi = 1.0$ and $EP = 0.0\%$, and (ii) $\phi = 1.11$ and $EP = 10.0\%$..

5.2.1 Shear Layer Properties

This section presents a comparison of the one-dimensional shear layer properties between the two cases, which is shown in Figure 4.11. This comparison highlights any fundamental differences that may be driving factors of the aforementioned effects of enriching fuel with oxygen.

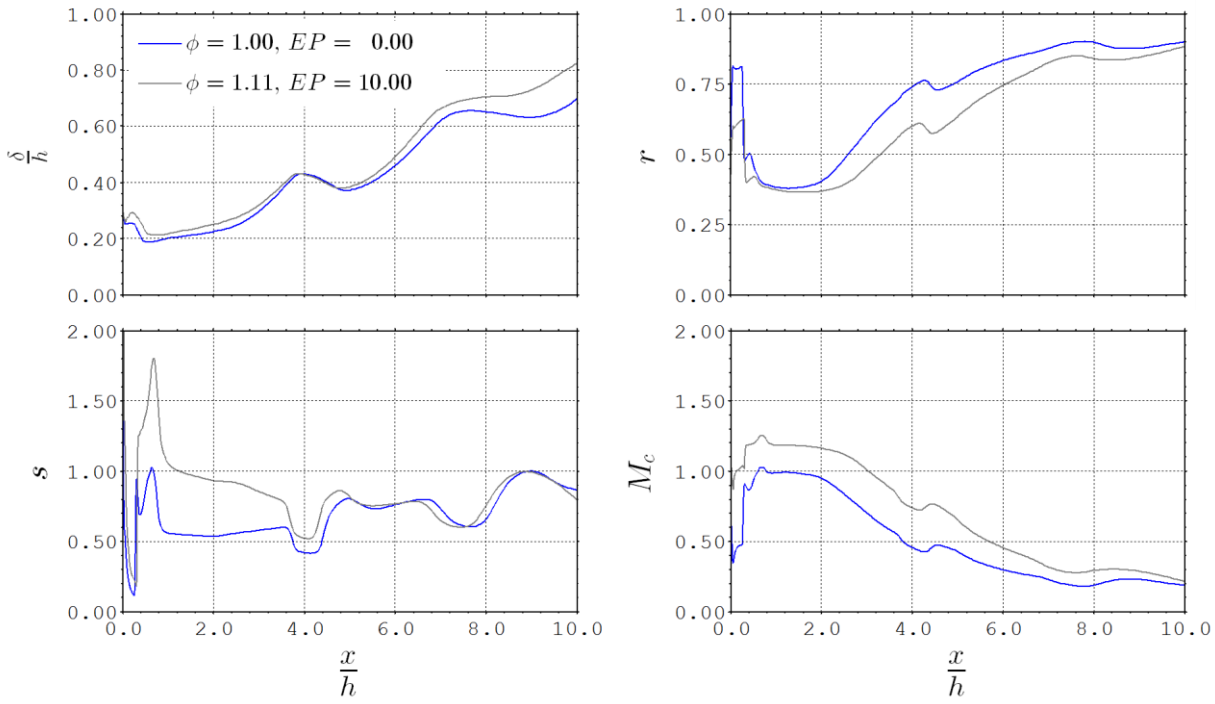

Figure 5.4: Comparison of mixing wake shear layer properties (clockwise from top left): transverse extent normalised by the duct height, velocity ratio, convective Mach number, and density ratio.

The initial transverse extent of mixing wake increases due to oxygen enrichment. This is a result of the dynamic effect of injecting a more massive fluid stream. It was illustrated in the preliminary studies that oxygen enrichment acted to increase the spreading rate of the initial mixing layers. The LES results support this conclusion, as the calculated spreading rate of these initial mixing layers in the oxygen enriched case is ~0.035, slightly greater than the pure fuel case with ~0.025. The theoretical incompressible growth rate of the initial, oxygen enriched mixing layers is ~0.17 (Dimotakis, 1986), whereas the theoretical compressible growth rates are ~0.035 (Dimotakis, 1991) and ~0.065 (Slessor, et al., 2000). Although the compressible shear layer growth rate prediction of Dimotakis (1991) matches that of the LES results, both compressible mixing layer models

incorrectly predict a reduction in the growth rate due to oxygen enrichment. The peak growth rate of the oxygen enriched mixing wake prior to the first shock-turbulence interaction, $x = 3.5h$, is ~0.15, which is slightly less than the pure fuel case. The empirically determined incompressible wake growth rate, using the velocity ratio across the mixing wake, at $x = 3.5h$ is ~0.21. As the pure fuel injection case experiences greater wake roll-up up-stream of the oxygen enriched case, the mixing wake width becomes equivalent for both cases by the first shock interaction at $x = 4.0h$. The first turbulence-shock interaction causes the same level of mixing wake contraction in both cases. The reestablishment of wake roll-up after the first shock interaction at $x \sim 5.5h$, causes the oxygen enriched mixing wake to achieve a growth rate of ~0.19 by $x \sim 6.5h$. This result exceeds the growth rate of the pure fuel mixing wake (~0.17) at the same location. The predicted growth rate of an incompressible wake with the same velocity ratio as the oxygen enriched mixing wake is ~0.10 at $x \sim 6.5h$.

The initial shearing velocity difference across the parallel mixing layers is almost identical in both cases. Although the oxygen enriched fuel is injected at a slower speed relative to the pure fuel case, deceleration of the core flow due to recompression is less pronounced. Deceleration of the injected flow down-stream of recompression is also milder in the oxygen enriched case, which suggests a smaller momentum deficit generated by the wake. The substantial increase of the velocity ratios across the mixing wake observed in the pure fuel case, due to the onset of wake roll-up, is delayed by two-thirds of a duct height in the oxygen enriched case. Once the rise in velocity ratio does occur, the rate matches that of the pure fuel case. The shock-turbulence interaction causes a similar drop in velocity ratio for both cases. As the flows travel downstream, nearing the domain exit, the velocity ratios of both cases become similar.

The density ratio of the oxygen enriched case is approximately a factor of two greater in the near-field than the pure fuel case. This is unsurprising given oxygen molecules are roughly eight times more massive than hydrogen molecules. The density ratio variation between the two cases abruptly diminished at the first shock-turbulence interaction. After the shock interaction, the density ratios are indistinguishable and, apart from the slight shift in the second shock-interaction location, remain so until the flow exits the domain. Another consequence of injecting oxygen enriched fuel is to increase the convective Mach number of the initial mixing layer from ~1.0 (pure fuel) to ~1.2. This

is a direct result of the reduced sound speed of the injected fluid stream. According to experimental mixing layer data, the spreading rate suppression due to compressibility reaches an asymptotic value for convective Mach numbers greater than ~1.0. This suggests that increases in convective Mach number by enriching the injected hydrogen fuel with oxygen will not alter spreading rate of the mixing layer. However, unlike the pure fuel injection case which exhibits a strong decline of the convective Mach number with stream-wise distance, the oxygen enrichment case maintains high values much further downstream. This indicates that compressible effects may be acting to delay the oxygen enriched wake roll-up.

5.2.2 Turbulence Statistics

This section will present a comparison of the turbulence statistics derived from both LES cases. It was concluded from the preliminary results that a rise in turbulence kinetic energy lead to an augmentation of the combustion between fuel and ingested oxygen. A comparison of the total Favre averaged turbulence kinetic energy of the two simulated mixing wake flows is shown in Figure 5.5.

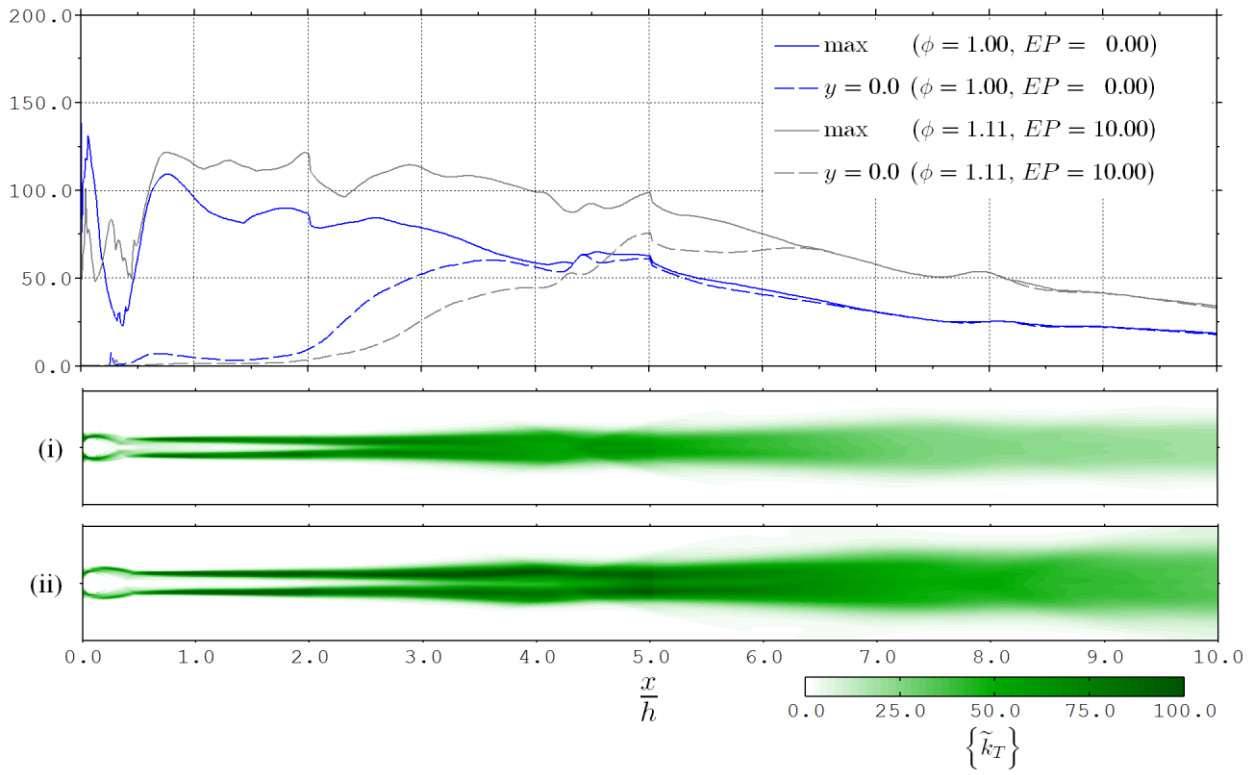

Figure 5.5: Comparison of Favre averaged turbulence kinetic energy (kJ/kg) trends with stream-wise location and contours with: (i) $\phi = 1.0$ and $EP = 0.0\%$, and (ii) $\phi = 1.11$ and $EP = 10.0\%$.

The LES results support the assertion that enriching the injected fuel with oxygen does enhance the turbulence kinetic energy generated within the mixing wake. Disregarding the near field, which contains laminar unsteadiness, the maximum levels of turbulence achieved in the oxygen enrichment case are consistently greater than those of the pure fuel case at any given stream-wise location. The percentage increase is also quite consistent, between 15-20%. As previously noted, the shearing velocity difference across the mixing layers is only marginally increased by oxygen enrichment and does not solely account for this turbulence kinetic energy enhancement. The

principal difference between the two cases, with respect to turbulence kinetic energy, is that the unsteadiness which forms at the edge of the over-expanded injected stream feeds directly into the parallel mixing layers which form down-stream. This does not occur in the pure fuel case, where the injected stream unsteadiness is directed into the fuel core flow and does not feed into the parallel mixing layers which form down-stream. Consequently, the level of turbulence kinetic energy within the oxygen enriched mixing layers is not adversely affected by the higher convective Mach number.

The dynamic effect of injecting a more massive fluid stream causes a greater displacement between the two symmetric mixing layers. Production of turbulence kinetic energy along the plane of symmetry is notably delayed in the oxygen enriched case. In the pure fuel case, the centre-line and cross-stream maximum turbulence kinetic energy levels are almost identical by $x \sim 3.8h$ (before the first shock interaction), where as for the enriched case this occurs much further downstream at $x \sim 6.5h$. The persistent confinement of turbulence kinetic energy within symmetrically opposed bands can be clearly observed in the contour plots.

As was noted in Chapter 4, compressible effects acted to reduce the cross-stream Reynolds normal stress before the wake began to roll-up. Visualisations of the cross-stream Reynolds normal stress (Figure 5.6) in the case of oxygen enriched fuel injection show that cross-stream turbulent fluctuations are suppressed in an equivalent manner. Before pure fuel wake roll-up, both cases display similar levels of the cross-stream Reynolds normal stress. Cross-stream fluctuations are more intense in the pure fuel case due to the wake roll-up at $x \sim 3.0h$. Cross-stream fluctuations on the plane of symmetry start to develop at similar locations for both cases, although the rate at which these stresses develop is reduced in the oxygen enriched case. The shock-turbulence interaction stimulates the cross-stream turbulence fluctuations in the same profound way for both cases. These high levels are maintained as the oxygen enriched fuel wake undergoes roll-up down-stream of the first shock interaction. The second shock interaction provides much better enhancement of these turbulence stresses in this case.

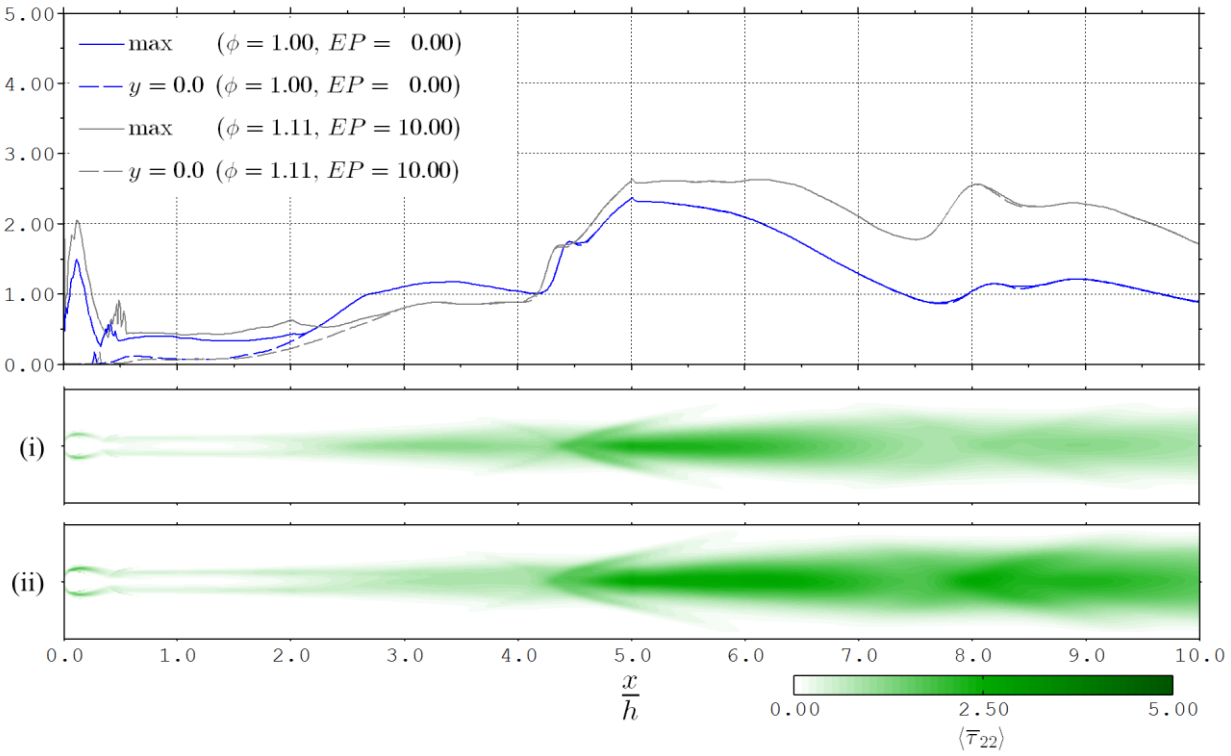

Figure 5.6: Comparison of Reynolds averaged cross-stream Reynolds normal stress (kPa) trends with stream-wise location and contours with: (i) $\phi = 1.0$ and $EP = 0.0\%$, and (ii) $\phi = 1.11$ and $EP = 10.0\%$.

5.2.2.1 Energy Spectra

From the static density gradient magnitude visualisations, it was noted that the wake roll-up frequency was discernibly lower in the case of oxygen enrichment. This can be confirmed by interrogating the turbulence energy spectra calculated at various locations with the flow, shown in Figure 5.7. As with the pure fuel case, the wake roll-up contains a majority of the turbulence kinetic energy in the oxygen enriched case. The associated roll-up frequency is 70 kHz, 35% less than the pure fuel case, with a Strouhal number based upon the strut height of 0.297. There is a very small range of higher frequencies, 100 - 150 kHz, down-stream of the first shock-turbulence interaction that matches the -5/3 slope expected for an inertial sub-range. Above this range of frequencies, the turbulence kinetic energy reduces at an increasing rate. The turbulence kinetic energy diminishes by approximately four orders of magnitude between the energy containing integral frequency and the sampling Nyquist frequency of 1.0 MHz. Taylor's hypothesis predicts that the associated wavelength of this instability at $x = 2.0h$ is ~17.0 mm, an increase of ~47% over the pure fuel wavelength . Acceleration of the wake flow causes the instability wavelength to grow with down-stream location. By $x = 8.0h$, the wavelength is approximately 38.5 mm.

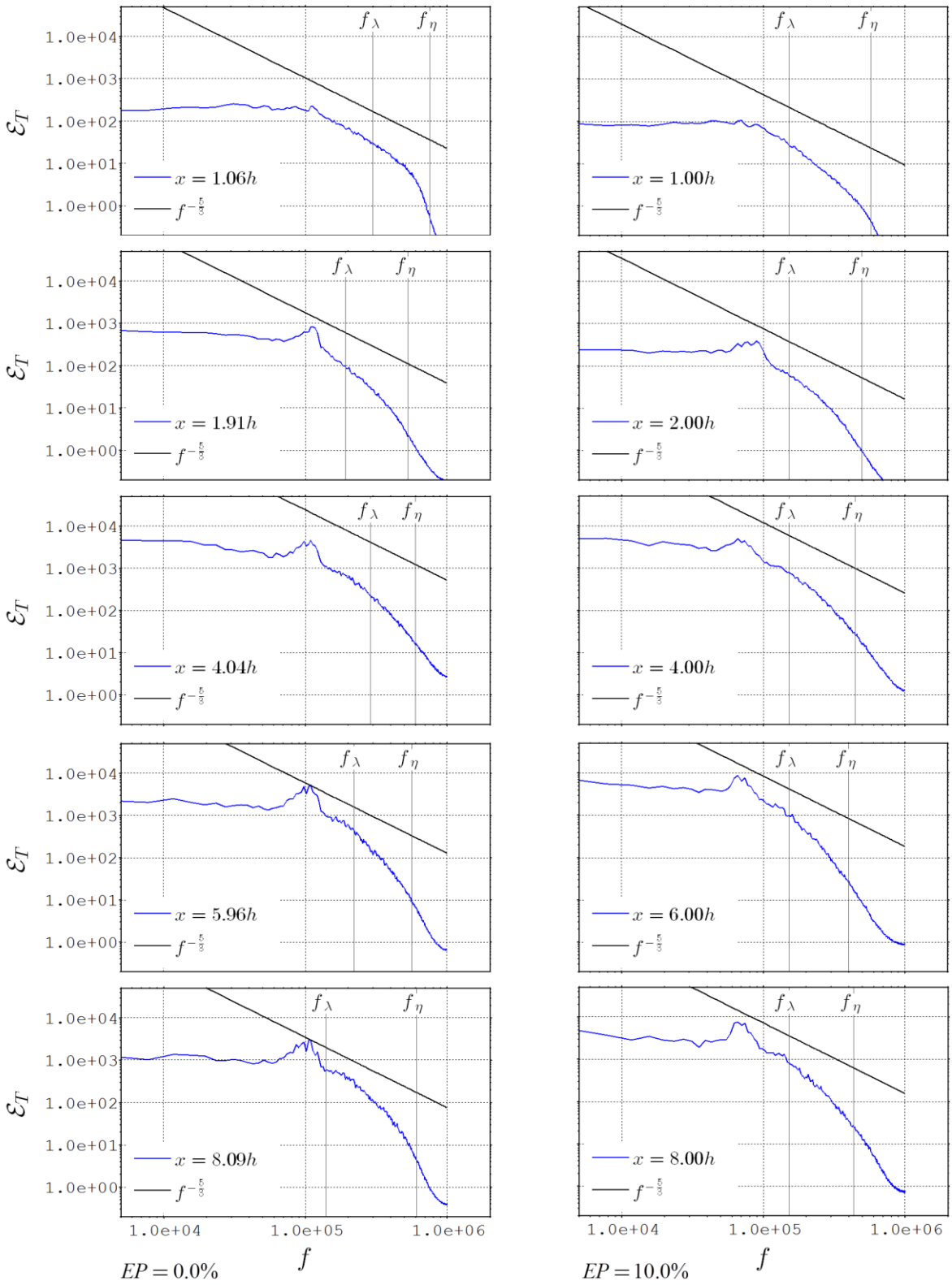

Figure 5.7: Comparison of logarithmic span-wise averaged turbulence energy spectra trend with frequency (Hz) taken at $y = 0.00$ with: (left) $\phi = 1.0$ and $EP = 0.0\%$, and (right) $\phi = 1.11$ and $EP = 10.0\%$..

5.2.3 Mixing and Entrainment

In this section, details of the entrainment process and mixing characteristics of the two simulated turbulent wake flows will be compared. Visualisations of the mixing interface generated from pure fuel and oxygen enriched fuel injection are shown in Figure 5.8. The initial symmetric mixing layers appear almost identical in both cases, characterised by near stream-wise aligned vortices. Three-dimensional interactions between these vortices can be observed before the first shock-turbulence interaction, but it is clear at this stage that the oxygen enriched fuel wake has not begun to roll-up. Larger oblique structures do begin to form down-stream of this shock interaction. It is not until the second shock-turbulence interaction at $x \sim 7.0h$ that large scale structures with span-wise coherence, similar to that of the pure fuel case, form. The reduced frequency of the oxygen enriched wake roll-up is also clearly evident.

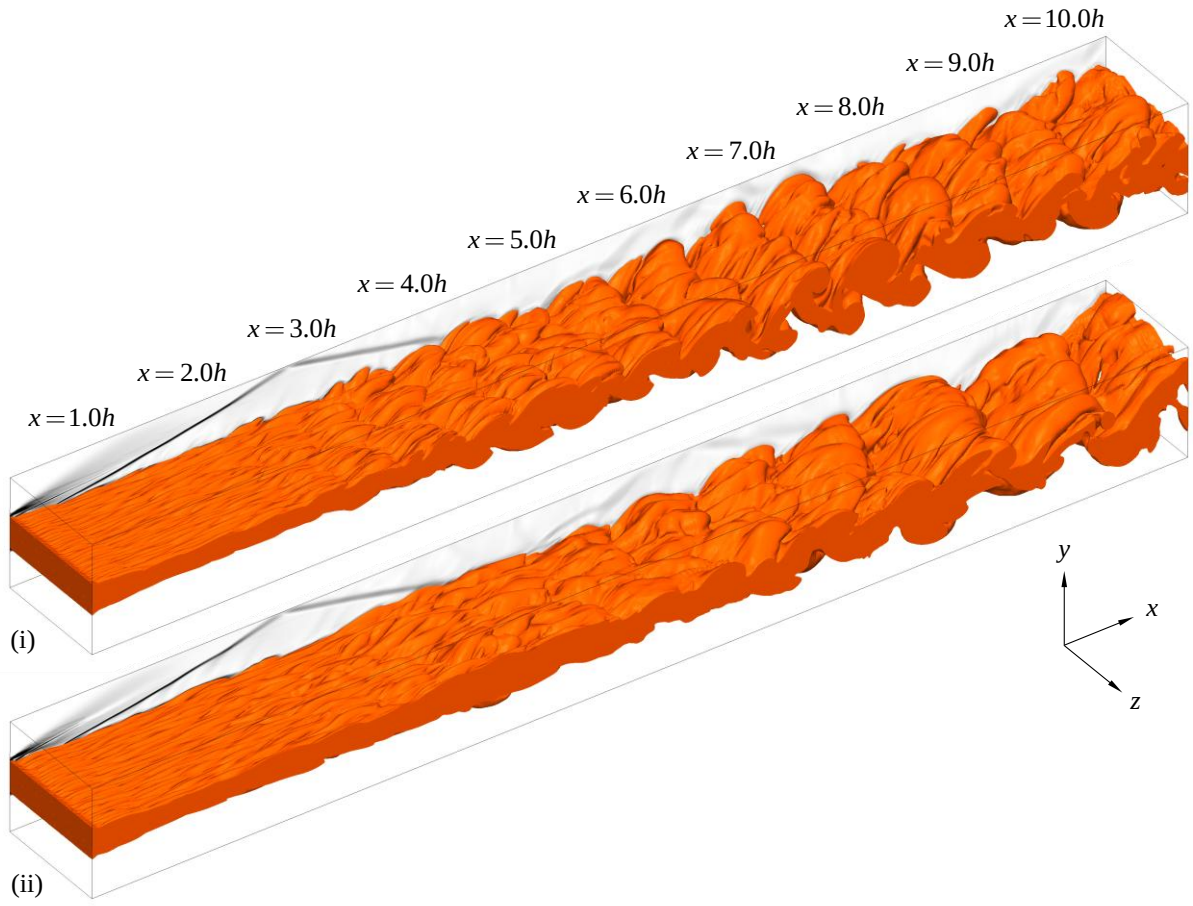

Figure 5.8: Comparison of the stoichiometric mixture iso-surface taken at $t = 4.0t_c$ with: (i) $\phi = 1.0$ and $EP = 0.0\%$, and (ii) $\phi = 1.11$ and $EP = 10.0\%$.

5.2.3.1 Modified Mixing Efficiency

Comparison of mixing and entrainment between the two LES cases is made more complex by the introduction of premixed oxygen into the injected stream. The previous definitions of mixing can be used, but these definitions will bias the case of oxygen enrichment due to the fuel-oxygen pre-mixing. In a similar vein to the treatment of combustion efficiency in Chapter 3, a modification to the mixing efficiency definition is proposed which isolates the mixing of ingested oxygen with fuel, defined as:

$$\eta_{mix}^{OxEn}(x) = \frac{\eta_{mix}(x) - EP}{1 - EP} \qquad 5.1$$

The concept also extends to the mass flux of ingested oxygen that is well mixed with injected hydrogen via:

$$\left(\dot{m}''\right)_{mix}^{OxEn} = \frac{\dot{m}''_{mix} - EP\dot{m}''_{H_2}}{1-EP} \qquad 5.2$$

Visualisations of the well mixed mass flux of hydrogen are shown in Figure 5.9. In the near-field of both cases, ingested oxygen is constrained to mix with fuel in the thin developing mixing layers. These regions of well mixed ingested oxygen start to display large three-dimensional undulation where the pure fuel wake begins to roll-up. Mixing in the oxygen enrichment case remains confined within the mixing layers until $x \sim 4.0h$. The first shock-turbulence interaction amplifies the mixing on the outer edges of the wake flow, but a fuel rich core flow persists. A three-dimensional break-up of the well mixed fluid regions begins to occur at $x \sim 6.0h$. This break-up continues as the flow travels downstream and large volume of ingested oxygen finally become entrained within the wake ($x \sim 7.0h - 10.0h$). Conversely, well mixed fuel can be observed traversing outward as far as the upper computational boundary ($x = 10.0h$), an event not seen in the pure fuel wake simulation.

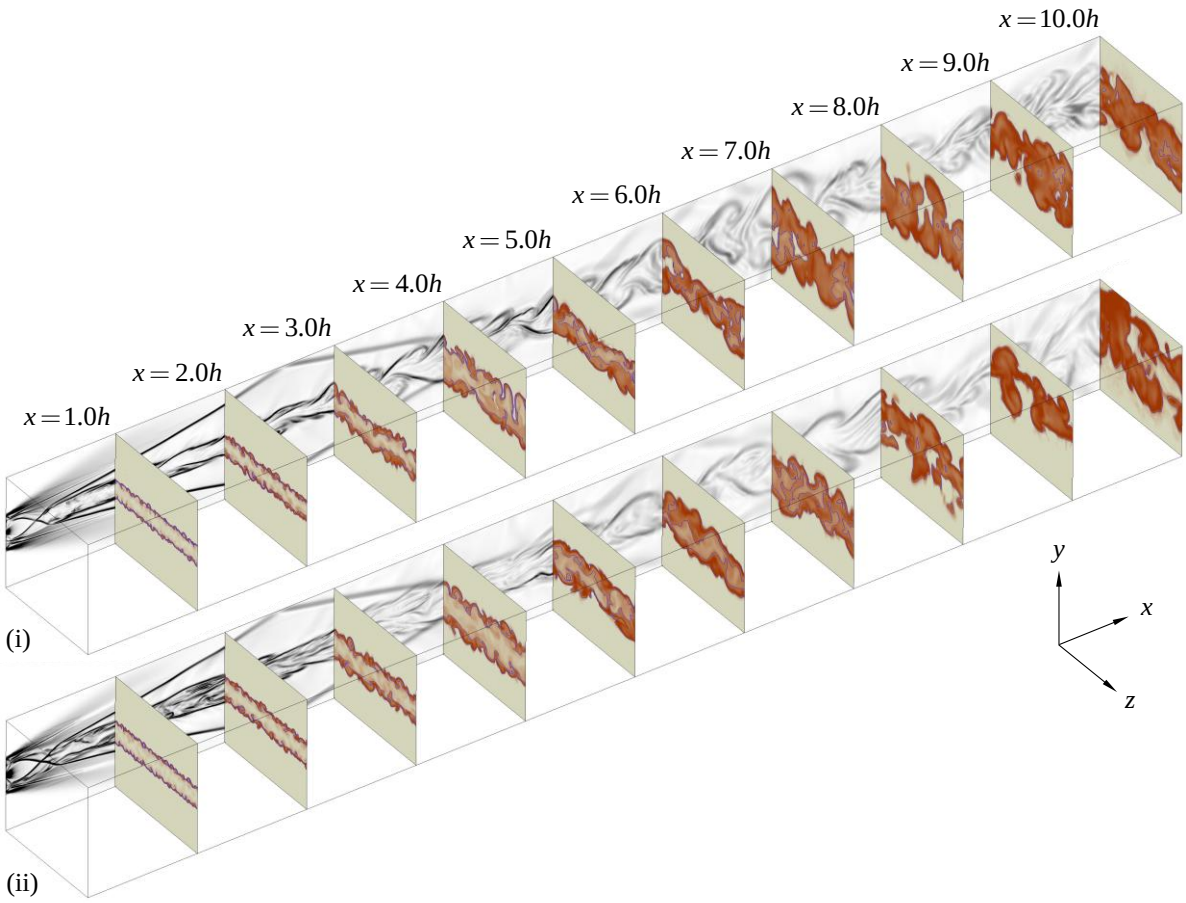

Figure 5.9: Stream-wise normal contours of well mixed hydrogen mass flux (kg/(m^2.s)) taken at the instant $t = 4.0t_c$ with: (i) $\phi = 1.0$ and $EP = 0.0\%$, and (ii) $\phi = 1.11$ and $EP = 10.0\%$.

It is important to explore how oxygen enrichment has altered the entrainment process of ingested air into the mixing wake. Formulating an equivalent modification to the entrainment of ingested oxygen is slightly different to those of the mixing parameters, which are based upon hydrogen mass flow rates. Excluding the pre-mixed oxygen from the total amount of entrained oxygen can be achieved using:

$$\left(\dot{m}''\right)_{ent}^{OxEn} = \left(1+\phi EP\right)\dot{m}''_{ent} - \phi EP\dot{m}''_{O_2} \qquad 5.3$$

Subsequently, the fraction of ingested oxygen that has been entrained into the mixing wake over the total amount of ingested oxygen is given by

$$\eta_{ent}^{OxEn}\left(x\right) = \left(1+\phi EP\right)\eta_{ent}\left(x\right) - \phi EP \qquad 5.4$$

The mean ingested oxygen entrainment fraction and hydrogen mixing efficiency for both LES cases is shown in Figure A1.24.

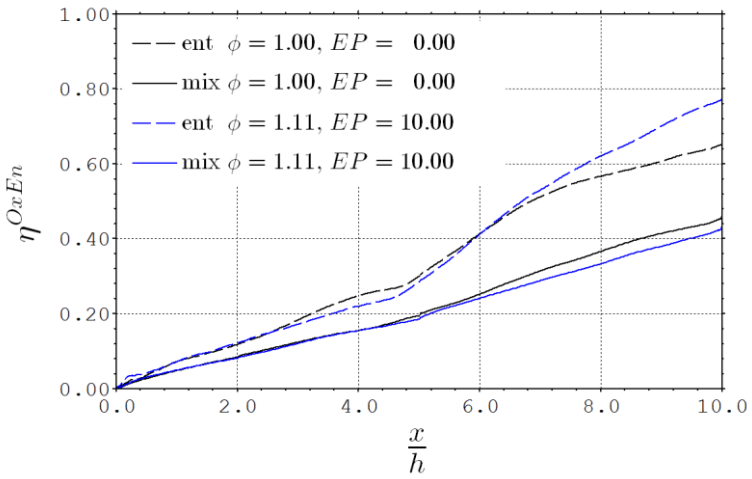

Figure 5.10: Trends of Reynolds averaged entrainment fraction and mixing efficiency with stream-wise location (pure and oxygen enriched fuel injection).

The reported entrainment rates of the initial mixing layers are identical of both pure fuel and oxygen enriched fuel. The entrainment rates of the two cases diverge where onset of wake roll-up occurs in the pure fuel case, at $x = 3.0h$. However, the entrainment rate of the oxygen enrichment case is greatly increased by the first shock-turbulence interaction, more so than the pure fuel case. The fraction of ingested oxygen that has been entrained into the mixing wake is equal in both cases at $x = 6.0h$. Further down-stream, the oxygen enriched mixing wake becomes more effective at entraining ingested oxygen in comparison to the pure fuel case. This is most pronounced where the flow exits the domain; by this stage the enriched case has entrained almost 80% of all ingested oxygen into the wake, which is ~12% more than the pure fuel wake.

The stream-wise trends in mixing efficiency are almost identical until the first shock turbulence interaction at $x = 5.0h$. Consistent with the pure fuel case, approximately 74% of the initially entrained oxygen mass is well mixed with hydrogen. In contrast to the pure fuel case, this percentage remains fairly constant until the first shock interaction. The pure fuel case generates a slightly greater mixing rate than the enriched case once the reflected shock has passed through the wake. This can be attributed to the mixing of additional oxygen entrained by the wake roll-up,

which only occurs before the shock interaction in the pure fuel case. The percentage of entrained oxygen that is well mixed markedly decreases downstream of the shock interaction in the OxEn case, to ~55% by $x = 7.0h$. This lower value persists until the domain exit, suggesting that the large scale turbulence has not begun to break-down and stimulate mixing in the oxygen enriched case. The overall mixing efficiencies of both cases continue to deviate until $x \sim 9.0h$. The mixing efficiency of the enriched is ~43% as the flow exits the domain.

The onset of wake roll-up appears crucial in boosting the entrainment of air into the wake. The first shock-turbulence interaction is effective at mixing entrained oxygen with fuel. The second shock interaction does not produce the same notable mixing. These results indicate that pure fuel injection achieves better mixing efficiencies by advancing the wake roll-up up-stream of the first shock interaction.

5.3 Local Flow Structures

There are obvious differences in behaviour of the two simulated flow fields based upon the overall flow features. The most surprising of these was a reduction in the mixing efficiency between ingested oxygen and injected hydrogen due to oxygen enrichment. This result is opposed to the findings of the preliminary RANS simulations. This section investigates the flow physics in greater detail at several key stages as the mixing wake develops to determine the underlying cause for the unexpected reduction in effective mixing efficiency. These regions of flow include the near-field and the first shock-turbulence interaction.

5.3.1 Near Field Flow Structure

The ingested stream of the oxygen enriched case enters the computational domain with exactly the same conditions as the pure fuel case. The centre-body trailing edges generate expansion fans which accelerate the stream to a Mach number of ~4.1. The injection of enriched fuel has three key differences from the pure fuel injection: (i) the static pressure is more than 50% greater, (ii) the density is a factor of 2.6 time greater, and (iii) the sound speed is ~25% slower. The ingested stream

is accelerated via this expansion to a maximum Mach number of ~5.0, slightly higher than the pure fuel case of $M \sim 4.5$.

Visualisations of the stream-wise velocity component in Figure 5.11 highlight the formation of recirculation regions behind the centre-body, which is displayed up-stream of the computational solutions and coloured grey. Superimposed on these contours are stream-traces of fluid contained within the in-flow laminar boundary-layers, near the centre-body walls. The boundary-layers that detach from the upper and lower walls of the centre-body are more frequently entrained into the recirculation region due to the greater expansion of the injected stream. Consequently, a larger volumetric portion of the recirculation region is air in the oxygen enrichment case. Greater static pressure causes the injected stream to experience more rapid expansion which pushes the recirculating fluid further away from the plane of symmetry. The injected stream also achieves greater penetration as it meets the ingested stream with greater momentum. The detached laminar boundary layer exhibits similar high frequency span-wise aligned disturbances noted in the pure fuel case (Figure 5.3). The greater cross-stream penetration of the injected stream does not correlate into a greater distortion of the mixing interface (Figure 5.8). The momentum deficit generated by the reverse flow is even milder in the case of oxygen enrichment. Although the oxygen enriched fuel core is injected at a much slower speed, the momentum deficit generated by the reverse flow is milder than the pure fuel case. Consequently, the wake component does not further decelerate the oxygen enriched fuel core to the same extent and the velocity ratio across the mixing layers at $x = 1.0h$ are almost identical in both cases (Figure 4.11). The ingested flow stream-wise velocity remains essentially unaffected by oxygen enrichment after $x = 0.3h$.

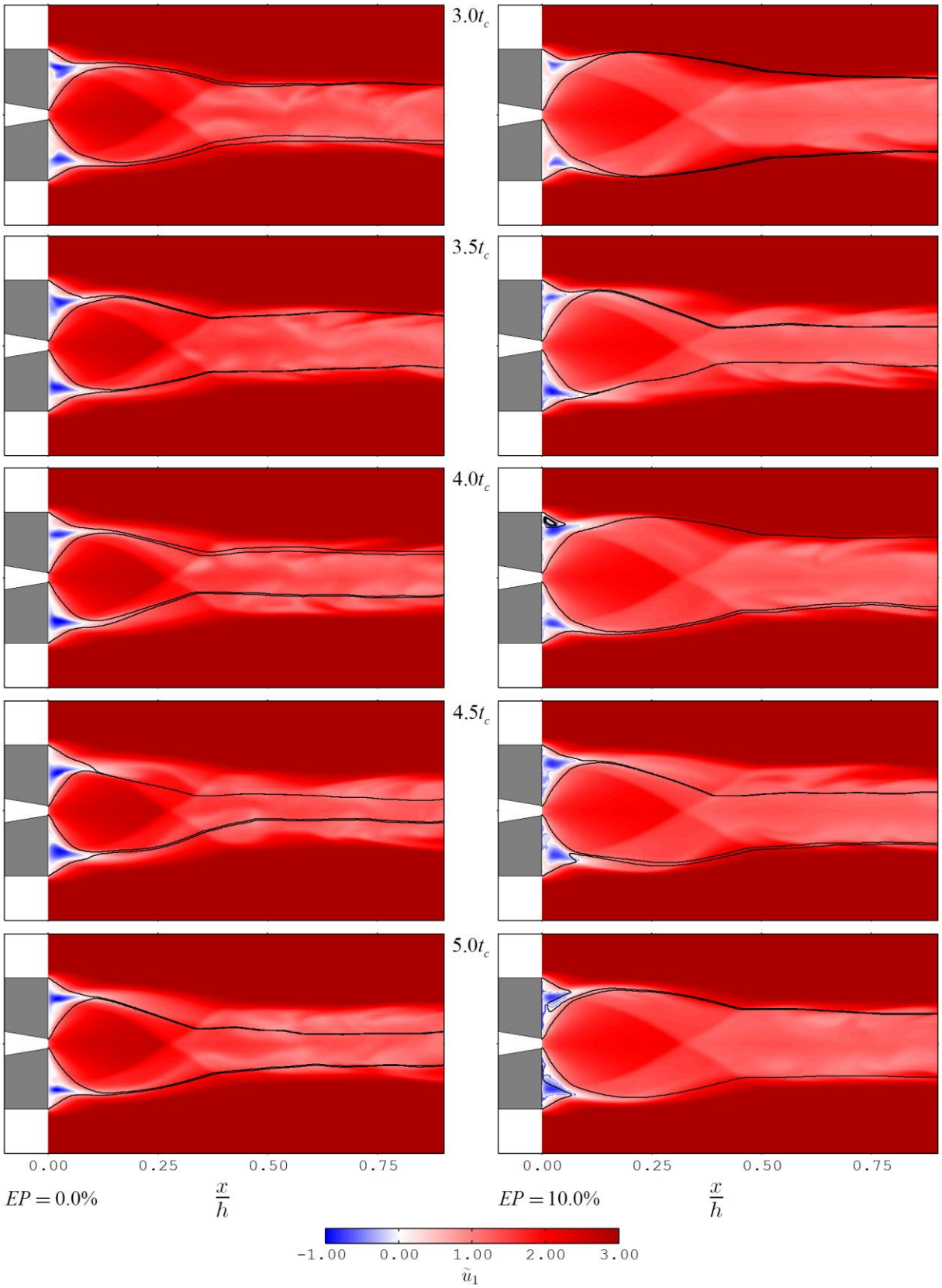

Figure 5.11: Span-wise normal $(z = 0.0)$ contours of stream-wise velocity (km/sec) behind the centre-body, with superimposed streamlines, for $EP = 0.0\%$ (left) and $EP = 10.0\%$ (right) taken at the instants (top to bottom): $t = 3.0t_c$, $t = 3.5t_c$, $t = 4.0t_c$, $t = 4.5t_c$, and $t = 5.0t_c$..

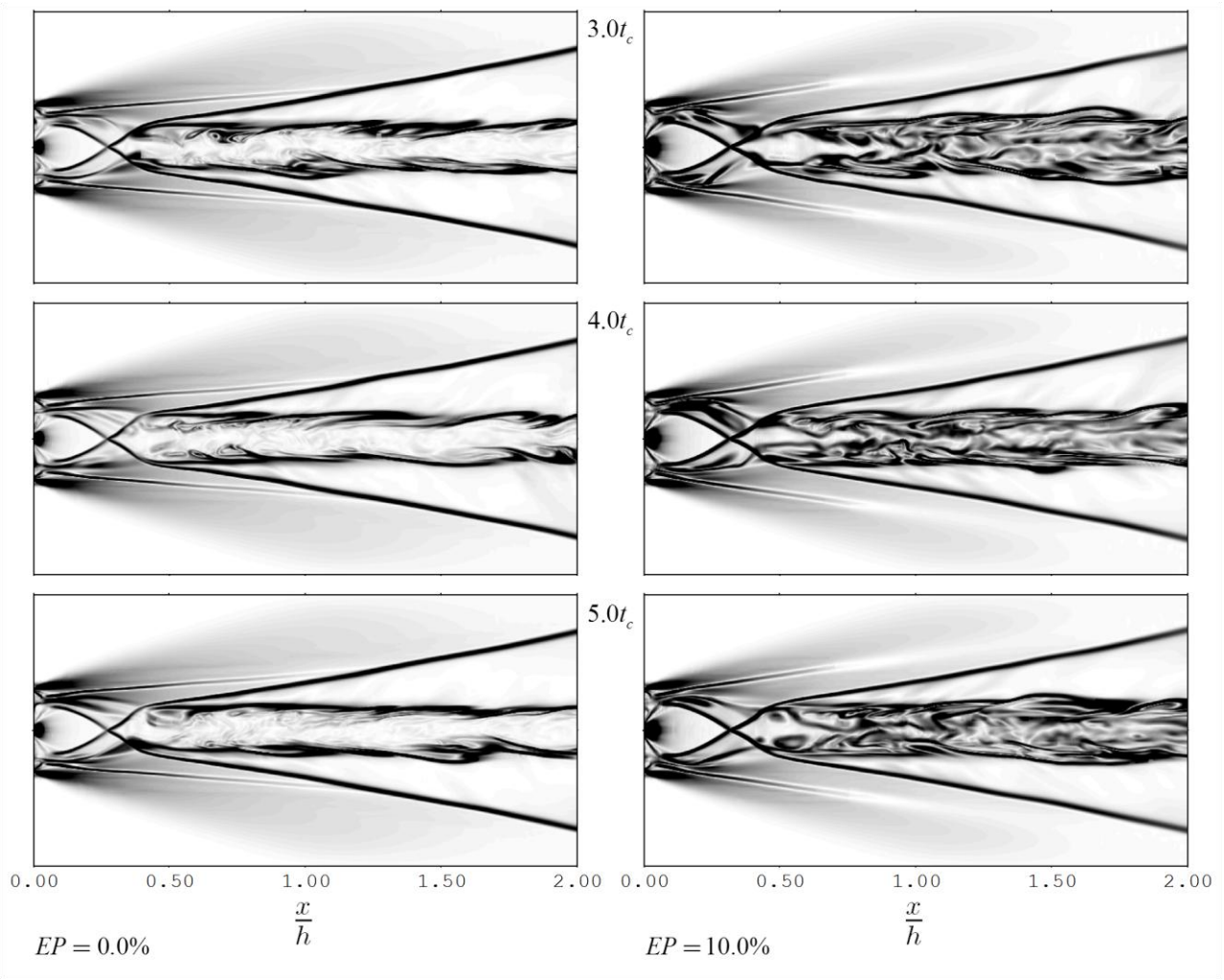

Figure 5.12: Span-wise normal $(z = 0.0)$ contours of static density gradient magnitude within the near field with $EP = 0.0\%$ (left) and $EP = 10.0\%$ (right) taken at the instant $t = 3.0t_c$ (top), $t = 4.0t_c$ (middle) and $t = 5.0t_c$ (bottom).

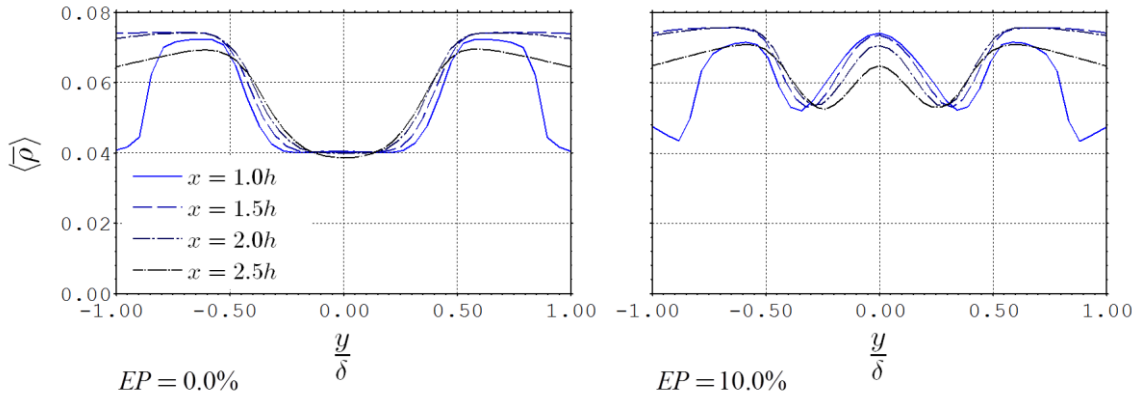

Figure 5.13: Comparison of Reynolds-averaged static density cross-stream profiles of the mixing wake between $x = 1.0h$ and $x = 2.5h$ with $EP = 0.0\%$ (left) and $EP = 10.0\%$ (right).

Figure 5.12 shows that greater expansion of the injected stream results in a strengthening of the recompression shock waves that process the ingested stream, which display a more obtuse angle. In contrast to the pure fuel case, these shocks do not coalescence with the major recompression shocks further downstream as they are weakened by the expansion fans originating from the centre-body trailing edges. The edges of the injected stream, which now transverses further in the cross-stream direction, experiences weaker supersonic over-expansion and subsequent recompression relative to the core of the injected stream. This has a stratifying effect across the injected stream with lower density fluid forming at the edges of the wake. This does not occur in the pure fuel case as the injected stream is more confined and evenly recompressed. This stratification of the injected oxygen enriched fuel stream is evident is the Reynolds averaged static density profiles across the near-field wake flow, shown in Figure 5.13.

The near field mixing interface shown in Figure 4.28 exhibits the same mushroom shaped structures, which evolves from a Richtmeyer-Meshkov instability, as the pure fuel case. The recompression shock wave stimulates mixing of the intruding air with the fuel rich wake but terminates further growth of the existing mushroom shaped structures. Instead, the previously discussed smaller, stream-wise aligned vortex streaks form within the mixing layers. Air does not penetrate the fuel rich core which is notably thicker than the pure fuel core. This is a dynamic effect resulting from the injection of more mass, which also further displaces the mixing layers away from

the wake core. Stratification of the wake generates larger density gradients within the injected stream, shown in Figure 4.29, but does not appear to supplement the distortion of the mixing layer. No large scale structure is evident in this region of the flow. The density gradients that exist within the wake slowly dissipate as the flow travels down-stream.

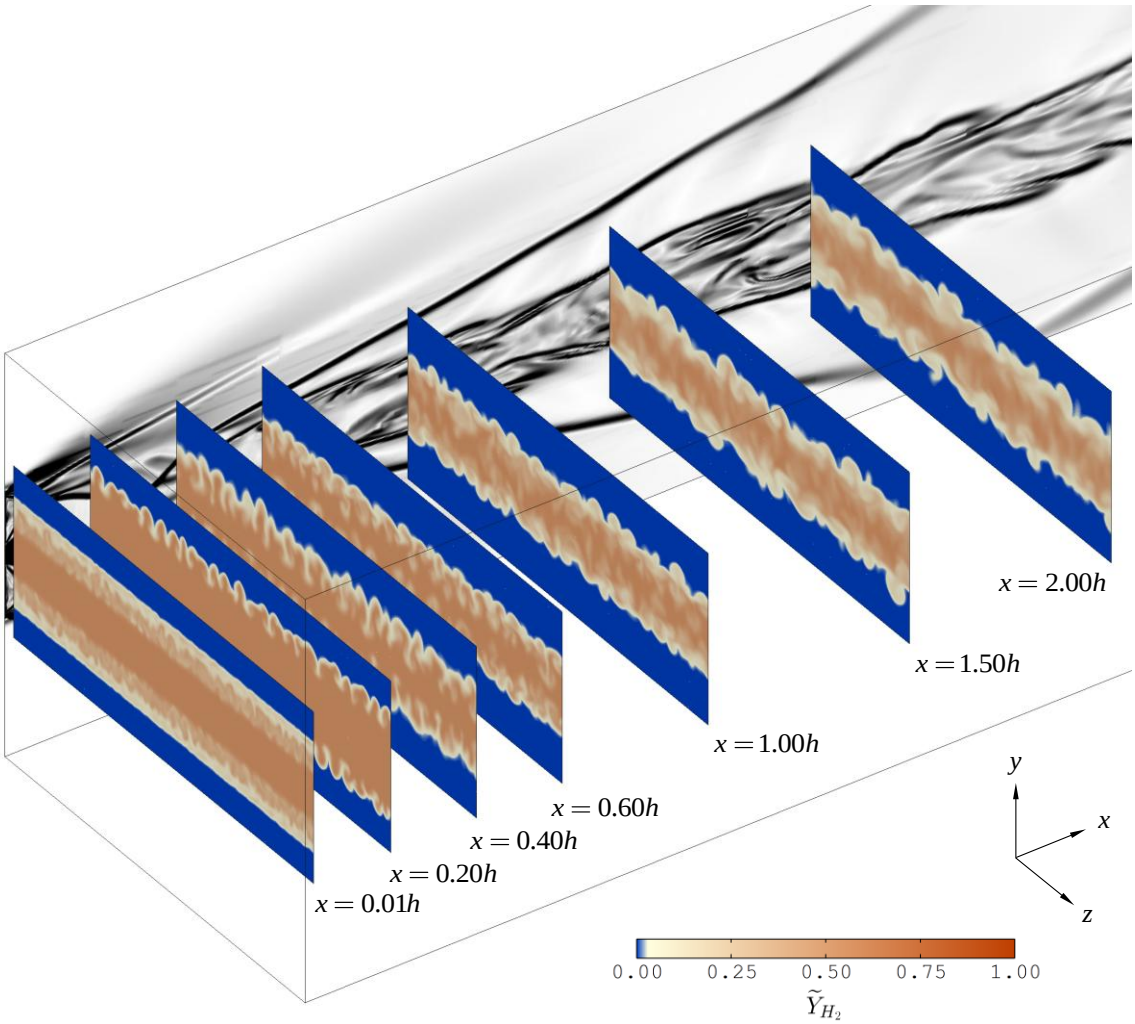

Figure 5.14: Contours of hydrogen mass fraction within the near field with $EP = 10.0\%$ taken at the instant $t = 4.0t_c$.

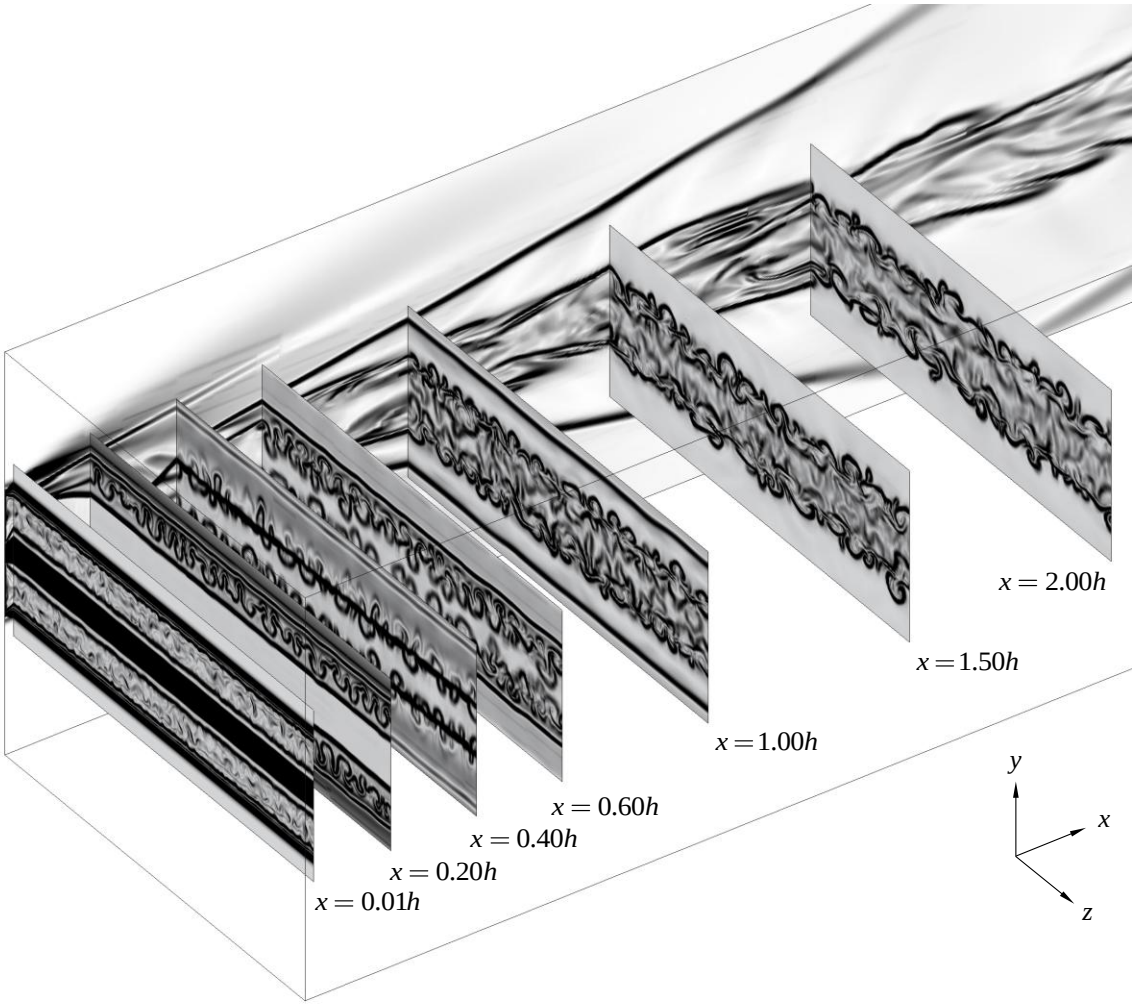

Figure 5.15: Contours of static density gradient magnitude within the near field with $EP = 10.0\%$ taken at the instant $t = 4.0t_c$.

Contour plots of velocity divergence, shown in Figure 5.16, confirm that these developing oxygen enriched mixing layers generate intensified shocklets. Oblique shocklets originating at the outer edge of the developing mixing layers are directed away from the wake flow, similar in nature to the weaker shocklets observed in the pure fuel case. The levels of compression and expansion within the mixing wake are also amplified by oxygen enrichment. This internal compression and expansion of the wake will generate pressure dilatation. As a consequence, turbulence production within the mixing wake will be limited as well as the communication of instabilities between the developing mixing layers. Internal compressible effects contribute towards the delay in oxygen enriched wake roll-up.

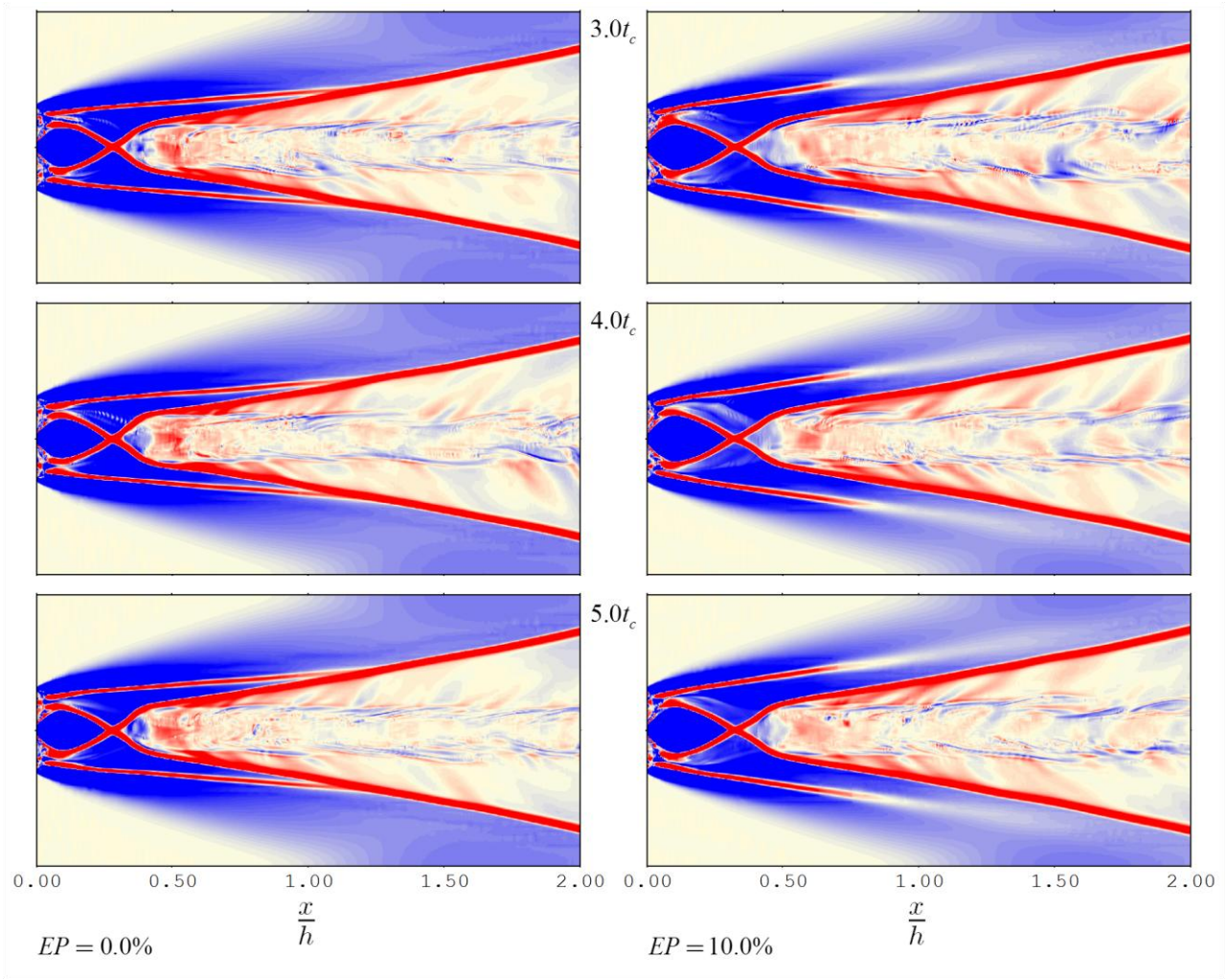

Figure 5.16: Span-wise normal $(z = 0.0)$ contours of velocity divergence within the near field with $EP = 0.0\%$ (left) and $EP = 10.0\%$ (right) taken at the instant $t = 3.0t_c$ (top), $t = 4.0t_c$ (middle) and $t = 5.0t_c$ (bottom).

5.3.2 Shock-Turbulence Interactions

The first shock interaction with the pure fuel mixing wake was shown to dramatically influence the turbulence behaviour which benefited fuel-air mixing. There are several competing factors which dictate how shock interactions influence an oxygen enriched fuel wake. It has been noted that the principal recompression shock wave becomes marginally stronger as a consequence of oxygen enrichment. This is notionally offset by a reduction in density ratio across the mixing wake, although the complex over-expansion and recompression of the injected stream causes localised

density gradients to occur within the wake flow. Visualisations of the entire wake have shown that large scale span-wise coherence does not begin to develop until several duct heights down-stream of the first shock turbulence interaction. Hence, the shock interaction does not appear directly responsible for wake transition.

Examination of the cross-stream profiles of the normalised Reynolds stresses taken as the first reflection of the recompression shock wave passes through the wake, shown in Figure 5.17, helps to elucidate the turbulent fluid flow behaviour in this region. These profiles provide clear evidence that the internal compressibility of the oxygen enriched wake has suppressed the Reynolds stresses in the fuel core flow. The stream-wise normal Reynolds stress continues to dominate the turbulence kinetics, with peak values occurring away from the symmetry plane. The other Reynolds stresses are amplified by the shock interaction, but not to the same relative extent as in the pure fuel case. Although the cross-stream normal Reynolds stress is stimulated by an equivalent magnitude in both cases (see Figure 5.6), it does not constitute the bulk turbulent stress. The turbulence generating Reynolds shear stress is substantially reduced by oxygen enrichment just up-stream of the shock-turbulence interaction. As the reflected shock wave passes through the oxygen enriched wake, this Reynolds stress is more effectively stimulated in comparison to the pure fuel case.

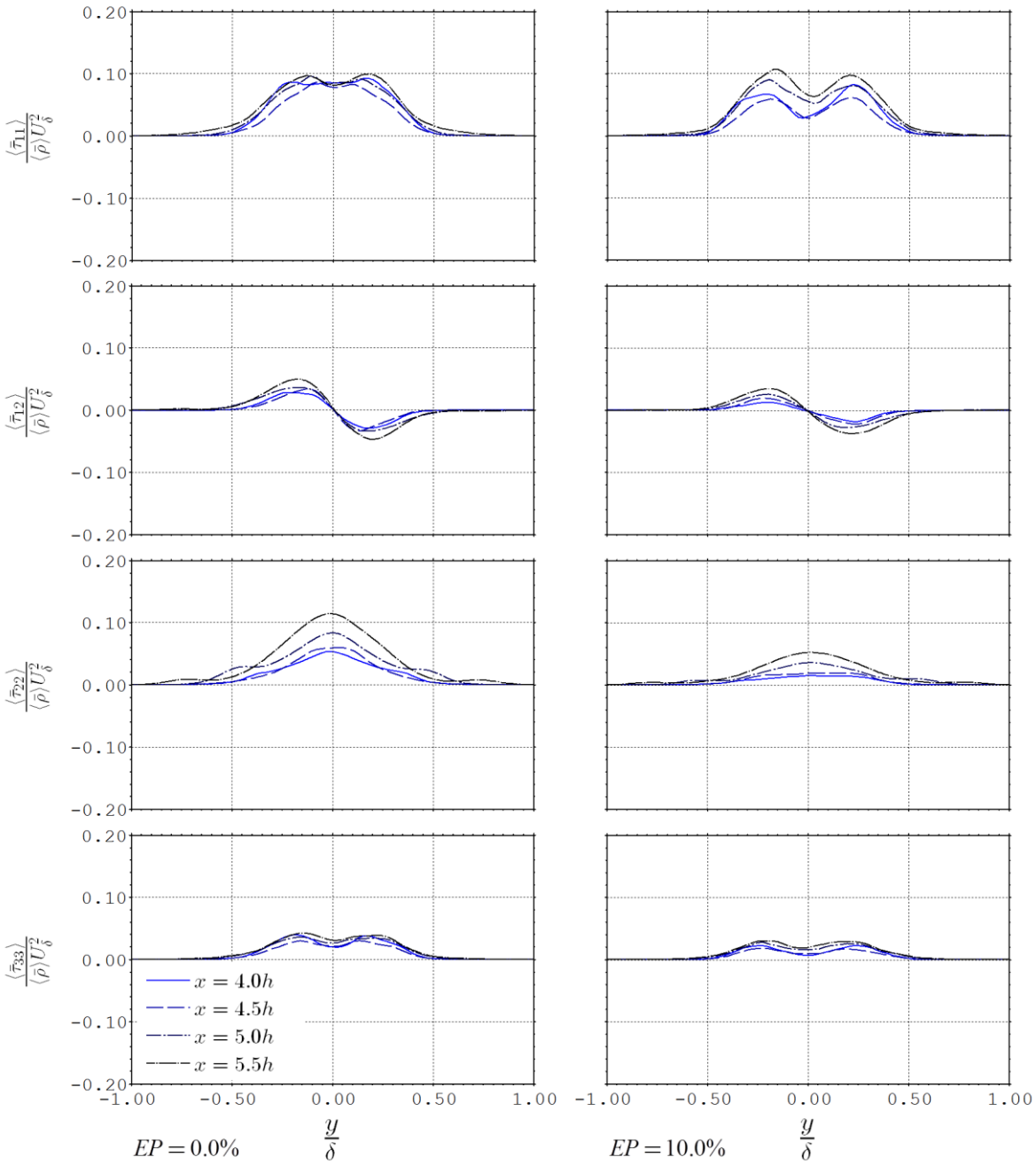

Figure 5.17: Normalised mean Reynolds stresses cross-stream profiles during the first shock turbulence interaction with $EP = 0.0\%$ (left) and $EP = 10.0\%$ (right)

5.4 LES - RANS Comparison

It has been concluded from the presented LES results that oxygen enrichment has an adverse effect on the mixing between ingested oxygen and injected hydrogen, although it does improve entrainment in the far-field which may lead to higher mixing in a longer duct. This finding is at odds with the preliminary RANS results, which showed combustion between these reactants was augmented. It is important to explore the different results of these two methodologies. The first step is to realise that the simulated flows are slightly different. The preliminary simulations included flow features generated up-stream of the duct, such as turbulent boundary-layers and weak oblique shock waves. There is also a slight discrepancy between the simulated duct heights. To conduct a true comparison, additional RANS simulations have been performed using boundary conditions (Chapter 4, section 4.1.3) that are equivalent to the LES simulations. As the RANS methodology does not employ adaptive mesh refinement, these simulations were performed on a uniform two-dimensional grid with the finest permissible LES grid spacing. Contour plots of the resultant static density gradient magnitudes are compared to the LES results for pure fuel (Figure 5.18) and oxygen enriched fuel (Figure 5.19) injection cases. There is good agreement in the recompression shock reflection and principal turbulence interaction locations between both methodologies. There is however, a smearing of the static density gradients in the mean LES data that is discernibly different from the RANS data which continues to display sharper gradients. This is due in part to the coarser grid spacing in regions were adaptive mesh is not active in the LES. However, the shock wave scattering that is observed in the LES also softens the mean density gradients. This effect is not apparent in the RANS visualisations.

One significant difference between the current and preliminary RANS results is how the injected stream is recompressed. It was previously noted that the near field turbulence behaviour was sensitive to the formation of a Mach disk rather than symmetric oblique shock waves. That the recompression Mach disk does not form in the current RANS results suggests that the condition of the up-stream boundary-layers influences its formation.

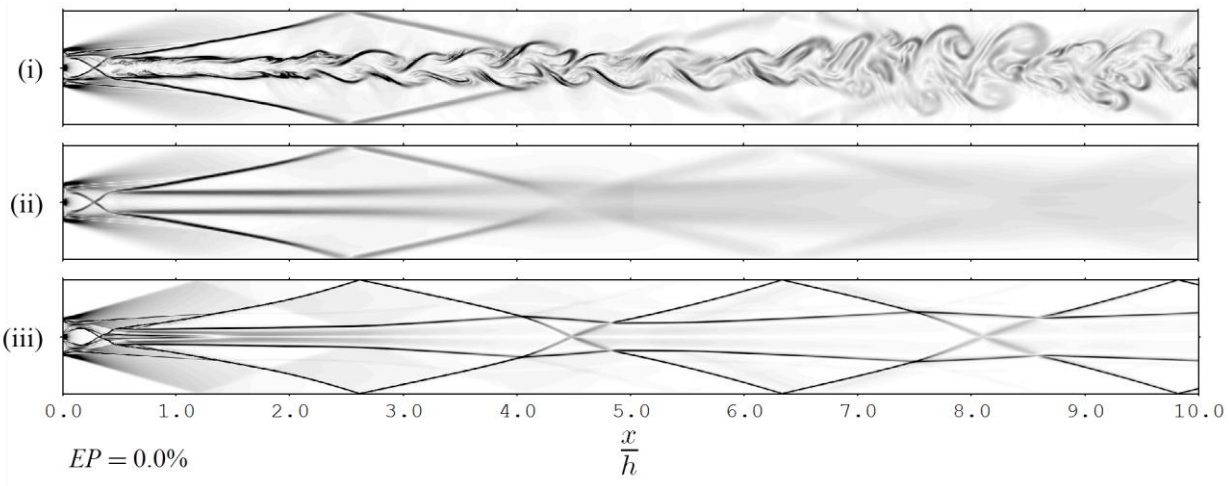

Figure 5.18: Span-wise normal $(z = 0.0)$ contours of static density gradient magnitude with $EP = 0.0\%$ using: (i) LES data taken at the instant $t = 4.0t_c$: (ii) Reynolds averaged LES data, and (iii) RANS data.

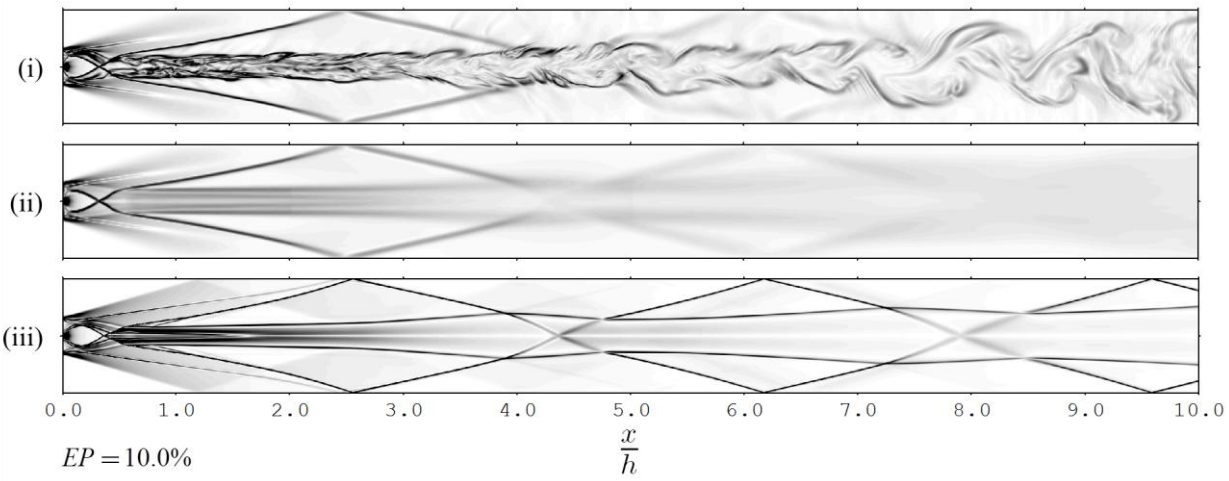

Figure 5.19: Span-wise normal $(z = 0.0)$ contours of static density gradient magnitude with $EP = 10.0\%$ using: (i) LES data taken at the instant $t = 4.0t_c$: (ii) Reynolds averaged LES data, and (iii) RANS data.

An increase in turbulence kinetic energy due to oxygen enrichment was reported both in the preliminary RANS and LES data. These preliminary results included the effects of chemical reactions and heat release so it is important to verify if this agreement exists between the non-reacting RANS simulations. Comparative contour plots between RANS and LES of the Favre-

averaged turbulence kinetic energy are shown in Figure 5.20 for the pure fuel case and Figure 5.21 for the oxygen enriched case.

The stream-wise trends of turbulence kinetic energy in the near field match fairly well, although RANS under predicts the maximum cross-stream levels by ~10% in this region. Transverse displacement between the parallel turbulent mixing layers is distinctly less in the RANS results. The onset of wake roll-up in the LES case causes a small rise in the maximum cross-stream levels which is not predicted by RANS, where the maximum levels continue to decrease down-stream. Turbulence kinetic energy along the centreline becomes measurable approximately half a duct height earlier in the RANS case. However, the levels of turbulence kinetic energy along the centreline are notably under predicted by RANS in the transitional wake roll-up region of the flow. The enhancement of turbulence kinetic energy due to shock-turbulence interactions is over-predicted in all situations. This compensates for the under predicted levels up stream such that, by $x \sim 5.5h$, both the RANS and LES turbulence kinetic energy levels are similar. The contour plots show that the transverse spreading of turbulence kinetic energy is less in the RANS case.

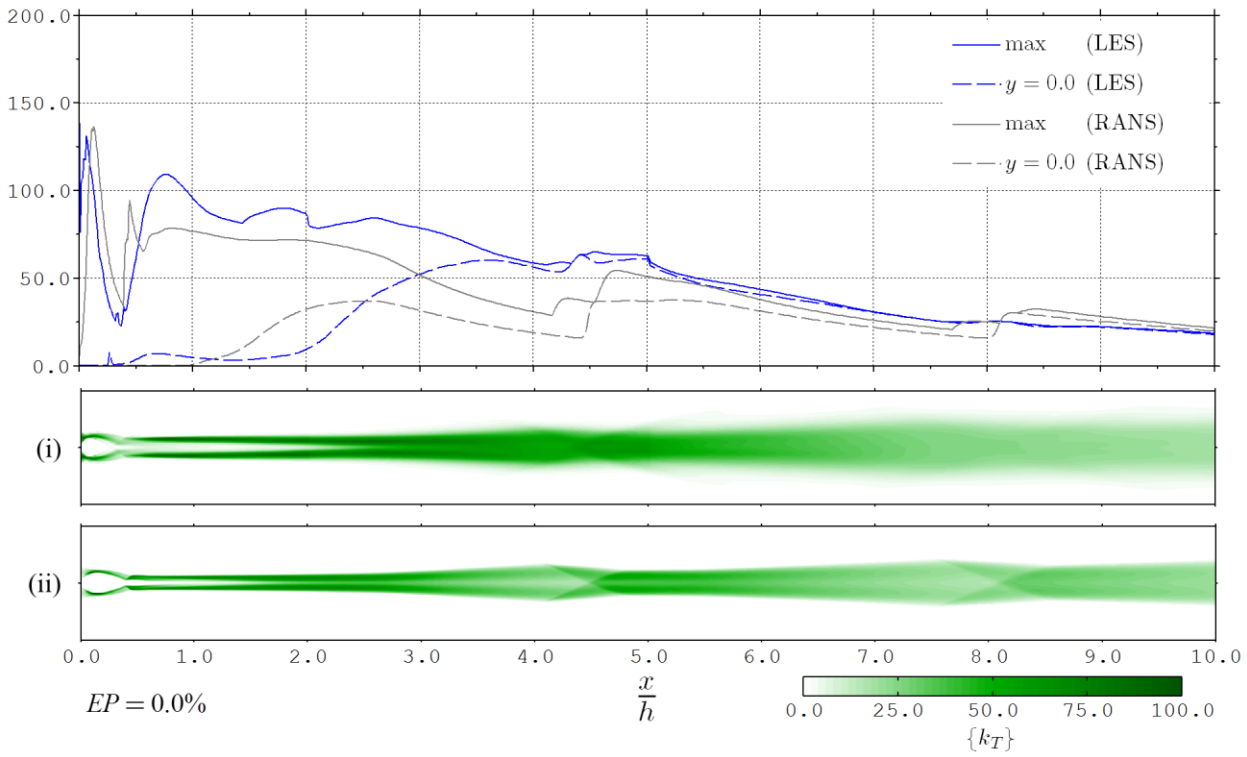

Figure 5.20: Comparison of Favre averaged turbulence kinetic energy (kJ/kg) trends with stream-wise location and contours with $EP = 0.0\%$ using: (i) LES data, and (ii) RANS data.

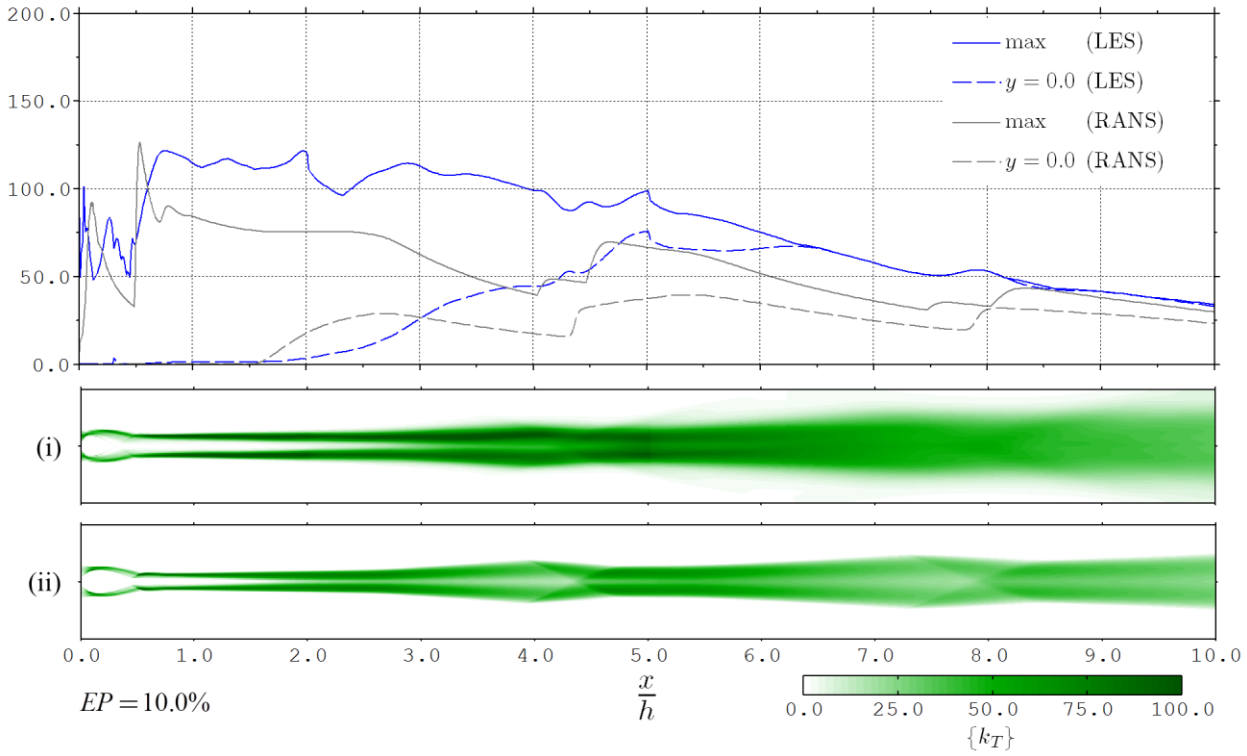

Figure 5.21: Comparison of Favre averaged turbulence kinetic energy (kJ/kg) trends with stream-wise location and contours with $EP = 10.0\%$ using: (i) LES data, and (ii) RANS data.

The observed under predictions made in regards to the RANS-LES pure fuel case appear intensified in the case of oxygen enriched fuel injection. The maximum cross-stream turbulence levels in the initial mixing layers are under predicted by ~30% in the OxEn case. As with the pure fuel case, the transverse displacement of these mixing layers is under predicted in the RANS results. Unlike the pure fuel case, turbulence level enhancement due to the principal shock interaction does not compensate the up-stream under predictions. It is not until the second shock-turbulence interaction that the turbulence intensities of the RANS simulation return to similar levels of the LES results. Cross-stream diffusion of turbulence is substantially under predicted in the OxEn case once wake roll-up is observed in the LES data. It is apparent from these findings that RANS does not successfully model the effects of the mixing wake roll-up.

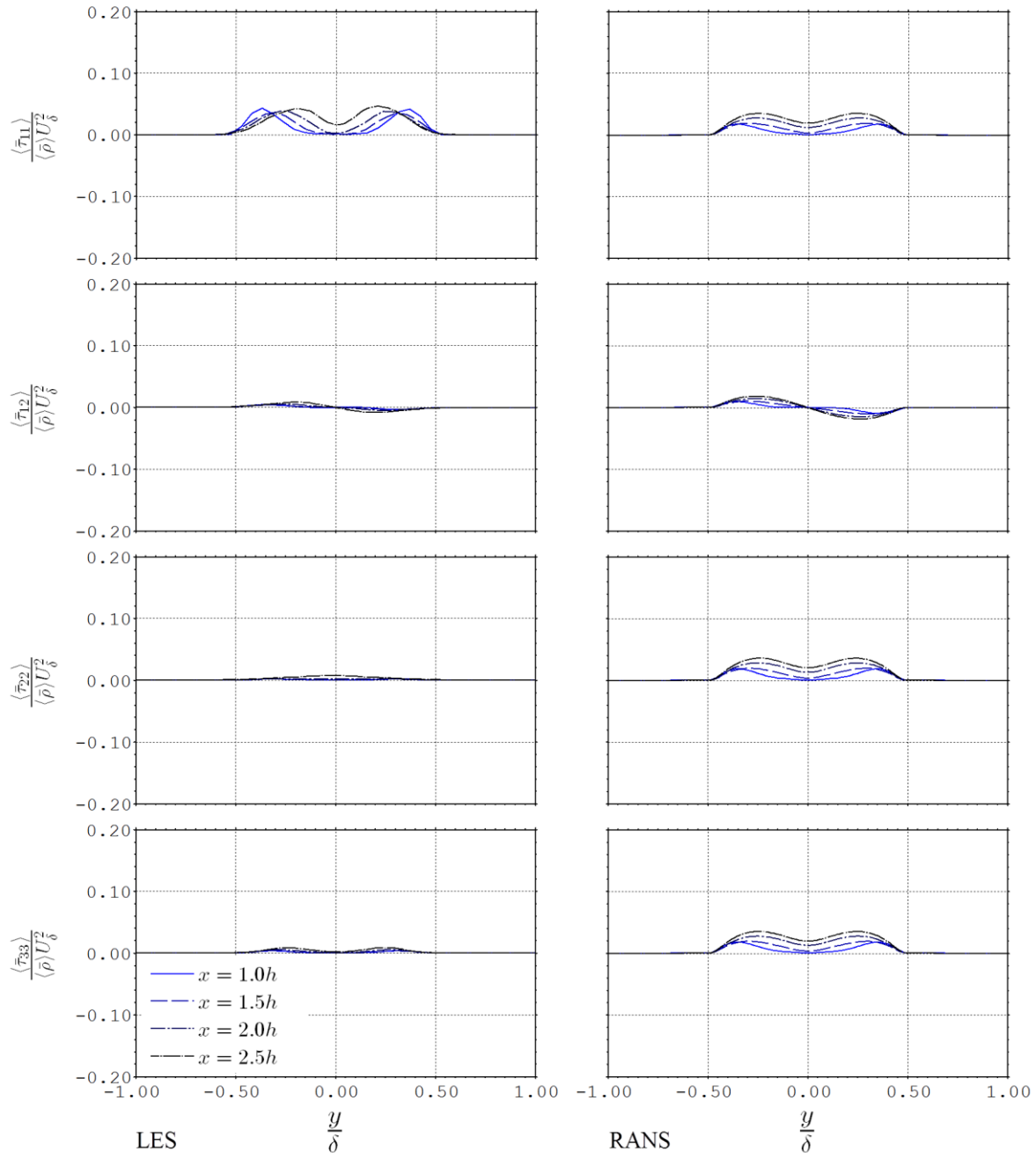

Figure 5.22: Normalised mean Reynolds stresses cross-stream profiles during the wake transition with $EP = 0.0\%$ using: (left) LES data, and (right) RANS data.

Normalised Reynolds stress profiles of the pure fuel wake transition, for both LES and RANS, are shown in Figure 5.22. The high degree of Reynolds normal stress anisotropy observed in the LES case is not replicated in the RANS results. All three of the RANS modelled Reynolds normal stresses are near identical. This is not an unexpected result as the RANS simulations used a two-

equation turbulence model that computes the evolution of the turbulence kinetic energy and the turbulence specific dissipation. The Boussinesq eddy-viscosity approximation does produce variations in the Reynolds normal stresses when there is strong local variation in mean shear. However, the resultant stress is proportional to an eddy viscosity calibrated to dissipate turbulence appropriately rather than model turbulence anisotropy. Further to this, a choice of scalar eddy viscosity may not even be appropriate for the modelling of such anisotropic turbulence.

Comparison of the mean mixing efficiency trends derived from the current RANS data and the LES data will determine if the changes to the problem definition have resulted in the less than expected mixing efficiency achieved by oxygen enrichment. These trends are shown in Figure 5.23. Current RANS results predict a marginally higher rate of mixing initially, in the region where turbulence is generated within symmetric, developing mixing layers. Over-prediction of the effect expansion has upon mixing results in these higher rates to drop below those of the LES. Discrepancies between RANS and LES results arise after the first shock interaction in the pure fuel case. The LES data shows that the shock turbulence interaction stimulates the mixing of oxygen which was entrained by the wake roll-up. The RANS data does not show the same intensified mixing as it is unable to capture the wake-roll up entrainment process. RANS continues to under-predict the turbulence diffusion of oxygen into the wake down-stream. The final mixing efficiency estimated by RANS is 34%, compared to 46% by LES, which is a sizeable disagreement. Agreement between RANS and LES is maintained further down-stream, until $x = 6.5h$, in the case of oxygen enrichment. These mixing rate trends diverge down-stream of this location once the enriched wake roll-up is apparent.

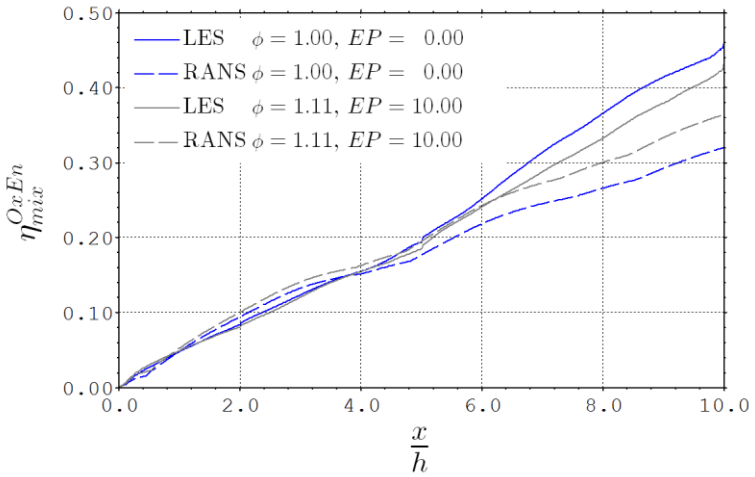

Figure 5.23: Comparison of Reynolds averaged mixing efficiency trends of with stream-wise location: RANS and LES; pure and oxygen enriched fuel injection.

The trends in mixing efficiency highlight the inability of the RANS turbulence model to successfully model the wake roll-up event. The LES turbulence statistics have shown a large degree of anisotropy, where cross-stream fluctuations are suppressed in near-field, then disproportionally intensified by shock interactions. It is not surprising that a two-equation turbulence model, which does not model each Reynolds stress independently, fails to predict this behaviour. LES predicts oxygen enrichment reduces the amount of ingested oxygen that is mixed with hydrogen, whereas RANS predicts the opposite. It is unfortunate that failing to predict the benefits of wake roll-up on mixing, and that oxygen enrichment delays it, results in a reversed conclusion to be made regarding the effects of oxygen enrichment.

5.5 Conclusions

This chapter has presented LES results of the oxygen enriched mixing wake flow. More extensive transverse expansion of the injected oxygen enriched fuel was found due to the dynamic effect of injecting more mass flow rate at a higher static pressure. Greater levels of compressibility were found to influence the initial turbulent mixing layers which form between the ingested and injected streams as a consequence of the lower injectant speed of sound and greater shearing velocity difference across the layers. Despite the higher levels of compressibility, oxygen enrichment was found to enhance the turbulence kinetic energy levels within the near field mixing layers due to up-stream turbulence generated between the over-expanded injected stream and the ingested stream being fed into these layers. Both the entrainment and mixing rates of ingested oxygen with injected fuel were found to be almost equivalent in both LES cases.

High levels of compressibility were found to persist further down-stream in the oxygen enriched mixing wake case. This observation correlates with a delay in the wake roll-up, which occurs downstream of the principal shock-turbulence interaction. Consequently, the entrainment rate of ingested air into the mixing wake is notably less than the pure fuel case just before the shock-turbulence interaction. Once oxygen enriched wake roll-up does occur, just down-stream of the principal shock interaction, it is characterised by dominant, span-wise coherent vortices which are spaced further apart and achieve greater transverse penetration into the ingested stream when compared to the pure fuel case. The entrainment rate subsequently increases once wake roll-up occurs and a larger fraction of the ingested oxygen becomes entrained in the OxEn mixing wake as the flow exits the domain. However, the large scale vortical structures which dominate the mixing wake structure do not appear to evolve into fully developed turbulence by the exit of the domain. This is evident in the slightly lower mixing efficiency between ingested oxygen and injected fuel in comparison to the pure fuel case.

Simulations of the mixing wake flow were also performed using a RANS methodology to determine if the LES results could be replicated. These results demonstrate that RANS was able to broadly predict the observed increase in turbulence kinetic energy within the initial mixing layers by enriching the injected fuel with oxygen. However, the exact turbulence levels and transverse diffusion of turbulence were under predicted. In addition, RANS was unable to predict the

substantial Reynolds stress anisotropy observed in the initial mixing layers. Despite this, good agreement of fuel-air mixing has been reported between LES and RANS in this region of the flow. The inability to predict the wake roll-up was a crucial inadequacy found with the RANS technique. Stream-wise trends of mixing efficiency between ingested oxygen and injected fuel predicted by LES and RANS begin to diverge at the onset of wake roll-up, for both pure and oxygen enriched fuel injection.

This numerical study found that oxygen enrichment is a potential enabling technology for a scramjet powered access-to-space system. Greater shear between air and fuel streams can be generated using oxygen enrichment due to decreasing the sound speed of the injectant. Despite generating more significant compressibility effects, this was shown to enhance the production of turbulence kinetic energy within the fuel-air mixing regions. These outcomes indicate that OxEn has the potential to augment mixing between fuel and ingested air. However, in the case studied, oxygen enrichment has also been shown to delay a large scale instability of the mixing wake which was detrimental to the mixing of ingested oxygen and injected fuel. Once the instability evolved into span-wise coherent vortical structures, the oxygen enriched mixing wake entrained a larger fraction of the total ingested air into the turbulent region which may lead to enhanced mixing further down-stream. These structures are specific to the mixing wake flow field and the influence of oxygen enrichment on instabilities of other flow fields must be examined on a case-by-case basis. High fidelity simulations of a more practical scramjet engine internal flow path must be performed to assess to true benefits of oxygen enrichment upon high altitude scramjet engine performance.

.

6 Conclusions

Both LES and RANS simulations of the hypervelocity mixing wake flow which forms behind a planar slot injection strut were performed. Both pure and oxygen enriched fuel injection cases were simulated, the results of which have been compared to equivalent RANS simulations. The principal findings of this study are summarised in section 6.1. These findings support the three research objectives of: characterising the hypervelocity mixing wake, identifying important flow physics that is altered by oxygen enrichment, and comparing the accuracy of RANS simulations with the LES results. This chapter concludes with several comments regarding future research into hypervelocity mixing and oxygen enrichment in section 6.2.

6.1 Principal Findings

A simple analysis of an access-to-space trajectory which maintains a constant dynamic pressure has shown that the captured air mass flow rate into an air-breathing engine decreases with increasing altitude/speed. This will adversely affect the engine performance. To supplement this reduction in air mass capture, additional oxidiser can be pre-mixed with fuel in a technique referred to as oxygen enrichment. Preliminary RANS simulations of a simplified scramjet engine have shown that oxygen enrichment provides additional benefits, such as enhanced combustion of fuel with ingested air. It was found that this enhanced combustion was due to greater shear and hence production of turbulence kinetic energy within the turbulent fuel-air mixing regions. A posteriori analysis of the turbulence scales predicted by the RANS simulations indicated that the mixing wake turbulence regime exhibits a truncated sub-inertial range and may not be well modelled.

LES of a hypervelocity planar mixing wake were performed to verify the findings of the preliminary RANS simulation. The LES of pure fuel injection into a planar wake has enabled the visualisation and characterisation of the mixing wake flow at conditions representative of those within a scramjet combustor operating at high altitude and at hypersonic speeds. It was found that the mixing wake exhibits several distinct characteristics as it develops. The near-field flow structure is dominated by the unstable recirculation region that forms between the over-expanded injected stream and the ingested stream. Parallel mixing layers then form after recompression of the injected stream which display highly compressible turbulence influenced by instabilities seeded from the recirculating flow structure. The presence of oblique shocklets emanating from the outer edges of the injected stream towards the ingested free-stream is the most acute effect of compressibility. The structure of the mixing layers is dominated by near stream-wise aligned vortices, characteristic of a highly compressible shear flow, which generate high levels of turbulence kinetic energy. However, the transverse growth of these stream-wise vortices is suppressed which confines the turbulent fluid motion within a thin layer. Consequently, the entrainment of ingested oxygen into the mixing wake occurs at a relatively slow rate. Of the oxygen that is entrained, approximately 74% is well mixed by the energetic turbulent fluid motion.

The dominant turbulent structures of the mixing wake undergo an observable transition from near stream-wise vortex streaks to larger span-wise coherent vortices that resemble a wake roll-up vortex sheet. Low-frequency span-wise oscillations are also apparent, giving rise to an undulating three-dimensional mixing interface. The smaller, stream-wise vortex streaks continue down-stream but are wrapped up by these larger structures. The vortex roll-up appears to be an intrinsic instability of the wake, the onset of which relies on interactions between the parallel mixing layers. The formation of larger structures within the mixing wake increases the entrainment rate of ingested oxygen into the mixing wake, but does not immediately lead to more effective mixing of ingested oxygen with fuel. The roll-up structures experience a transverse contraction due to the principal shock turbulence interaction which adversely affects the entrainment rate of air into the mixing wake. The turbulence kinetic energy within the mixing wake is mildly stimulated by this interaction. More significantly, the shock interaction increases the cross-stream Reynolds normal stress within the mixing wake by more than a factor of two. Growth of the wake roll-up recommences immediately down-stream of the shock-turbulence interaction and the entrainment rate of air returns to similar levels calculated during the wake roll-up onset. As the mixing wake continues to develop, it exhibits a remarkable similarity to an incompressible wake flow despite the persistent formation of weak oblique shocks at the edge of the largest turbulent eddies. One possible explanation is that these weak shocks are only influential at the outer edges of the mixing wake, and at the largest scales, leaving the turbulent fluid motion within the wake unabated.

In addition to the pure fuel case, Large Eddy Simulations of oxygen enriched fuel injection into the planar wake have also been performed. In the near-field, equivalent high frequency span-wise aligned wave-like disturbances within the recirculation region are observed in both LES cases. The dynamic effect of injecting more mass causes greater transverse penetration of the over-expanded jet into the ingested stream. Another effect of oxygen enrichment is to reduce the sound speed of the injected stream which, in the case of sonic injection, results in a slower moving core flow. The formation of parallel mixing layers down-stream of the recompression structure experiences higher levels of compressibility in the case of oxygen enrichment principally due to the reduced acoustic speed of the injectant but also a mild increase in the shearing velocity difference across the layers. This is matched with greater Reynolds stress anisotropy due to a greater suppression of the cross-stream Reynolds normal stress. Stratification of high density injectant core flow and lower density

fluid within the mixing layers is observed as a result of varying levels of recompression of the injected stream in the near-field. Higher levels of turbulence kinetic energy, with respect to the pure fuel case, are detected within these initial mixing layers. This was a result of up-stream turbulence generated at the edge of the over-expanded injected stream feeding directly into the layers, which did not occur to the same extent in the pure fuel case. The mixing rate of fuel with ingested oxygen remains effectively the same, despite the increased turbulence kinetic energy level, as entrainment of ingested oxygen into the wake is limited by a lack of larger turbulent structures in the near field.

The most significant character change of the oxygen enriched mixing layer is the delayed wake roll-up. In contrast to the pure fuel case, the formation of larger, span-wise coherent vortical structures does not occur until after the principal shock-turbulence interaction. This is most likely a consequence of higher levels of compressibility experience, which remains prominent over a longer period of the early mixing wake development. The suppression of cross-stream turbulent fluctuations, in addition to the dynamic effect of injecting more mass which further displaces the initial mixing layers, prevents the unstable interaction between the parallel mixing layers until further down-stream. Whilst the OxEn mixing wake roll-up is delayed, there is discernibly less entrained ingested oxygen within the OxEn mixing wake in comparison to the pure fuel case. Once the OxEn mixing wake undergoes roll-up, as the flow nears the domain exit, the entrainment of ingested oxygen exceeds that of the pure fuel mixing wake. However, this does not translate into better mixing between ingested oxygen and fuel by the extent of the domain as the large scale structures have not yet broken-down into fully developed turbulence.

The mixing characteristics derived from the LES results are at odds with the combustion efficiency trends with oxygen enrichment that were observed in the preliminary RANS simulations. Two additional RANS simulations were performed so that a direct comparison with the LES cases could be made. The predicted fuel-air mixing within the initial mixing layers by RANS was found to have good agreement with the LES. Both numerical methods demonstrate a similar enhancement of turbulence kinetic energy within the near field mixing layers, despite increasing the convective Mach number by ~20%. This agreement extends to the near field fuel-air mixing characteristics, in which both methods predict pure fuel and OxEn cases achieve near equivalent mixing rates between ingested oxygen and injected fuel. There are, however, several notable deficiencies in the ability of RANS to predict the mixing wake behaviour observed in the LES, which include: the failure to

predict the substantial Reynolds normal stress anisotropy in the initial mixing layers, the wake roll-up and transition towards a fully developed turbulent wake flow, and the effective diffusion of the recompression shock wave due to its scattered refraction as it interacts with the turbulent eddies. The inability to predict wake roll-up is most telling in the calculated fuel-air mixing rate as LES and RANS stream-wise trends in mean mixing efficiency diverge at the onset of the roll-up. Thus, whilst RANS predicted a continuation of improved mixing performance of the oxygen enriched case, the earlier onset of wake roll-up in the pure fuel LES causes it to surpass the enriched LES case.

6.2 Recommendations for Future Work

This study has revealed some important physical aspects of fuel-air mixing within a hypervelocity wake. Discrepancies were found between the results of the two numerical techniques used and direct comparison with experimental data was not possible as several simplifications were made. Comparison to experimental data provides the best means of validating numerical results and it is recommended that the findings of this work should be supplemented by more realistic high fidelity simulations of Razzaqi & Smart (2011) experiments. The first item to address is the boundary-layers which form on the walls of the duct. These boundary-layers directly influence the direction and strength of the shock reflection that subsequently interacts with the mixing wake, as well as potentially interacting with the mixing wake down-stream causing wall blockage. This would require an alternative numerical approach such as a hybrid RANS/LES methodology. Consideration must also be given to the realistic condition of the ingested stream as it enters the duct, such as three-dimensional effects and radical chemical species generated in the high enthalpy T4 impulse facility. Finally, the physical effects of combustion and turbulence-chemistry interactions require treatment to replicate the experimental conditions. This would also allow assessment of the combustion characteristics of the scramjet engine, which is more closely related to the overall engine performance. Tackling these items demands state-of-the-art numerical methods, in particular the modelling of sub-grid scale turbulence-chemistry interactions, and represents a much larger computational effort than the simulations performed for this work.

A more natural extension of this work would be the exploration of the hypervelocity mixing wake flow physics at a different flight conditions. This would be aligned with the envisaged use of oxygen enrichment, which aims to supplement the reducing mass capture of atmospheric air. It would be advantageous to perform a comparative study between a lower altitude condition with pure fuel injection, and a higher altitude condition that maintains the injected mass flow rate of fuel whilst ensuring a stoichiometric ratio with available oxidiser by using OxEn. These two conditions would better represent the application of oxygen enrichment during a true flight and highlight how the internal flow physics varies with altitude/speed.

The larger design problem of high altitude operation of a scramjet engine with oxygen enrichment requires further attention. The benefits of oxygen enrichment upon scramjet combustion initially found using RANS have been challenged by an apparent inability to accurately model the mixing wake turbulence. Higher fidelity LES showed that the fuel-air mixing characteristics of the wake flow were adversely affected by oxygen enrichment, albeit modestly. In fact, these results also suggest that down-stream mixing beyond the computational domain extent may be enhanced by oxygen enrichment as better entrainment of air into the fuel wake is achieved. It is also important to note that the overall mixing efficiency did increase due to the introduction of pre-mixed oxygen into the fuel. Consequently, oxygen enrichment remains a potentially enabling technology for scramjet powered access-to-space systems. As the conclusions found in this thesis are based upon a simplified scramjet engine geometry, questions remain regarding the ability of oxygen enrichment to enhance fuel-air mixing within a more practical engine design. For example, changes of fuel injection configuration and three dimensional effects generated within the inlet will strongly influence the larger turbulent structures which control the entrainment of air into regions of fuel rich fluid flow. This report recommends that such questions would be most appropriately answered by a combined experimental/high fidelity numerical approach which simulates a more realistic scramjet design operating at a high altitude condition and utilising OxEn. Once performance trends with oxygen enrichment are quantified for a more practical engine, optimised trajectory studies of a scramjet launcher systems can be undertaken to determine if oxygen enrichment can extend the operation limits of the air-breathing engine whilst maintaining better overall performance with regards to multi-stage rocket launchers.

Reference List

Andrews, E. & Mackley, E., 1994. *NASA's Hypersonic Research Engine Project: A Review,* s.l.: NASA.

Aupoix, B., 2004. Modelling of Compressibility Effects in Mixing Layers. *Journal of Turbulence,* Volume 5, p. N7.

Barone, M., Oberkampf, W. & Blottner, F., 2006. Validation Case Study: Prediction of Compressible Turbulent Mixing Layer Growth Rate. *AIAA Journal,* July, 44(7), pp. 1488-1497.

Barthelemy, R., 1989. The National Aero-Space Plane Program. *AIAA Paper,* Volume 1989-5001.

Batchelor, G. K., 1959. Small-scale Variation of Convected Quantities Like Temperature in Turbulent Fluid: Part 1. General Discussion and the Case of Small Conductivity. *Journal of Fluid Mechanics,* Volume 5, pp. 113-133.

Baurle, R. A. & Edwards, J. R., 2010. Hybrid Reynolds-Averaged/Large-Eddy Simulations of a Coaxial Supersonic Freejet Experiment. *AIAA Journal,* March, 48(3), pp. 551-571.

Bell, J. H. & Mehta, R. D., 1990. Development of a Two-Stream Mixing Layer from Tripped and Untripped Boundary Layers. *AIAA Journal,* 28(12), pp. 2034-2042.

Berglund, M., E., F., Fureby, C. & Tegnér, J., 2010. Finite Rate Chemistry Large-Eddy Simulation of Self-Ignition in a Supersonic Combustion Ramjet. *AIAA Journal,* March, 48(3), pp. 540-550.

Berglund, M. & Fureby, C., 2007. LES of Supersonic Combustion in a Scramjet Engine Model. *Proceedings of the Combustion Institute,* January, 31(2), pp. 2497-2504.

Bernal, L. P. & Roshko, A., 1986. Streamwise Vortex Structure in Plane Mixing Layers. *Journal of Fluid Mechanics,* Volume 170, pp. 499-525.

Billig, F. S., 1995. Supersonic Combustion Ramjet Missile. *Journal of Propulsion and Power,* 11(6), pp. 1139-1146.

Birch, S. F. & Eggers, J. M., 1972. *A Critical Review of the Experimental Data for Developed Free Turbulent Shear Layers.* Hampton, Virginia, s.n., pp. 11-40.

Bogdanoff, D., 1983. Compressibility Effects in Turbulent Shear Layers. *AIAA Journal,* 21(6), pp. 926-7.

Boussinesq, J., 1877. Theorie de l'écoulement Tourbillonant. *Mem. Pres. Acad. Sci. Inst. Fr.,* 23(Boussinesq_1877), pp. 46-50.

Bradshaw, P., 1977. Compressible Turbulent Shear Layers. *Annual Review of Fluid Mechanics,* 9(1), pp. 33-52.

Bradshaw, P., 1981. *Compressibility Effects on Free-Shear Layers.* Stanford, California, Stanford University, p. 364–368.

Brown, G. L. & Roshko, A., 1974. On Density Effects and Large Structure in Turbulent Mixing Layers. *Journal of Fluid Mechanics,* Volume 64, pp. 775-816.

Casey, R. T., 1990. *An Investigation of Supersonic and Hypersonic Hydrogen Mixing and Combustion.* Brisbane, QLD, Australia: The University of Queensland.

Chapman, D. K., 1979. Computational Aerodynamics Development and Outlook. *AIAA Journal,* 17(12), pp. 1293-1313.

Chapuis, M. et al., 2013. A Computational Study of the HyShot II Combustor Performance. *Proceedings of the Combustion Institute,* 34(2), pp. 2101-2109.

Chong, M., Perry, A. & Cantwell, B., 1990. A General Classification of Three-Dimensional Flow Fields. *Physics of Fluids,* 2(5), pp. 765-777.

Chow, F. K. & Moin, P., 2003. A Further Study of Numerical Errors in Large-Eddy Simulations. *Journal of Computational Physics,* 184(2), pp. 366-380.

Clark, R. A., Ferziger, J. H. & Reynolds, W. C., 1979. Evaluation of Subgrid-scale Models Using an Accurately Simulated Turbulent Flow. *Journal of Fluid Mechanics,* Volume 91, pp. 1-16.

Clemens, N. T. & Mungal, M. G., 1992. Two- and Three-Dimensional Effects in the Supersonic Mixing Layer. *AIAA Journal,* April, 30(4), pp. 973-981.

Clemens, N. T. & Mungal, M. G., 1995. Large-Scale Structure and Entrainment in the Supersonic Mixing Layer. *Journal of Fluid Mechanics*, Volume 284, pp. 171-216.

Commonwealth of Australia, 2013. *Australia's Satellite Utilisation Policy*, Canberra, ACT, Australia: Commonwealth of Australia.

Coopersmith, J., 2011. The Cost of Reaching Orbit: Ground-Based Launch Systems. *Space Policy*, 27(2), pp. 77-80.

Curran, E. T. & Murthy, S. N. B., 2000. *Scramjet propulsion.* s.l.:American Institute of Aeronautics and Astronautics.

Cutler, A. D. & White, J. A., 2001. *An Experimental and CFD Study of a Supersonic Coaxial Jet.* s.l., s.n.

Deardorff, J. W., 1970. A Numerical Study of Three-dimensional Turbulent Channel Flow at Large Reynolds Numbers. *Journal of Fluid Mechanics,* 41(2), pp. 453-480.

Dimotakis, P. E., 1986. Two-Dimensional Shear-Layer Entrainment. *AIAA Journal,* November, 24(11), pp. 1791-1796.

Dimotakis, P. E., 1991. Turbulent Mixing and Combustion. In: S. N. B. Murthy & E. T. Curran, eds. *High-Speed Flight Propulsion Systems.* s.l.:American Institute of Aeronautics and Astronautics, pp. 265-340.

Dimotakis, P. E., 2000. The Mixing Transition in Turbulent Flows. *Journal of Fluid Mechanics*, Volume 409, pp. 69-98.

Drummond, J. P., 1988. *A Two-Dimensional Numerical Simulation of a Supersonic, Chemically Reacting Mixing Layer,* s.l.: s.n.

Elliott, G. S. & Samimy, M., 1990. Compressibility effects in free shear layers. *Physics of Fluids,* 2(7), pp. 1231-1240.

Favre, A., 1965. Equations des Gaz Turbulents Compressibles. *Journal de Mécanique,* 4(3), pp. 361-390.

Ferri, A., 1973. Mixing-Controlled Supersonic Combustion. *Annual Review of Fluid Mechanics,* 5(1), pp. 301-338.

Ferri, A., Moretti, G. & Slutsky, S., 1965. Mixing Processes in Supersonic Combustion. *Journal of the Society for Industrial and Applied Mathematics,* March, 13(1), pp. 229-258.

Foysi, H. & Sarkar, S., 2010. The Compressible Mixing Layer: an LES Study. *Theoretical and Computational Fluid Dynamics,* 24(6), pp. 565-588.

Fureby, C., Chapuis, M., Fedina, E. & Karl, S., 2011. CFD analysis of the HyShot II scramjet combustor. *Proceedings of the Combustion Institute,* 33(2), pp. 2399-2405.

Génin, F. & Menon, S., 2010. Simulation of Turbulent Mixing Behind a Strut Injector in Supersonic Flow. *AIAA Journal,* 48(3), pp. 526-539.

Germano, M., 1992. Turbulence: the Filtering Approach. *Journal of Fluid Mechanics,* Volume 238, pp. 325-336.

Germano, M., Piomelli, U., Moin, P. & Cabot, W. H., 1991. A Dynamic Subgrid-scale Eddy Viscosity Model. *Physics of Fluids,* July, 3(7), pp. 1760-1765.

Gerrard, J. H., 1966. The Mechanics of the Formation Region of Vortices Behind Bluff Bodies. *Journal of Fluid Mechanics,* 25(2), pp. 401-413.

Ghosal, S., 1996. An Analysis of Numerical Errors in Large-Eddy Simulations of Turbulence. *Journal of Computational Physics,* Volume 125, pp. 187-206.

Ghosal, S. & Moin, P., 1995. The Basic Equation for the Large Eddy Simulation of Turbulent Flows in Complex Geometry. *Journal of Computational Physics,* Volume 118, pp. 24-37.

Goebel, S. G. & Dutton, J. C., 1991. Experimental Study of Compressible Turbulent Mixing Layers. *AIAA Journal,* April, 29(4), pp. 538-546.

Goebel, S. G., Dutton, J. C., Krier, H. & Renie, J. P., 1990. Mean and Turbulent Velocity Measurements of Supersonic Mixing Layers. *Experiments in Fluids,* 8(5), pp. 263-272.

Hank, J. M., Murphy, J. S. & Mutzman, R. C., 2008. *The X-51A Scramjet Engine Flight Demonstration Program.* Dayton, Ohio, U.S.A., s.n.

Heiser, W. H. & Pratt, D. T., 1994. *Hypersonic Airbreathing Propulsion.* s.l.:Washington, D.C. : American Institute of Aeronautics and Astronautics.

He, Y. & Morgan, R. G., 1994. Transition of Compressible High Enthalpy Boundary Layer Flow Over a Flat Plate. *Aeronautical Journal,* 98(972), pp. 25-34.

Hill, D. J., Pantano, C. & Pullin, D. I., 2006. Large-Eddy Simulation and Multiscale Modelling of a Richtmyer-Meshkov Instability with Reshock. *Journal of Fluid Mechanics,* Volume 557, pp. 29-61.

Hill, D. & Pullin, D. I., 2004. Hybrid Tuned Center Difference - WENO Method for Large Eddy Simulations in the Presence of Strong Shocks. *Journal of Computational Physics,* March, 194(Issue 2), pp. 435-450.

Hunt, J. L. & Martin, J. G., 2000. Rudiments and Methodology for Design and Analysis of Hypersonic Air-Breathing Vehicles. In: E. T. Curran & S. N. B. Murthy, eds. *Scramjet Propulsion.* s.l.:American Institute of Aeronautics and Astronautics, pp. 939-978.

Hussain, A. K. M. F., 1986. Coherent Structures and Turbulence. *Journal of Fluid Mechanics,* Volume 173, pp. 303-356.

Kármán, T. v., 1911. Uber den Mechanismus des Widerstandes, den ein bewegter Körper in einer Flüssigkeit erfärt. 1.. *Nachr. Ges. Wiss. Göttingen. Math.-Phys. Kl.,* pp. 509-517.

Kármán, T. v., 1912. Uber den Mechanismus des Widerstandes, den ein bewegter Körper in einer Flüssigkeit erfärt. 1.. *Nachr. Ges. Wiss. Göttingen. Math.-Phys. Kl.,* pp. 547-556.

Kawai, S. & Lele, S. K., 2010. Large-Eddy Simulation of Jet Mixing in a Supersonic Turbulent Crossflow. *AIAA Journal,* September, 48(9), pp. 2063-2083.

Kolmogorov, A. N., 1941. The Local Structure of Turbulence in Incompressible Viscous Fluid for Very Large Reynolds Numbers. *Dokl. Akad. Nauk SSSR,* Volume 30, pp. 301-305.

Kosovic, B., Pullin, D. I. & Samtaney, R., 2002. Subgrid-Scale Modeling for Large-Eddy Simulations of Compressible Turbulence. *Physics of Fluids,* Volume 14, pp. 1511-1522.

Laney, C. B., 1998. *Computational Gasdynamics.* s.l.:Cambridge University Press.

Launder, B. & Sharma, B., 1974. Application of the Energy-Dissipation Model of Turbulence to the Calculation of Flow Near a Spinning Disc. *Letters in Heat and Mass Transfer,* 1(2), pp. 131-137.

Lax, P. & Wendroff, B., 1960. Systems of Conservation Laws. *Communications on Pure and Applied Mathematics,* 13(2), pp. 217-237.

Lee, S., Lele, S. K. & Moin, P., 1991. Eddy Shocklets in Decaying Compressible Turbulence. *Physics of Fluids,* 3(4), pp. 657-664.

Lele, S. K., 1994. Compressibility Effects on Turbulence. *Annual Review of Fluid Mechanics,* 26(1), pp. 211-254.

Leonard, A., 1974. Energy Cascade in Large-eddy Simulations of Turbulent Fluid Flows. *Advances in Geophysics,* Volume 18, p. 237.

Lilly, D., 1992. A Propsed Modification of the Germano Subgrid-scale Closure Method. *Physics of Fluids,* March, 4(3), pp. 633-635.

Lombardini, M. a. D. R. a. P. D. I., 2008. Large Eddy Simulations of the Richtmyer–Meshkov Instability in a Converging Geometry. In: J. a. G. B. J. a. S. P. Meyers, ed. *Quality and Reliability of Large-Eddy Simulations.* s.l.:Springer Netherlands, pp. 283-294.

Lundgren, T., 1982. Strained Spiral Vortex Model for Turbulent Fine Structure. *Physics of Fluids,* 25(12), pp. 2193-2203.

Martin, M. P., Piomelli, U. & Candler, G. V., 2000. Subgrid-scale Models for Compressible Large-eddy Simulations. *Theoretical and Computational Fluid Dynamics,* Volume 13, pp. 361-376.

Matheou, G., Bonanos, A. M., Pantano, C. & Dimotakis, P. E., 2010. Large-eddy Simulation of Mixing in a Recirculating Shear Flow. *Journal of Fluid Mechanics,* Volume 646, pp. 375-414.

McBride, B. J., Gordon, S. & Reno, M. A., 1993. *Coefficients for Calculating Thermodynamic and Transport Properties of Individual Species,* s.l.: s.n.

McClinton, C. R., Rausch, V. L., Nguyen, L. T. & Sitz, J. R., 2005. Preliminary X-43 Flight Test Results. *ACTA Astronautica,* 57(2), pp. 266-276.

Menter, F. R., 1994. Two-Equation Eddy-Viscosity Turbulence Models for Engineering Applications. *AIAA Journal,* 32(8), pp. 1598-1605.

Meshkov, E. E., 1969. Instability of the Interface of Two Gases Accelerated by a Shock Wave. *Fluid Dynamics,* 4(5), pp. 101-104.

Misra, A. & Pullin, D. I., 1997. A Vortex-based Subgrid Stress Model for Large-eddy Simulation. *Physics of Fluids,* August, 9(8), pp. 2443-2454.

Morkovin, M. V., 1962. Effects of Compressibility on Turbulent Flow. In: A. Favre, ed. *The Mechanics of Turbulence.* Paris: Gordon and Breach, p. 367.

Morris, P. J., Giridharan, M. G. & Lilley, G. M., 1990. On the Turbulent Mixing of Compressible Free Shear Layers. *Proceedings: Mathematical and Physical Sciences,* 431(1882), pp. pp. 219-243.

NASA, 1976. *U.S. Standard Atmosphere,* s.l.: s.n.

Nicholls, J. A., Jr., T. C. A. & Morisson, R. B., 1963. Ignition Time Delay of Hydrogen-Oxygen-Diluent Mixtures at High Temperatures. *AIAA Journal,* October, 1(10), pp. 2253-2257.

OECD, 2014. *The Spce Economy at a Glance 2014,* s.l.: OECD Publishing.

Olds, J. R. & Budianto, I. A., 1998. *Constant Dynamic Pressure Trajectory Simulation with POST.* Reno, NV, AIAA.

Pantano, C., Deiterding, R., Hill, D. & Pullin, D., 2007. A Low Numerical Dissipation Patch-Based Adaptive Mesh Refinement Method for Large-Eddy Simulation of Compressible Flow. *Journal of Computational Physics,* January, 221(Issue 1), pp. 63-87.

Pantano, C. & Sarkar, S., 2002. A Study of Compressibility Effects in the High-Speed Turbulent Shear Layer Using Direct Simulation. *Journal of Fluid Mechanics,* Volume 451, pp. 329-371.

Papamoschou, D. & Roshko, A., 1988. The Compressible Turbulent Shear Layer: An Experimental Study. *Journal of Fluid Mechanics,* Volume 197, pp. 453-477.

Paull, A., Alesi, H. & Anderson, S., 2002. HyShot Flight Program and How it Was Developed. Volume AIAA-02-4939.

Peterson, D. M., Boyce, R. R. & Wheatley, V., 2013. Simulations of Mixing in an Inlet-Fueled Axisymmetric Scramjet. *AIAA Journal,* 51(12), pp. 2823-2832.

Peterson, D. M. & Candler, G. V., 2010. Hybrid Reynolds-Averaged and Large-Eddy Simulation of Normal Injection into a Supersonic Crossflow. *Journal of Propulsion and Power*, Volume 26, pp. 533-544.

Peterson, D. M. & Candler, G. V., 2011. Simulations of Mixing for Normal and Low-Angled Injection into Supersonic Crossflow. *AIAA Journal,* 49(12), pp. 2792-2804.

Pike, J., 1999. The Choice of Propellants: A Similarity Analysis of Scramjet Second Stages. *Philosophical Transactions: Mathematical, Physical and Engineering Sciences,* August, 357(1759), pp. 2357-2378.

Piomelli, U., 2008. Wall-Layer Models for Large-Eddy Simulations. *Progress in Aerospace Sciences,* 44(6), pp. 437-446.

Poinsot, T. & Lele, S., 1992. Boundary Conditions for Direct Simulations of Compressible Viscous Flows. *Journal of Computational Physics,* 101(1), pp. 104-129.

Pointwise, Inc., 2012. *Pointwise User Manual.* Fort Worth: s.n.

Pomraning, E. & Rutland, C. J., 2002. Dynamic One-Equation Nonviscosity Large-Eddy Simulation Model. *AIAA Journal,* 40(4), pp. 689-701.

Pope, S. B., 1990. *Computations of Turbulent Combustion: Progress and Challenges.* Ithaca, New York, U.S.A., The Combustion Institute, pp. 591-612.

Pope, S. B., 2000. *Turbulent Flows.* s.l.:Cambridge ; New York : Cambridge University Press.

Pope, S. B., 2004. Ten Questions Concerning the Large-Eddy Simulation of Turbulent Flows. *New Journal of Physics,* Volume 6, pp. 35-58.

Potturi, A. S. & Edwards, J. R., 2014. Hybrid Large-Eddy/Reynolds-Averaged Navier–Stokes Simulations of Flow Through a Model Scramjet. *AIAA Journal,* 52(7), pp. 1417-1429.

Prandtl, L., 1945. Uber ein neues Formelsystem fur die ausgebildete Turbulenz. *Nacr. Akad. Wiss. Gottingen Math-Phys. Kl.,* pp. 6-19.

Pullin, D. I., 2000. A Vortex-based Model for the Subgrid Flux of a Passive Scalar. *Physics of Fluids,* September, 12(9), pp. 2311-2319.

Pullin, D. I. & Lundgren, T. S., 2001. Axial Motion and Scalar Transport in Stretched Spiral Vortices. *Physics of Fluids,* 13(9), pp. 2553-2563.

Razzaqi, S. A., 2011. *Oxygen Enrichment in a Hydrogen Fuelled Scramjet,* s.l.: s.n.

Razzaqi, S. A. & Smart, M. K., 2011. Hypervelocity Experiments on Oxygen Enrichment in a Hydrogen-Fueled Scramjet. *AIAA Journal,* July, 49(7), pp. 1488-1497.

Reynolds, O., 1895. On the Dynamical Theory of Incompressible Viscous Fluids and the Determination of the Criterion. *Proceedings of the Royal Society of London,* Volume 186, pp. 123-164.

Richardson, L. F., 1922. *Weather Prediction by Numerical Process.* s.l.:Cambridge, The University press.

Richtmyer, R. D., 1960. Robert D. Richtmyer. *Communications on Pure and Applied Mathematics,* 13(2), pp. 297-319.

Roache, P. J., 1997. Quantification of Uncertainty in Computational Fluid Dynamics. *Annual Review of Fluid Mechanics,* Volume 29, pp. 123-160.

Roshko, A., 1954. *On the Development of Turbulent Wakes from Vortex Sheets,* s.l.: NACA Rep..

Roshko, A., 1961. Experiments on the Flow Past a Circular Cylinder at Very High Reynolds Number. *Journal of Fluid Mechanics,* 10(3), pp. 345-356.

Roshko, A., 1993. Perspectives on bluff body aerodynamics. *Journal of Wind Engineering and Industrial Aerodynamics,* 49(1-3), pp. 79-100.

Rudakov, A. S. & Krjutchenko, V. V., 1990. *Additional Fuel Component Application for Hydrogen Scramjet Boosting.* s.l., s.n.

Rudy, D. H. & Strikwerda, J. C., 1980. A Nonreflecting Outflow Boundary Condition for Subsonic Navier-Stokes Calculations. *Journal of Computational Physics,* 36(1), pp. 55-70.

Sabin, C. M., 1965. An Analytical and Experimental Study of the Plane, Incompressible, Turbulent Free-Shear Layer With Arbitrary Velocity Ratio and Pressure Gradient. *Trans A.S.M.E. D,* 87(2), pp. 421-428.

Saddoughi, S. G. & Veeravalli, S. V., 1994. Local Isotropy in Turbulent Boundary Layers at High Reynolds Number. *Journal of Fluid Mechanics,* 268(1), pp. 333-372.

Samimy, M., Reeder, M. F. & Elliott, G. S., 1992. Compressibility Effects on Large Structures in Free Shear Flows. *Physics of Fluids,* 4(6), pp. 1251-1258.

Samtaney, R., Pullin, D. I. & Kosovic, B., 2001. Direct Numerical Simulation of Decaying Compressible Turbulence and Shocklet Statistics. *Physics of Fluids,* 13(5), pp. 1415-1430.

Sandberg, R. D. & Fasel, H. F., 2006. Numerical Investigation of Transitional Supersonic Axisymmetric Wakes. *Journal of Fluid Mechanics,* Volume 563, pp. 1-41.

Sandham, N. D. & Reynolds, W. C., 1990. Compressible Mixing Layer: Linear Theory and Direct Simulation. *AIAA Journal,* April, 28(4), pp. 618-624.

Sandham, N. D. & Reynolds, W. C., 1991. Three-Dimensional Simulations of Large Eddies in the Compressible Mixing Layer. *Journal of Fluid Mechanics,* Volume 224, pp. 133-158.

Santiago, J. G. & Dutton, J. C., 1997. Velocity Measurements of a Jet Injected into a Supersonic Crossflow. *Journal of Propulsion and Power,* 13(2), pp. 264-273.

Sarkar, S., 1995. The Stabilizing Effect of Compressibility in Turbulent Shear Flow. *Journal of Fluid Mechanics,* Volume 282, pp. 163-186.

Sarkar, S., Erlebacher, G., Hussaini, M. Y. & Kreiss, H. O., 1991a. The Analysis and Modelling of Dilatational Terms in Compressible Turbulence. *Journal of Fluid Mechanics,* Volume 227, pp. 473-493.

Simon, F. et al., 2007. Numerical Simulation of the Compressible Mixing Layer Past an Axisymmetric Trailing Edge. *Journal of Fluid Mechanics,* Volume 591, pp. 215-253.

Slessor, M. D., Zhuang, M. & Dimotakis, P. E., 2000. Turbulent Shear-Layer Mixing: Growth-Rate Compressibility Scaling. *Journal of Fluid Mechanics,* Volume 414, pp. 35-45.

Smagorinsky, J., 1963. General Circulation Experiments with the Primitive Equations: I. The Basic Experiment. *Monthly Weather Review,* Volume 91, pp. 99-164.

Smart, M. K., 1999. Design of Three-Dimensional Hypersonic Inlets with Rectangular-to-Elliptical Shape Transition. *Journal of Propulsion and Power,* May-June, 15(3), pp. 408-416.

Smart, M. K., 2007. Scramjets. *Aeronautical Journal,* 111(1124), pp. 605-619.

Smart, M. K. & Tetlow, M. R., 2009. Orbital Delivery of Small Payloads Using Hypersonic Airbreathing Propulsion. *Journal of Spacecraft and Rockets,* 46(1), pp. 117-125.

Smith, K. M. & Dutton, J. C., 2001. The Effects of Expansion Strength on Large-scale Structures in Compressible Free Shear Layers. *Physics of Fluids,* July, 13(7), pp. 2076-2086.

Smits, A. J. & Dussauge, J.-P., 2006. *Turbulent Shear Layers in Supersonic Flow.* 2nd ed. s.l.:New York : Springer.

Spalart, P. R. & Allmaras, S. R., 1992. *A One-Equation Model for Aerodynamic Flows.* Reno, NV, The United States of America, AIAA.

Spalart, P. R., Jou, W. H., Strelets, M. & Allmaras, S. R., 1997. *Comments on the Feasibility of LES for Wings, and on a Hybrid RANS/LES Approach.* Ruston, Louisiana, U.S.A., Greyden, pp. 137-147.

Suraweera, M. V. & Smart, M. K., 2009. Shock Tunnel Experiments with a Mach 12 REST Scramjet at Off-Design Conditions. *Journal of Propulsion and Power,* 25(3), pp. 555-564.

Taylor, G. I., 1935. Statistical Theory of Turbulence. *Proceedings of the Royal Society of London,* Volume 151, pp. 421-444.

Turner, J. & Smart, M., 2009a. *Experimental Investigation of Inlet Injection in a Scramjet with Rectangular to Elliptical Shape Transition.* s.l., Springer Berlin Heidelberg, pp. 1117-1122.

Voelkl, T., Pullin, D. I. & Chan, D. C., 2000. A Physical-Space Version of the Stretched-Vortex Subgrid-Stress Model for Large-Eddy Simulation. *Physics of Fluids*, 12(7), pp. 1810-1825.

Vreman, A. W., Geurts, B. & Kuerten, H., 1995. Subgrid-modelling in LES of Compressible Flow. *Applied Scientific Research*, Volume 54, pp. 191-203.

Vreman, A. W., Sandham, N. D. & Luo, K. H., 1996. Compressible Mixing Layer Growth Rate and Turbulence Characteristics. *Journal of Fluid Mechanics*, Volume 320, pp. 235-258.

Vreman, B., Geurts, B. & Kuerten, H., 1997. Large-eddy Simulation of the Turbulent Mixing Layer. *Journal of Fluid Mechanics*, Volume 339, pp. 357-390.

Waidmann, W. et al., 1995. Supersonic Combustion of Hydrogen/Air in a Scramjet Combustion Chamber. *Space Technology*, 15(6), pp. 421-431.

Weber, R. J. & MacKay, J. S., 1958. *An Analysis of Ramjet Engines Using Supersonic Combustion*, s.l.: NACA.

Weinstein, A. S., Osterle, J. F. & Forstall, W., 1956. Momentum Diffusion from a Slot Jet into a Moving Secondary. *Journal of Applied Mechanics*, 23(3), pp. 437-443.

White, J. & Morrison, J., 1999. A Pseudo-Temporal Multi-Grid Relaxation Scheme for Solving the Parabolized Navier-Stokes Equations. *AIAA Journal*, Volume 99-3360, p. 15.

Wilcox, D. C., 1992. Dilatation-dissipation Corrections for Advanced Turbulence Models. *AIAA Journal*, November, 30(11), pp. 2639-2646.

Wilcox, D. C., 1998. *Turbulence Modeling for CFD.* 2nd ed. s.l.:La Cañada, Calif. : DCW Industries.

Wilcox, D. C., 2006. *Turbulence Modeling for CFD.* 3rd ed. s.l.:La Cañada, Calif. : DCW Industries.

Wilcox, D. C., 2008. Formulation of the k-omega Turbulence Model Revisited. *AIAA Journal*, November, 46(11), pp. 2823-2838.

Wilke, C. R., 1950. A Viscosity Equation for Gas Mixtures. *The Journal of Chemical Physics*, April, 18(4), pp. 517-519.

Williamson, C. H. K., 1996. Vortex Dynamics in the Cylinder Wake. *Annual Review of Fluid Mechanics*, 28(1), pp. 477-539.

Winant, C. D. & Browand, F. K., 1974. Vortex Pairing: the Mechanism of Turbulent Mixing-layer Growth at Moderate Reynolds Number. *Journal of Fluid Mechanics*, 63(2), pp. 237-255.

Zeman, O., 1990. Dilatation Dissipation: the Concept and Application in Modeling Compressible Mixing Layers. *Physics of Fluids*, February, 2(2), pp. 178-188.

Zhuang, M. & Dimotakis, P. E., 1995. Instability of Wake-dominated Compressible Mixing Layers. *Physics of Fluids*, October, 7(10), pp. 2489-2495.

A1 Governing Equations

The following mathematical expressions provide a description of the behaviour of thermally perfect gaseous mixtures. This description includes: the constitutive equations which govern fluid motion, the equations of state which relate various thermodynamic properties of gases, the transport properties which are used to determine various forms of diffusion, and the compressible laminar boundary-layer equations used to define the mixing wake in-flow.

A1.1 Constitutive Equations of Fluid Mechanics

For convenience, Einstein tensor notation will be used with summations performed for all indices except *i*, or any of the indices used to define a tensor element.

A1.1.1 Conservation of Mass

The conservation of total mass without nuclear reactions is given by:

$$\frac{\partial}{\partial t}(\rho)+\frac{\partial}{\partial x_j}\left(\rho u_j\right)=0 \qquad \text{A1.1}$$

A1.1.2 Conservation of Linear Momentum

The conservation of the i^{th} Cartesian component of linear momentum is given by:

$$\frac{\partial}{\partial t}\left(\rho u_i\right)+\frac{\partial}{\partial x_j}\left(\rho u_i u_j+p\delta_{ij}-\sigma_{ij}\right)=0 \qquad \text{A1.2}$$

For a Newtonian fluid, the viscous stress is linearly related to the viscous-strain rate. Stokes Law for mono-atomic gases dictates that the viscous stress tensor element is defined by

$$\sigma_{ij}=2\mu S_{ij}^{*} \qquad \text{A1.3}$$

Where μ is the kinematic viscosity transport parameter and S_{ij}^{*} is the trace-less viscous rate of strain tensor element, given by:

$$S_{ij}^{*}=\frac{1}{2}\left(\frac{\partial u_i}{\partial x_j}+\frac{\partial u_j}{\partial x_i}\right)-\frac{1}{3}\frac{\partial u_k}{\partial x_k}\delta_{ij} \qquad \text{A1.4}$$

The velocity gradient tensor is related to the symmetric strain rate tensor, S_{ij}, and the anti-symmetric vorticity tensor, Ω_{ij}, via:

$$\frac{\partial u_i}{\partial x_j}=S_{ij}+\Omega_{ij} \qquad \text{A1.5}$$

The dimensionless Reynolds number is defined as the ratio of internal momentum to viscous momentum, given by:

$$\mathrm{Re}_L=\frac{\rho UL}{\mu} \qquad \text{A1.6}$$

Where U is a characteristic velocity, and L is a characteristic length of the fluid flow.

A1.1.3 Conservation of Total Internal Energy

The equation governing the transport of mass specific total internal energy:

$$\frac{\partial}{\partial t}(\rho e_t) + \frac{\partial}{\partial x_j}\left(\rho e_t u_j + p u_j + q_j - \sigma_{jk} u_k\right) = 0 \qquad \text{A1.7}$$

The total internal energy is given as the sum of the static internal energy and the kinetic energy:

$$e_t = e + \frac{1}{2} u_k u_k \qquad \text{A1.8}$$

Fourier's law of heat conduction defines the heat flux as:

$$q_j = -\lambda \frac{\partial T}{dx_j} \qquad \text{A1.9}$$

Where λ is the thermal conductivity transport property. The dimensionless Prandtl number is defined as the ratio of momentum diffusivity to thermal diffusivity, given by:

$$\text{Pr} = \frac{c_p \mu}{\lambda} \qquad \text{A1.10}$$

A1.1.4 Conservation of a Passive Scalar

The equation governing the transport of passive scalar is given by:

$$\frac{\partial}{\partial t}\left(\rho Y_{S_i}\right) + \frac{\partial}{\partial x_j}\left(\rho Y_{S_i} u_j + J_{S_i j}\right) = 0 \qquad \text{A1.11}$$

Fick's law of diffusion defines the scalar flux as:

$$J_{S_i j} = -\rho D_{S_i} \frac{\partial Y_{S_i}}{dx_j} \qquad \text{A1.12}$$

Where D_{S_i} is the mass diffusivity transport parameter of chemical species S_i. The dimensionless Schmidt number is defined as the ratio of viscous diffusivity to mass diffusivity, and for chemical species S_i is given by:

$$\mathrm{Sc}_{S_i} = \frac{\mu}{\rho D_{S_i}} \qquad \text{A1.13}$$

A1.2 Equations of State

In order to close the Navier-Stokes equations, both a thermal and caloric equation of state must be prescribed. The thermal equation of state relates the static temperature and static pressure. The caloric equation of state defines the internal energy of a fluid at a particular condition, which can be determined by appealing to the combined laws of thermodynamics.

A1.2.1 Ideal Gas Law

It is assumed that the simulated fluid can be represented as a mixture of chemical species, each behaving as an ideal gas. The ideal gas law in a molar basis of a single chemical species S_i within a mixture of ideal gases provides a thermal equation of state, defined as:

$$p_{S_i} dV = \widehat{R}_U T dn_{S_i} \qquad \text{A1.14}$$

Where p_{S_i} is the partial static pressure of the chemical species S_i, V is the volume occupied by the gas, n_{S_i} is the number of moles of chemical species S_i, $\widehat{R}_U$ is the universal gas constant taken as 8.31434 J/mol.K, and T is the static temperature. Performing a sum for all locally present chemical species gives the ideal gas law of the local mixture:

$$\begin{gathered} \sum_{i=1}^{N_S} p_{S_i} dV = \sum_{i=1}^{N_S} \widehat{R}_U T dn_{S_i} \\ p dV = \widehat{R}_U T dn \end{gathered} \qquad \text{A1.15}$$

Where N_S is the total number of chemical species present, p is the static pressure of the local mixture of chemical species, and n is the total number of moles of the local mixture. By dividing

the ideal gas law of the individual chemical species with the ideal gas law of the mixture, it can be shown that:

$$\frac{p_{S_i}}{p} = \frac{dn_{S_i}}{dn} \tag{A1.16}$$

The molar faction is a convenient parameter for describing the composition of a local mixture of chemical species, which is define as:

$$X_{S_i} = \frac{dn_{S_i}}{dn} \tag{A1.17}$$

Hence it can be shown that:

$$\sum_{i=1}^{N_S} X_{S_i} = 1 \tag{A1.18}$$

It is appropriate at this point to introduce the partial static density of chemical species S_i, which is defined as:

$$\rho_{S_i} = \frac{dm_{S_i}}{dV} \tag{A1.19}$$

The ideal gas law can also be written in a mass basis by substituting the definition of static density of chemical species S_i into the law, which yields:

$$\rho_{S_i} \hat{R}_U T dn = p dm_{S_i} \tag{A1.20}$$

Performing a sum for all locally present chemical species gives the ideal gas law in a mass basis of the local mixture:

$$\begin{gathered} \sum_{i=1}^{N_S} \rho_{S_i} \hat{R}_U T dn = \sum_{i=1}^{N_S} p dm_{S_i} \\ \rho \hat{R}_U T dn = p dm \end{gathered} \tag{A1.21}$$

By dividing the ideal gas law of the individual chemical species in a mass basis with the law of the mixture, it can be shown that:

$$\frac{\rho_{S_i}}{\rho} = \frac{dm_{S_i}}{dm} \tag{A1.22}$$

In an equivalent fashion to molar fraction, the mass fraction can also be used to describe the composition of a local mixture of chemical species, which is defined as:

$$Y_{S_i} = \frac{dm_{S_i}}{dm} \tag{A1.23}$$

Hence it can be shown that:

$$\sum_{i=1}^{N_S} Y_{S_i} = 1 \tag{A1.24}$$

Converting between a molar basis and mass basis is achieved using a constant of proportionality, called the molar mass, which for chemical species S_i is defined as:

$$\widehat{m}_{S_i} = \frac{dm_{S_i}}{dn_{S_i}} \tag{A1.25}$$

The molar mass of hydrogen is 2.01588×10^{-3} kg/m^3, the molar mass of oxygen is 3.19988×10^{-2} kg/m^3, and the molar mass of nitrogen is 2.80134×10^{-2} kg/m^3. The representative molar mass of a local gaseous mixture can be determined by performing a sum of the product of the local mole fraction and molar mass of each locally present chemical species, which yields:

$$\begin{gathered}\sum_{i=1}^{N_S} \frac{dm_{S_i}}{dn} = \sum_{i=1}^{N_S} \frac{dm_{S_i}}{dn_{S_i}} \frac{dn_{S_i}}{dn} \\ \widehat{m} = \sum_{i=1}^{N_S} \widehat{m}_{S_i} X_{S_i}\end{gathered} \tag{A1.26}$$

Alternatively, the inverse representative molar mass of a local gaseous mixture can be determined from the sum of the quotient of the local mass fraction and molar mass of each locally present chemical species, given by:

$$\frac{1}{\widehat{m}} = \sum_{i=1}^{N_S} \frac{Y_{S_i}}{\widehat{m}_{S_i}} \qquad \text{A1.27}$$

By dividing the molar mass of the individual chemical species with the molar mass of the mixture, it can be shown that

$$\frac{\widehat{m}_{S_i}}{\widehat{m}} = \frac{dm_{S_i}}{dm}\frac{dn}{dn_{S_i}} = \frac{Y_{S_i}}{X_{S_i}} \qquad \text{A1.28}$$

A1.2.2 Specific Gas Constant

The mass specific gas constant of a local mixture of chemical species can be computed using:

$$\begin{aligned} R\left(Y_{S_i}\right) &= \frac{\widehat{R}_U}{\widehat{m}} \\ &= \widehat{R}_U \sum_{i=1}^{N_S} \frac{Y_{S_i}}{\widehat{m}_{S_i}} \end{aligned} \qquad \text{A1.29}$$

A1.2.3 Specific Heat Capacity

The temperature dependence of the isobaric molar specific heat capacity of chemical species S_i, $\widehat{c}_{p,S_i}$, can be approximated using empirically derived thermodynamic coefficients (McBride, et al., 1993):

$$\frac{\widehat{c}_{p,S_i}\left(T\right)}{\widehat{R}_U} = \frac{a_{1,S_i}}{T^2} + \frac{a_{2,S_i}}{T} + a_{3,S_i} + a_{4,S_i}T + a_{5,S_i}T^2 + a_{6,S_i}T^3 + a_{7,S_i}T^4 \qquad \text{A1.30}$$

The values of these coefficients are tabulated for the following chemical species: molecular hydrogen in Table A1.1, molecular oxygen in Table A1.2, and molecular nitrogen in Table A1.3.

For each species, different thermodynamic polynomial curve fits apply over three temperature ranges: a lower range with $T \geq 2.0\times10^{2}$ K and $T < 1.0\times10^{3}$ K, a middle range with $T \geq 1.0\times10^{3}$ K and $T < 6.0\times10^{3}$ K, and an upper range with $T \geq 6.0\times10^{3}$ K and $T < 2.0\times10^{4}$ K. The isochoric molar specific heat capacity of chemical species S_i, $\hat{c}_{\upsilon,S_i}$, can also be calculated using:

$$\frac{\hat{c}_{\upsilon,S_i}\left(T\right)}{\hat{R}_U} = \frac{\hat{c}_{p,S_i}\left(T\right) - \hat{R}_U}{\hat{R}_U} = \frac{\hat{c}_{p,S_i}\left(T\right)}{\hat{R}_U} - 1 \tag{A1.31}$$

The isobaric mass specific heat capacity of a local mixture of chemical species can be determined using:

$$c_p\left(T;Y_{S_i}\right) = \hat{R}_U \sum_{i=1}^{N_S} \frac{Y_{S_i}}{\hat{m}_{S_i}} \left(\frac{\hat{c}_{p,S_i}\left(T\right)}{\hat{R}_U} \right) \tag{A1.32}$$

The isochoric mass specific heat capacity of a local mixture of chemical species can be determined using:

$$\begin{aligned} c_\upsilon\left(T;Y_{S_i}\right) &= \hat{R}_U \sum_{i=1}^{N_S} \frac{Y_{S_i}}{\hat{m}_{S_i}} \left(\frac{\hat{c}_{V,S_i}\left(T\right)}{\hat{R}_U} \right) \\ &= \hat{R}_U \sum_{i=1}^{N_S} \frac{Y_{S_i}}{\hat{m}_{S_i}} \left(\frac{\hat{c}_{p,S_i}\left(T\right)}{\hat{R}_U} \right) - \hat{R}_U \sum_{i=1}^{N_S} \frac{Y_{S_i}}{\hat{m}_{S_i}} \\ &= c_p\left(T;Y_{S_i}\right) - R\left(Y_{S_i}\right) \end{aligned} \tag{A1.33}$$

Finally, the ratio of specific heats is define as:

$$\begin{aligned} \gamma\left(T;Y_{S_i}\right) &= \frac{c_p\left(T;Y_{S_i}\right)}{c_\upsilon\left(T;Y_{S_i}\right)} \\ &= \left(1 - \sum_{i=1}^{N_S} \frac{Y_{S_i}}{\hat{m}_{S_i}} \Bigg/ \sum_{i=1}^{N_S} \frac{Y_{S_i}}{\hat{m}_{S_i}} \left(\frac{\hat{c}_{p,S_i}\left(T\right)}{\hat{R}_U} \right) \right)^{-1} \end{aligned} \tag{A1.34}$$

Table A1.1: Empirical thermodynamic coefficients of molecular hydrogen

	$T \geq 2.0\times10^{2}$ K $T < 1.0\times10^{3}$ K	$T \geq 1.0\times10^{3}$ K $T < 6.0\times10^{3}$ K	$T \geq 6.0\times10^{3}$ K $T < 2.0\times10^{4}$ K
a_{1,H_2}	4.07832321×10^{4}	5.60812801×10^{5}	4.96688412×10^{8}
a_{2,H_2}	-8.00918604×10^{2}	-8.37150474×10^{2}	-3.14754715×10^{5}
a_{3,H_2}	8.21470201×10^{0}	2.97536453×10^{0}	7.98412188×10^{1}
a_{4,H_2}	-1.26971446×10^{-2}	1.25224912×10^{-3}	-8.41478921×10^{-3}
a_{5,H_2}	1.75360508×10^{-5}	-3.74071619×10^{-7}	4.75324835×10^{-7}
a_{6,H_2}	-1.20286027×10^{-8}	5.93662520×10^{-11}	$-1.37187349\times10^{-11}$
a_{7,H_2}	3.36809349×10^{-12}	$-3.60699410\times10^{-15}$	1.60546176×10^{-16}
b_{1,H_2}	2.68248466×10^{3}	5.33982441×10^{3}	2.48843352×10^{6}

Table A1.2: Empirical thermodynamic coefficients of molecular oxygen

	$T \geq 2.0\times10^{2}$ K $T < 1.0\times10^{3}$ K	$T \geq 1.0\times10^{3}$ K $T < 6.0\times10^{3}$ K	$T \geq 6.0\times10^{3}$ K $T < 2.0\times10^{4}$ K
a_{1,O_2}	-3.42556342×10^{4}	-1.03793902×10^{6}	4.97529430×10^{8}
a_{2,O_2}	4.84700097×10^{2}	2.34483028×10^{3}	-2.86610687×10^{5}
a_{3,O_2}	1.11901096×10^{0}	1.81973204×10^{0}	6.69035225×10^{1}
a_{4,O_2}	4.29388924×10^{-3}	1.26784758×10^{-3}	-6.16995902×10^{-3}
a_{5,O_2}	-6.83630052×10^{-7}	-2.18806799×10^{-7}	3.01639603×10^{-7}
a_{6,O_2}	-2.02337270×10^{-9}	2.05371957×10^{-11}	$-7.42141660\times10^{-12}$
a_{7,O_2}	1.03904002×10^{-12}	$-8.19346705\times10^{-16}$	7.27817577×10^{-17}
b_{1,O_2}	-3.39145487×10^{3}	-1.68901093×10^{4}	2.29355403×10^{6}

Table A1.3: Empirical thermodynamic coefficients of molecular nitrogen

	$T \geq 2.0\times10^{2}$ K $T < 1.0\times10^{3}$ K	$T \geq 1.0\times10^{3}$ K $T < 6.0\times10^{3}$ K	$T \geq 6.0\times10^{3}$ K $T < 2.0\times10^{4}$ K
a_{1,N_2}	2.21037150×10^{4}	5.87712406×10^{5}	8.31013916×10^{8}
a_{2,N_2}	-3.81846182×10^{2}	-2.23924907×10^{3}	-6.42073354×10^{5}
a_{3,N_2}	6.08273836×10^{0}	6.06694922×10^{0}	2.02026464×10^{2}
a_{4,N_2}	-8.53091441×10^{-3}	-6.13968550×10^{-4}	-3.06509205×10^{-2}
a_{5,N_2}	1.38464619×10^{-5}	1.49180668×10^{-7}	2.48690333×10^{-6}
a_{6,N_2}	-9.62579362×10^{-9}	$-1.92310549\times10^{-11}$	$-9.70595411\times10^{-11}$
a_{7,N_2}	2.51970581×10^{-12}	1.06195439×10^{-15}	1.43753888×10^{-15}
b_{1,N_2}	7.10846086×10^{2}	1.28321041×10^{4}	4.93870704×10^{6}

A1.2.4 Specific Enthalpy and Internal Energy

The molar specific static enthalpy of chemical species S_i is related to the molar specific isobaric heat capacity via the combined laws of thermodynamics, given by:

$$\widehat{h}_{S_i}(T) = \widehat{h}_{S_i,ref} + \int_{T_{ref}}^{T} \widehat{c}_{p,S_i}(t)\,dt \tag{A1.35}$$

Substituting the empirical coefficients into the enthalpy expression yields:

$$\frac{\widehat{h}_{S_i,ref}}{\widehat{R}_U} + \int_{T_{ref}}^{T} \frac{\widehat{c}_{p,S_i}(t)}{\widehat{R}_U}\,dt = \begin{array}{l} -\dfrac{a_{1,S_i}}{T} + a_{2,S_i}\ln(|T|) + a_{3,S_i}T + \dfrac{a_{4,S_i}}{2}T^2 \\ + \dfrac{a_{5,S_i}}{3}T^3 + \dfrac{a_{6,S_i}}{4}T^4 + \dfrac{a_{7,S_i}}{5}T^5 + b_{1,S_i} \end{array} \tag{A1.36}$$

The values of these coefficients are tabulated for the following chemical species: molecular hydrogen in Table A1.1, molecular oxygen in Table A1.2, and molecular nitrogen in Table A1.3. The mass specific static enthalpy of a local mixture of chemical species can be determined using:

$$h\left(T;Y_{S_i}\right)=\widehat{R}_U\sum_{i=1}^{N_S}\frac{Y_{S_i}}{\widehat{m}_{S_i}}\left(\frac{\widehat{h}_{S_i,ref}}{\widehat{R}_U}+\int_{T_{ref}}^{T}\frac{\widehat{c}_{p,S_i}\left(t\right)}{\widehat{R}_U}dt\right) \quad \text{A1.37}$$

The combined laws of thermodynamics relate the internal energy and of a mixture of ideal gases via:

$$e\left(T;Y_{S_i}\right)=h\left(T;Y_{S_i}\right)-\frac{p}{\rho} \quad \text{A1.38}$$

A1.3 Transport Properties

Sutherland's law for predicting variations in kinematic molecular viscosity and thermal conductivity of a single chemical species with static temperature is given by:

$$\mu_{S_i}=\mu_{S_i}^0\left(T/T_{S_i}^0\right)^{\frac{3}{2}}\frac{1+S_{S_i}/T_{S_i}^0}{T/T_{S_i}^0+S_{S_i}/T_{S_i}^0} \quad \text{A1.39}$$

$$\lambda_{S_i}=\lambda_{S_i}^0\left(T/T_{S_i}^0\right)^{\frac{3}{2}}\frac{1+S_{S_i}/T_{S_i}^0}{T/T_{S_i}^0+S_{S_i}/T_{S_i}^0} \quad \text{A1.40}$$

The hydrogen, oxygen and nitrogen Sutherland coefficient values for: the kinematic molecular viscosity are defined in Table A1.4, and the thermal conductivity are defined in Table A1.5.

Table A1.4: Sutherland coefficients of kinematic molecular viscosity

S_i	$\mu_{S_i}^0$	$T_{S_i}^0$	S_{S_i}
H_2	8.97383478×10^{-6}	3.00000000×10^{2}	1.30667324×10^{2}
O_2	2.07429854×10^{-5}	3.00000000×10^{2}	1.49774296×10^{2}
N_2	1.79059092×10^{-5}	3.00000000×10^{2}	1.36773324×10^{2}

Table A1.5: Sutherland coefficients of thermal conductivity

S_i	$\lambda_{S_i}^0$	$T_{S_i}^0$	S_{S_i}
H_2	1.87808749×10^{-1}	3.00000000×10^{2}	1.66395528×10^{2}
O_2	2.65963673×10^{-2}	3.00000000×10^{2}	2.53134992×10^{2}
N_2	2.61504985×10^{-2}	3.00000000×10^{2}	1.97055369×10^{2}

Wilke's law (Wilke, 1950) for estimating a representative molecular viscosity of a mixture of chemical species

$$\mu = \sum_{i=1}^{N_S}\left(X_{S_i}\mu_{S_i} \Big/ \sum_{j=1}^{N_S} X_{S_j}\phi_{S_i}^{S_j} \right) \qquad \text{A1.41}$$

Where,

$$\phi_{S_i}^{S_j} = \left(1+\sqrt{\frac{\mu_{S_j}}{\mu_{S_i}}\sqrt{\frac{\widehat{m}_{S_j}}{\widehat{m}_{S_i}}}} \right)^2 \Bigg/ \sqrt{8\left(1+\frac{\widehat{m}_{S_i}}{\widehat{m}_{S_j}}\right)} \qquad \text{A1.42}$$

Wassajewa's law for estimating a representative thermal conductivity of a mixture of chemical species is given by:

$$\lambda = \sum_{i=1}^{N_S} \left(X_{S_i} \lambda_{S_i} \Big/ \sum_{j=1}^{N_S} X_{S_j} \varphi_{S_i}^{S_j} \right) \tag{A1.43}$$

Where,

$$\varphi_{S_i}^{S_j} = \left(1 + \sqrt{\frac{\lambda_{S_j}}{\lambda_{S_i}} \sqrt{\frac{\widehat{m}_{S_j}}{\widehat{m}_{S_i}}}} \right)^2 \Bigg/ \sqrt{8 \left(1 + \frac{\widehat{m}_{S_i}}{\widehat{m}_{S_j}} \right)} \tag{A1.44}$$

The binary mass diffusion coefficient of chemical species S_i into species S_j can be calculated using the Chapman-Ergonsk theory, which states:

$$D_{S_i}^{S_j} = \frac{C_D T^{\frac{3}{2}}}{p \Lambda_{S_i}^{S_j} \Omega_D} \sqrt{\frac{1}{\widehat{m}_{S_i}} + \frac{1}{\widehat{m}_{S_j}}} \tag{A1.45}$$

Where C_D is a diffusion scaling factor, $\Lambda_{S_i}^{S_j}$ is the characteristic collision length between particles of chemical species S_i with species S_j, and Ω_D is the dimensionless collision integral. The diffusion scaling factor is dependent on the molar masses of the diffusing chemical species, which is estimated using:

$$C_D = \frac{1.533 \times 10^{-23}}{\sqrt{10}} + 3.52 \times 10^{-26} \sqrt{\frac{1}{\widehat{m}_{S_i}} + \frac{1}{\widehat{m}_{S_j}}} \tag{A1.46}$$

The characteristic collision length of: hydrogen is 2.92×10^{-10} m, oxygen is 3.51×10^{-10} m, and nitrogen is 3.69×10^{-10} m. Using the Lorentz-Berthelot combination rules, the characteristic collision length for binary diffusion is given by arithmetic mean:

$$\Lambda_{S_i}^{S_j} = \frac{\Lambda_{S_i} + \Lambda_{S_j}}{2} \tag{A1.47}$$

The dimensionless collision integral is approximated by the analytic formulation of Poling et al. (2000):

$$\Omega_D = \frac{1.06036}{T_D^{\,0.1561}} + \frac{0.1930}{e^{0.47635T_D}} + \frac{1.03587}{e^{1.52996T_D}} + \frac{1.76474}{e^{3.89411T_D}} \qquad \text{A1.48}$$

Where T_D is a dimensionless temperature defined as:

$$T_D = \frac{k_B T}{\mathrm{E}_{S_i}^{S_j}} \qquad \text{A1.49}$$

Here the Boltzmann constant, k_B, is assumed to be $1.3806488 \times 10^{-23}$ J/K, and using the Lorentz-Berthelot combination rules again yields a characteristic collision potential energy for binary diffusion as the geometric mean:

$$\mathrm{E}_{S_i}^{S_j} = \sqrt{\mathrm{E}_{S_i}\mathrm{E}_{S_j}} \qquad \text{A1.50}$$

The characteristic collision potential energy of: hydrogen is 5.20×10^{-22} J/particle, oxygen is 1.59×10^{-21} J/particle, and nitrogen is 1.28×10^{-21} J/particle. Combining the Chapman-Ergonsk theory with the ideal gas law provides the following definition of the Schmidt number:

$$\begin{aligned} \mathrm{Sc}_{S_i}^{S_j} &= \frac{\mu}{\rho D_{S_i}^{S_j}} \\ &= \frac{\mu R \Lambda_{S_i}^{S_j} \Omega_D}{C_D} \sqrt{\frac{\hat{m}_{S_i}\hat{m}_{S_j}}{T\left(\hat{m}_{S_i} + \hat{m}_{S_j}\right)}} \end{aligned} \qquad \text{A1.51}$$

Note that the Schmidt number of binary diffusion is dependent on the local gas composition. The Schmidt number of hydrogen, oxygen and nitrogen diffusion permutations is shown in Figure A1.24. It is reasonable to assume that for temperatures above 500 K the Schmidt number of hydrogen, oxygen and nitrogen diffusion permutations remains temperature invariant, but that diffusion between the various species takes notably different values, namely: $\mathrm{Sc}_{H_2}^{O_2} = \mathrm{Sc}_{H_2}^{N_2} = 0.2$, $\mathrm{Sc}_{N_2}^{O_2} = \mathrm{Sc}_{O_2}^{N_2} = 0.9$, and $\mathrm{Sc}_{O_2}^{H_2} = \mathrm{Sc}_{N_2}^{H_2} = 1.5$.

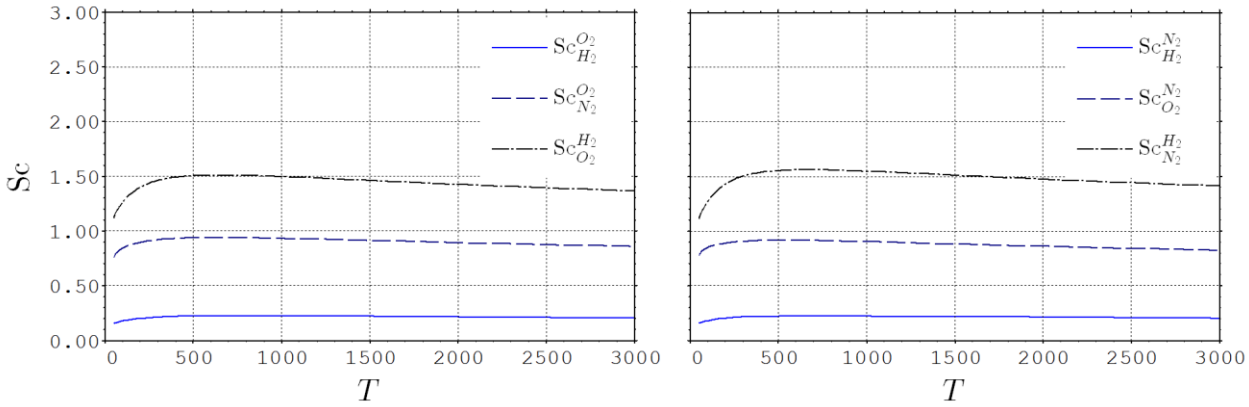

Figure A1.24: Trends in Schmidt number with static temperature for binary mixing between hydrogen, oxygen and nitrogen.

Wilke derived from the Maxwell-Stefan equations that the mass diffusion coefficient of chemical species S_i into a mixture of chemical species can be determined using:

$$\rho D_{S_i} = \left(1 - X_{S_i}\right)\left[\sum_{\substack{j=1 \\ j\neq i}}^{N_S} \frac{X_{S_j}}{\rho D_{S_i}^{S_j}}\right]^{-1} \qquad \text{A1.52}$$

Substituting the definition of the Schmidt number into Wilke's derivation yields

$$\rho D_{S_i} = \mu \sum_{\substack{j=1 \\ j\neq i}}^{N_S} \frac{Y_{S_j}}{\hat{m}_{S_j}} \left[\sum_{\substack{j=1 \\ j\neq i}}^{N_S} \frac{Y_{S_j}}{\hat{m}_{S_j}} \mathrm{Sc}_{S_i}^{S_j}\right]^{-1} \qquad \text{A1.53}$$

A1.4 Compressible Laminar Boundary-Layer

The boundary layer equations of a compressible fluid were solved to provide the in-flow profiles of the mixing wake simulation. These equations can be transformed into self-similar coordinates using a variety of methods. For this analysis, the Illingworth-Levy transformation is employed. These equations are represented by a system of two coupled ordinary differential equations which are dependent on a normalised cross-stream coordinate, η, and are given by:

$$\frac{d}{d\eta}\left(C\frac{d^2 f}{d\eta^2}\right)+f\frac{d^2 f}{d\eta^2}=0 \qquad \text{A1.54}$$

$$\frac{d}{d\eta}\left(\frac{C}{\mathrm{Pr}}\frac{dg_h}{d\eta}\right)+f\frac{dg_h}{d\eta}+C\frac{U_e^{\,2}}{h_e}\frac{d^2 f}{d\eta^2}^{\,2}=0 \qquad \text{A1.55}$$

Where the subscript e represents the edge, or free-stream, condition of the boundary-layer, and the following expressions apply:

$$\frac{df}{d\eta}(\eta)=\frac{U(\eta)}{U_e},\quad g_h(\eta)=\frac{h(\eta)}{h_e},\quad C=\frac{T_e}{T(\eta)}\frac{\mu\left(T(\eta)\right)}{\mu_e},\quad \mathrm{Pr}=\frac{\mu c_p}{\lambda}$$

The transformed enthalpy function can be written as a function of temperature using:

$$g_h\left(T(\eta)\right)=\frac{h\left(T(\eta)\right)}{h_e} \qquad \text{A1.56}$$

Apply the chain rule provides the following relationships:

$$\frac{dg_h}{d\eta}=\frac{c_p}{h_e}\frac{dT}{d\eta} \qquad \text{A1.57}$$

$$\frac{d^2 g_h}{d\eta^2}=\frac{1}{h_e}\left(\frac{dc_p}{dT}\frac{dT}{d\eta}^{\,2}+c_p\frac{d^2 T}{d\eta^2}\right) \qquad \text{A1.58}$$

It is advantageous to introduce the transformed temperature function which is defined as:

$$g(\eta)=\frac{T(\eta)}{T_e} \qquad \text{A1.59}$$

Subsequently:

$$T=T_e g,\quad \frac{dT}{d\eta}=T_e\frac{dg}{d\eta},\quad \frac{d^2 T}{d\eta^2}=T_e\frac{d^2 g}{d\eta^2}$$

Substituting these terms into the original differential equations and re-writing them as a function of the transformed velocity and temperature functions yields:

$$\frac{d^3 f}{d\eta^3} = -\left(\left(\frac{T_e}{\mu}\frac{d\mu}{dT} - \frac{1}{g}\right)\frac{dg}{d\eta} + \frac{f}{C}\right)\frac{d^2 f}{d\eta^2} \qquad \text{A1.60}$$

$$\frac{d^2 g}{d\eta^2} = -\left(\left(\frac{T_e}{\lambda}\frac{d\lambda}{dT} - \frac{1}{g}\right)\frac{dg}{d\eta} + \Pr\frac{f}{C}\right)\frac{dg}{d\eta} - \frac{\Pr}{c_p}\frac{U_e^{\,2}}{T_e}\frac{d^2 f}{d\eta^2}^2 \qquad \text{A1.61}$$

In order to solve these differential equations, the following boundary conditions were applied:

$$\eta = 0: \quad \frac{df}{f\eta} = 0, \quad g = \frac{300}{T_e}$$

$$\eta \to \infty: \quad \frac{df}{f\eta} = 1, \quad \frac{d^2 f}{f\eta^2} = 0, \quad g = 1$$